A TOPOLOGICAL STUDY ON INDETERMINATE-ORIGIN JETS

Thesis submitted in accordance with the requirements of the
University of Liverpool for the degree of Doctor in Philosophy

by

Dimitris E. Tsovolos

July 2010

STATEMENT OF ORIGINALITY

This thesis has been submitted for the degree of Doctor of Philosophy, at the School of Engineering of the University of Liverpool

The research herein, unless otherwise stated, was carried out by the author in the Fluids Engineering Division of the School of Engineering, at The University of Liverpool.

No part of this thesis has been submitted for a degree to any other university or educational establishment.

Dimitris E. Tsovolos

July 2010

Dedicated to,

Jessie R. Parry and William G. Parry

ABSTRACT

An experimental study has been conducted to elucidate the flow-field characteristics of unsteady jets issued from circular and elliptic indeterminate-origin (IO) nozzles. A Reynolds number of 2100 was used throughout and axial flow perturbation was imposed on all test cases presented within this thesis. The circular test nozzles consisted of A- and V-shaped notches, while the elliptic nozzles only incorporated V-shaped lip modifications, which were imposed across the major (V-major nozzle) or minor (V-minor nozzle) axis of the elliptic geometry. For both circular and elliptic nozzles, two sets of designs with different peak and trough sharpness were manufactured and tested.

For comparative purpose, two reference nozzle geometries were used, a circular and an elliptic case respectively. The reference nozzles did not incorporate any lip modifications and produced plane-symmetric flow-fields. The circular case resulted in stable main ring vortices which propagated downstream by approximately five jet-diameters before breaking down, while the elliptic nozzle produced main ring vortices that underwent axis-switching. The potential core lengths were measured at 5.8 and 5.2 jet-diameters for the circular and elliptic nozzle respectively.

The circular IO jets showed that peaks and troughs cause significant flow-field changes compared to the reference case. Non-circular jet cross-sections were achieved with preferential spreading along the plane consisting of the nozzle peaks. It was also shown that the peaks where responsible for increasing the generation of streamwise vortices and turbulence. The V-notched nozzle geometry, compared to the A-notched nozzle, showed an increase in flow activity along the peak locations, producing larger streamwise vortices and a wider jet spread. The high aspect-ratio test cases increased the breakdown of the main ring vortices and promoted a faster transition to turbulence. Finally, it was found that both A- and V-notched nozzles demonstrated elliptic-like flow fields, resulting in the main ring vortices undergoing axis-switching.

The elliptic jets were also affected by the peaks and troughs. Depending on the orientation of the V-notched cut, the resultant large scale coherent structures as well as the generation of streamwise vortices were affected. Extraneous flow features arose, which in some cases were shown to promote loss of large-scale coherent structuring and faster transition to turbulence. Interestingly, the axis-switching behaviour, which is inherent in elliptic jets of moderate aspect-ratio, was manipulated by the location of the V-notch and the relative sharpness of the imposed cut. Results from the V-minor geometry, showed that the location at which axis-switching occurred shifted downstream, while when the V-major geometry

was tested, axis-switching was suppressed altogether. Increasing the relative sharpness of the nozzles had different effects for both nozzles. In the V-minor case, an increase of the jet potential core was noticed and the axis-switching location moved further downstream. The V-major nozzle, caused a reduction of the jet potential core, possibly due to an increased interaction between the jet and the surrounding ambient fluid.

TABLE OF CONTENTS

LIST OF FIGURES

ACKNOWLEDGEMENTS

The author would like to sincerely thank, first and foremost, his parents who provided economic assistance for the first year of the research program and ample encouragement throughout the whole process. Without their help, this PhD study would not have materialised.

I would like to extend my gratitude to my supervisors, Dr T.H. New and Professor I. Owen, for the time spent and effort put into guiding me through the experimental techniques and providing me with a well-planned and well-structured research program. Additionally, I would like to thank Dr T.H. New, for his vital effort and contribution towards both journal and conference publications generated from this research study. Finally I would like to thank him for his effort and patience when proof-reading my thesis drafts.

I am grateful to Professor G.D. Padfield, for his pivotal role in providing me an EPSRC-DTA funding at the end of the first year.

I would like to thank my examiners, Dr S. Zhong, and Dr M.W. Johnson, for their time and effort reading through and correcting this thesis.

I would like to kindly thank the secretarial staff at the University of Liverpool postgraduate office and especially Mrs Lesia Swain and Mrs Denise Bain for their prompt and efficient assistance, whenever needed.

Last, but in no way least, I would like to thank my colleagues and friends at the University of Liverpool fluids research office. Additionally, my humble gratitude and appreciation is extended to Dr Kosmas G. Panagiotidis, Dr Panagiotis Grammatikopoulos, Dr Konstantinos Gerogakopoulos and Dr Vassilis Ioakimidis, for including me in fierce philosophical (scientific, political and social) debates. Admittedly, in most cases the discussions rose beyond my mental ability, but nevertheless, I gained much.

NOMENCLATURE

AR	Aspect ratio
D	Equivalent diameter (m)
d	Particle diameter (m)
f	Forcing frequency (Hz)
IO	Indeterminate-origin
k	Mass diffusivity (m^2/s)
px	Pixel
U_0	Mean jet exit velocity (m/s)
$U_{x/d}$	Maximum jet velocity at a given cross-stream location
ν	kinematic viscosity (m^2/s)
u'	Velocity fluctuation along X-axis (m/s)
v'	Velocity fluctuation along Y-axis (m/s)
w'	Velocity fluctuation along Z-axis (m/s)
$y_{0.5}$	Half jet width (m)
Re	Reynolds number ($=U_0D/\nu$)
St_D	Strouhal number ($=fD/U_0$)
TKE	Turbulent kinetic energy (J)
$\overline{u'u'}/U_0^2$	Normalised normal Reynolds stress (x-axis)
$\overline{v'v'}/U_0^2$	Normalised normal Reynolds stress (y-axis)
$\overline{w'w'}/U_0^2$	Normalised normal Reynolds stress (z-axis)
$\overline{u'v'}/U_0^2$	Normalised Reynolds shear stress (xy-plane)
$\overline{w'v'}/U_0^2$	Normalised Reynolds shear stress (zy-plane)
θ	Momentum thickness defined as $\vartheta = \frac{1}{2}\int_{u_{0.1}}^{u_{0.9}} \frac{u(x)}{U_{x/d}}\left(1-\frac{u(x)}{U_{x/d}}\right)dy$
ν/k	Schmidt number
σ_u	Root-mean-square error in the velocity measurement

1 MOTIVATION AND OBJECTIVES

1.1 Introduction

The study of jets, sprays and vortex rings have been research topics which have generated a lot of interest. A plethora of practical applications exist in which fluid is issued by an orifice or a nozzle. These applications range from aeroengines (2002; Papamoschou, 2004, 1997; Papamoschou and Debiasi, 2001, 1999), to combustion processes (Nathan *et al.*, 2006; Wong *et al.*, 2008), commercial spray painting processes (Shu, 2005; Shu *et al.*, 2005) and even to volcano eruptions as was recently demonstrated in Iceland by the Eyjafjallajokul volcano (April 2010). The interest as well as the applicability of the subject, contributed towards maintaining the research momentum for many years.

Amongst the broad range of interest, the field of aeroacoustics has been researched heavily. Particularly in recent times, where jet noise pollution and its environmental implications is a high priority for many governing authorities. As far back as 1952 the study of sound generation was investigated and theories were stipulated. It was found that aerodynamic sound was generated due to velocity fluctuations (or turbulence in the flow) (Lighthill, 1952, 1962). Following on from and based on the general theory governing sound radiation from fluid flow, further studies were concentrated towards the sound generation and sound control in jets (Lighthill, 1963). Since then, the notion of noise control is still being investigated and is particularly important with aeroengine development. Major contributors to this research area have used passive flow control techniques such as indeterminate-origin nozzles in the form of chevrons to reduce the sound pressure levels by as much as 6dB (Callender *et al.*, 2005). Others have used annular (Papamoschou, 1997) and eccentrically positioned dual stream arrangements. In the first instance the Mach waves radiated by the jet plume can be eliminated thus resulting in reduced jet noise while in the latter instance the better mixing between the two streams resulted in the reduction of the potential core of the jet, which is related to the jet noise emission levels. Additionally, a change in the direction of the sound wave propagation was achieved, as the downward directed sound produced by the jet was cancelled out due to the eccentric coflow (Papamoschou and Debiasi, 2001; Murakami and Papamoschou, 2002). Recently the application of noise reducing nozzles has been tested by major commercial aircraft manufacturers such as Boeing. During their QTD2 (quiet technology demonstrator) program a chevron nozzle geometry was tested and resulted in a sound reduction of up to 15dB. When it came to designing the new B-787 Dreamliner aircraft, a reduction in the cabin sidewall insulation was made, thus reducing the overall aircraft weight and also allowing for a better passenger seating configuration (Boeing, 2010).

Developments in the reduction of the jet heat signature have also been researched and the use of indeterminate origin nozzle geometries have been noticed. Unfortunately due to the restricted nature of such research, it is difficult to find information in open literature. However by observing the design history embraced by aircraft manufacturers one can see a change from conventionally shaped symmetric nozzles, towards asymmetric indeterminate origin ones. Good examples are the Lockheed Martin F-22 (rhomboid shaped nozzle) and F-35B (chevron shaped nozzle) aircrafts (Lockheed, 2010).

1.1.1 Study of jet development and coherent structures

More relevant to this particular study is the research associated with fluid issued from nozzles. Within this broad area of interest, studies on vortex rings and jets exist. Despite the large deviation in flow conditions found between jet flows and the impulsive generation of vortex rings, coherent flow features can be detected in both cases. It has been shown that coherent and ordered structures exist in jet flow regimes ranging from laminar, $Re=10^3$ to turbulent, $Re=10^5$. These organised structures start off as shear layer rollups and as the Reynolds number increases transform to a train of waves and puffs (Crow and Champagne, 1971). Additionally it was shown that the jet-noise spectrum peaked at a Strouhal number (St_D) of 0.3 and thus was suggested that the underlying wave structures could be responsible for the generation of sound (Mollochristensen *et al.*, 1964), which inferred to the correlation between coherent structures and jet noise. Another study, by Hussain (1986), focused on the definition of coherent structures, their identification and on the techniques that assisted the study of such structures. Like other researchers, the relationship between coherent vortical structures and noise generation was also investigated. He derived an analytical solution for sound intensity prediction, which was in agreement with findings from previous studies (Lighthill, 1952). However, using the equation it was shown that an additional factor also contributed to sound emission. This was the degree of vorticity concentration in the flow. Thus the pairing process and interactions of vortical structures, responsible for aerodynamic sound emission, could be explained by study of vorticity dynamics.

Vortex rings are coherent structures which can be formed when a slug of fluid undergoes impulsive movement. Several specific areas have been studied such as, the mixing and entrainment process of vortex rings (Maxworth.T, 1972; Oshima, 1972; Maxworth.T, 1974; Cantwell, 1986; Glezer, 1988; Gharib *et al.*, 1998; Kida *et al.*, 1991), sound generation due to the rings (Minota *et al.*, 1988; Kambe *et al.*, 1993) and the interaction of ring with other rings or wall structures. Within the last category, interactions such as vortex leapfrogging, vortex ring collisions (Kida *et al.*, 1991; Lim and Nickels, 1992) (head-on or at an angle) and collisions with "slip" or "no-slip" walls are the most prominent. Some recent studies

have also conducted experiments of indeterminate-origin nozzles (Lim, 1998; Webster and Longmire, 1998; Troolin and Longmire, 2010). It was shown that vortices produced from inclined nozzles were tilted with respect to the nozzle centreline and consequently moved away from it as they propagated downstream. Results showed that the non-uniform circulation around the circumference of the vortex rings caused the movement. Thus a passive technique for controlling the resultant coherent vortical structures was demonstrated. The use of inclined nozzles with the intention of controlling a jet flow field has also been studied and will be presented in the next section.

Due to the direct application to problems such as, the emission of effluent into the atmosphere via a chimney, gas turbine blade cooling as well as exhaust gas cooling, the study of jets in cross flow has led the way towards understanding the associated complex flow patterns (Chassain.P *et al.*, 1974; Andreopoulos, 1985). Using flow visualisation techniques as well as hot wire anemometry in conjunction with the critical point theory, several coherent structures were identified and are represented in Fig. 1.1 (Kelso *et al.*, 1996). The main structures identified were as follows; a horseshoe vortex system found upstream of the jet, a separation region inside the jet situated close to the jet exit, the rollup of the jet shear layer forming counter-rotating Kelvin-Helmholtz vortices and a boundary

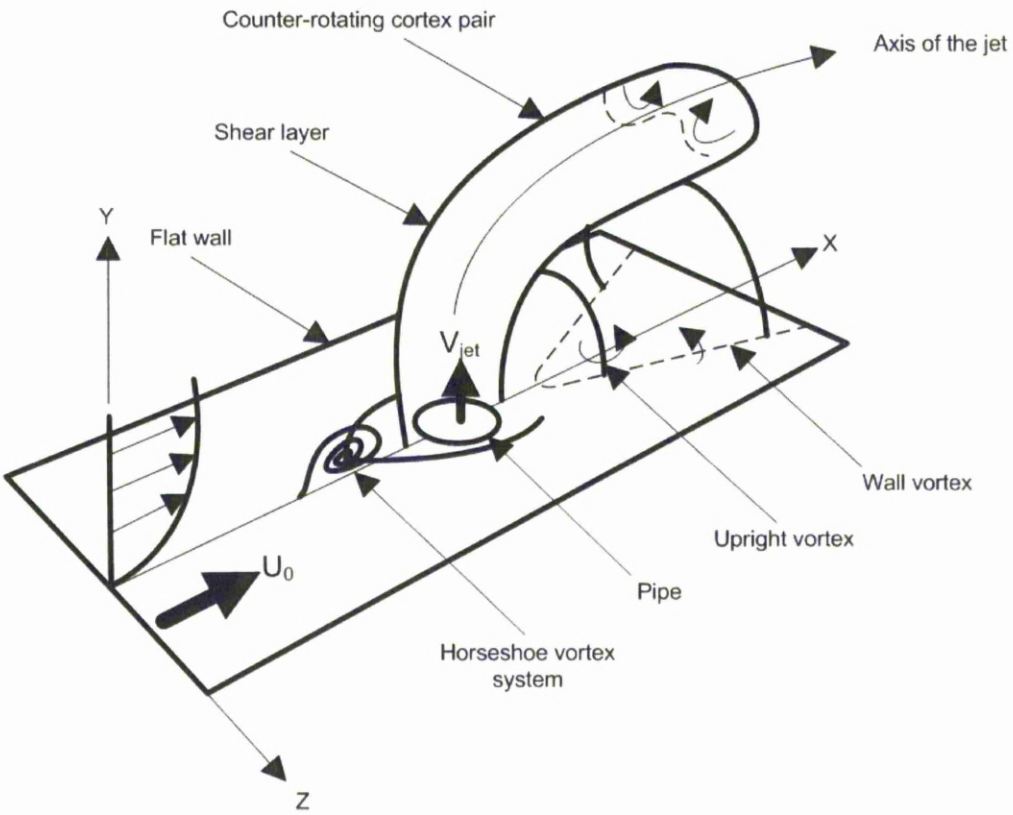

Figure 1.1 Schematic illustration of a jet in cross flow

layer separation leading to the formation of a wake-type vortex street situated downstream of the jet. More specifically these structures depend on the jet to free-stream velocity ratio as well as the jet Reynolds number. For example when experiments were carried out at a Reynolds number of 1600 and a velocity ratio of 4, the counter rotating vortex structure broke down which contributed towards better mixing properties of the jet. More recently elliptic jets in cross flow have been examined (Lim *et al.*, 2006; New, 2008). The first study concluded that in addition to the jet initial conditions such as velocity profile and boundary layer thickness which have been shown to alter the jet trajectory, the jet exit geometry also has an effect on it. The second study focused on effects of higher aspect ratio jets with the use of particle image velocimetry. Findings show that compared to circular jets, elliptic jets produce higher peak vorticity values and when the ellipse aspect ratio is increased, stronger flow reversals occur. However the increased aspect ratio did not promote more intense counter-rotating vortex pairs and in effect, did not promote better mixing.

1.1.2 Flow field control of near-nozzle region

Understanding the flow mechanisms and eventually controlling the near-nozzle flow field in a predictable manner has many beneficial implications. There are two methods for controlling the flow field of a jet. The first is by passive control, where external energy is not required to perturb the flow. Usually nozzle designs with asymmetric cross-sections, indeterminate-origins and nozzles with lobbed exits, thrive in this category. By promoting the generation of streamwise vortices, these nozzles are able to alter and control the flow field. The second category is active control, where external energy is required to control the flow. Although this method can result in better flow control and very large amounts of mixing, energy expenditure and the fact that they rely on an external source make them less efficient, more costly and in some cases more difficult to implement in real applications. Actuated flaps (Suzuki *et al.*, 2004; Angele *et al.*, 2006), synthetic and air jets arranged circumferentially around the jet (Raman and Cain, 2002; Yuan *et al.*, 2004) well as electric discharge plasmas (Samimy *et al.*, 2007) have been used as means to control the resultant flow field.

a) Passive control

The term "indeterminate-origin" jet was first used by (Wlezien and Kibens, 1986) and was used to characterise a nozzle whose exit axial lip position changed around the nozzle circumference. Another way of describing such nozzle geometries is effectively, nozzles whose exit (lip) circumference does not lie on the same plane. Examples include nozzles with inclined exits (Webster and Longmire, 1997; Lim, 1998; Webster and Longmire, 1998), stepped nozzles (Wlezien and Kibens, 1986; Longmire and Duong, 1996), crown-shaped

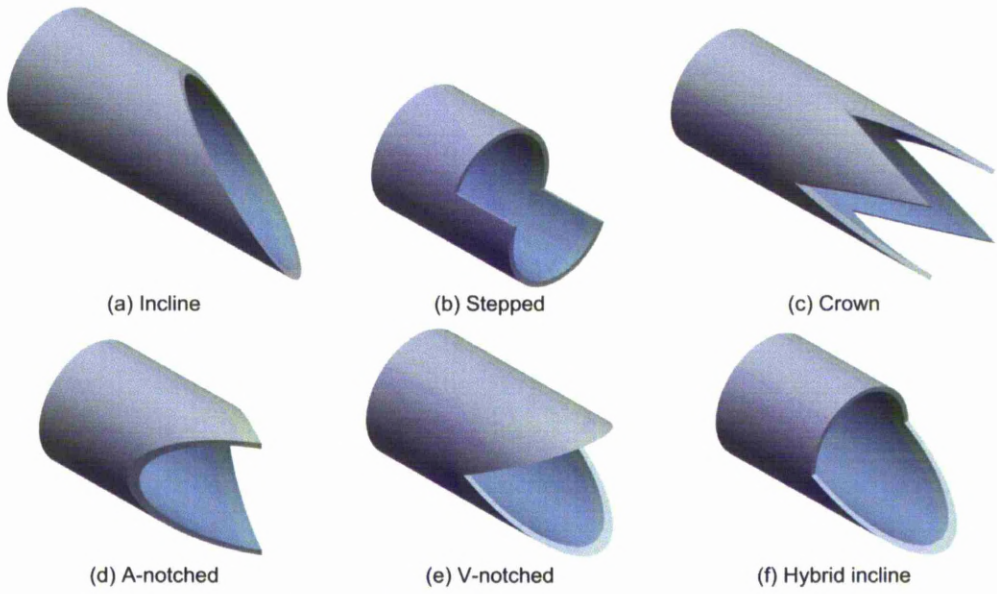

Figure 1.2 A selection of indeterminate-origin nozzle geometries

geometries (Longmire *et al.*, 1992a; Shu *et al.*, 2005; Tsovolos and New, 2008), A- and V-notched nozzles (New *et al.*, 2005; New and Tsai, 2007), as well as hybrid inclined nozzles (New and Tsovolos, 2009b). In Fig. 1.2, an array of indeterminate-origin nozzle geometries is shown.

Incline and stepped geometries

Incline and stepped nozzle geometries were amongst the first to be investigated. These geometries were easy to construct and set the path for many following studies on the subject. An experimental study conducted on incline nozzles, using particle image velocimetry (PIV) measurements, showed that the vortex ring formation followed the incline angle of the nozzle, however the speed and penetration distance of the ring decreased as the incline angle increased. Thus, faster vortex breakdown was achieved by increasing the incline angle. Additionally, apart from the main ring formation, secondary vortical structures appeared which initiated from the short side of the nozzle. These vortical structures were thought to be formed as a result of the increased entrainment from the main vortex ring (Webster and Longmire, 1998). A very recent study which made use of a state-of-the-art volumetric PIV technique showed that these secondary structures were also caused by the sudden stopping of the piston and interacted with the main vortex ring (Troolin and Longmire, 2010). Between the first and second studies, an investigation using flow visualisation shed light on the breakdown process associated with the vortex ring (Lim, 1998). Several incline angles were examined and was postulated that increasing the incline angle causes faster vortex breakdown. The reason behind this phenomenon was due to circumferential flow in the core caused by a differential rate of vortex stretching. The circumferential flow was thought to be

linked to the nozzle incline angle and thus when the angle increases the breakdown process manifested rapidly. A study conducted on jets issued form stepped and sawtooth geometry nozzles also found that the primary vortex rings followed the nozzle lip contour (Longmire and Duong, 1996). Additionally, secondary structures were found that were oriented in the longitudinal direction. The presence of steps (or discontinuities) in the nozzle geometry promoted the development of longitudinal vorticity. Finally, under axial forcing at a St_D of 0.32 it was shown that the jet bifurcated and produced the greatest diversion of the jet column. Taking all of the available information on board (New and Tsovolos, 2009b) conducted an experimental study at a low Reynolds number under forced conditions using flow visualisation and PIV techniques. The "hybrid-inclined" nozzles used, consisted of two half-nozzles put together and was similar to the stepped nozzle used in previous studies. However, the top half was circular and the bottom half had a peak of elliptic planform, as shown in Fig. 1.2(f). This nozzle geometry incorporated flat sections, a peak and two distinct discontinuities (kinks) where the flat and inclined sections met. Flow visualisation results showed that the main ring vortices that formed, similar to the ones formed form an inclined nozzle, followed the nozzle lip contour and thus formed inclined with respect to the jet axis. Quantitative results showed that the resultant flow field was asymmetric and that streamwise oriented vortices formed at the peak of the nozzle. These vortices ejected fluid radially outwards and thus increased the jet-spread asymmetrically.

Crown geometry

When research interest moved to crown-shaped IO nozzles, several designs were implemented. These designs ranged from many peaks (usually called chevron nozzles) to only two peaks (Longmire *et al.*, 1992a; Shu *et al.*, 2005). A typical example of a crown-shaped nozzle geometry is show in Fig. 1.2(c). Although, particular nozzle designs and experimental parameters differ from study to study, common flow features can be observed. Longmire *et al.*, (1992b) showed that peaks produce streamwise vortices which interact with the main azimuthal vortices and promote their breakdown. It was also stated that these streamwise vortices were responsible for the gross momentum exchange between the jet and the surrounding ambient fluid and the distortion of the overall distribution area of the original jet fluid. Shu *et al.*, (2005) on the other hand, used a four peak crown nozzle which was tapered and protruded into the flow. Using PIV along the streamwise and cross-stream directions it was shown that the IO nozzle caused higher dissipation of the turbulent kinetic energy in the near-field region of the jet, when compared to a conventional circular nozzle without lip modifications. In the same study, it was stated that increased mixing was expected due to the induced velocity of the streamwise vortex pairs. A recent study (Tsovolos and New, 2008) examined experimentally the flow field difference between sharp

and smooth peaks on a crown-shaped nozzle consisting of four peaks and four troughs. It was shown that the smooth peaks were more influential to the flow field, producing visually larger streamwise vortices and increasing the turbulence generation in the near field. Additionally, vorticity dissipation was increased and thus high levels of vorticity were mostly present in the near-nozzle region of the jet.

Noncircular geometries

Noncircular jets have also been studied for their capability of "passively" manipulating the flow field. They have been used in applications where jet-noise reduction, thrust vectoring control and increased heat transfer are preferable. Interestingly, many shapes evolved but most of them fall into three main categories, nozzles with corners (triangular, square, rectangular) (Schadow *et al.*, 1988; Zaman *et al.*, 1994; Grinstein *et al.*, 1995; Zaman, 1996; Gutmark and Grinstein, 1999; Tam and Zaman, 2000; Grinstein, 2001; Rembold *et al.*, 2002; Quinn, 2005a, b), lobbed jets (Hu *et al.*, 1999; Hu *et al.*, 2000a; Hu *et al.*, 2000b, 2001a; Hu *et al.*, 2001b; Hu *et al.*, 2002a, b) and elliptic jets. Both nozzles with corners and lobbed jets promote the generation of coherent structures aligned along the jet centreline, which generate streamwise vorticity. Due to the orientation of the streamwise vortices, they can augment the interactions between the jet and the ambient fluid. Fluid can be injected into, or ejected out from the jet, depending on the rotational sense of the vortices. Apart from exchanging momentum between the jet and the surrounding fluid, the interaction of these vortices with other coherent flow structures, such as main ring vortices, is also important. Some of the pre-referred studies concentrated on the cross-sectional shape of the nozzle, while others added tabs located at the end of the asymmetric nozzles which protruded into the jet (Samimy *et al.*, 1993; Zaman *et al.*, 1994; Reeder and Samimy, 1996; Zaman, 1996; Tam and Zaman, 2000). More specifically, Schadow *et al.* (1988) conducted a study on triangular nozzles and showed that different flow conditions existed at positions corresponding to the vertices and to the flat sides of the nozzle. Along the flat sides, coherent structures were formed but along the vertices, highly turbulent small-scale eddies were dominant. The resultant effect led to a faster breakdown of the large scale structures. The same concept, i.e. the breakdown of large-scale coherent structures and puffs in the jet plume, has been applied in the past to reduce jet-noise, albeit in axisymmetric nozzles (Bradbury and Khadem, 1975). Following on from that study, Grinstein *et al.* (1995) showed that square jets axis-switch by 45°. The initially square filament is distorted under the effect of the self-induced velocity in the neighbourhood of the corners. In the same study, axis-switching was found responsible for the increased fluid entrainment which was comparable to values obtained from an elliptic jet. At approximately the same time, the application of tabs that protruded into the jet, acting as vortex-generators was also being tested with

success (Reeder and Samimy, 1996). Each tab could produce a pair of counter-rotating vortices, aligned in the streamwise direction. The rotational sense of these vortices was such that the jet shear layer interacted and impeded onto the jet core region. Results showed that using tabs increased the development of the mixing layer and also increased Reynolds shear and normal stress levels, thus indicating an increase in turbulence. Another important study, which is also relevant to the current research theme, was conducted by Zaman (1996). In his study, Zaman demonstrated that manipulating axis-switching in rectangular nozzles is possible. This was achieved by the positioning of vortex generators (tabs) in particular locations around the nozzle periphery. Due to the relevance between the two studies, a more detailed analysis will follow in the next section. In another study by Tam and Zaman (2000), several asymmetric nozzle configurations were tested for their ability to reduce jet-noise. It was shown that rectangular and elliptic nozzles do not achieve noise level reduction compared to a circular nozzle, but produce an asymmetric sound pattern. Tabbed jets on the other hand did reduce the sound levels, while a six-lobbed nozzle was the most beneficial towards sound reduction. The lobbed nozzle was able to suppress the sound emission caused by the large scale turbulence structures. Finally, a model for predicting the noise reduction depending on the number of tabs and tab geometry was proposed. Based on the results it was shown that careful tab design could reduce the perceived noise level by shifting the emission frequency. A computational study by Rembold *et al.* (2002) tested rectangular nozzle designs and findings showed that varying the initial momentum thickness of the jet, different jet-spreads were achieved. At small initial momemtum thickness the jet-spread associated with the minor axis of the rectangular nozzle was largest. Results agreed well with previous experimental studies on rectangular nozzles.

Lobbed jets

Hu *et al.*(1999) conducted a comparative study, examining the flow field and mixing associated with different lobbed nozzles. Due to the inherent design of a lobed nozzle, it was shown that nozzles which substantially increased mixing (rectangular aligned lobbed nozzle geometries) also increased the pressure drop. In the papers, (Hu *et al.*, 2000a; Hu *et al.*, 2000b), Hu et al. focused on the process behind the peculiar flow structures and the effect that the nozzle contour had on the large-scale coherent structures. Using laser induced fluorescence visualisation and particle image velocimetry measurement techniques, the group observed that the large scale structures broke down into smaller eddies thus causing an increase in Reynolds stress and turbulence generation. The increased mixing associated with lobbed jets was attributed to the joint effect of the streamwise vortices, which are produced by the contour of the lobbed nozzle, and the Kelvin-Helmholtz instability which increases the shearing and stretching of the main ring vortices. According to the Helmholtz vorticity

law, when a vortex is stretched, the scale of vortices will be reduced. Additionally, the jet centreline decay rate was also higher when compared to a conventional round jet of equivalent diameter. Further studies using advanced measurement methods such as stereoscopic PIV and Dual-plane stereoscopic PIV focused on the cross-stream evolution of the streamwise vortices (Hu *et al.*, 2001a; Hu *et al.*, 2001b; Hu *et al.*, 2002a, b). It was found that streamwise vortices do increase the mixing within the near-nozzle region of the jet. Increased turbulent kinetic energy magnitudes were detected within the same region. Interestingly, downstream of the near-nozzle region, the streamwise vortices broke down and thus in their absence, the turbulent kinetic energy values reduced.

Elliptic jets

Although elliptic jets lie within the general noncircular jet category discussed earlier, they were not included in the particular section intentionally. Due to their relevance with the current study, more background information will be provided and thus they will be introduced separately. Elliptic rings and jets issued from elliptic nozzles has been a topic that has been studied extensively in the past. In the 70's, Oshima (1972), conducted an experimental study on circular and lenticular orifices in water. He observed that elliptic rings axis-switched several times before they broke down. A part-numerical, part-experimental study by Dhanak and Debernardinis (1981) was conducted in an effort to mathematically describe the evolution of an elliptic ring as it convected downstream. Several aspect ratios were investigated and it was found that as the aspect ratio (elliptic eccentricity) increased, axis switching was reduced. It was predicted that for extreme aspect ratios the elliptic rings would separated into two individual vortex rings. Their numerical findings agreed well with their experimental results as well as with the earlier study (Oshima, 1972). Ho & Gutmark (1987) used a small-aspect-ratio elliptic jet to show that entrainment was increased as a result of higher induced velocities due to the non-constant radii of the elliptic ring-vortices. Some of the most cited papers on elliptic nozzles were studies conducted by Hussain and Husain (1989) and Husain and Hussain (1991; 1993). They conducted extensive studies which covered elliptic rings as well as elliptic jets under both forced and unforced conditions. Amongst other important findings, they also showed that an elliptic jet, similar to an elliptic ring, of moderate aspect-ratio (AR) has the inherent tendency to undergo axis-switching. Of course, differences between the propagation of rings and jets exist due to the inherent differences between jets and rings. Propagating vortex rings work against viscosity and diffusive effects, as well as, against ring-instabilities (Crighton, 1973), however jets on the other hand, compete against additional factors such as shear layers and interactions within the braid region of the jet. For this reason, rings formed in jet flow transist to turbulence faster than vortex rings formed by impulsive fluid movement.

Collar jets

The final category that will be introduced briefly, consists of nozzles used to control the jet flow-field by passive means, is collar jets. Collar jets are formed by nozzles which have an outer nozzle (collar) sleeved onto an inner one, as shown in the schematic in Fig. 1.3. Effectively, these two concentric nozzles form a backward-facing step which perturbs the jet flow and may even cause flow separation. Hussain and Hasan (1983) discovered that as the collar (outer concentric cylinder) was moved downstream a tone appeared. They appropriately termed this type of jet as, the "whistler jet". Several characteristic parameters were found to influence the frequency and amplitude of the tone, such as the jet velocity, the length of the collar, the step height and the diameter of the inner nozzle. More recent studies make use of the expansion ratio (collar equivalent diameter normalised by the nozzle equivalent diameter), instead of the step height, to characterise the nozzle geometry (Nathan *et al.*, 2006; New *et al.*, 2007; Wong *et al.*, 2008; Zeng *et al.*, 2009). The reason behind this change was because non-circular jet configurations were used and thus the step height varied around the nozzle circumference. These types of nozzles were studied because of their ability to produce significantly altered flow-fields when compared to a conventional nozzle without a collar. The high mixing capability of the jet, which could be predictably induced by different flow modes made the applicability of these jets, in areas such as jet noise reduction and combustion, highly feasible. Hussain and Hasan (1983) showed that the whistler jet produced a tone which was caused by the coupling of two independent resonance mechanisms. Additionally, an increase in jet spread was measured. The dominant flow mechanism, was caused by the impingement of the shear layer on the collar lip. The flow mechanism was strongest when the self-excitation frequency was close to the "preferred-

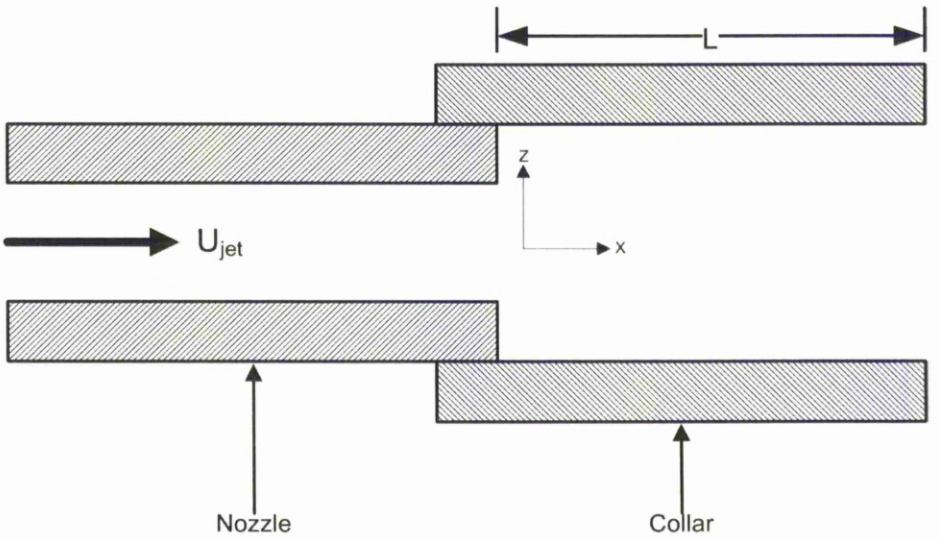

Figure 1.3 Schematic illustration of a collar jet

mode" of the jet (St_D=0.3 - 0.6) (Hussain and Zaman, 1981). A later study by Husain and Hussain (1999) tested an elliptic collar jet with an aspect-ratio of 2. It was shown that the jet did not axis-switch, but did however increase the jet-spread and mass entrainment. The reason behind the breakdown of the axis-switching mechanism was due to the formation of secondary vortical structures at the lip of the nozzle, which promoted the "tearing" of the main ring vortices. Nathan *et al.* (1998), Nathan *et al.* (2006) and Wong *et al.* (2008) showed that precessing collar jets achieved large scale mixing in the downstream field. The studies mostly focused on the region within the collar (fluidic nozzle) as improving the mixing and flame stability in this region is beneficial for combustion. The resultant jet was shown to have two modes, the "precessing jet" mode and the "axial jet" mode. The first mode achieved an asymmetric jet spread and cause rapid fluctuation of the pressure field and thus was more beneficial for mixing purposes, while the second mode produced a more conventional jet flow-field with fewer fluctuations. However, the two modes were competing and could not co-exist and thus by reducing the amount of time spent in axial-jet mode, by careful nozzle design, one could improve combustion efficiency and reduce NO_X emissions by as much as 50% (Nathan *et al.*, 2006). Following on from previous studies with non-circular nozzles, New *et al.* (2007) tested circular, triangular and square collars, while and Zeng *et al.* (2009) examined the effects of A- and V-notched collars. In the first study, apart from testing different collar geometries, several expansion ratios and collar lengths were also tested. It was shown that the flow mechanisms, present within the collar, were different when comparing the circular to the asymmetric collars. The circular collar led to an equidistant re-attachment of the flow along the collar wall, while the asymmetric nozzles formed a counter-rotating vortex-pair which for small collar lengths did not allow flow reattachment. Results showed that out of all collars, the triangular geometry produced the largest centreline velocity decay and the most turbulence intensity, achieved by using the largest collar length. Additionally, the maximum jet-spread associated with the triangular collar was also the largest. The second study using A- and V-notched collars, came up with unexpected results. The centreline decay increased rate was not predominately affected by the notches , but by the collar length. Also comparing with to the previous study, smaller turbulence intensities were achieved.

b) Active control

Traditionally active flow control was achieved by flaps which were driven by actuators. Development in the area of electronics and micro-electro-mechanical systems (MEMS), has produced more efficient and flexible types of actuators (Wiltse and Glezer, 1993). In the case of jets, these flaps are usually arranged circumferentially around the periphery of the nozzle and located close to the exit. When triggered correctly, the disturbance can influence

the flow field to a large extent. It has been shown that a round jet could undergo bifurcation and trifurcation when axial and azimuthal forcing is applied to it (Lee and Reynolds, 1982; Reynolds *et al.*, 2003). It was found that the forcing condition under which bifurcation existed was when the azimuthal to axial forcing frequency ratio was two. It was shown that the orbital (azimuthal) forcing caused the main ring vortices to form off-axis with repect to the nozzle centreline. Due to this adjacent rings were eccentrically positioned with respect to each other. These eccentrically aligned rings develop mutual induction and tilt away from the main nozzle centreline as they propagate downstream. Thus with the addition of axial forcing, bifurcation is achieved (Parekh *et al.*, 1983). The effects of jet bifurcation have been researched in depth due to the associated increase in heat transfer and jet mixing when compared to conventional unexcited jets (Monkewitz and Bechert, 1988; Smith *et al.*, 2001; Suzuki *et al.*, 2004; Angele *et al.*, 2006).

Recently the use of electric discharge plasmas for flow control, has risen allowing faster control frequencies (up to 200kHz). This method is used for high speed control of boundary layers, in the case of external flow, and shear layers, in the case of jets. Flow control can be achieved experimentally(Samimy *et al.*, 2007) even at high Mach numbers of 1.3. It was shown that maximum mixing was achieved at a Strouhal number of 0.33 and compared well to previous studies conducted at low Reynolds number flow regimes (Hussain and Zaman, 1981; Gutmark and Ho, 1983).

1.1.3 Relevance to the current study

The present work is focused on the passive control of jets using indeterminate-origin nozzles and is divided into two parts. The first part examines circular indeterminate-origin nozzles, while the second part is concentrated on incorporating IO nozzle principles into elliptic nozzle geometries and to investigate the influence of nozzle lip-modifications on the resultant elliptic jet behaviour, something, which to the authors awareness, has not been published before, at least in open literature.

Following on from the research conducted on circular A- and V-notched nozzles (New *et al.*, 2005; New and Tsai, 2007), this study tries to further the knowledge regarding the underlying flow physics by using nozzle geometries with subtle differences as well as different flow regimes. The use of new experimentation methods such as particle image velocimetry will aid this investigation and help to address unanswered question posed in the previous studies.

Using previous non-circular studies as a solid foundation, the notion of incorporating lip-modifications to elliptic nozzles was a natural and exciting progression. The higher

entrainment and mixing capabilities of elliptic nozzles (Ho and Gutmark, 1987) makes them a suitable choice for the current study which focuses on the near-nozzle flow field, such as the evolution of coherent structures and jet-spread. Particularly relevant to this study were the findings associated with triangular tabs which protruded into the jet, issued from a rectangular nozzle of 3:1 aspect ratio (Zaman, 1996). Although the nozzle is not of IO geometry, the results from that study are closely related to the current study. Depending on the position of the tabs, axis-switching was manipulated and could be augmented or stopped altogether. When the tabs were positioned on the long side of the rectangle, axis switching was stopped while when the tabs were situated on the ends of the nozzle (short side), axis switching was augmented and took place further upstream that when no tabs were used. This behaviour was attributed to the mutual interaction and cancellation of the azimuthal (axis-switching) and streamwise (caused by the protruding tabs) vortex dynamics. Similarly, with the use of V-notched elliptic nozzles, the present study shows that altering the flow field and manipulating axis-switching is possible. If so, benefits over the tabbed method exist due to the elimination of blockage effects, as no section of the nozzle protrudes into the jet, thus reducing the amount of power loss (thrust in some applications) due to pressure drop.

1.2 Objectives

The objectives set for the current study are as follows:

- Experimentally test circular and elliptic indeterminate-origin nozzles, through the use of flow visualisation and particle image velocimetry techniques
- Discern and understand the underlying flow physics driven by the indeterminate-origin nozzles and compare the differences to conventional nozzles without such lip-modifications
- Evaluate and comment on each nozzle design with respect to flow field attributes such as, jet-spread, axis-switching capability and turbulence generation
- Finally, based on the experimental results, produce a coherent flow interpretation representing and explaining the gross behaviour of the resulting large-scale structures

2 EXPERIMENTAL SETUP

2.1 Recirculating water tank

The experimental facility used at the School of Engineering, University of Liverpool is shown in Fig. 2.1. The recirculating water jet facility consists of the following major components: Starting at the centrifugal water pump, which was used to drive the flow, and continuing with a needle valve in conjunction with a rotameter which was used to monitor and regulate the flow. The flow was conditioned within the jet apparatus which consisted of a diffuser, a honeycomb structure along with three fine screens and finally, a contraction section which incorporated a 25:1 contraction ratio. The flow-conditioned fluid was discharged through the nozzle into the main tank section. Any overflowing fluid was directed through a series of PVC piping to a reservoir, thus closing the recirculating loop.

A recirculating water tank was used, with internal dimensions of 400mm (W) x 400mm (H) x 800mm (L) which, in non-dimensional terms corresponded to 20D (W) x 20D (H) x 40D (L). The tank dimensions were chosen such that the interactions between the jet and the tank boundaries were kept to a minimum. The entire tank structure was constructed of 15mm clear Plexiglas sheets to allow easy optical access and to reduce light aberration effects due to bulging.

A 110W March May centrifugal pump was used which operated at a constant 2800 revolutions per minute. The specific pump was chosen due to the fact that the main components that were submerged in water, namely the inlet, the impeller and the outlet were constructed from a composite material to avoid water based degradation such as rusting.

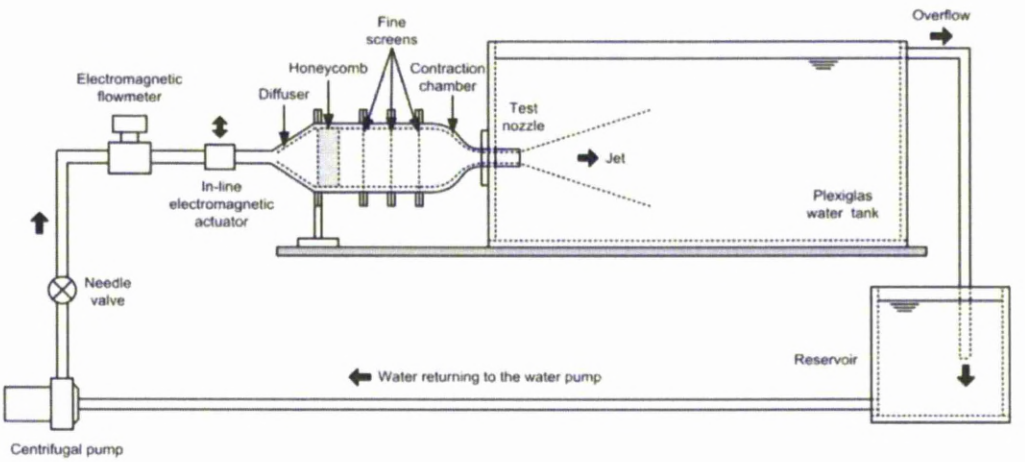

Figure 2.1 Recirculating water jet facility

The Blue-White Industries Ltd F-400 rotameter was calibrated against a Fischer and Porter 10DS4111 electromagnetic flow meter and the whole process was verified using the Dantec DC-PIV system.

Flow forcing, if required, was achieved using an electromagnetic actuated piston, controlled by a function generator. The piston was used to push the malleable tubing against a solid back-plate, replicating a squeezing action. The forcing amplitude and frequency were set using a TG 315 function generator from TTi Ltd. A sine wave signal was used to drive the actuator in a progressive way, reducing any unwanted impulse from disturbing the flow. The amplitude of the flow perturbation was measured at the centre of the jet (y/D=0) and was estimated at 2.2% of the free-stream axial velocity, U_o, similar to what was noted by Husain and Hussain, (1993). Perturbing low Reynolds number flows is a common experimental procedure (Longmire *et al.*, 1992b; Longmire and Duong, 1996; New *et al.*, 2005; New and Tsai, 2007; Keiderling *et al.*, 2009). A small perturbation was used to disturb the shear layer and cause it to rollup and produce coherent structures at distinct periodic time intervals. The non-dimensional frequency of these periodic disturbances–rollups is dictated by the experimental arrangement and is known as the Strouhal number ($St_D=fD/U_0$), where f is the forcing frequency, D is the nozzle hydraulic diameter and U_0 is the mean jet exit velocity. The Strouhal number was set to $St_D=0.5$ throughout the current study. The reasons for selecting such a value are because firstly $St_D=0.5$ lies within the natural instability range of freely exhausting jets (Gutmark and Ho, 1983; Wlezien and Kibens, 1986), thus less amount of external perturbation is required, and secondly it stands as a means of comparison with other researchers (Husain and Hussain, 1983; Longmire *et al.*, 1992b; Husain and Hussain, 1993).

2.2 Nozzle designs

In this section, the nozzles will be presented in groups based on their geometric features. A total of ten nozzles were studied. The two main groups contain nozzles that differ with respect to the shape of their cross-section. The first group contains nozzles of circular cross-section, while the second group contains nozzles of elliptic cross-section. The nozzles have been arranged further in subgroups according to their lip modifications.

The test nozzles consisted of a two-piece design (Fig. 2.2). A base-plate, which was used to attach the nozzle assembly to the jet apparatus, and the actual nozzle stem which was being tested. An interference fit (press fit) was used to connect the nozzle stem to the base plate. Eight radial holes were drilled onto the base-plate which enabled the rotation of the nozzle at

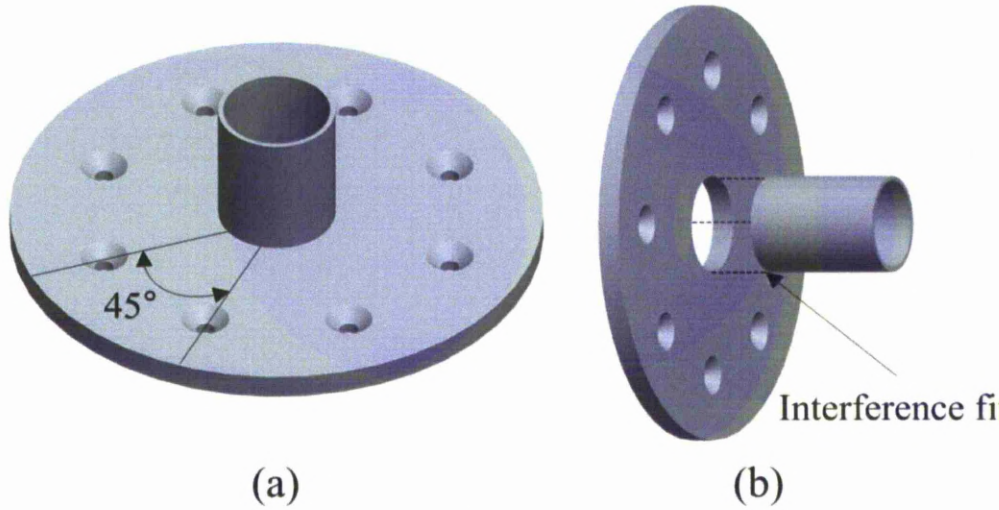

Figure 2.2 Test nozzle two-piece assembly

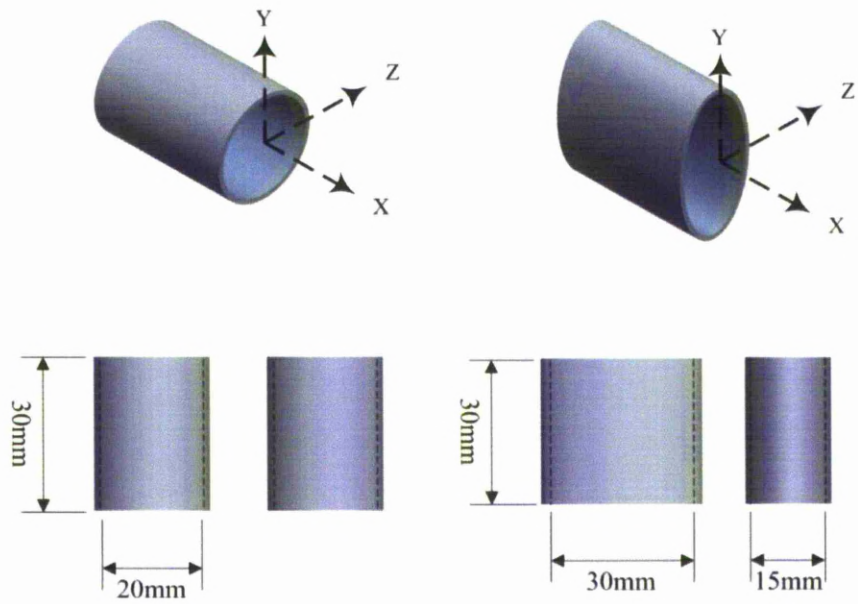

Figure 2.3 Schematic representation of reference nozzles, (a) circular and (b) elliptic

discrete steps of 45°. Apart from the axi-symmetric circular reference nozzle, which required no rotation, all other nozzles were rotated by 90° in order to capture and measure the flow effects from all the features of the nozzle. For machining purposes, the back-plate was constructed from brass, while stainless steel was chosen for the nozzle stem to ensure corrosion resistance.

Figure 2.3 depicts the nozzles used as benchmark cases. The circular reference nozzle (Fig. 2.3(a)) was designed such that it had an internal diameter of D=20mm. The elliptic reference nozzle (Fig. 2.3(b)) had an elliptic cross-section of aspect ratio two. The dimensions were chosen to give a hydraulic diameter similar to the circular case at D=19mm.

Both the indeterminate-origin circular and elliptic nozzles were designed such that the mean height, defined as the average height between troughs and peaks, was kept to a constant value of approximately 1.5D. Due to this fact, the mean height was chosen as the starting point (x/D=0) for all graphs in this thesis.

The circular group of nozzles consists of A-notched (Fig. 2.4) and V-notched (Fig. 2.5) geometries. The A-notched nozzles were designed so that the combination of sharp peaks along with smooth troughs could be tested. Effectively an "A-shaped" section was cut away from a standard cylindrical nozzle design, resulting in nozzle contour resembling two half-ellipses, as shown in Fig. 2.4. For consistency, the aspect ratio of the trough has been used to distinguish between the shorter and longer A-notched nozzles. The shorter nozzle (Fig. 2.4(a)) has a trough contour, corresponding to a half-ellipse with an aspect ratio (AR) of two, while the long nozzle (Fig. 2.4(b)) has a tough contour corresponding to an aspect-ratio of four. The reason for designing two nozzles of the same shape, but of different length, was to study the flow field effects associated with the increased relative sharpness. In contrast, the

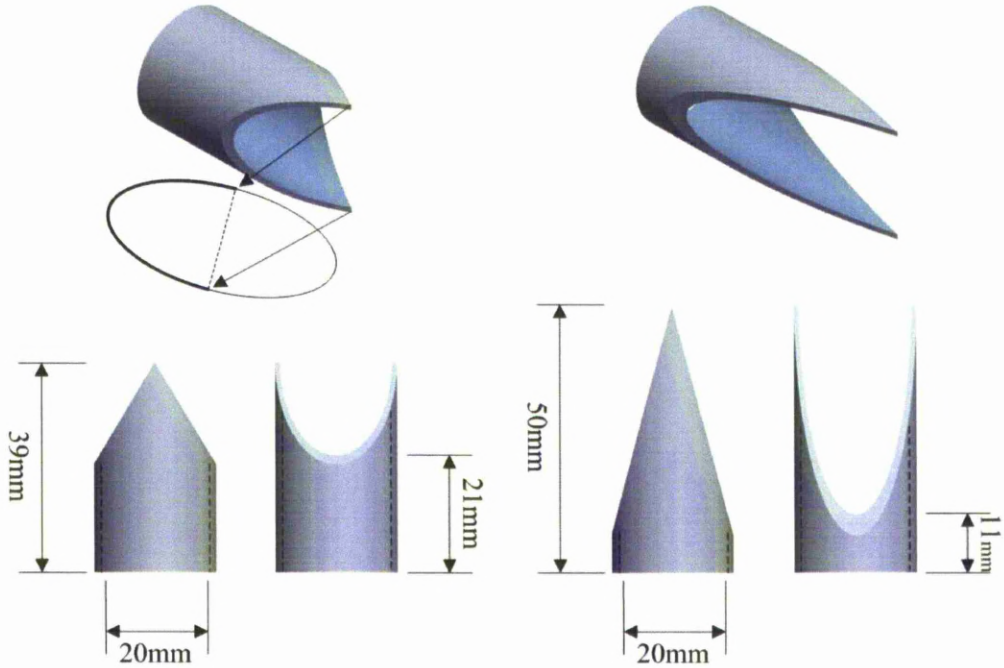

Figure 2.4 Schematic representation of A-notched nozzle group, (a) AR2 and (b) AR4

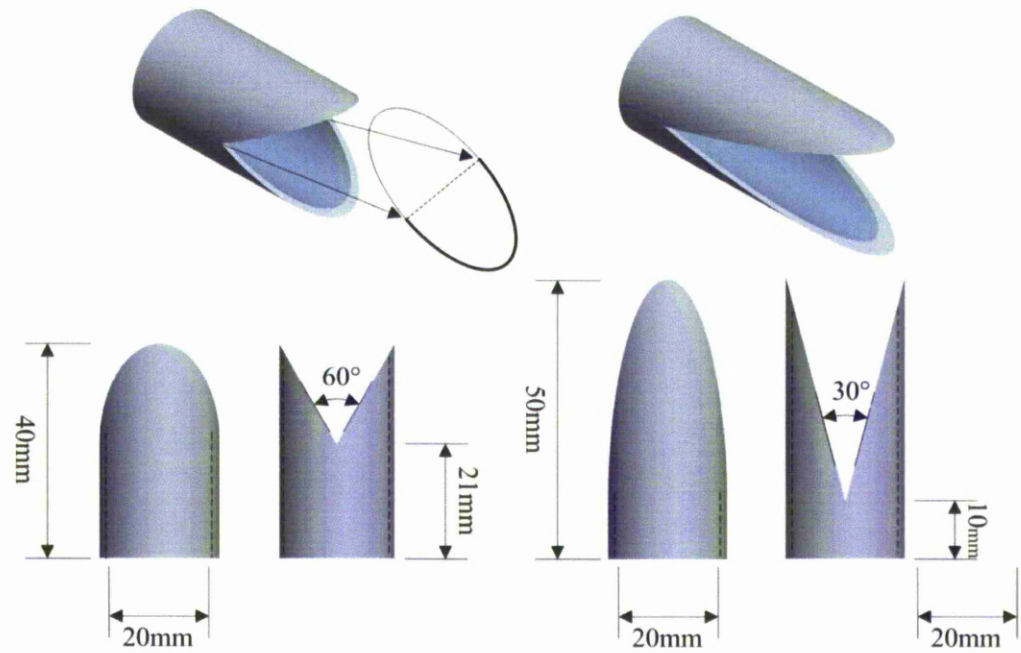

(a) AR2 (b) AR4

Figure 2.5 Schematic representation of V-notched nozzle group, (a) AR2 and (b) AR4

V-notched nozzles (Fig. 2.5) were designed to incorporate a smooth peak along with a sharp trough combination. By taking a "V-shaped" cut from a cylindrical hollow pipe, a nozzle with half-elliptic peaks was formed. The categorisation of the V-notched nozzles was based on the aspect-ratio of the half-elliptic peaks. The shorter nozzle (Fig. 2.5(a)) formed a half-ellipse of aspect-ratio two, while the longer nozzle (Fig. 2.5(b)) formed an aspect-ratio of four.

The elliptic indeterminate-origin nozzles can be separated into two categories, with the first including nozzles that have a V-notched cut across their major axis (Fig. 2.6) and the second that have a V-notched cut across their minor axis (Fig. 2.7). Following the same design methodology of the circular nozzles, for each case, two nozzles of different sharpness have been constructed. To separate between the shorter and longer nozzles, the included angle of the V-notched cut has been used as a reference. The longer V-major nozzle (Fig. 2.6(a)) had an included angle of 60° while the shorter nozzle (Fig. 2.6(b)) had an included angle of 120°. It follows that the 60° nozzles contain sharper peaks as well as sharper troughs when compared to the 120° nozzles. The effects of increasing the peak and trough sharpness have been studied.

The V-minor elliptic nozzle group is shown in (Fig. 2.7) .The V-notched cut across the minor axis produced nozzles with sharp troughs located at the ends of the major axes and

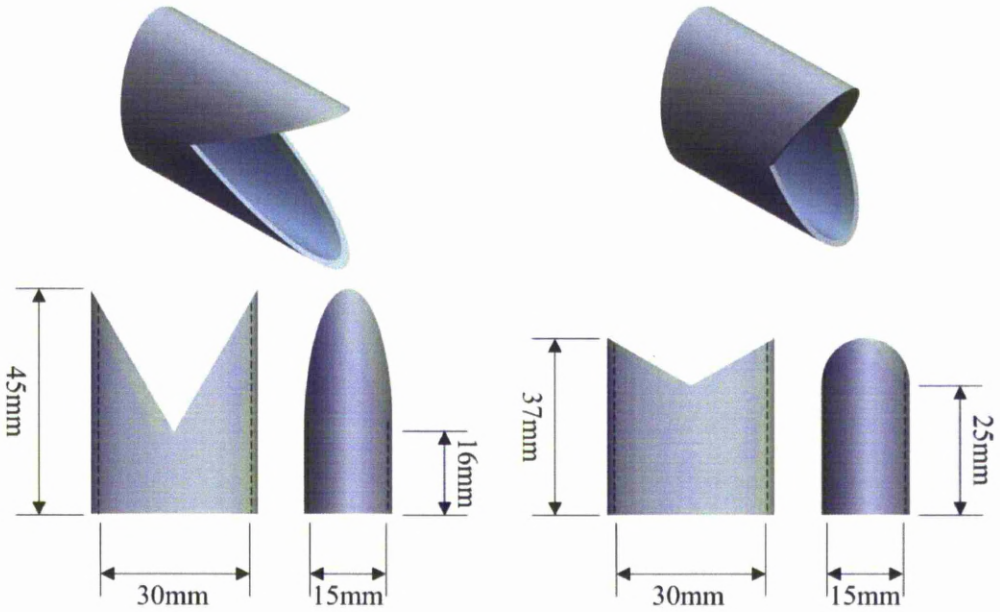

Figure 2.6 Schematic representation of V-major elliptic test nozzles

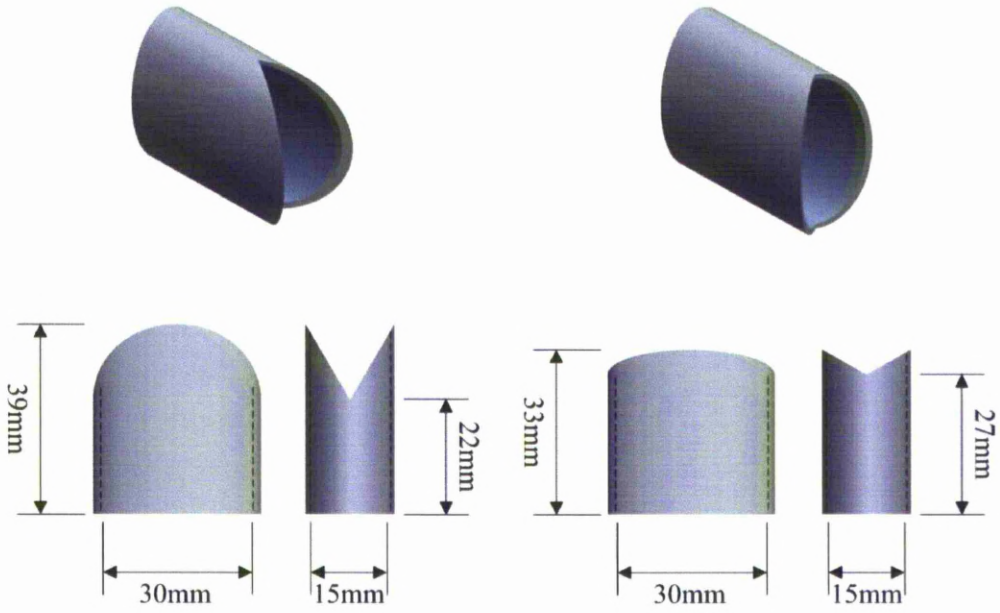

Figure 2.7 Schematic representation of V-minor elliptic test nozzles

smooth peaks of large curvature at the ends of the minor axes. When combined with the V-major nozzles, the influence that the peak curvature as well as the location of the sharp troughs have on the flow field, can be studied. The V-minor nozzles were also categorised

with respect to the included angle of the V-notched cut. The longer nozzle (Fig. 2.7(a)) had an included angle of 60° while the shorter nozzle (Fig. 2.7(b)) had an included angle of 120°.

2.3 Flow visualisation

A part of the current study was focused on conducting flow visualisation experiments. Using different methods of flow visualisation, one can either capture slices of the flow field or get a general holistic view. Intricate flow details and vortex interactions can be identified. Although qualitative, flow visualisation is a valuable tool when combined with particle image velocimetry and in many cases can help interpret quantitative results.

Two separate flow visualisation methods were used; shear layer dye injection and laser induced fluorescence (LIF). For the former, blue coloured food-dye was used to highlight the shear layer and its consequent evolution as it propagated downstream, while for the latter, fluorescent dye was injected into the bulk of the flow to elucidate vortex interactions within the jet column.

2.3.1 Shear layer visualisation

A gravity feed mechanism was chosen to inject the blue coloured dye for reasons of

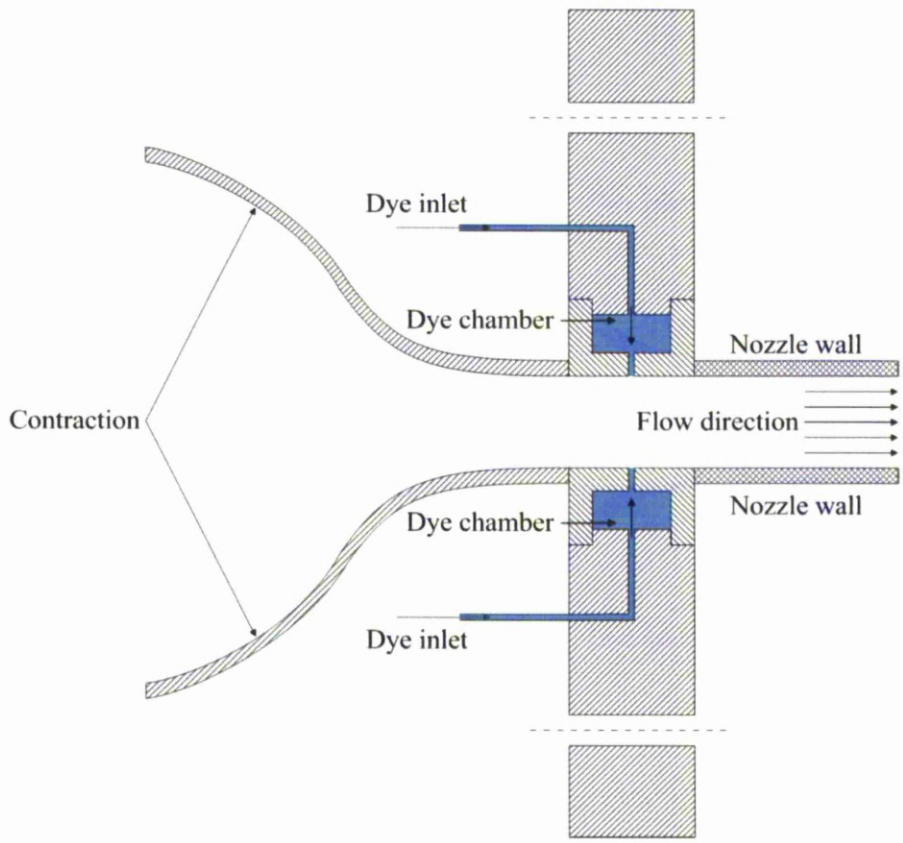

Figure 2.8 Schematic representation of gravity-fed mechanism used for dye injection experiments

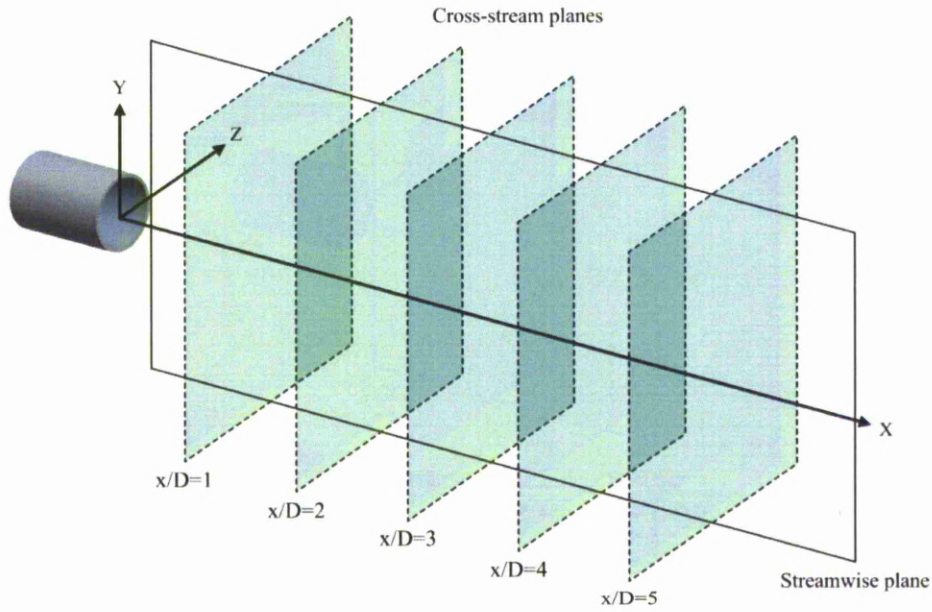

Figure 2.9 Schematic representation highlighting streamwise and cross stream measurement planes

robustness, repeatability and simplicity of design. A schematic of the mechanism is shown in Fig. 2.8. The dye was directed from an overhead container to the Perspex chamber using PVC transparent tubing with an internal diameter of 2 mm (Fig. 2.8). The flow rate of dye was regulated by a variable clamp imposed on the soft tubing. Dye was injected into the boundary layer through a 1 mm circumferential slit within the Perspex chamber. The location of the Perspex chamber was between the contraction section and the nozzle. The shear layer visualisation technique was only used for experiments conducted along the streamwise view, as shown in Fig. 2.9. The dye, although not neutrally buoyant, had a specific gravity close to one, thus not requiring the addition of alcohol.

2.3.2 Laser Induced Fluorescence

A similar setup to the shear layer injection technique was used for the LIF experiments with the main differences found in the injection method, location and the injection dye. Fluorescein disodium dye salt was pre-mixed with water and injected into the overfill reservoir, immediately upstream of the pump section. A 5Watt diode-pumped solid-state (DPSS) Laser Quantum Elite series laser, with a beam size of 3mm and a wavelength of 532nm was used as a light source. The beam was guided to a rotating mirror by beam steering optics and once targeted onto the rotating mirror was shaped into a plane. The laser sheet was used to illuminate whichever plane of the jet needed to be examined. When illuminated by the laser, Fluorescein re-emits energy concentrated within the green light spectrum. Throughout all of the testing, two illumination orientations were used, namely streamwise and cross stream as shown in Fig. 2.9. During streamwise illumination the laser

was aligned along the XY-plane which meant that the laser was directed down the middle of the jet column. In a similar way, during the cross stream illumination and depending on the nozzle, the laser was aligned along the YZ-plane at several downstream locations. For longer test nozzles, the starting cross-stream location was suitably chosen further downstream, such that the laser plane did not intersect with the nozzle.

2.3.3 Limitations

The following paragraphs describe the main limitations associated with the use of flow visualisation as a tool to understanding fluid flow.

First, when visualising flows which are dominated by vortex stretching as found in the shear layer of a jet, it must be understood that the time evolution of the dye tracer will not be the same to that of the vorticity (Lim, 2000). By looking at the vorticity and scalar transport Equations (Equation 2.1 and 2.2) the differences become clearer. The vorticity transport equation is governed by

$$\frac{\partial \omega}{\partial t} = -V \cdot \nabla \omega + \omega \cdot \nabla V + \nu \nabla^2 \omega \qquad 2.1$$

The first term on the right hand side is the advection of the vorticity by the local mean velocity, and the second term is related to the vortex stretching by the local strain, while the last term represents the diffusion of the vorticity due to viscous effects. The scalar transport equation is defined as

$$\frac{\partial S}{\partial t} = -(V \cdot \nabla) S + \kappa \nabla^2 S \qquad 2.2$$

It can be seen when comparing the scalar to the vorticity transport equation that the stretching term is absent. The absence of this term causes the difference in the behaviour between the vorticity and the tracer dye. If the stretching term is small in comparison to the advection term in a particular flow experiment, then, provided that the Schmidt number (ν/k where k is the mass diffusivity) is unity, the tracer will advect and diffuse in a similar way to the vorticity. In contrast though, in flows where the stretching term is much greater than the advective term, such as shear layer roll-ups, there vorticity will not be traced accurately, especially as the time progresses. However in this situation care must be taken when analysing the flow field as the absence of tracer dye does not necessarily correspond to absence of vorticity as shown by (Kida *et al.*, 1991). To avoid such deviations, flow visualisation experiments were conducted in the near-field region of the jet (up to six diameters downstream distance), where large streamwise velocity components are dominant, thus keeping the influence of the stretching term and the time evolution to a minimum.

The second limitation is the effects of viscous diffusion. If dye is released at the location of vorticity generation, then provided that the Schmidt number is unity, the tracer will follow the vorticity indefinitely. For the current experiments, the Schmidt number of the dye used is typically of $O(1000)$, which means that the dye will only follow the vorticity during the initial stages of flow development. As the time increases, the dominant viscous diffusion term will dominate and thus the vorticity will diffuse away from the dye.

Finally, as shown by (Cimbala *et al.*, 1988), the final dye visualisation pattern depends on the injection location. Since the dye is influenced by flow perturbations as it propagates downstream, it has been shown that the final dye visualisation pattern is a result of the accumulated distortion which the dye tracer has undergone since its introduction at an arbitrary upstream location. For the same flow field, if the dye injection location changes so will the corresponding dye visualisation result.

The experimental setup was designed to reduce the effect of the pre-referred limitations. During all experiments, the measurement area used was at the most 6 diameters from the reference point along the x-direction, so the dye was only affected by the local shearing effects for a small amount of time and distance thus reducing the effects of the stretching term found in Equation 2.1. The location of the dye port was designed such that it was located immediately upstream of the nozzle exit. However in any case, the flow visualisation techniques were used in conjunction with quantitative results obtained from the PIV experiments and were not solely used to investigate the resulting flow-field characteristics.

2.4 Particle image velocimetry (PIV)

Over the past decade the PIV measurement technique has been developed and used extensively in many fluid dynamic and aerodynamic research applications. In the area of jet research studies have also made use of numerous PIV setups such as 2D-PIV (Fincham and Spedding, 1997; Hu *et al.*, 2002a), 3D-PIV (Ganapathisubramani *et al.*, 2005; Hu *et al.*, 2002b; Hu *et al.*, 2001b; Prasad and Adrian, 1993) and with the latest development including volume mapping PIV (Troolin and Longmire, 2010). The PIV measurement method consists of four components: (a) light reflecting particles, (b) a source of illumination, usually in the form of a Nd:YAG laser, (c) a camera setup to capture the light reflected from the particles and finally (d) a workstation to analyse the data and compute the associated velocity field. A schematic showing the interaction between the components for streamwise testing can be seen in Fig. 2.10.

In this study, a Dantec Dynamics DC-PIV system was used throughout. A New Wave Research 50mJ Nd:YAG double pulsed laser in conjunction with a FlowSense 8-bit

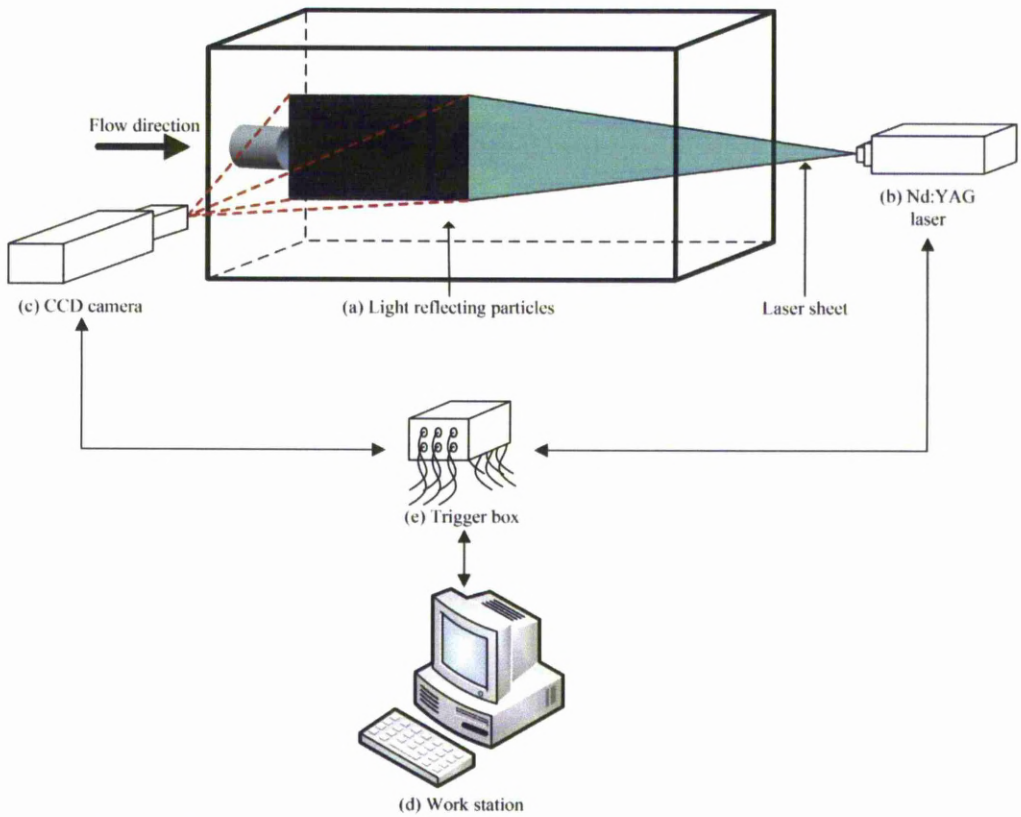

Figure 2.10 Main components required to conduct PIV measurements along the streamwise plane

greyscale CCD camera of 1600 x 1200 pixels was used. For experiments along the streamwise direction a Nikon f2.8 60mm fixed-focal lens was used, while for cross-stream experiments a 105 Sigma f 2.8 105mm fixed-focal lens was chosen. The system was operated in double frame/single exposure mode, which refers to the method used to measure the flow field. Effectively, for each flow instance two frames were captured. The average particle shift and time difference (dt) was analysed by a workstation computer which then produced the resultant vector field. The maximum attainable repetition rate that the system could operate at was 15Hz, which was adequate to capture flow formations and vortex ring propagation. Similar to flow visualisation testing, experiments were performed along streamwise and cross-stream planes as shown in Fig. 2.11. The specific PIV parameters used, such as interrogation window size and validation methods is explained separately in section 2.4.1

Low Reynolds number testing was conducted throughout at Re=2100. Two experimental procedures were used to measure the flow-fields associated with each nozzle, namely, time-averaged and phase-averaged. During phase-averaged operation, the flow was pulsed at a St_D=0.5 (f=2.5Hz), similar to what was done during the flow visualisation testing, and the

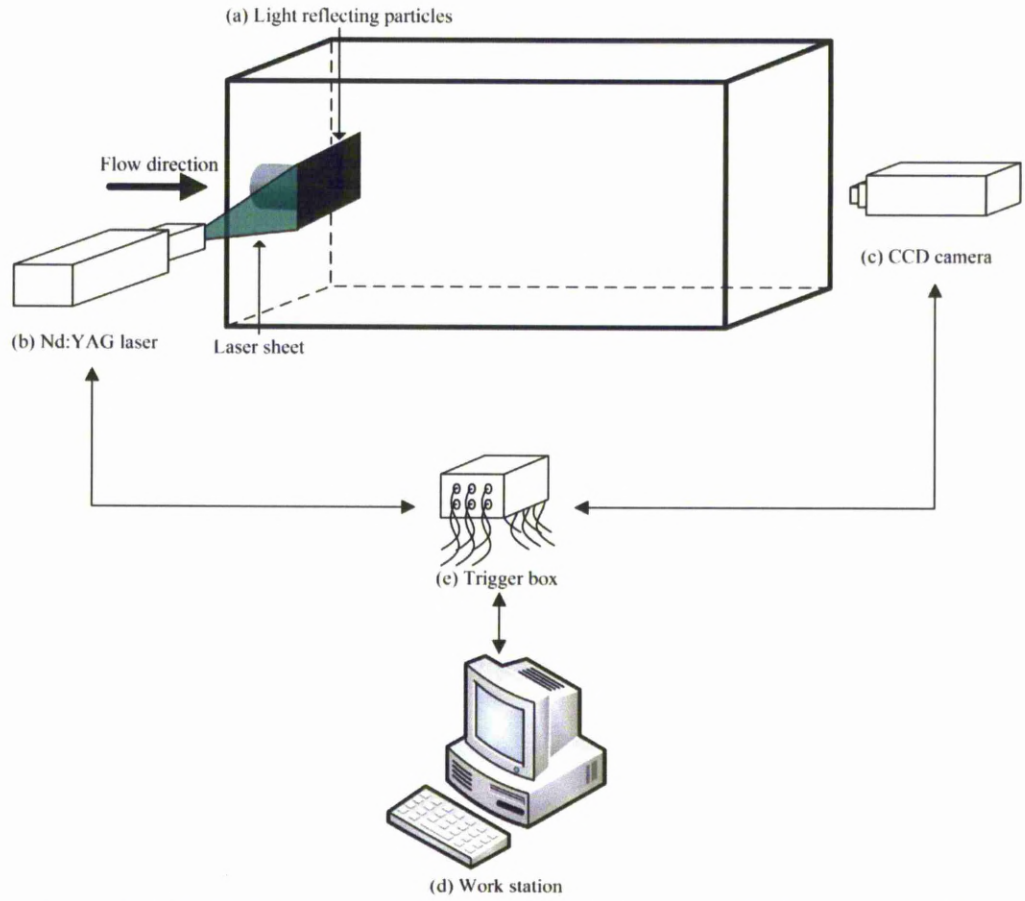

Figure 2.11 Main components required to conduct PIV measurements along the cross-stream plane

system was triggered to acquire a dataset at each pulse. The effect of this synchronisation technique was to capture the dominant flow structures and "freeze" them in space. The resulting phase-averaged results help to identify the evolution of main ring vortices and important attributes such as axis-switching. On the other hand, during the time-averaged experiments, with all other parameters such as, flow velocity, flow perturbation and laser timings, being the same, the PIV system was set to the maximum attainable acquisition rate of 15Hz and was independent of the flow perturbation phase. The instantaneous results tracked the evolution of individual flow structures and showed their evolution as they convect downstream. When averaging the results, a time-averaged representation of the flow field was determined. The timing between each image pair for experiments along the streamwise direction was set to $d\tau$=5ms and for experiments along the cross stream direction $d\tau$=20ms. The timing value was set according to the Nyquist theorem as explained in (Raffel, 1998).

The effectiveness of the flow conditioning apparatus can be viewed when looking at Figs. 2.12 and 2.13. Figure 2.12 shows the centreline velocity profile evolution for the circular

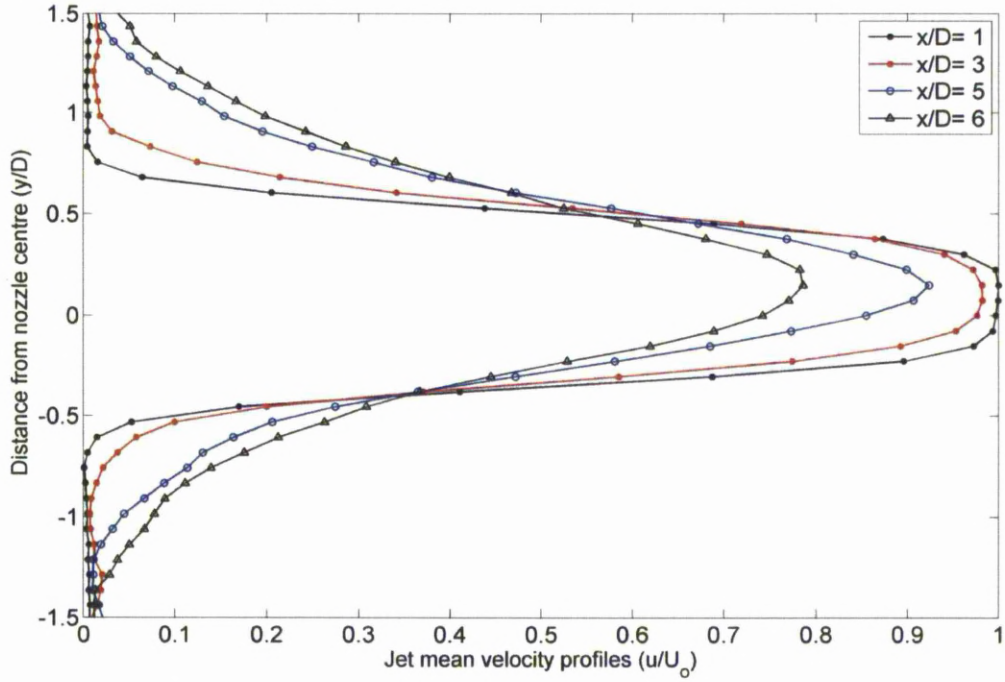

Figure 2.12 Centreline jet velocity profile at several cross-stream locations

reference nozzle, measured at several cross-stream locations x/D=1, 3, 5 and 6. It can be seen that the velocity profile in the remote vicinity of the nozzle exit, is uniform (top hat profile). As the cross-stream distance increases, the profile becomes parabolic (Gaussian) and the jet maximum velocity decreases, while the jet begins to spread. This behaviour is typical of axisymmetric jets and agrees well with theory (Pai, 1954). Another important parameter when characterising jets is the turbulence intensity (T_u). For two-dimensional flow can be defined as:

$$T_u = \frac{u_{rms}}{U} \tag{2.3}$$

where

$$u_{rms} = \sqrt{\frac{1}{2}\left(u_x'^{\,2} + u_y'^{\,2}\right)} \tag{2.4}$$

and

$$U = \sqrt{u_x^2 + u_y^2} \tag{2.5}$$

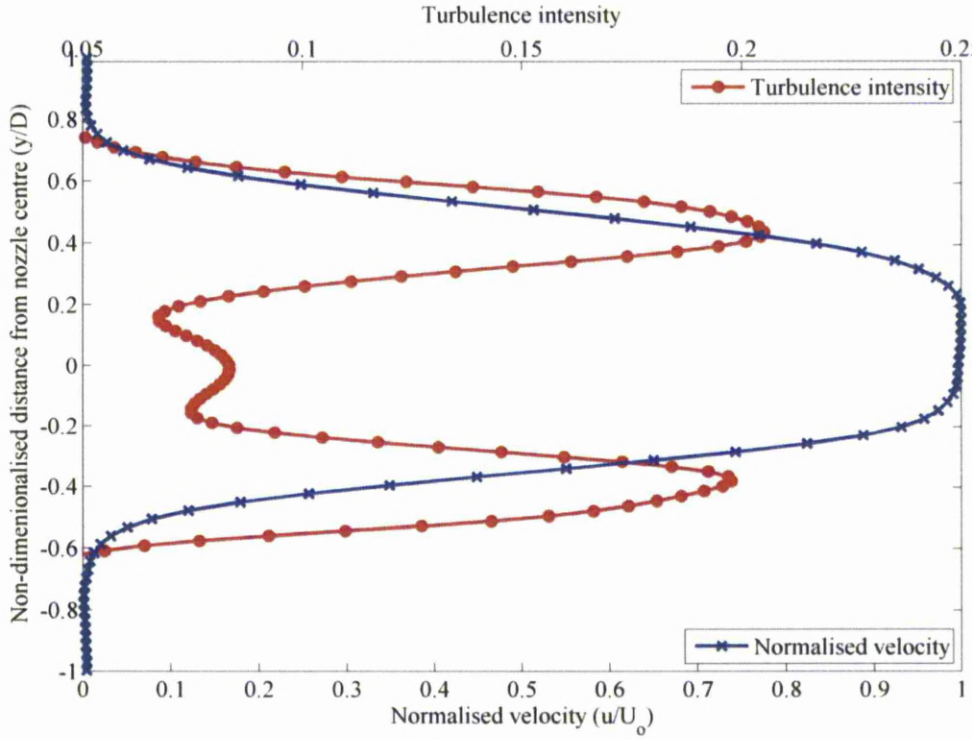

Figure 2.13 Centreline jet velocity profile and turbulence intensity at a cross-stream distance x/D=0.1

Turbulence intensity shows how steady the flow is within the test section. Good flow characteristics are essential for producing repeatable, high-quality, results. As both streamwise and cross-stream measurements were two-dimensional (2D-PIV), Equation 2.4 was simplified by eliminating the third component of the velocity tensor (u_z). Figure 2.13 shows the non-dimensionalised jet mean centreline exit velocity and turbulence intensity measured at a cross-stream distance of x/D=0.1 from the nozzle exit (note that for the circular reference nozzle, the mean height and nozzle exit coincide). Within the potential core region of the jet, T_u was measured at T_u=7%, while within the shear layers it was approximately T_u=20%. A small asymmetry between the left and right shear layer is apparent, which may be due to manufacturing or assembly inaccuracies or slight flow asymmetries.

All averaged results have been averaged over five hundred datasets for experiments along the streamwise direction and one thousand datasets for experiments conducted along the cross-stream direction. Figure 2.14 shows how the mean velocity and vorticity is influenced by the total number of averaging datasets. The points selected to probe the flow were located within the shear layer of the jet for both streamwise and cross-stream results, as these regions contain high velocity fluctuations and would be the last to settle down.

As the vorticity is the first spatial derivative of the velocity tensor as shown in Equation 2.6:

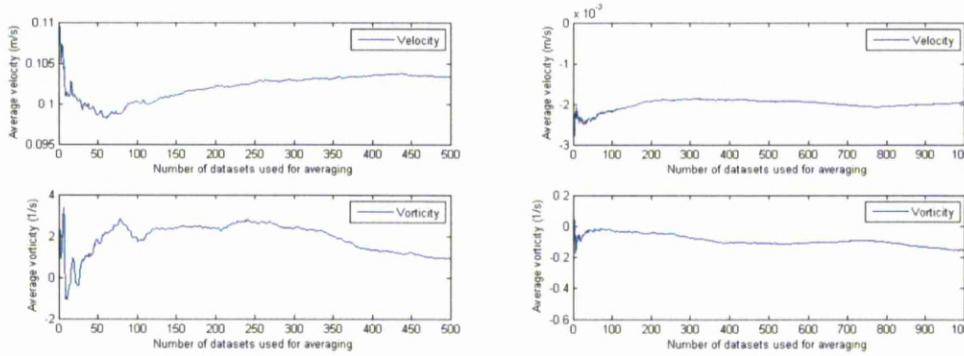

(a) Elliptic reference nozzle, streamwise view (b) Circular reference nozzle, cross stream view x/D=0

Figure 2.14 Line plots showing the averaged velocity and vorticity fluctuations for experiments along (a) streamwise and (b) cross-stream planes

$$\omega_z = \frac{\partial v}{\partial x} - \frac{\partial u}{\partial y} \qquad 2.6$$

any fluctuations in the velocity will be accentuated (more on uncertainty in section 2.4.2). It can therefore be seen that the velocity is the driving parameter and for this reason we will concentrate on the velocity plots of Fig. 2.14. For the streamwise case (Fig. 2.14(a)) the average velocity fluctuates rapidly within the first one hundred datasets, but settles down thereafter. At 475 datasets, the average velocity fluctuation per dataset, defined as the amount that the average velocity value will change when the number of datasets is increased by one, is less than 2%. The addition of more datasets will not decrease the fluctuation any further and for this reason five hundred datasets were chosen as an optimum averaging quantity for all streamwise experiments. Within the same region, the average vorticity has also settled down (Fig. 2.16(a)). For the cross-stream case shown in Fig. 2.14(b), large fluctuations occur within the first two hundred datasets. The average velocity is considered settled after nine hundred datasets by which the fluctuation of the average velocity is within 2%. As expected, one thousand datasets were used to average all cross-stream results.

2.4.1 PIV analysis parameters

A multi-step procedure was used in order to obtain flow field measurements. The use of Dantec Dynamics FlowManager software provided a good platform for obtaining such results with ease. Once the optimum settings were achieved, an automated process was set up to avoid human errors. In the following paragraphs, a description of the steps comprising the automated analysis sequence (Fig. 2.15) will be conducted. Furthermore, the subsequent analysis performed on the resultant velocity field results is explained.

Two-pass multigrid cross-correlation analysis with a final interrogation window of 32 x 32 pixels along the streamwise view and 16 x 16 pixels along the cross-stream view were used.

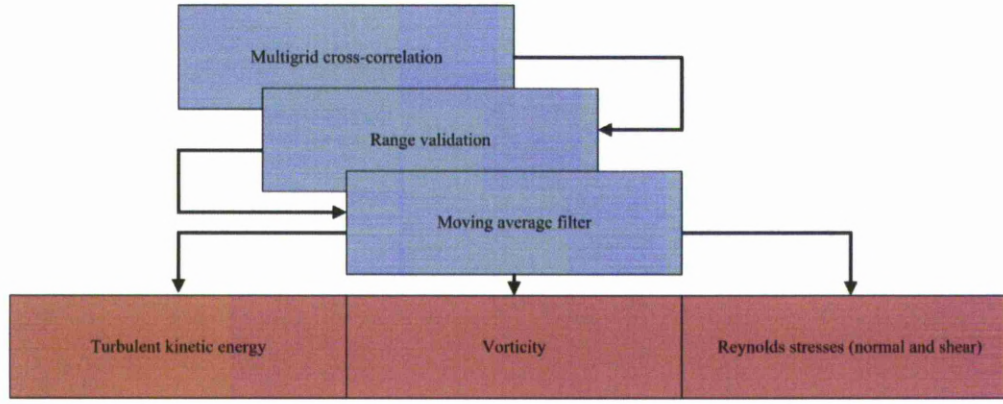

Figure 2.15 Automated analysis sequence performed for each image pair

A multigrid cross-correlation enhances the measurement dynamic range. The dynamic range is defined as the mean velocity divided by the accuracy of the measurement and for standard cross-correlation is approximately 100. When the multigrid cross-correlation is used, the measurement dynamic range increases approximately by a factor of 4 (for a two-pass iteration). The reason behind the increase in dynamic range is due to the fact that multigrid cross-correlation uses an iterative process that manipulates the grid size and grid offset parameters. From an initial guessed offset value, an offset is introduced from the first window (the interrogation area in the image frame from the first laser pulse) to the second window (the second laser pulse). The obtained vector is validated and used as a new estimate for the offset. A new run is made, but this time with a smaller interrogation area. Since a two-pass iterative process was used, the initial interrogation window was 128 x 128 pixels for streamwise experiments and 64 x 64 pixels for cross-stream experiments. This type of cross-correlation is more computationally intensive, but offers increased flexibility in capturing flow characteristics when conducting experiments. A final point is made by stating that the experimental procedures were set up using the "less forgiving" cross-correlation parameters so that the accuracy could be maintained as high as possible.

Although the final interrogation area (grid size) measured 32 x 32 pixels for streamwise and 16 x 16 pixels for cross-stream experiments, the actual measurement resolution was finer. Oversampling (overlap) of the PIV images was enforced, which meant that the interrogation interval (sample points) was smaller than the interrogation area dimensions (Raffel, 1998). By using 50% overlap in both directions for all experiments, the measurement resolution was half of the mesh size. Effectively, two vectors per original interrogation area were calculated. Any further increase in overlap would increase the total measurement error as explained in the following section (2.4.2)

After producing the vector field, a range validation was applied. Such a validation was beneficial, especially round the nozzle area, where many erroneous vectors were calculated.

Although masking was applied to the nozzle area and the algorithm did not calculate any vectors within the masked area, it was the mask boundary that produced the main problems. At the mask boundary there is a large particle-pair loss and thus the true velocity cannot be calculated accurately. Very large erroneous vectors are sometimes calculated, which will bias the averaged velocity field results. The validation criterion was based on the vector length or vector magnitude. If the estimated vector was above the set criterion value, it was rejected. The vector magnitude cut-off point set for low Reynolds number runs was 0.14 m/s. Based on the experimental results, the expected averaged maximum velocity magnitude for low Reynolds number forced runs was 0.12 m/s.

Having rejected the erroneous vectors, a moving average filter is used to substitute each vector with the uniformly weighted average of the vectors in a neighbourhood of a specified size m x n as shown in Equation 2.7. m and n are odd number of vector cells symmetrically arranged about the point of interest (x,y).

$$\vec{v}(x,y) = \left(\frac{1}{mn}\right) \sum_{i=x-\frac{n-1}{2}}^{x+\frac{n-1}{2}} \sum_{j=y-\frac{n-1}{2}}^{y+\frac{n+1}{2}} v(i,j) \qquad 2.7$$

The resultant filtered flow field is what was used to derive several flow characteristics such as vorticity, velocity fluctuations, obtain velocity profiles and so forth. The vector quantity of the measurement plane was 99 x 73 vectors for experiments along the streamwise direction and 199 x 146 along the cross-stream direction.

Vorticity (ω_i) is a localised property of the flow field and is used to quantify rotation. In all instances it was calculated from the flow field data described in the previous paragraph. Vorticity is a vector field and is defined as half of the curl of a velocity field. It is shown mathematically in Equation 2.8 (Durst, 2008):

$$2\omega_i = \nabla \times U = -\epsilon_{ijk}\left(\frac{\partial U_j}{\partial x_i}\right) = \left(\frac{\partial U_j}{\partial x_i} - \frac{\partial U_i}{\partial x_j}\right) \qquad 2.8$$

where ϵ_{ijk} is the alternating tensor and U_j is the velocity vector. It is therefore preferential to obtain all three velocity components simultaneously in order to compute all three vorticity components at once. The 2D-PIV system used was only capable of measuring two velocity components within the illumination plane. Therefore, only one vorticity component (with direction normal to the laser plane) could be calculated at each experimental orientation. For this reason, both streamwise and cross-stream measurements of the flow were taken. Through the use of Dantec Dynamics FlowManager software, a second order centre difference scheme was used to obtain estimates for the first derivatives (Equation 2.9).

$$\left(\frac{df}{dx}\right)_i \approx \frac{f_{i+1} - f_{i-1}}{2\Delta x} \qquad 2.9$$

The vorticity calculations were verified in Matlab using a script which calculated the vorticity of a velocity field. Both results matched up and thus flow manager was the preferred tool for vorticity calculations, due to ease of use. The vorticity field is useful for identifying shear characteristics such as rollups, shear layers and discrete vortices.

Flow fluctuations can be used to derive turbulent kinetic energy (TKE) and flow stress information. Normalised turbulent kinetic energy, defined as (TKE=$\overline{(u'^2 + v'^2)}/{U_o}^2$) where u'^2 and v'^2 are the second order streamwise and cross-stream velocity fluctuation moments respectively, provides useful insight to the location and distribution of the turbulence mechanisms. Normal Reynolds stress along the streamwise direction ($\bar{u}'\bar{u}'/{U_0}^2$), normal Reynolds stress along the cross-stream direction ($\bar{v}'\bar{v}'/{U_0}^2$) and Reynolds shear stress ($\bar{u}'\bar{v}'/{U_0}^2$) were also calculated. Regions containing high turbulence can be expected to achieve high levels of mixing. Matlab script files were produced to calculate the normalised turbulent kinetic energy and the flow stresses described above. These scripts are available in the Appendix section.

The jet momentum thickness was calculated using the PIV results along the streamwise direction. The numerical integration was performed using the trapezoidal rule. It must be noted that a jet has two shear layers and thus when calculating the momentum thickness for symmetric nozzles, the average value is used. This explains the ½ term found in the notation section. A final note is that the momentum thickness was normalised with respect to the nozzle diameter and thus all plots depict the normalised momentum thickness, averaged between the top and bottom shear layers. Similar to the other quantities, a script was written in Matlab which read-in the PIV results and exported the required momentum thickness results.

2.4.2 Uncertainty analysis

Several parameters can affect the accuracy of PIV measurements. The PIV system calculates the mean displacement of particles within an interrogation window during the time between two laser pulses to arise. Knowing the displacement and the time duration between each pulse, first order time derivatives, such as the velocity tensor, can be calculated. Of course, errors that exist in the measurement of the displacement will propagate into the velocity calculation and any subsequent calculations based on the displacement without neglecting the finite errors introduced by the calculations themselves. Thus, minimizing the displacement error will improve the general accuracy of the PIV system.

An inherent residual uncertainty exists, that accounts for the tolerances within which the physical components that comprise the PIV system, such as CCD chip, camera lens, electronic trigger box, particle sizing, were constructed and in many cases cannot be compensated for. Purchasing high quality research-grade equipment is essential for the reduction of such errors. Another type of error, namely the systematic error, can also help to produce a false displacement measurement. It is related to the effectiveness of the statistical method of cross-correlation in the estimation of particle displacement. Systematic errors can be affected by many parameters such as background noise, particle image density and velocity gradients within an interrogation window and out-of-plane motion (Raffel, 1998). These parameters can be set to an optimum which will reduce the systematic error substantially. An in-depth study regarding the measurement of noise and uncertainty is given in (Raffel, 1998). It is the author's belief that, through thought, planning and experimentation, these parameters have been optimised for each experimental PIV situation. The following paragraph explains how each parameter was set.

a) Particle sizing

Different particle sizing was used for experiments conducted along the streamwise view and along the cross-stream view. Dantec dynamics polyamid particles of diameter d=50μm were used for all streamwise experiments. When considering the field of view (150 x 110 mm) along with the resolution of the camera (1600 x 1200 pixels) and taking into account the magnification factor (12.8), it can be shown that each pixel on the CCD chip i.e. the chip resolution is equal to 94 μm in the measurement plane along the streamwise direction, chip resolution=150/1600=0.0938 mm. The ideal particle diameter (d) for the current setup should be two pixels in diameter, which results in the smallest measurement uncertainty. In our case, the nominal particle diameter in terms of pixels was d=0.53px, however the actual diameter of each particle as captured by the camera was measured at approximately two pixels in diameter. The reasons behind the discrepancy are due to the focusing of the particles and the finite thickness of the laser sheet. It is impossible to focus all particles within the laser sheet, because not all particles are at exactly the same distance from the camera lens. The difference in focusing may not be apparent when looking at the whole field of view, but when looking at individual particles it becomes evident. Thus finally, the actual particle diameter can be estimated to d=2px and the root-mean-square (rms) error in the velocity measurement, σ_u=2 mm/s (Kim *et al.*, 2004). The minimum resolvable velocity fluctuation is acceptably small compared to the typical measured velocities of 12cm/s.

When conducting cross-stream experiments, Dantec polyamid particles of diameter d=20μm were used. The reason for using particles of smaller diameter along with a finer interrogation

Table 2.1 System measurement specifications for streamwise and cross-stream experiments

	Streamwise	Cross-stream (x/D=0)	Cross-stream (x/D=5)
Field of view (mm)	149.8 x 110.4	111.7 x 82.5	103.3 x 76.3
Measurement resolution (mm)	1.51	0.56	0.52
CCD chip resolution (mm/px)	0.0936	0.0698	0.0646
Rms uncertainty (mm/s)	2	0.2	

mesh when compared to streamwise testing, was to increase the measurement resolution. The dominant flow structures (streamwise-oriented vortices) captured during cross-stream testing, are much smaller that the large-scale rollups (main ring vortices) seen along the streamwise view and thus require a higher measurement resolution. The laser sheet was set to illuminate the flow at certain cross-stream locations downstream of the nozzle exit. The camera on the other hand was not moved, which meant that, the field of view and as a consequence the measurement resolution, was different at each downstream location. At x/D=0 the field of view was at the maximum, while the resolution was at the minimum. At x/D=5 the field of view was at the minimum and the resolution at the maximum. Specific values for the field of view, measurement resolution and CCD chip resolution at two cross-stream locations have been calculated and presented in Table 2.1. The worst case CCD chip resolution (at x/D=0) was 0.0698 mm/px and the rms uncertainty was calculated to σ_u=0.2 mm/s. It must be noted however, that even though the cross-stream σ_u is reduced compared to the streamwise arrangement, the ratio between the rms uncertainty to the typical measured velocity has risen to approximately 14% compared to 1.7% for the streamwise case. This shows that between the two arrangements, the cross-stream measurements are less accurate. The physical size of the interrogation window used for cross-stream experiments was 16px X 16px, which according to (Raffel, 1998) introduced a higher inaccuracy when calculating particle movement through the use of cross-correlation. Finally, according to the Mie light scattering theory (Hulst, 1981) the reflective intensity of a particle is related to $\sim d^2$ and so the selection of particle size may be restricted by the lack of laser illumination power (Raffel, 1998). In this case larger particles and/or a brighter lens (lower *f* number) combination could help transfer more light to the CCD chip.

In order for the particles to follow the flow accurately they are required to have a Stoke's number lower than one. The Stoke's number is defined as:

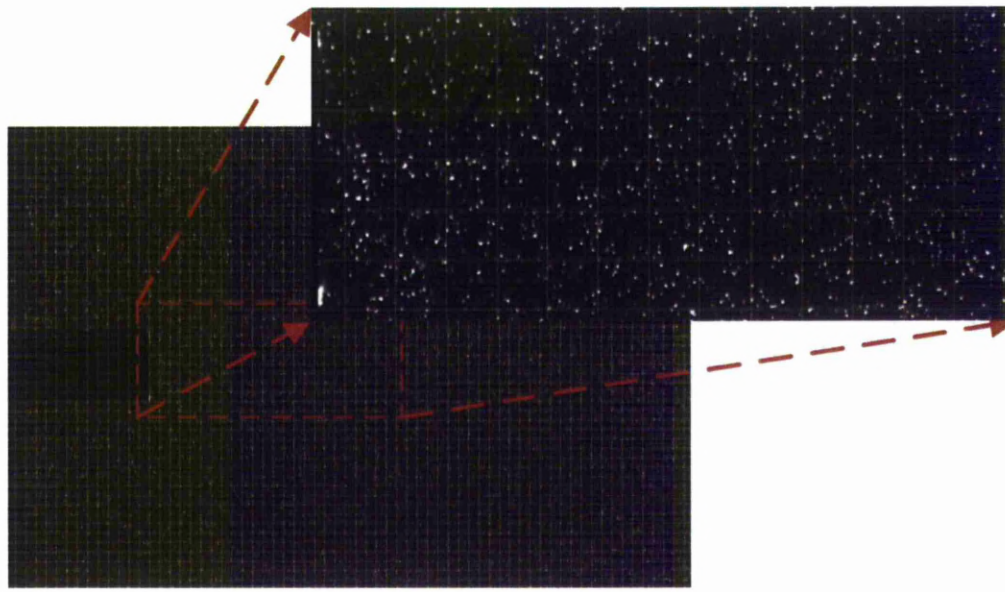

Figure 2.16 Particle density for 32 x 32 pixel grid used for streamwise experiments

$$S_{tk} = \frac{d^2 V}{18 l \nu} \qquad 2.10$$

Where d is the particle diameter, V is the maximum attainable velocity, l is the structure scale and ν is the kinematic viscosity of water at 15° C. When small-scale structures want to be analysed accurately it is necessary to use particles with a small diameter. Structures smaller than the grid resolution cannot be measured and thus substituting the PIV resolution with l in Equation 2.10 and including the rest of the test parameters, a Stokes number of S_{TK} =0.0025 was calculated. It can therefore be said that the particles will adequately follow the flow as documented by Shu,(2005).

b) Particle image-density

Along the streamwise direction a 32 x 32 grid was used while a 16 x 16 grid was used for cross-stream experiments. The amount of particles within an interrogation window, depending on PIV imaging scheme used, can affect the probability of valid displacement detection. High particle density increases the probability of valid displacement detection, as there are more particles to take place in the cross-correlation. To achieve 95% valid displacement detection rate using single exposure double-frame cross-correlation, there should be at least 6 particles within the interrogation window (Keane and Adrian, 1992). An example of the particle density used during streamwise experiments can be seen in Fig. 2.16. Each interrogation area consists of at least six particles.

c) Effects of velocity gradients

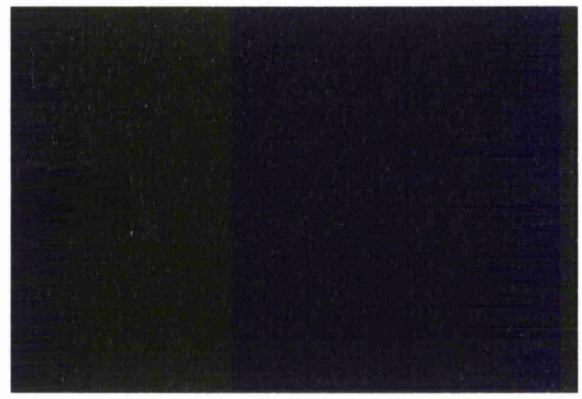

(a) particle image map

(b) Particle movement through the addition of frame A and frame B

(d) velocity vectors highlighting velocity gradients

(c) 32 x32 interrogation mesh

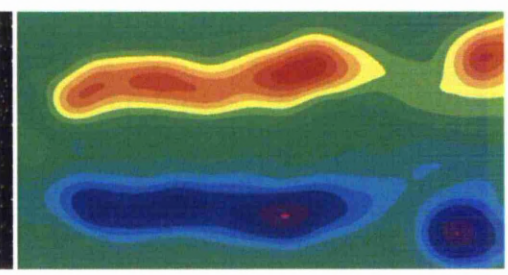

(e) Calculated vorticity field

Figure 2.17 The effective measurement of large-scale velocity gradients is demonstrated. The sequences displayed above are screen-captures from Dantec FlowManager software

Each interrogation window is used to calculate the average straight-line displacement of particle groups within it. Higher order time derivatives such as curvature and acceleration information cannot be obtained from a single image pair. Thus it is important when analysing flow with velocity gradients to minimise this effect within an interrogation window. This can be done by choosing an appropriate size of the interrogation window, which should be small enough to treat the velocity within it as non-rotational and without velocity gradients. Fig. 2.17 shows the particle image map during the testing of the circular reference nozzle along the streamwise view. It can be seen that the interrogation window chosen for this study is sufficiently small enough to detect vortices as shown form the superimposed velocity map and the vorticity map (Fig. 2.17(d) and (e)).

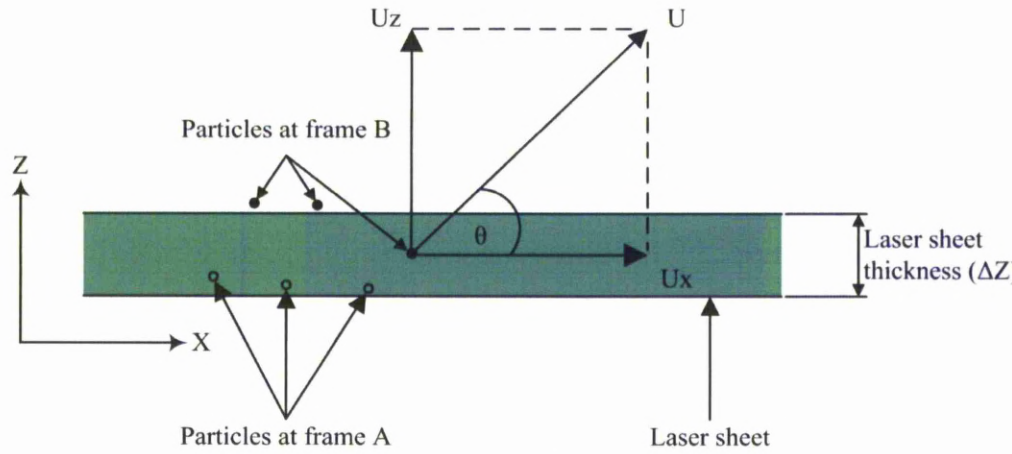

Figure 2.18 Schematic representation of error caused by out-of-plane particle movement

d) Out-of-plane motion

Since all PIV measurements were conducted using the 2-dimensional capability of the system, it was important to reduce the effects caused by velocity components normal to the laser plane (U_z).The velocity component normal to the laser plane is effectively lost as shown in Fig. 2.18. This provides an erroneous displacement measurement. By reducing the time delay between each laser pulse or by reducing the thickness of the laser sheet, these errors can be avoided. The laser sheet should be thin enough such that the measured velocity field is a good representation of that on the prescribed measurement plane and the displacement particles can be treated as linear. It is worth noting that the laser thickness was kept at a constant 2mm for all experiments. Due to the absence of specific beam optics which could converge the laser sheet, the sheet thickness was set with the use of a 2mm slit in front of the laser head. This method wasted laser power and as the slit became smaller, less power was left to illuminate the measurement area. Thus the minimum attainable laser thickness was restricted by the light intensity required for the measurement.

e) Vorticity uncertainty

Contour plots showing regions of similar vorticity are calculated from the velocity fields as discussed in section 2.4.1. The uncertainty associated with the calculation of the vorticity field depend on the finite difference scheme used. For a central difference scheme, as used by FlowManager software, the order of accuracy when applying the Taylor series expansion is two. As shown previously, the central differencing scheme, Equation 2.9 is applied.

The uncertainty is approximately given by (Raffel, 1998),

$$Vorticity \cong 0.7\frac{\epsilon_U}{\Delta X} \qquad 2.11$$

where ϵ_u is the uncertainty in the velocity measurement ($\epsilon_U = 0.05\%$). It can now be seen that if the overlap were to be doubled as proposed in "i PIV analysis parameters" section, the vorticity uncertainty would double as ΔX would be reduced by a factor of two while the measurement uncertainty for the velocity, ϵ_u, would be the same (Equation 2.11). Therefore the optimum overlap balance between uncertainty and resolution was chosen.

2.5 Concluding remarks

The experimental setup along with both qualitative and quantitative techniques, were described. The advantages and limitations of both experimental methods were depicted. The combination of flow visualisation in conjunction with quantitative methods such as PIV, LDA or hot-wire anemometry is key to understanding the formation and interactions of coherent structures. Each method alone cannot aid the researcher, but together they complement each other. Hussain (1983), elegantly stated that: "flow visualisation presents excessive information but very little hard data, and anemometer data give some hard data but very limited flow physics. Consequently, efforts should be made to pursue in parallel both flow visualisation and quantitative data in coherent structure investigations".

3 FLOW CHARACTERISTICS OF A- AND V-NOTCHED CIRCULAR NOZZLES[1]

3.1 Chapter overview

The following chapter presents and analyses the experimental results obtained from the study of circular jets, issued from nozzles incorporating A- and V-shaped notches. The methods used to conduct the study consist of both flow visualisation techniques and two-dimensional PIV measurements, along streamwise and cross-stream directions. The first section will cover the flow visualisation results, mainly focusing on the vortex interactions, while in the second section, quantitative findings obtained from the PIV measurements will be presented and subsequently analysed. Having taken into consideration all of the results, a graphic representation will be presented, describing the flow development for each nozzle configuration.

3.2 Results and discussion

3.2.1 Flow visualisation

a) Flow visualisation using dye injection

Figures 3.1 to 3.9, show flow images of the nozzles that have been analysed in this chapter. Figure 3.1 shows the circular reference nozzle which is the benchmark case to which all other nozzles are compared. Figures 3.2 to 3.5 concentrate on the shorter, less sharp, AR2 nozzles while the latter four figures depict the sharper AR4 nozzles.

An image sequence showing the shear layer rollup associated with the reference nozzle can be seen in Fig. 3.1. From the images, it can be noticed that once the shear layer rollups (main ring vortices from now on) have occurred, they are very stable and propagate to a large downstream position before breaking down. Vortex rings breakdown due to Widnall instabilities (Widnall and Sullivan, 1973; Widnall *et al.*, 1974) and viscous effects. It has been found for vortex rings, that as the vortex progress downstream, instabilities in the form of waves initiate around their azimuth. These waves grow in amplitude until the coherent vortices break down into non-coherent eddy-containing fluid. Unlike distinct vortex rings, the main ring vortices found in jets compete against viscous effect, shear layer interactions and inherent instabilities as explained previously and thus it is common for them to break down within a shorter downstream distance. For the reference case, the breakdown position of the main ring vortices is situated approximately 5 diameters (Fig. 3.1(g)) from

[1] Results from this study have been published in New and Tsovolos, (2009a, c)

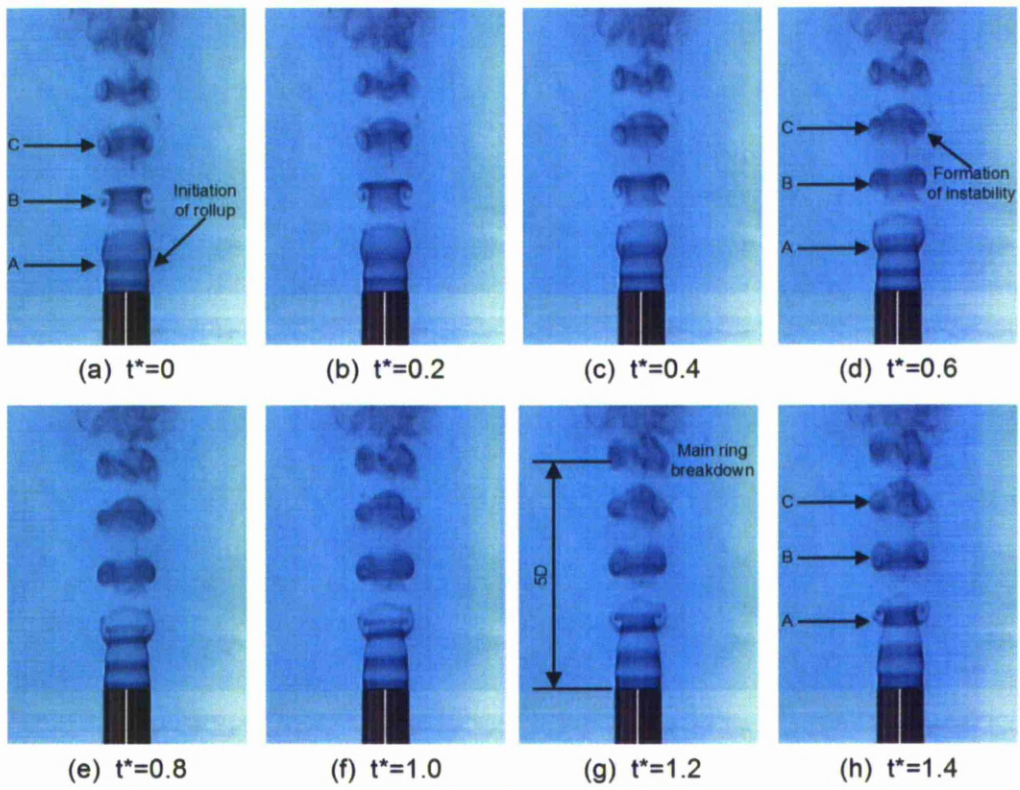

Figure 3.1 Flow visualisation of circular reference nozzle under forced conditions at Re= 2100

the nozzle exit (which for the reference case coincides with the mean height). The breakdown position can provide a visual reference to the end of the jet potential core, although qualitative results presented in the next section pinpoint the exact location. It can be understood that due to the large length of the potential core, little interaction between the jet column and the surrounding ambient fluid must take place. It has been shown that streamwise oriented vortices do exist within the braid region of the jet (region between two ring vortices) (Liepmann and Gharib, 1992). However, looking at Fig. 3.1 their effects cannot be discerned. Another point worth making, is that the main ring vortices (indicated as A, B and C) rollup parallel to the nozzle lip and continue downstream without changing their inclination angle. The behaviour of the reference jet was expected and has been reported in the past by researchers (Oshima, 1972; Hussain and Zaman, 1980; Zaman and Hussain, 1980; Hussain and Zaman, 1981).

Due to the stability of the vortices formed from the circular reference nozzle, the selected time sequence depicted in Fig. 3.1 has captured vortices that initiated from previous forcing cycles. A newly formed vortex A, a vortex from the previous forcing cycle B, and the vortex from the flow cycle previous to that, C are observed in Fig. 3.1. The length of the time sequence has been chosen such that 1.4 of a forcing cycle is shown. The time marker has

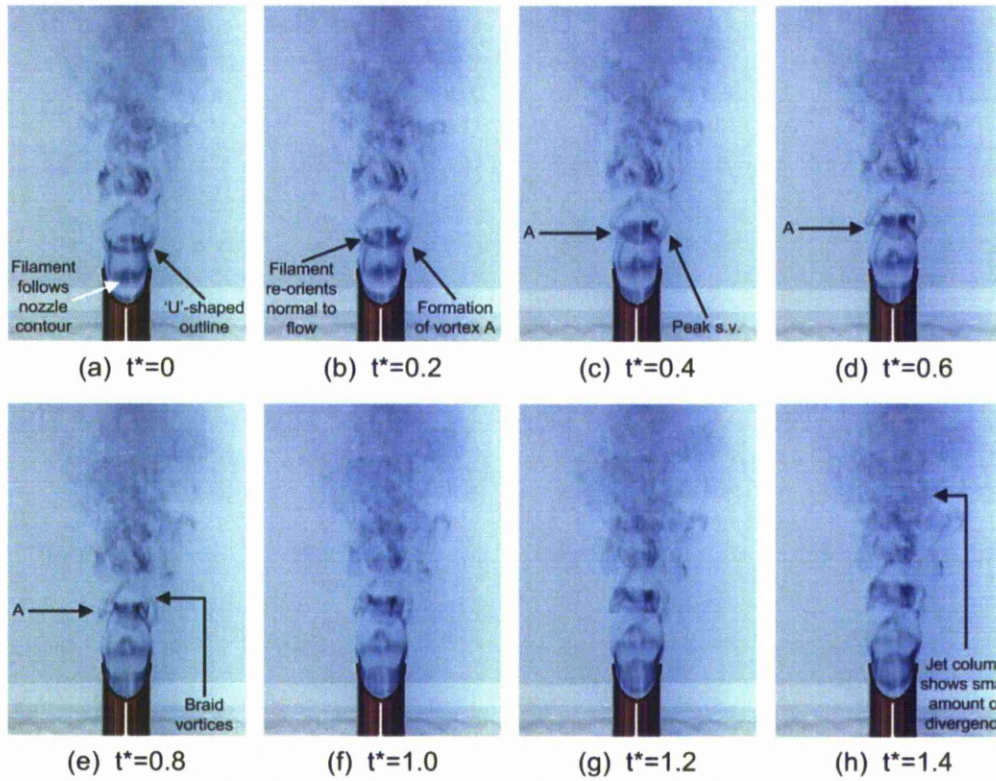

Figure 3.2 Flow visualisation of AR2 A-notched nozzle, PP view

been non-dimensionalised by the forcing period of the flow perturbation, (t*=t/T), where t=0 at the first flow image and T is the forcing period. Effectively following filament A, the time evolution of the shear layer rollup can be seen. Vortex B shows an typical steady vortex and how it propagated towards the downstream location, while vortex C illustrates how instabilities start, affect it and lead towards breakdown.

Looking at the flow field created by the AR2 A-notched nozzle, shown in Figs. 3.2 and 3.3, and comparing it with the reference case, differences immediately emerge. The first impression is that the flow fields along both views are more intense and less organised. The main ring vortices break up much earlier than what was seen for the reference case. Comparing the main ring vortex evolution of the IO nozzles to the reference case, most IO nozzles create more intense flow field conditions, as shown in Figs. 3.1 to 3.9. For an IO nozzle, the time required for the shear layer to rollup, convect downstream and reach the breakdown can be captured by a time length of approximately two forcing cycles, while within the same timescale the reference case is still at the initial stages of flow development, vortex A in Figs. 3.1(a)-(h). It turns out that the flow development is faster for most IO nozzles.

Figures 3.2 and 3.3 show both orientations of the AR2 A-notched nozzle. In Fig. 3.2 the influence of the sharp peaks can be seen (PP-plane from now on), while in Fig. 3.3 the effect

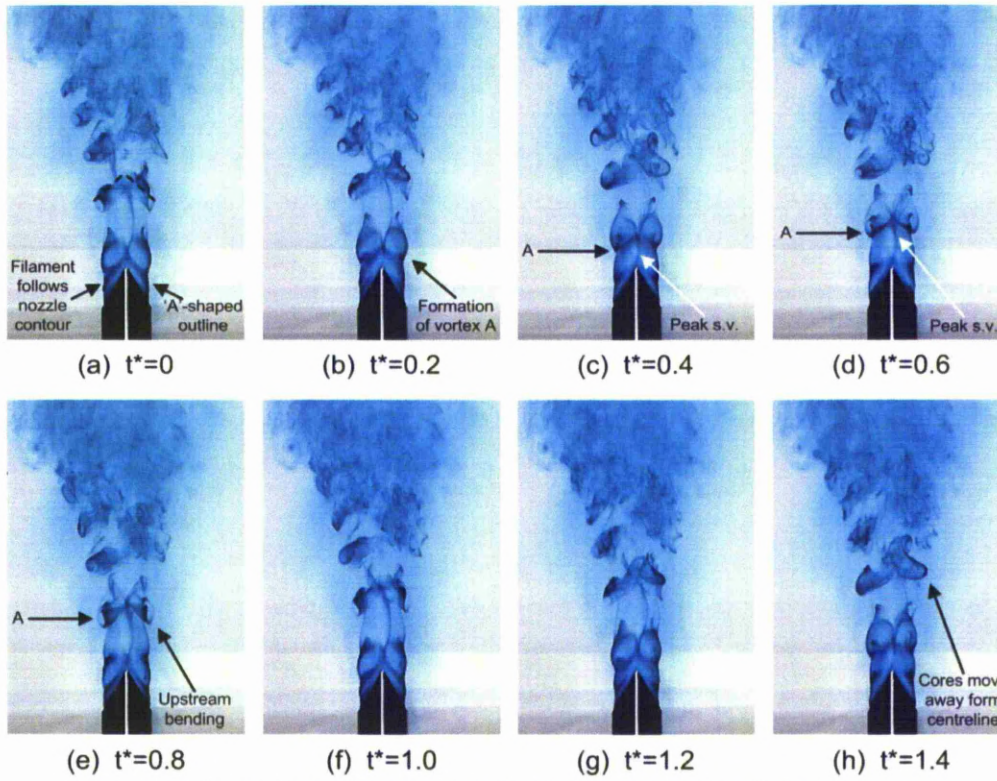

Figure 3.3 Flow visualisation of AR2 A-notched nozzle, TT view

of the smooth troughs are evident (TT-plane from now on). Looking at the image sequence shown in Fig. 3.2, the formation and development of filament A is shown. Initially the filament follows the contour of the smooth trough but as it propagates downstream it quickly re-orientates itself normal to the direction of the flow.

The shear layer rolls up and in doing so, entrains the streamwise orientated vortices produced by the peaks (named streamwise vortices from now on). The streamwise vortices are highlighted as thin streaks originating from the sharp nozzle peaks. Visually, they do not seem to have any drastic effects on the jet. Longmire *et al* (1992a) found that streamwise vortices are responsible for the gross momentum exchange between the jet and the surrounding ambient fluid, but in this case, they are too weak to have any such effects. Interestingly, the jet column does not diverge as expected, but can be seen to move laterally towards the nozzle centreline at approximately three diameters from the nozzle mean height. This behaviour indicates that the cross sectional shape of the jet changes with distance. This has also been reported in the past for crown shaped IO nozzles with two as well as four peaks (Longmire *et al.*, 1992a).

The flow field associated with the TT-plane can be seen in Fig. 3.3. Similarly to the PP-plane, the filament initially follows the nozzle contour and is bent into an "A-shaped" outline. As the filament propagated downstream and the shear layer rolls up, a bent main

ring vortex is formed as shown in Fig. 3.3(d). When comparing to the main ring vortex produced along the PP-plane with the ring produced along the TT-plane it is clear that the sharp peaks cause a greater manipulation than the smooth trough. As shear layer rolls up, indicated by vortex A, a bending and a spreading motion occurs. The main ring vortex bends toward the upstream direction, resembling an A-shaped outline, while the vortex cores move away from the nozzle centreline. This upstream and outward motion of the main ring vortices causes the jet to spread. As expected, the spreading is much greater along the plane being examined than along the PP-plane. The final image-sequence, shown in Fig. 3.3(h) indicates clear main ring vortex bending (vortex A) as well as motion away from the jet centreline. It can clearly be seen that the ends of vortex A have extended away from each other by a distance greater than the nozzle width.

Moving on to the V-notched nozzle of aspect-ratio two, a similar flow field can be seen, albeit with a few flow differences that will be described shortly. Comparing the two planes, in Figs. 3.4 and 3.5 respectively, a similar occurrence is observed. The shear layer rollup along the PP-plane, undergoes bending but does not spread as it propagates downstream, while along the TT-plane bending of opposite direction and spreading is apparent. It can therefore be stated that A and V-notched nozzles generate similar flow fields in a visual

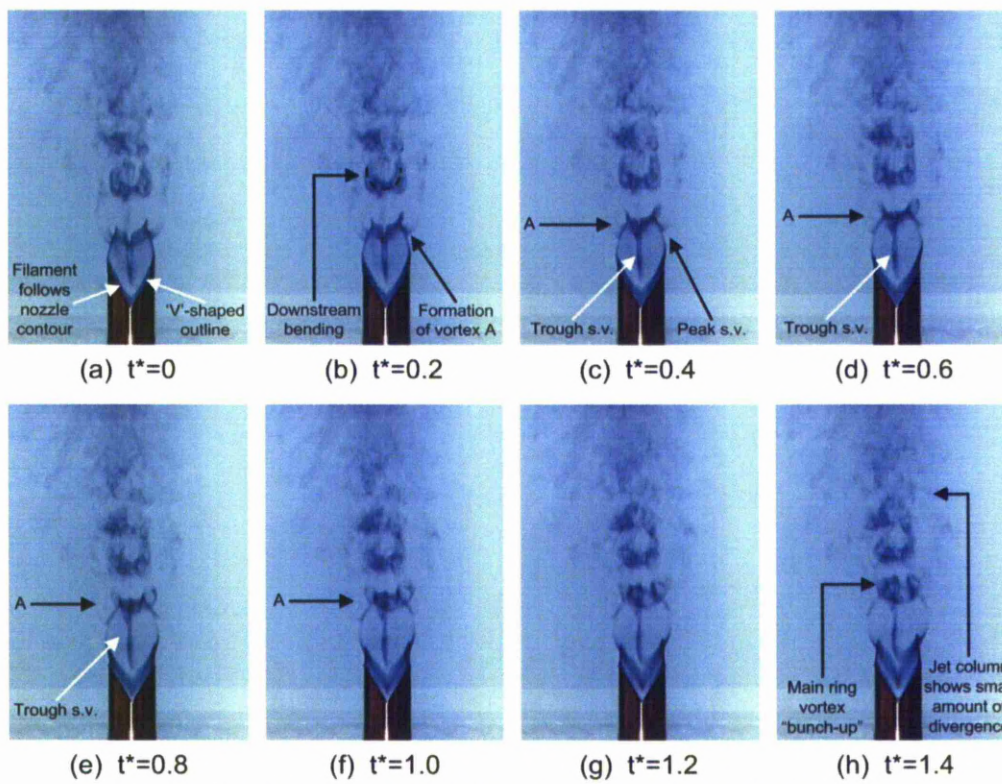

Figure 3.4 Flow visualisation of AR2 V-notched nozzle, PP view

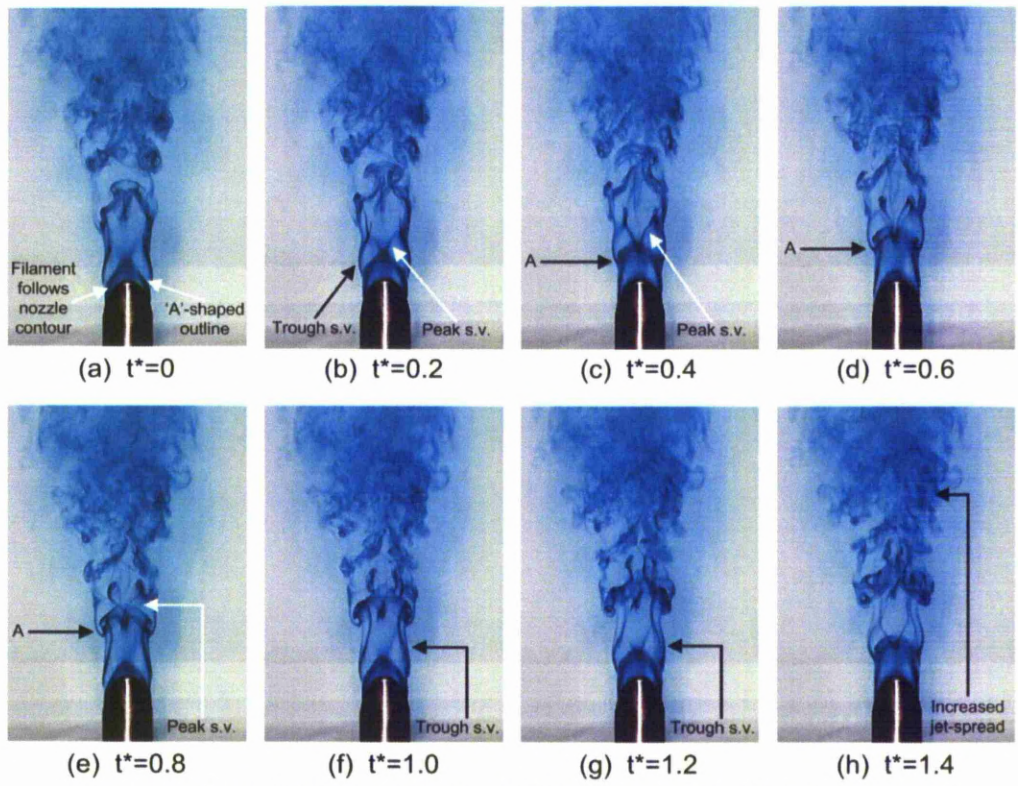

Figure 3.5 Flow visualisation of AR2 V-notched nozzle, TT view

sense, but still have distinct differences in the vortical structure arrangement.

Following the shear layer rollup in Fig. 3.4 indicated by A, main ring bending towards the downstream direction is evident. As the main rings form, they follow the nozzle contour and as they progress downstream their curvature decreases which brings the vortex ends towards the nozzle centreline. The ends of the main ring vortices continue to move towards the jet centreline until they "bunch-up" as shown in Fig. 3.4(h). Similarly to the A-notched IO nozzle, the main jet body does not diverge substantially which could also be explained by the bending and movement of the main ring vortices. Streamwise vortices are formed consistently at the sharp troughs and are identified as thin streaks. It has been shown that they are formed by vortex filaments rollup following the contour of the V-shaped trough. As these filaments develop, they coalesce, reduce the included angle between them and align parallel to the nozzle centreline direction. Although sharp discontinuous troughs and peaks tend to produce visually smaller streamwise vortices, their impact on the main ring vortices is still noticed. Their interaction with the main ring vortices is clearly visible in Figs. 3.4(a)-(d). They appear to distort the main ring vortex and cause the middle section to retard thus causing the distinct V-shaped ring.

Studying the nozzle along the TT-plane, the filament orientation is reversed. The main ring rollup A is bent in the opposite direction to the PP-plane. The ring forms an A-shaped

outline following the smooth peak contour. As stated earlier the main ring vortices spread apart with a direction away from the nozzle centreline, which increases the jet spread in a visual sense. The streamwise vortices formed form the smooth peaks are quite unstable and tend to meander. Due to the absence of a sharp discontinuity along the peak contour, the point on the nozzle peak from which the streamwise vortices form varies between two extremes in the vicinity of the peak. The region of influence associated with streamwise vortices formed from smooth peaks is greater than for sharp troughs. Their interaction with the main ring vortices is shown in Figs. 3.5(b) to (h), in which the streamwise vortices distort the main ring, cause the middle section of it to retard and finally contribute towards the main ring vortex breakdown. Along this view the interaction between the streamwise vortices formed from the sharp troughs and the main ring vortices can also be seen. Effectively, the streamwise vortices retard the middle of the ring as explained earlier and as a result of the interaction get entrained by main ring vortices, highlighted in Figs. 3.5(e)-(g). This entrainment process however, was not visible when looking along the PP-plane. Similarly, the peak streamwise vortices also get entrained by the main ring vortices which can be seen in Figs. 3.4(e) to 3.4(h).

The same flow mechanisms described above for the nozzles with an aspect-ratio of two, apply to the sharper nozzles of aspect-ratio four. In Figs. 3.6 to 3.9, flow fields of higher intensity can be seen which lead to the formation of less coherent main ring vortices and to faster ring breakdown. In some cases, due to sharper nozzle geometry the streamwise vortices interact with the main vortices to a larger extent. Apart from the streamwise vortex strength, which will be investigated in the next section when analysing the PIV data, the location at which it form plays an important role on the effect it will have on the flow field or the main ring vortex. In most cases concerning the AR4 A and V-notched geometries, streamwise vortices formed at the peaks (sharp-peaks in the case of A-notched and smooth in the case of V-notched) are very close to the shear layer rollup location. Thus interactions between streamwise vortices and main ring vortices will be increased and depending on the strength of the streamwise vortices will affect the breakdown of the main ring vortices and the general jet flow field.

Figures 3.6 and 3.7 illustrate the PP and TT-plane respectively, of the A-notched nozzle with an aspect-ratio of four. Along the PP-plane, the flow structuring is not very clear and the main ring vortex breaks down immediately after its formation. The large-scale structures remain coherent for approximately three diameters downstream of the reference height. As the shear layer rolls up it also entrains the streamwise vortices formed at the sharp peaks. As stated earlier, the downstream location of the shear layer rollup is near the nozzle peaks from which the streamwise vortices originate. Streamwise vortices formed at the nozzle peaks

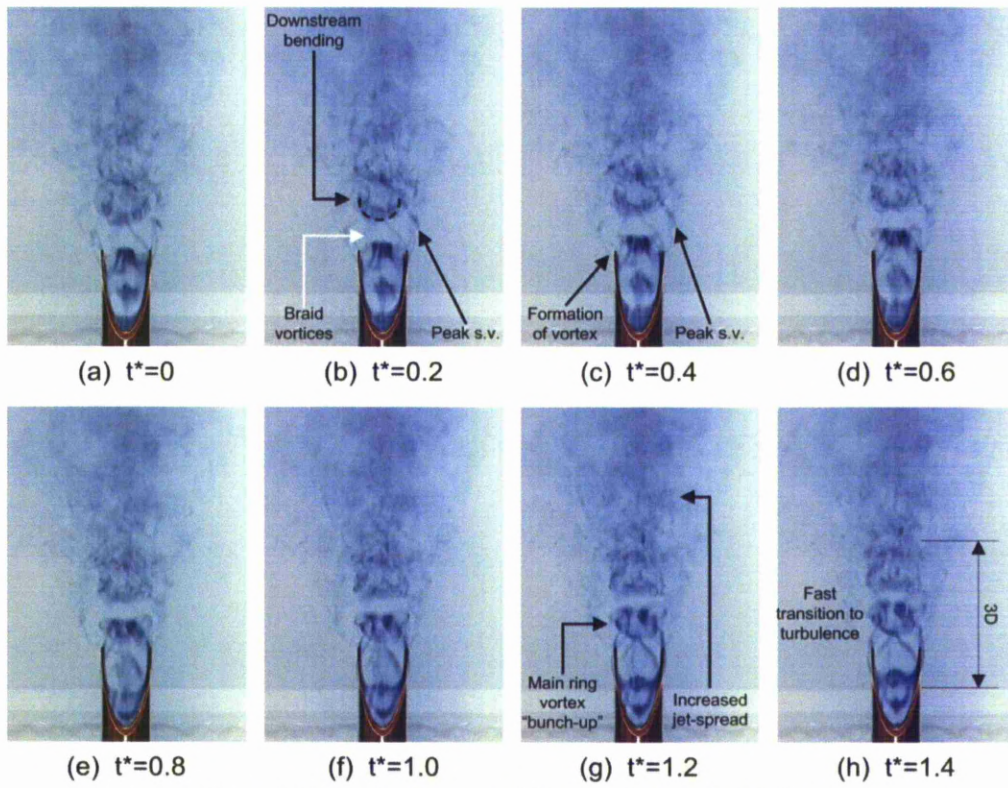

Figure 3.6 Flow visualisation of AR4 A-notched nozzle, PP view

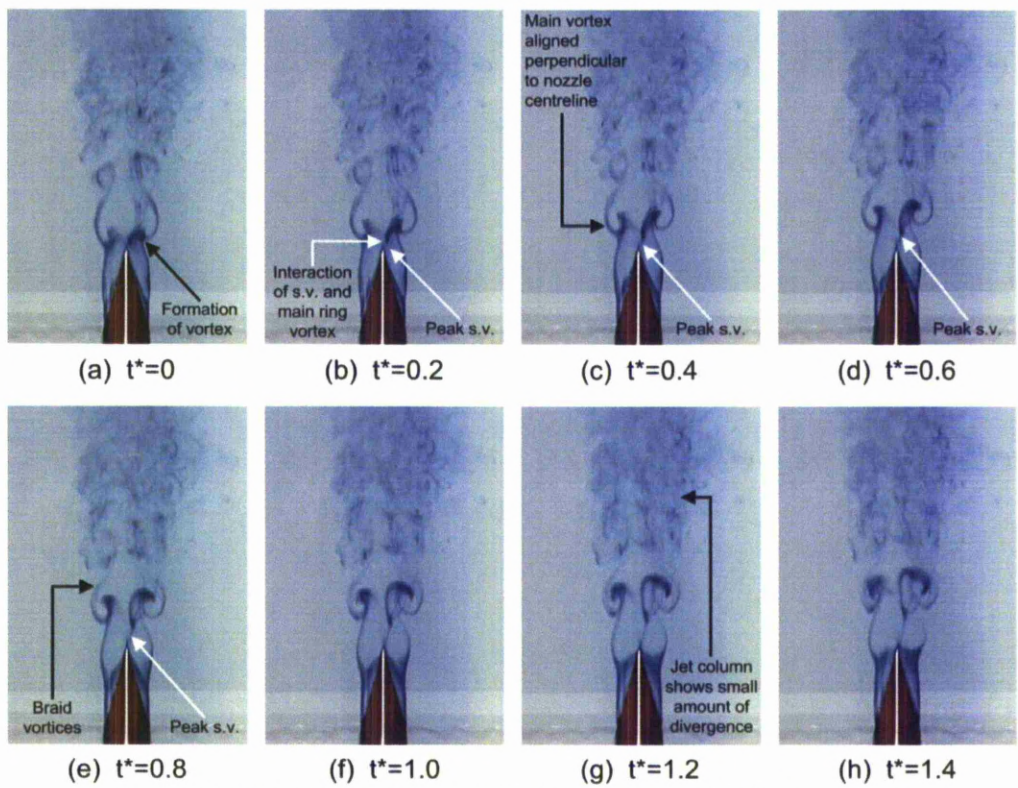

Figure 3.7 Flow visualisation of AR4 A-notched nozzle, TT view

have a larger influence on the jet than the vortices formed at the smooth trough locations. Similar to observations made with the previous test cases, smooth troughs generate visually weak streamwise vortices which do not influence the main jet flow field to a large extent. Contrary to what was seen for the less sharp case (AR2), along the PP-plane the jet spread is increased, mainly due to the streamwise vortices formed at the sharp peaks. The ring vortices which form are bent toward the downstream direction following the nozzle contour and "bunch-up" as they move downstream. Along the TT-plane, shown in Fig. 3.7, the view of the main ring is clearer. An interesting difference between the two aspect-ratio nozzles (AR 2-4) is that the ring vortices of the high aspect-ratio case do not follow the nozzle contour as precisely as was noticed for the less sharp aspect-ratio two nozzle geometry. The shear layer rolls up slightly downstream of the nozzle peak and does not resemble an A-shaped outline as expected from the previous test case. Most of the ring vortex is aligned perpendicular to the nozzle centreline, similar to the reference case. Clearly there is a limit to the amount of manipulation imposed on the main vortex rings in a jet by a passive means such as IO nozzle design. The jet body remains largely unaffected and does not diverge more that the reference case which should be expected as the smooth trough streamwise vortices are weak. A final observation is made on the peak streamwise vortices and their interaction with the main ring vortices. As the main ring vortex forms, depicted in Figs. 3.7(a)-(f), it is possible that the middle section of the ring is retarded by the boundary layer formed between the jet flow and the nozzle peak, due to the non-slip condition present at a solid boundary. As the middle section of the ring is slowed, portions of the ring on either side of the midpoint are rotated and aligned along the nozzle centreline, thus creating streamwise vortices. Visually, the middle section of the main ring vortex is "pinched" as shown in Fig. 3.7 (b).

In Figs. 3.8 and 3.9, some interesting flow characteristics can be observed. Along the PP-plane, the main ring vortex behaves similar to the A-notched case. After the rollup has initiated, the ring vortices move towards the nozzle centreline, coalesce and break up approximately three diameters from the mean height position. Again, the streamwise vortices formed at the peaks interfere with ring vortices and promote faster main ring breakdown. Similar to the A-notched nozzle with an aspect ratio of two, in this case the sharp troughs also produce well formed streamwise vortices which are stable and remain aligned with the nozzle centreline as they propagate downstream. The interaction of these sharp-trough streamwise vortices is evident throughout the image sequence in Fig. 3.8, although their effect is better understood in Fig. 3.9 when viewing the nozzle along the TT-plane. The sharp-trough streamwise vortices retard portions of the main ring vortex and cause it to bend and move away from the nozzle centreline. As discussed for the less sharp (AR2) nozzle, the streamwise vortices formed at the smooth peaks are visually more intense

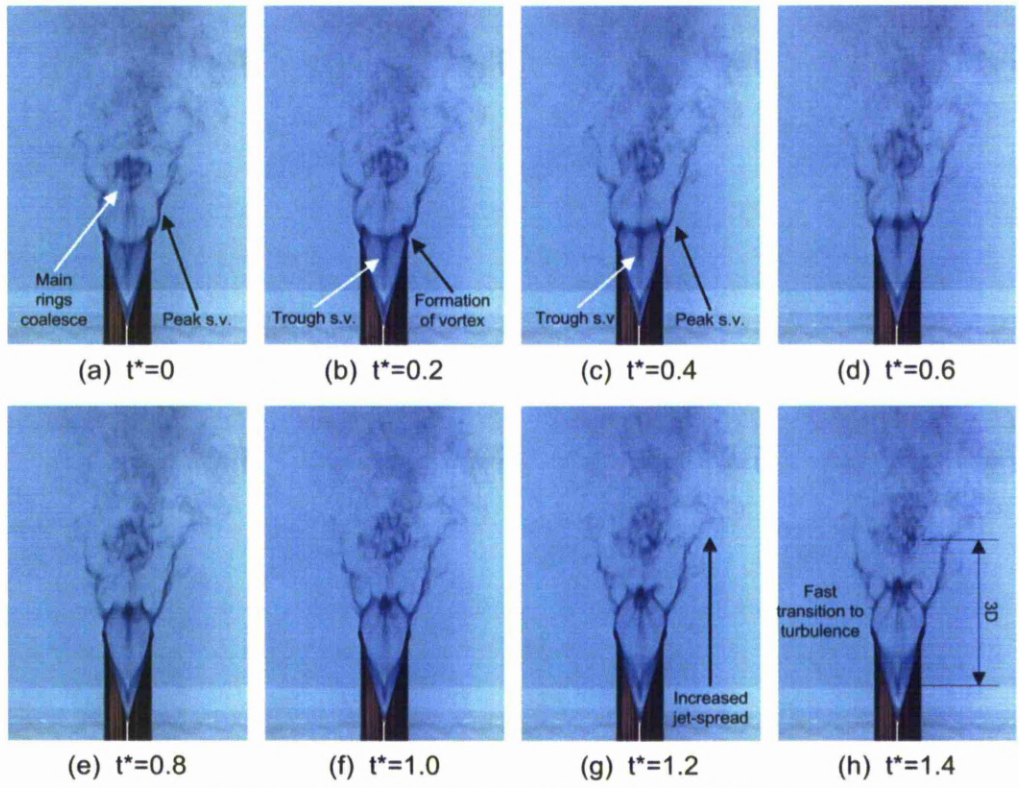

Figure 3.8 Flow visualisation of AR4 V-notched nozzle, PP view

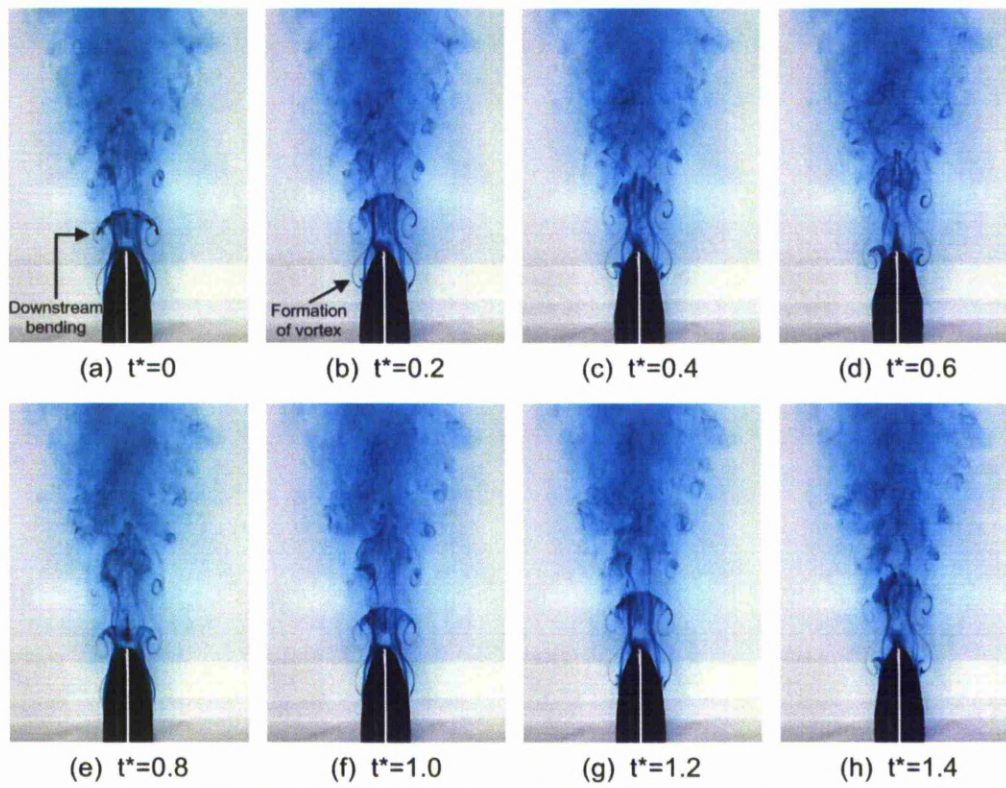

Figure 3.9 Flow visualisation of AR4 V-notched nozzle, TT view

(Fig. 3.8). The added sharpness associated with the increase in aspect-ratio from two to four seems to produce stronger streamwise vortices at the peaks. The effects of these stronger vortices are seen along the TT-plane, where, contrary to the main ring vortex movement, the jet spread is significantly greater when compared to the rest of the nozzle cases. The effects postulated by Longmire *et al.,*(1992a) are clearly visible. Visually, the streamwise vortices move outwards and appear to mix the main jet body with the surrounding quiescent flow.

Examining all of the flow visualisation results some general flow characteristics which were common to all nozzles became apparent. Importantly, the flow mechanisms associated with main vortex ring bending and the generation of streamwise vortices were similar between all nozzles. It was shown that smooth peaks of AR4 and sharp troughs produced more visible streamwise orientated structures and intense flow fields. Another important parameter which was not highlighted greatly was the fact that all nozzles manipulated the main ring vortices in a similar way, the underlying flow mechanisms were the same. This manipulation in turn, had the effect of changing the cross-section of the jet as a function of the downstream distance. More specifically, a resemblance between jets issued from A and V-notched nozzles and elliptic jets can be seen. The axis-switching phenomenon in elliptic jets was studied by (Ho and Gutmark, 1987) and states that the main vortex rings produced by an elliptic nozzle do not remain constant in cross-sectional shape as they propagate downstream. The initial major axis of the ellipse finally becomes the minor axis and vice versa. The change in cross-sectional shape is caused by main ring bending, similar to what was observed for the A and V-notched nozzles. A more in-depth explanation of the axis switching phenomenon has been presented in chapter 4. Thus based on the flow images it is thought that the A and V-notched nozzles undergo axis-switching. Quantitative proof of this hypothesis follows in section 3.2.4 where half-jet width and momentum thickness plots are shown.

b) LIF streamwise

Figures 3.10 to 3.18 show streamwise LIF results and Figs. 3.19 to 3.28 show cross-stream sections of the flow using the LIF experimental method. For the sake of consistency, the circular reference nozzle was tested initially, shown in Fig. 3.10. The LIF flow visualisation along the streamwise direction is very similar to the dye visualisation presented earlier. Following vortex A as it forms and propagates downstream, a symmetric rollup and behaviour is observed. As expected, instabilities within the main ring vortices start approximately at five jet-diameters downstream of the nozzle exit.

Focusing on the PP-plane of the AR2 A- and V-notched nozzles, in Figs. 3.11 and 3.13 respectively, one can see that that the streamwise vortices formed at the peaks have a large

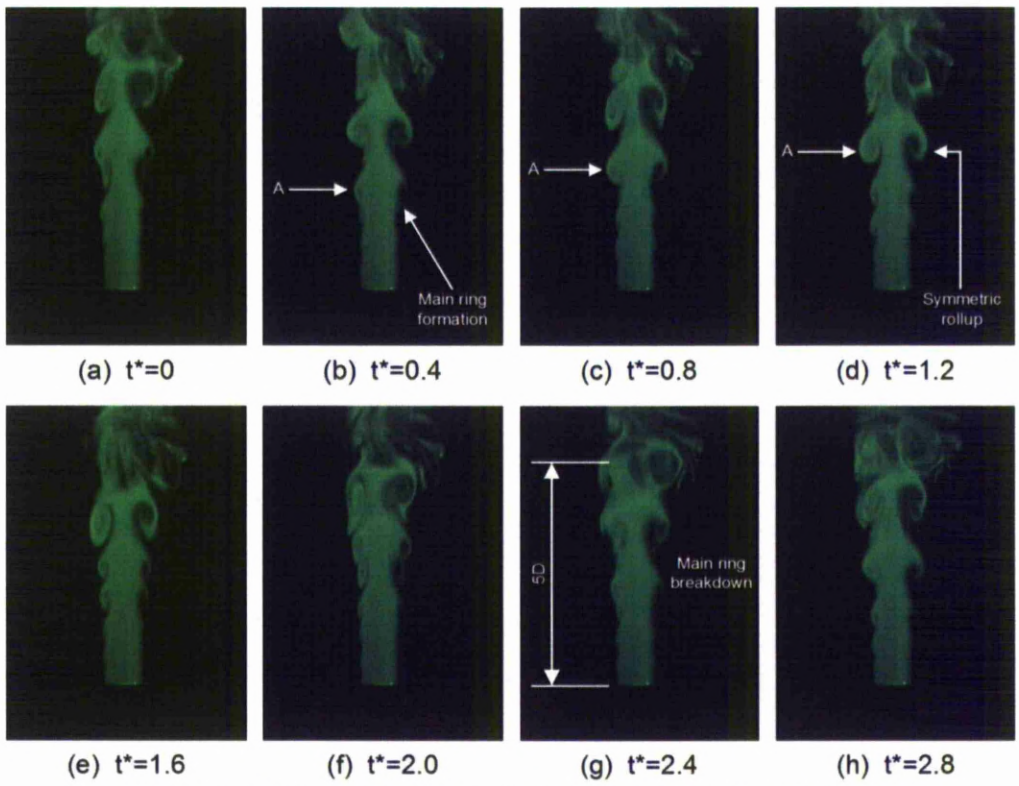

Figure 3.10 Streamwise LIF visualisation of circular reference nozzle

influence on the jet spread. In both cases the jet diverges more compared to the corresponding TT-plane of each nozzle, shown in Figs. 3.12 and 3.14, and also compared to the reference nozzle. The formation of "rib-like" structures is apparent. These structures have also been reported by Husain and Hussain, (1991). They showed that these structures form on the periphery of the jet and tend to spread in an outward sense, away from the nozzle centreline. Other reports such as Longmire *et al.*,(1992a) and Shu *et al.*,(2005) have also detected these "rib-like" structures. In their studies the structures were characterised as streamwise aligned counter rotating vortex pairs which also spread in an outward sense as they propagate downstream. It was also shown that streamwise vortices formed at the nozzle peaks have a tendency to spread the jet, which coincides with the present findings. As seen in the dye visualisation section, smooth peaks produce streamwise vortices that interact with the main jet column to a greater extent.

Continuing the analysis along the PP-plane of the AR2 A- and V-notched nozzles, but focusing on the main ring vortex dynamics, interesting observations can be made. In both cases, the main ring vortices gradually move towards the nozzle centreline. This indicates that the main flow mechanisms associated with the two nozzles are similar. As the main rings form (vortices A in both cases), they rollup and form bent filaments. It is worth noting at this stage that the bending direction for the AR2 and AR4 A-notched nozzles, shown in

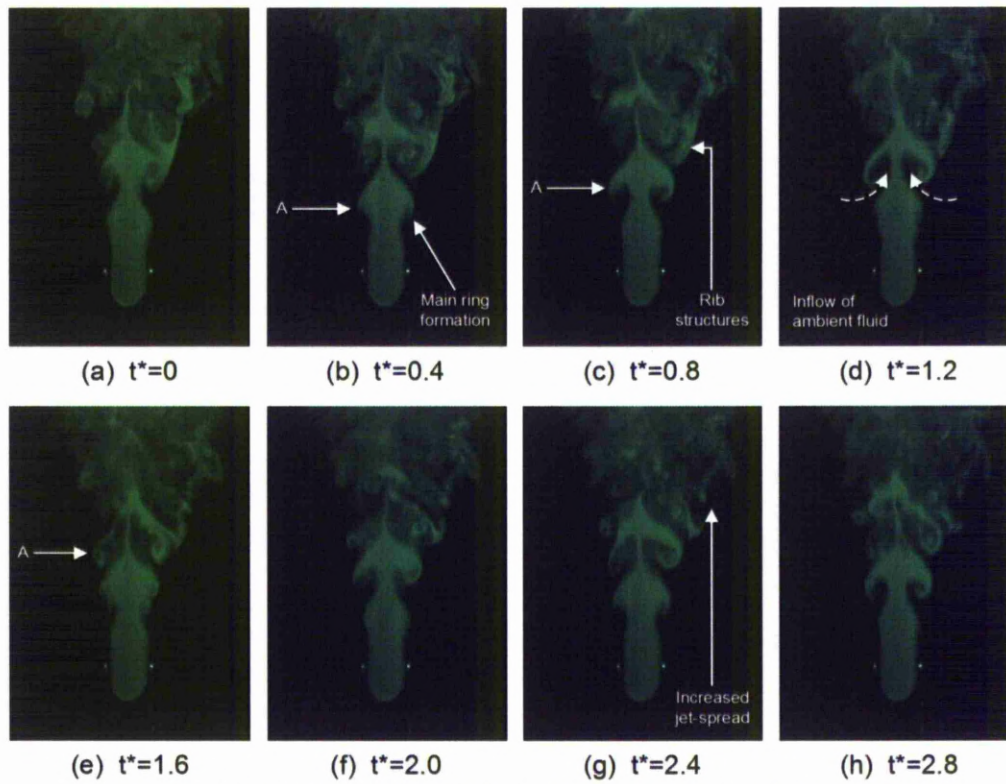

Figure 3.11 Streamwise LIF visualisation of AR2 A-notched nozzle, PP view

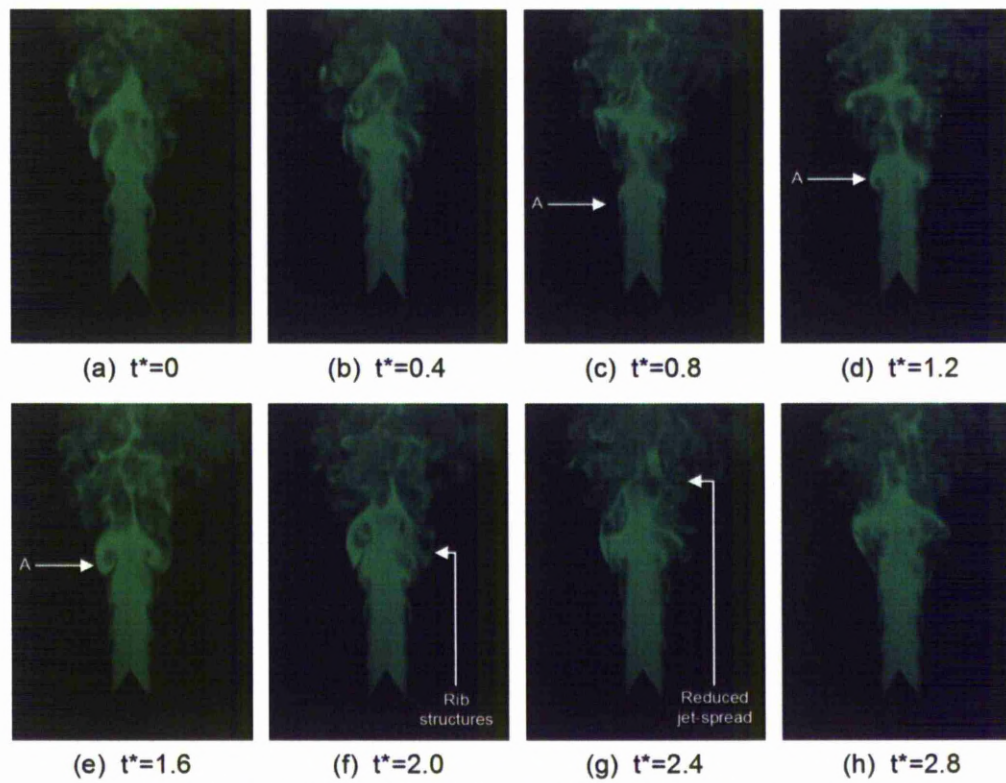

Figure 3.12 Streamwise LIF visualisation of AR2 A-notched nozzle, TT view

Figs 3.11 and 3.15 respectively, do not coincide with what was observed earlier. The inconsistency can be attributed to the difference in the experimental method used. To observe vortex bending, the filament has to be illuminated by injecting dye into the shear layer. For the LIF experiments, dye was injected into the main jet body and a laser plane was used to illuminate a slice along the nozzle centreline. So it is more valid to talk about the main ring vortex position than bending orientation. Ambient fluid inflow between two successive ring vortices, also known as the braid region, is observed along the PP-plane for A- and V-notched nozzles, shown in Figs. 3.11 and 3.13. These inflow regions are marked as black patches in the jet column as entrained ambient fluid does not contain fluorescent dye.

Along the TT-plane a very different flow scenario exists. Again the flow fields associated with AR2 A- and V-notched nozzles are similar. In both cases, there is a reduced amount of jet spreading and the main ring vortex rollup is less intense. Main ring vortex cores, although not as well defined as seen along the PP-plane, gradually move away from the nozzle centreline, similar to what was observed in the dye visualisation section. The main differences found can be attributed to the shape of the trough. It can be seen that the streamwise vortices produced at the V-notched nozzle sharp troughs do manifest and interfere with the jet body to a greater extent with respect to the A-notched nozzle.

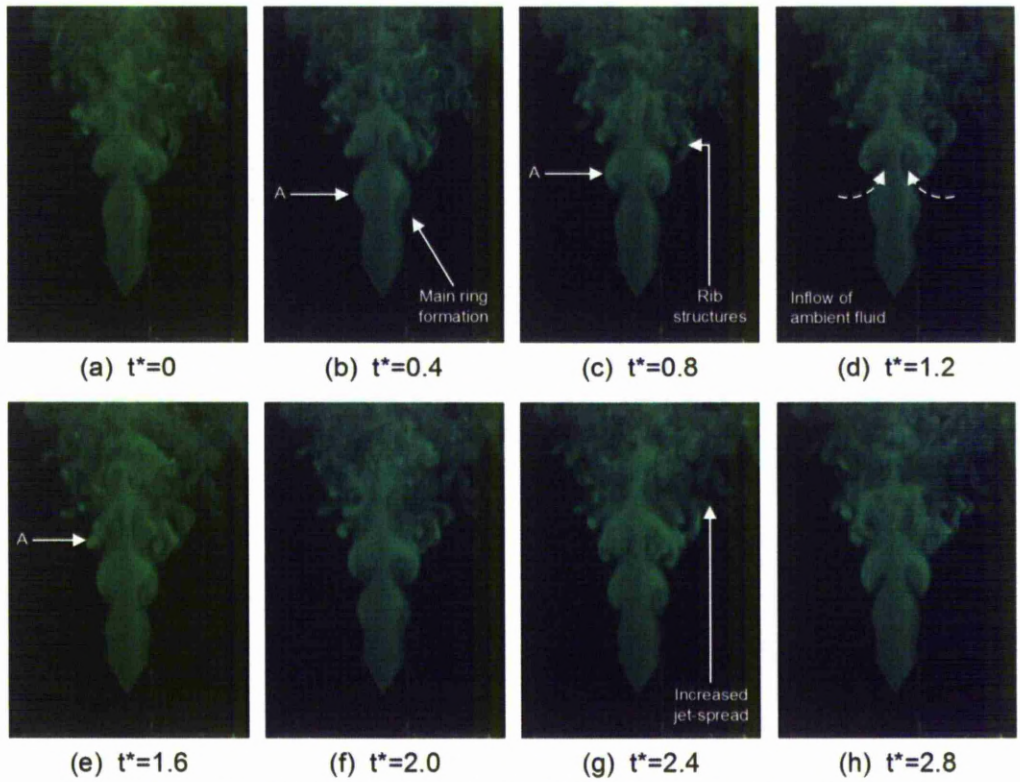

Figure 3.13 Streamwise LIF visualisation of AR2 V-notched nozzle, PP view

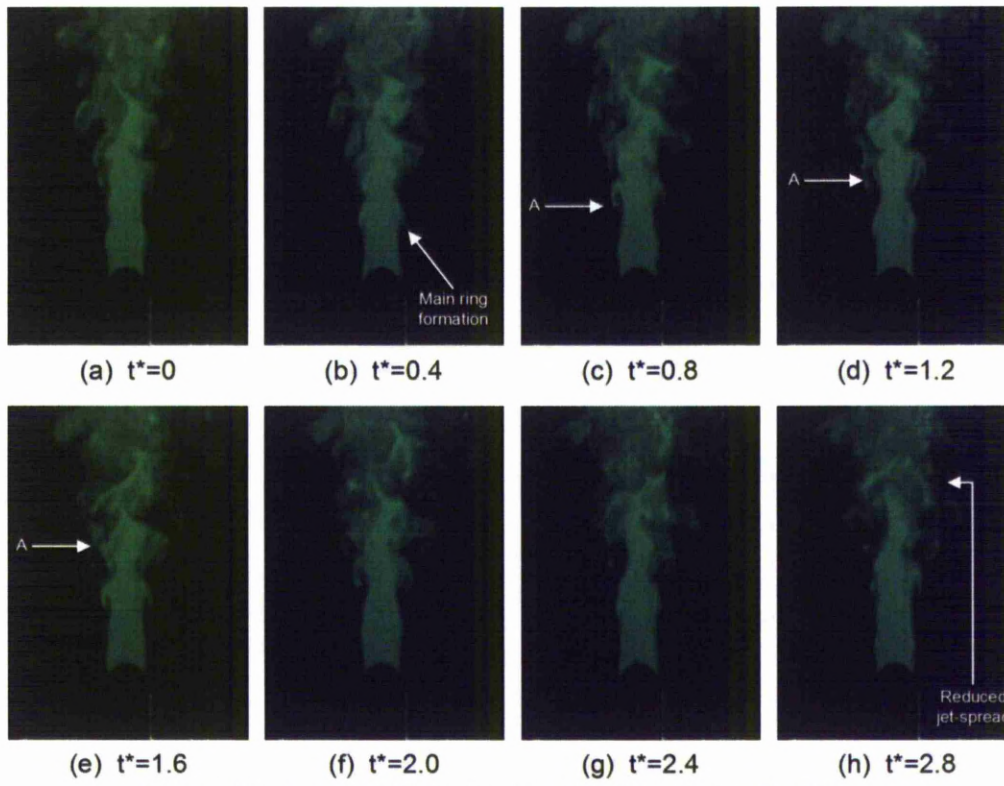

Figure 3.14 Streamwise LIF visualisation of AR2 V-notched nozzle, TT view

When the nozzle sharpness is increased from AR2 to AR4 the flow field is intensified and vortex stretching is visible, as shown in Figs. 3.15 to 3.18. This promotes a faster break down of large-scale coherent structures, such as main ring vortices, and possibly additional generation of flow stresses. High stress regions are visible in the braid region of the jets and the formation of braid vortices is also evident. These structures are linked with increased mixing, as they promote the jet-to-ambient fluid, interactions (Liepmann and Gharib, 1992). However, the general trend of the flow features remains unchanged. The vortices along the PP plane converge towards the nozzle centreline, while along the TT plane lateral movement away from the nozzle centreline is still dominant and thus for sake of brevity and reader satisfaction, important differences will only be highlighted.

Wider jet spreads and visually larger streamwise vortices are noticed as well as better-formed vortices along the TT-plane for both nozzles, are shown in Figs. 3.16 and 3.18. It can be noticed that the increased nozzle sharpness affects the flow field to a greater extent along the TT plane than along the PP plane. Specifically, a substantial increase in the formation of "rib-like" structures is observed for the A-notched nozzle, shown in Fig. 3.16. These structures cause an increase in the overall jet-spread, and so, the increase in sharpness does improve the generation of streamwise vortices along the smooth troughs. Along the TT-plane of the V-notched nozzle a very different flow field is present. Compared to the less

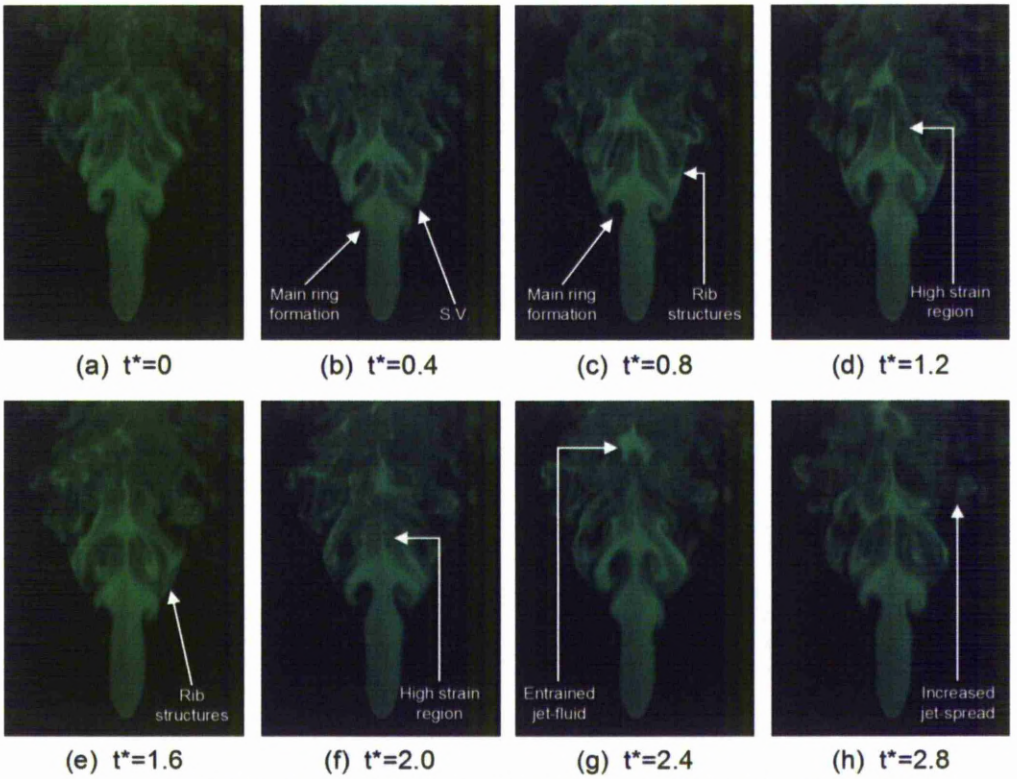

Figure 3.15 Streamwise LIF visualisation of AR4 A-notched nozzle, PP view

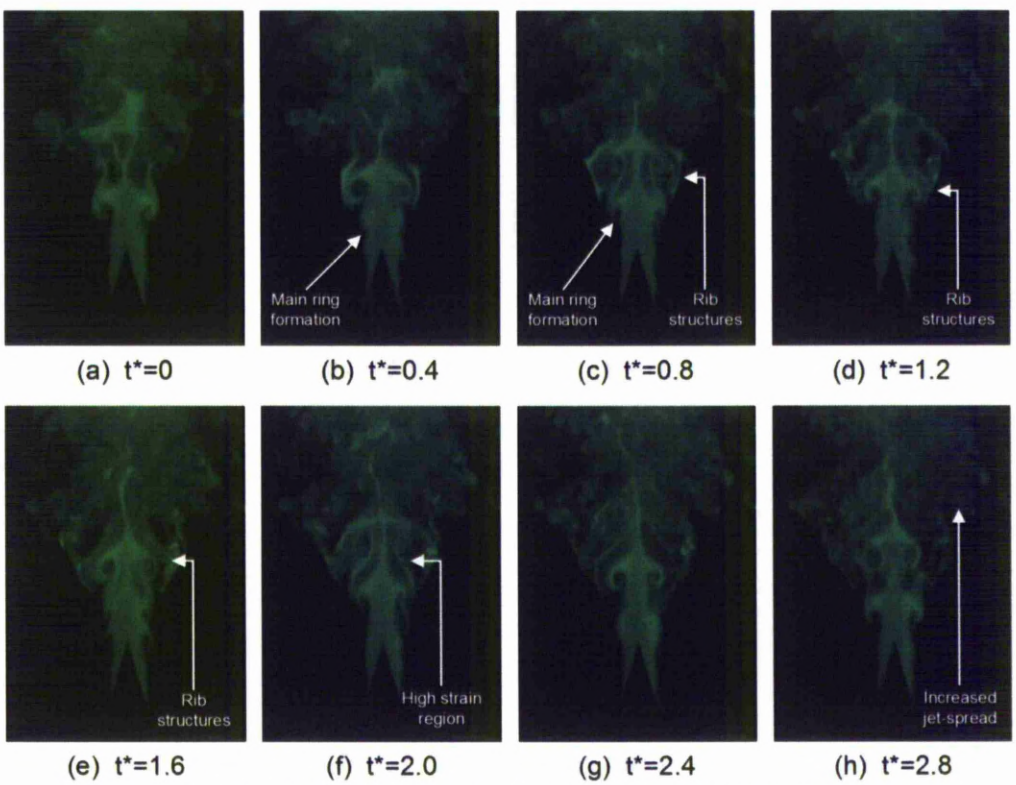

Figure 3.16 Streamwise LIF visualisation of AR4 A-notched nozzle, TT view

sharp V-notched AR2 nozzle, the formation of better-defined main ring vortices is noticed. Additionally, faster formation, development and breakdown of main ring vortices is also observed. Between successive main ring vortices, the main jet body seems very slender which may be due to the inflow of ambient fluid which does not contain fluorescent dye. Thus, it can be inferred that along the TT plane, a substantial increase in the amount of ambient fluid entrainment exists. A final point can be made concerning the evolution of the main ring vortices for both nozzles and both views. When the ring vortices approach the point where instabilities set in, influence from the previous flow cycle becomes apparent. The main ring vortex which precedes, in a spatial frame of reference, distorts the ring by entraining the centre portion of it (seen as an area of concentrated dye). This has the effect of stretching the main ring vortex and augments breakdown as well as increasing the local strain rate. The location at which these "high strain" regions initiate have been annotated in Figs. 3.15 to 3.18 for each nozzle geometry. Strictly, one cannot comment on strain rate without measuring it. But the existence of high strain in the braid region of the jet has been documented by researchers in the past (Liepmann and Gharib, 1992)

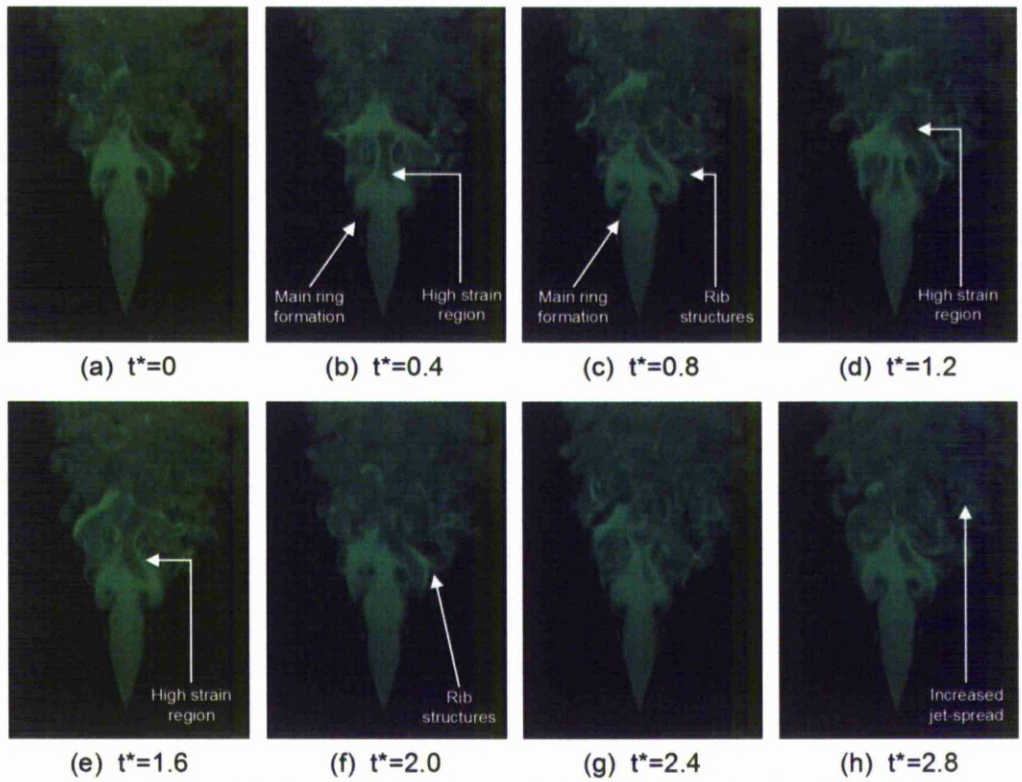

Figure 3.17 Streamwise LIF visualisation of AR4 V-notched nozzle, PP view

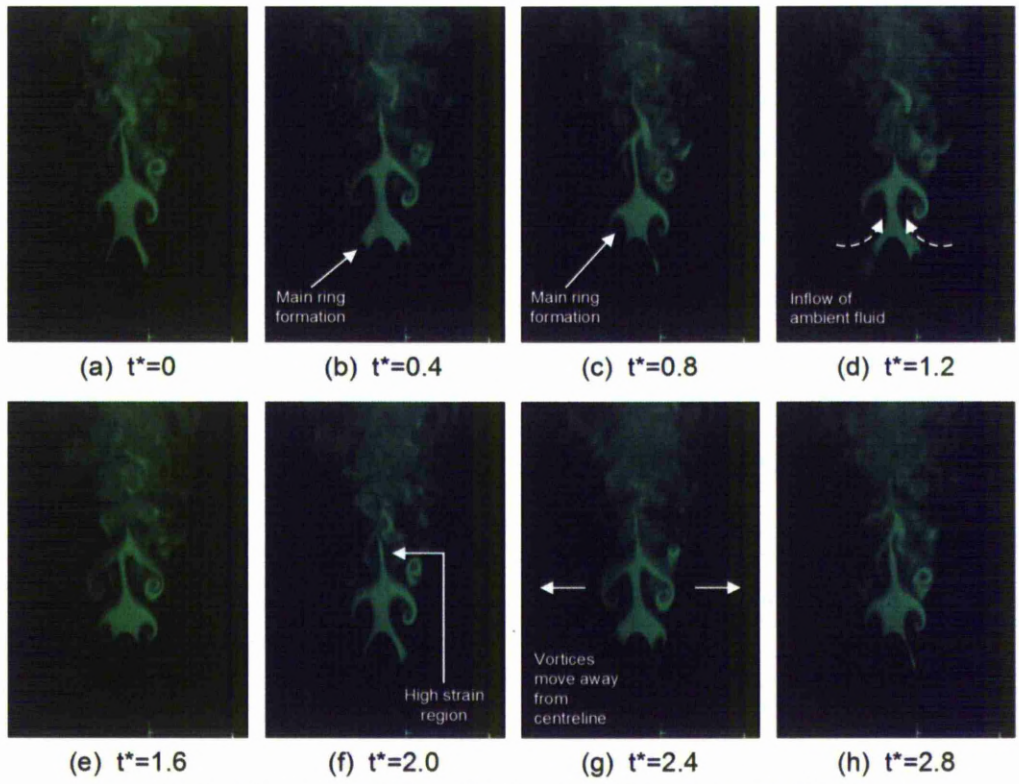

Figure 3.18 Streamwise LIF visualisation of AR4 V-notched nozzle, TT view

c) Cross stream LIF testing

Flow development as a function of cross-stream distance

The only way of visualising the formation and effects of the small-scale streamwise vortices as well as the cross-sectional shape of the jet body was by taking cross-stream cuts of the jet flows. Figures 3.19 to 3.23, show cross-stream slices of the flow field taken at several downstream locations which were kept consistent for all nozzles. In an effort to keep result presentation concise, slices where the nozzle protruded into the laser plane and interfered with the visual outcome, particular the AR4 nozzles, as well as slices taken further downstream, where turbulence had set in and no distinguishable flow features could be discerned, are not shown. For all nozzles the peaks were set to left-right orientation and the troughs to top-bottom orientation respectively. For each downstream location three flow cycles were extracted. Depending on the formation of the cross-stream structures one image was selected to represent the flow field at each downstream plane.

Cross-sections of the circular reference nozzle reveal that the jet body remains circular throughout most downstream locations. Main vortex ring rollup is apparent at x/D=2.5, where inflow of ambient fluid is indicated by a concentric circular dark ring. Further instabilities that promote main ring breakdown start to arise at x/D=3 and the formation of streamwise structures is clearly visible. Further downstream (x/D=4), formation of outward

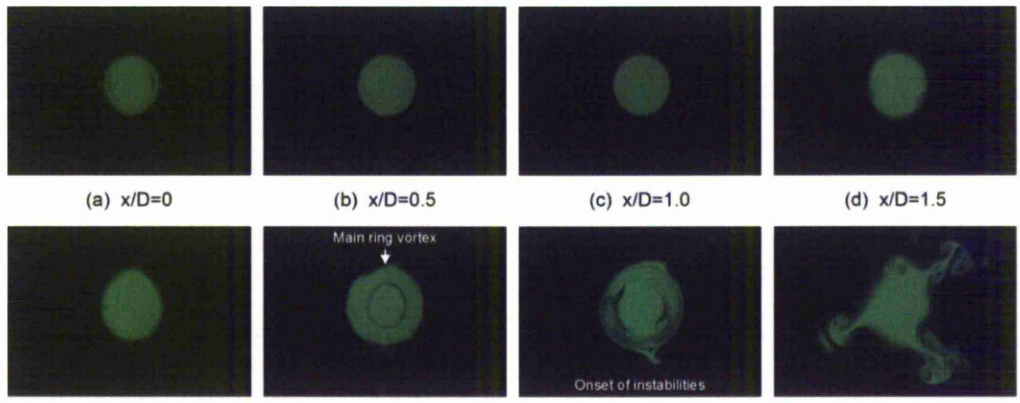

Figure 3.19 Cross-stream LIF flow visualisation of circular reference nozzle

spreading streamwise vortices is increased which mix the main jet body with the surrounding ambient fluid. The jet body cross-sectional shape has increased in area and the circular shape found at upstream locations does not exist. At location x/D=5 the whole jet was turbulent and no coherent structures could be determined (not shown in image selection).

The AR2 A-notched nozzle, shown in Fig. 3.20 starts off having a circular cross-section (x/D=0.5 and x/D=1) but as the downstream distance increases (x/D=1.5), bulging at the peak locations is evident. The jet body becomes elliptic with the major axis aligned along the nozzle peaks. At this particular flow phase (which depends on which image was selected to represent the particular cross-stream plane), it is evident that the jet body has the tendency to eject fluid to its surroundings. At x/D=2 outward spreading streamwise vortices form at the sharp peaks, as seen throughout the flow visualisation section presented earlier. Interestingly, outward spreading can also be observed at the trough locations which indicates the formation of weak streamwise vortices which were not visible along the streamwise view. As the flow progressed downstream, less organised structures are observed, although

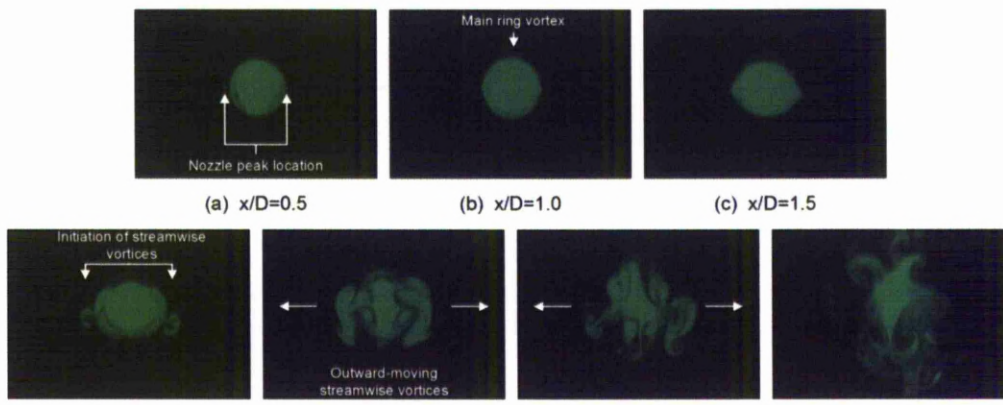

Figure 3.20 Cross-stream LIF flow visualisation of AR2 A-notched nozzle

the outward spreading of the streamwise vortices is still apparent. At x/D=4 large scale coherent structures cannot be distinguished from the rest of the eddy containing jet fluid. Compared to the reference case, it can be inferred that, the potential core is reduced which indicates an increase in mixing between the jet and the surrounding ambient fluid. The generation of additional consistently-formed streamwise vortices help the mixing process.

Comparing the flow field associated with AR2 V-notched nozzle to the AR2 A-notched, it can be seen that most flow images are similar, with the main differing flow feature being the formation of strong streamwise vortices at the sharp troughs, as shown in Fig. 3.21. Initially, the AR2 V-notched jet is circular (x/D=0.5) but quickly changes shape to elliptic with the major axis along the TT- plane (x/D=1) and then along the PP-plane (x/D=1.5). Formation of trough streamwise vortices with an outward rotational sense are evident as early as x/D=1.5. From this view it can be shown that sharp troughs are more effective in producing streamwise vortices. As the flow propagates downstream, the effects from the smooth peaks become apparent (x/D=2, 2.5 and 3). Visually large outward flowing streamwise vortices form at the peak locations and spread the jet body. Comparing sharp to smooth peaks, Figs. 3.20(d) and 3.21(d) respectively, it can be seen that smooth peaks may be more beneficial for mixing purposes by virtue of larger vortices being formed. Mixing between the jet and the surrounding fluid can be detected by the black regions where ambient fluid has been entrained (x/D=2.5). Similar to the AR2 A-notched nozzle, most of the large-scale structure coherence is lost by x/D=4, with the only difference being that the spreading along both PP- and TT-planes is similar.

It was shown in the section 3.2.1.(a) that increasing nozzle sharpness has the effect of intensifying the flow field and augmenting the role of the peaks and troughs. The same can be seen in the cross-sections of the flow. The sharper nozzles produce structures that are coherent and interact more with the surrounding fluid. Looking at Fig. 3.22 the jet body

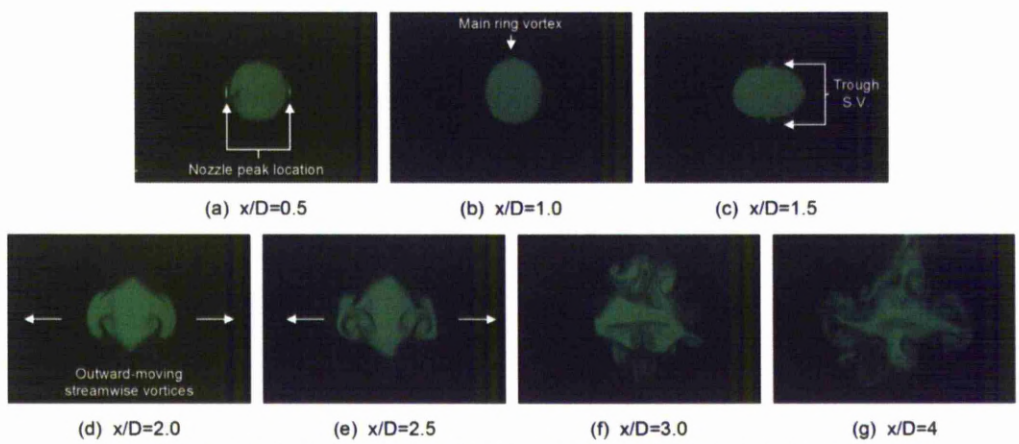

Figure 3.21 Cross-stream LIF flow visualisation of AR2 V-notched nozzle

evolution of the AR4 A-notched nozzle is presented. Initially the jet is square with rounded corners. A shadow which has been cast along the PP-plane is due to the nozzle peaks protruding into the laser plane and should not be misunderstood as ambient fluid entrainment. At the next cross-stream location (x/D=1.5) ambient fluid entrainment is evident at the four corners of the jet body. The entrainment may be caused by the formation of outward spreading streamwise vortices formed at the peaks and troughs as shown in the vortex model presented in section 3.2.2 or by the influence of a main vortex ring immediately downstream of the current location. As the downstream distance increases the jet body cross-sectional area increases and the streamwise vortices increase in size and maximise mixing. Due to the increased mixing of the jet and the ambient quiescent fluid, loss of large-scale structure coherency is accelerated. By x/D=4 no structures within the jet body can be distinguished.

The effects of the sharp trough were enhanced when the AR4 V-notched nozzle was tested as shown in Fig. 3.23. Large inflowing streamwise vortices are observed at the sharp trough locations, x/D=2 and x/D=2.5 respectively. Regions marked with ambient fluid resemble mushroom-shapes and indicate the inward direction of the streamwise vortices. By drawing in ambient fluid, enhanced mixing is achieved. This behaviour, although is dependent on the particular pulsing phase, is different to what was seen for the rest of the circular nozzle geometries. This also explains the distinct slender jet body found when studying the streamwise view of the same nozzle, found in Fig. 3.18. The streamwise vortices formed at the peak locations are, as expected, outward flowing and inject jet fluid to the surroundings. The effect caused by trough and peak streamwise vortices having opposite radial directions

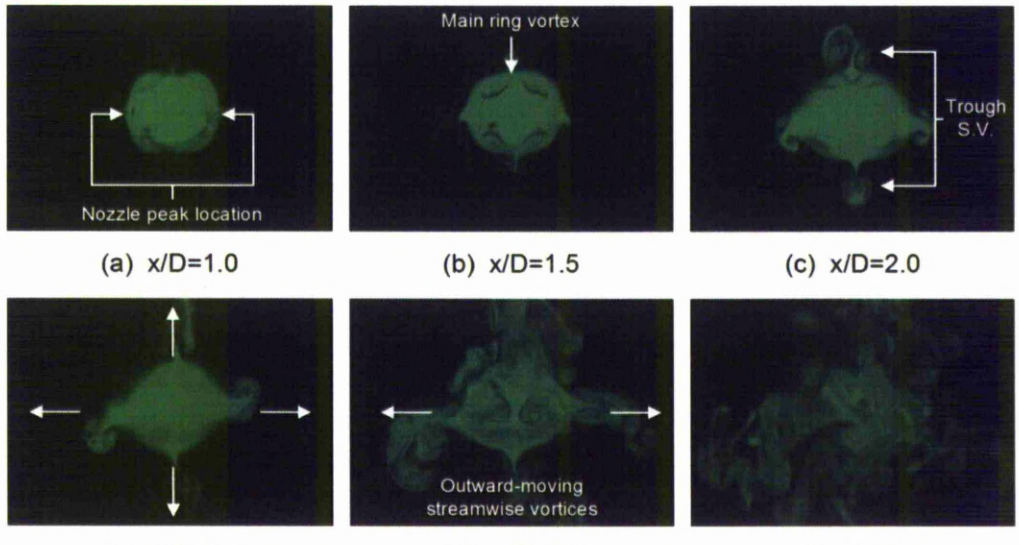

Figure 3.22 Cross-stream LIF flow visualisation of AR4 A-notched nozzle

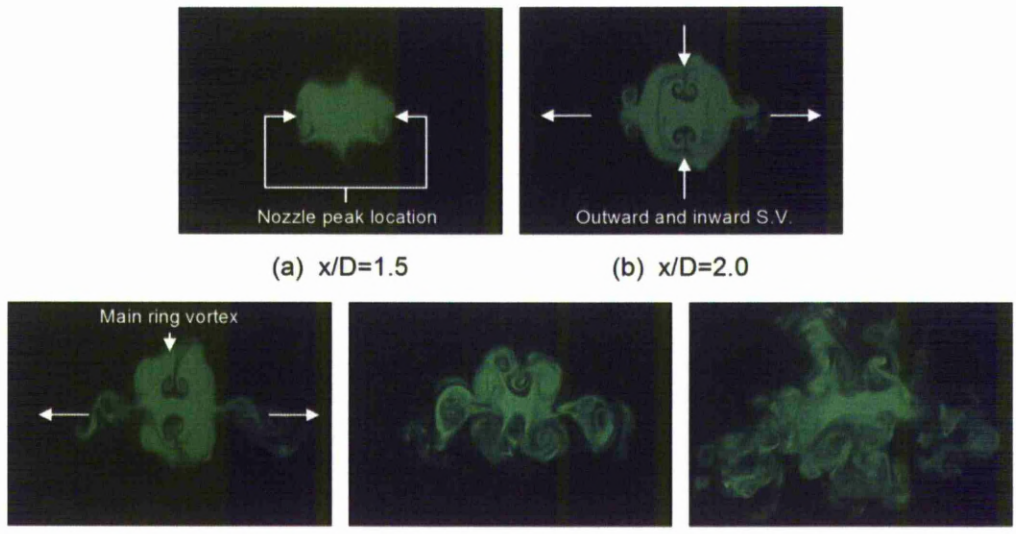

Figure 3.23 Cross-stream LIF flow visualisation of AR4 V-notched nozzle

is to increase the jet spread along the PP-plane and reduce it along the TT-plane, thus causing the jet body to grow asymmetric. When considering the difference in structure formation, there is not much difference between AR4 A- and V-notched nozzles in a visual sense. Both peaks eject jet fluid and the final jet spread along the PP-plane is similar as seen in Figs. 3.22(e) and 3.23(e).

One plausible explanation for the occurrence of inflowing trough streamwise vortices associated with the AR4 V-notched nozzle, could be due to the position of a main ring vortex with respect to the laser plane. If for example the main ring vortex has just passed the laser sheet, a region of inflow will dominate at the laser sheet position thus causing the required inflow. However if a main ring vortex is captured before it passes the laser sheet, then a region of outflow will dominate.

Finally, before moving onto the next section it must be mentioned that the instantaneous flow fields presented so far were dependent on the pulsing phase t*. If a different phase was chosen, then a different flow field would be captured (time dependant, unsteady flow). This is of particular importance, especially when characterising the effects and orientation of the streamwise vortices. To avoid such ambiguity, a time evolution of the jet cross-stream is presented next.

Evolution of coherent flow structures at constant downstream location

To aid the understanding of the flow development, time-sequenced images covering a full flow cycle have been captured and are presented below. A suitable downstream location at which the flow structures are clearly visible was chosen independently for each nozzle.

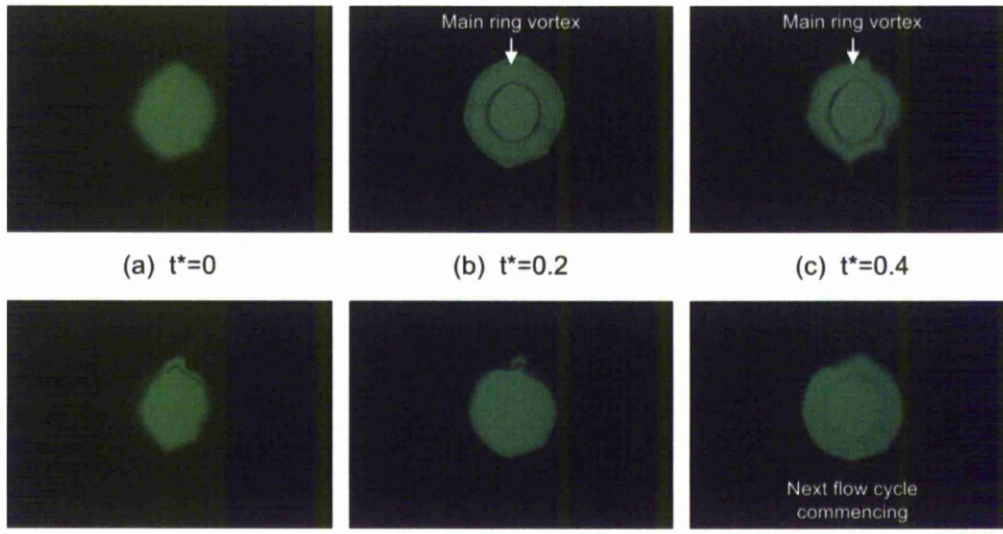

Figure 3.24 Flow evolution of reference nozzle, at x/D=2.5

The evolution of the reference nozzle is shown in Fig. 3.24. Due to the particular cross-stream position, which is close to the nozzle exit (x/D=2.5), the flow field is stable and the existence of large scale coherent structures is evident. In images (b) and (c) the main ring vortex can be seen to pass through the illumination plane. As expected, no bending is detected and the cross-sectional area of the ring is constant around its azimuth. Small disturbances manifest within the braid region of the jet, influenced by both upstream and downstream main ring vortex rollups. Such behaviour as well as the generation of streamwise vorticity in circular jets has been studied extensively by Liepmann and Gharib,(1992).

Figure 3.25 shows the cross-stream flow evolution of the AR2 A-notched nozzle. Radially outward-spreading streamwise vortices exist along the PP-plane. Although the vortices are visually small and not well distinguished, this flow pattern was expected and agrees well with results shown previously in the streamwise flow visualisation sections, 3.2.1.(a) and 3.2.1.(b) respectively. In the image sequence, the main ring vortex is seen to be elongated (eccentric), similar to an elliptic main ring vortex. Upon formation, the main ring vortex is stretched along the TT-plane and indications of bending are also present, as shown in Fig. 3.25(a). As the ring passes through the illumination sheet it is obvious that the sections of the main ring vortex along the PP-plane move faster and are further downstream than the rest of the main ring filament. Outward spreading streamwise vortices form within the braid region of the jet as shown in Fig. 3.25(c), where the time marker is at approximately 40 per cent of the flow cycle. The formation of these structures is influenced by the bending of the main ring vortex and the unequal shear rates caused by them. As the main ring passes through the illumination plane and before the next flow cycle initiates, the streamwise

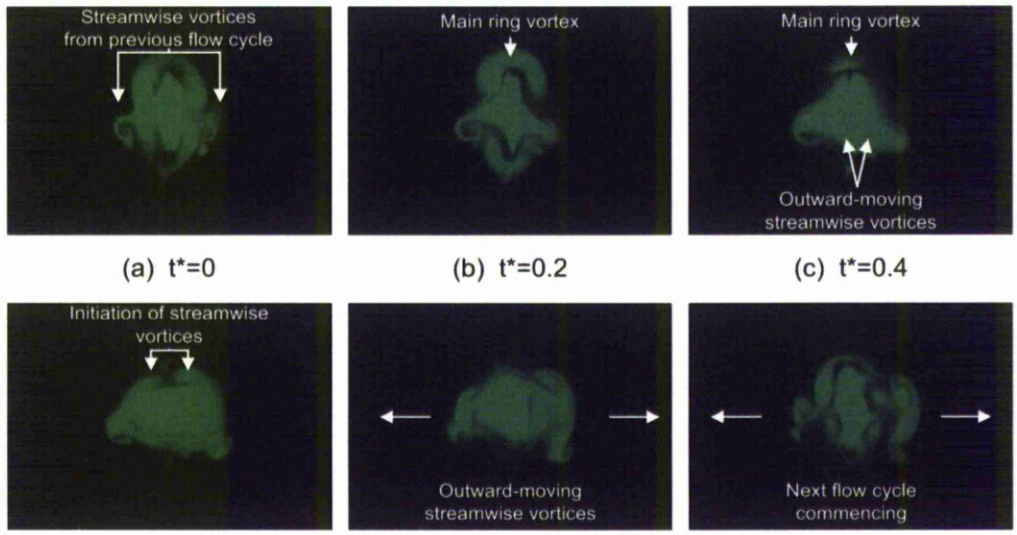

Figure 3.25 Flow evolution of AR2 A-notched nozzle, at x/D=2.5

vortices are influenced by the following main ring vortex and are moved outwards as shown in images (d) and (e). This process repeats itself indefinitely.

The flow structures associated with the AR2 V-notched nozzle are coherent and well-formed. The cross-stream evolution of the jet is shown in Fig. 3.26. Similar to the previous test case, the main ring vortex is elongated along the TT-plane and also shows indications of bending. Studying the images, the bending orientation can be determined. The sections of the main ring filament along the PP-plane are bent downstream and thus lead the rest of the ring vortex. Similar to an elliptic ring, the bending of the main ring vortex causes the formation of streamwise-aligned vortices in the braid region of the jet. This can clearly be

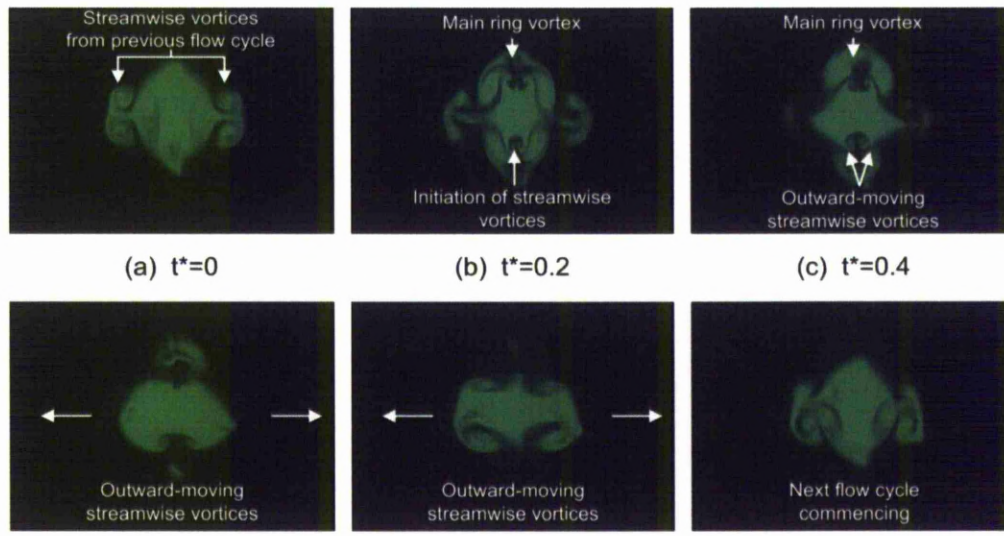

Figure 3.26 Flow evolution of AR2 V-notched nozzle, at x/D=2.5

observed in Figs 3.26(b) and (c). Compared to the A-notched nozzle design, the V-notched shown here seems to produce more organised flow features. The streamwise vortices seem stronger and have the ability of engulfing ambient fluid. The movement of the streamwise vortices is towards the periphery of the jet and move under the influence of the following main ring vortex as shown in Figs. 3.26(d) to (f). Compared to the reference case, both A- and V-notched nozzles produce flow-fields that evolve with significant differences.

Increasing the aspect-ratio of the A-notched nozzle has a large effect on the cross-stream dynamics of the flow as seen in Fig. 3.27. The main ring vortex filament shape is square-like and in this series of flow images does not seem to be bent to a great extent. However closer inspection of the flow images at a smaller time increment (t*=0.1) revealed that a small amount of bending exists. Sections of the main ring vortex aligned with the PP-plane of the nozzle lag behind the rest of the filament. Another distinct difference is the prominent formation of four streamwise vortices at both peak and trough locations. This finding is different to what Longmire *et al.*(1992a) showed for a two-peak nozzle (geometrically similar to the A-notched case used in this study). In their study it was found that inward spreading occurs along the TT-plane while outward spreading was present along the PP-plane. These flow differences could be attributed to the difference in Reynolds number between the two experimental investigations (Re=19000 compared to Re=2100) and to the difference in flow forcing amplitude. In their study the centreline velocity fluctuation caused by forcing was set to 11%, while in this study a more subtle 2.2% was used. The Forcing amplitude as well as the forcing frequency can have a large effect on the resultant flow field (Crow and Champagne, 1971; Hussain and Zaman, 1980, 1981; Lee and Reynolds, 1982; Gutmark and Ho, 1983; Husain and Hussain, 1983) It seems that the increase in trough

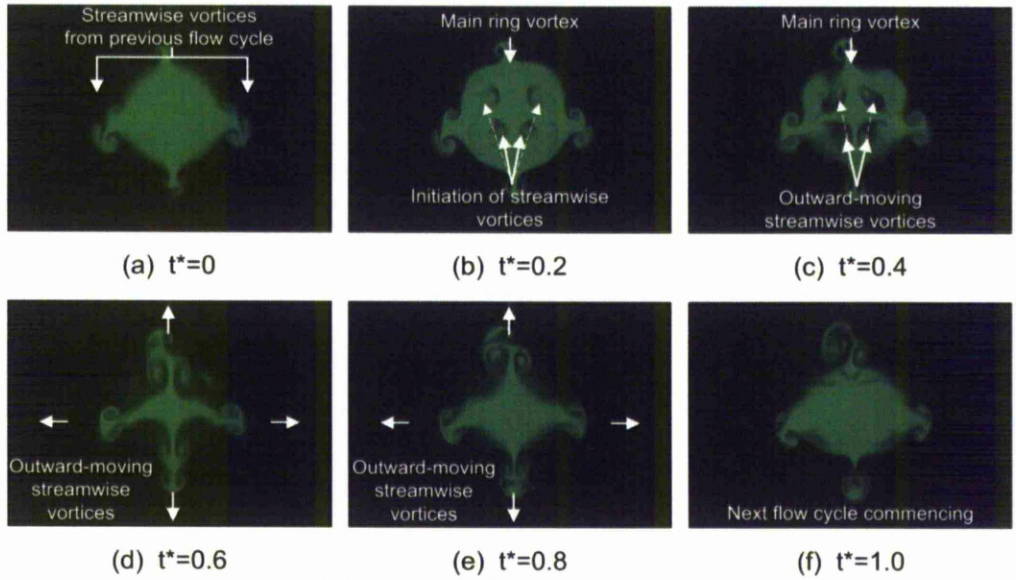

Figure 3.27 Flow evolution of AR4 A-notched nozzle, at x/D=2

sharpness is beneficial to the formation of streamwise vortical structures. As portions of the main ring vortex pass though the illumination plane, two pairs of streamwise vortices are formed. These vortices grow and move towards the periphery of the jet. From these findings it is evident that increasing the aspect-ratio of the nozzle introduces additional flow features. Whether these structures are beneficiary to the mixing ability of the nozzle is discussed in the last section of this chapter.

The remaining cross-stream flow evolution is presented in Fig. 3.28. The AR4 V-notched nozzle produces large outward flowing streamwise vortices. In Fig. 3.28(b) the initiation of the formation of the streamwise structures is visible. The influence of the sharp troughs seems to intensify these structures as an increase in ambient fluid engulfment is detected by the black regions within the core of the jet. As the flow cycle progresses, the streamwise oriented structures develop and at t*=0.6 start to move towards the periphery of the jet, influenced by the preceding main ring vortex further upstream. Interestingly, the movement of the streamwise structures is faster compared to the rest of the nozzle geometries. Similar to the AR4 A-notched case and the flow visualisation results of the V-notched nozzle presented in New *et al,*.(2005), the main ring vortices have a square-like shape. Additionally, the main ring vortices are bent, with the sections aligned along the PP-plane leading the rest of the filament. This behaviour is illustrated when observing image sequences in Figs 3.28(b) to (d). As stated previously, flow-fields associated to all IO cases differ greatly from the reference case and illustrate an extensive array of extraneous flow features.

3.2.2 Vortex flow model

Taking the results into consideration, a flow representation is proposed. This representation

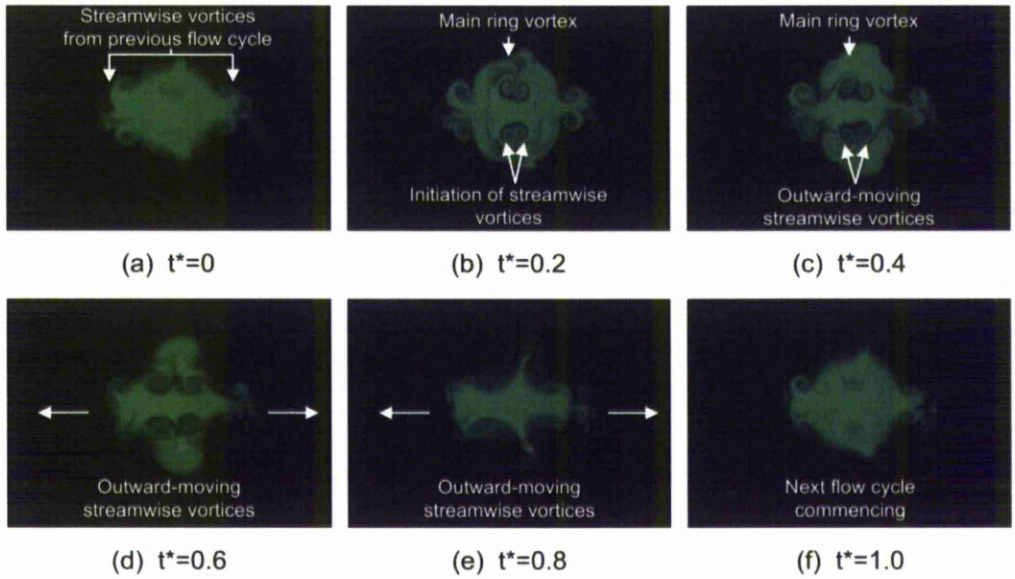

Figure 3.28 Flow evolution of AR4 V-notched nozzle, at x/D=2

will assist the reader in understanding the basic flow structures responsible for the resultant flow fields. Due to brevity, one representation per nozzle geometry group will be presented, as increasing the nozzle aspect ratio does not change the underlying structures, but merely accentuates them. The flow field associated to the A-notched nozzle geometry is depicted in Fig. 3.29(a), while the V-notched case is shown in Fig. 3.29(b). For both representations, four stages of flow development have been drawn. The main ring vortex filaments are highlighted by thick lines, while streamwise and braid vortices are sketched with thinner dashed lines. The direction in which the main ring vortex bends is shown by solid arrows.

Focusing on the A-notched geometry initially, it can be seen that as the main ring vortex rolls up, it follows the nozzle contour, as shown in Fig. 3.29(a). This results in the formation of a bent main ring vortex. Viewing the main ring vortex along the PP plane a U-shaped filament is observed, while when viewed from the TT plane, an A-shaped filament is seen. As the main ring vortex propagates downstream it changes shape, and by doing so influences the shape of the jet. Sections of the filament that follow the peak contour have a small radius due to the specific geometry of the A-notched nozzle. Thus these filament sections will move downstream faster than the remaining sections, due to the higher induced velocity associated with the reduced radius (Hussain and Husain, 1989). Studying the flow representation in Fig. 3.29(a), it can be seen that sections of the filament that correspond to the peak locations move faster. This movement however causes an increase in bending along the trough plane. When this bending reduces the radius substantially, the trough sections of the filament start to move faster downstream, as indicated in the schematic at the 3rd and 4th

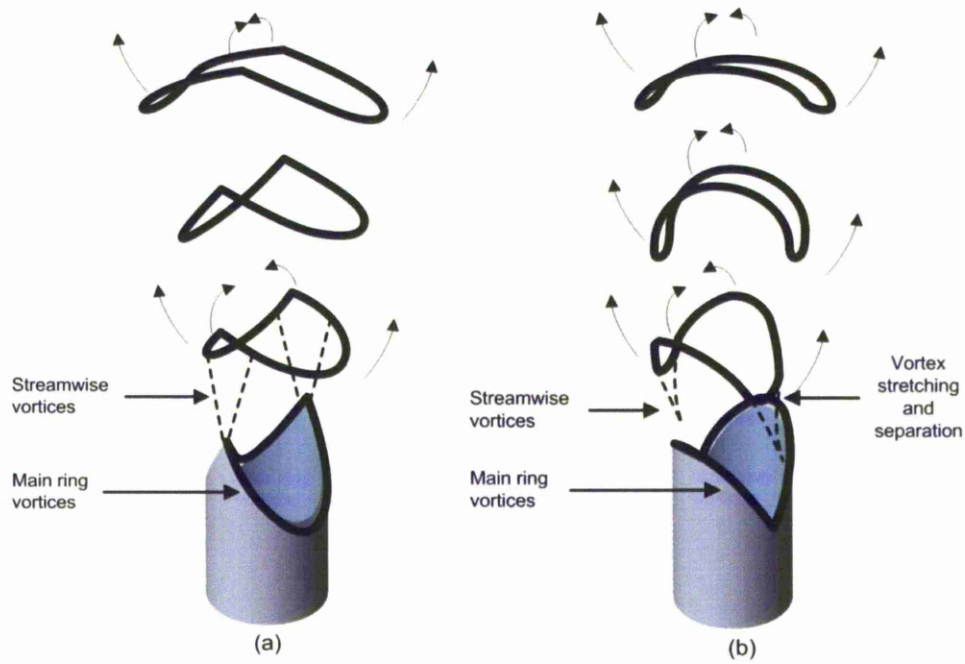

Figure 3.29 Flow representation for (a) A-notched nozzle and (b) V-notched nozzle

main ring vortex position. From the preceding section it can be inferred that the jet issuing form the A-notched nozzle will not be axi-symmetric and that main ring vortices with elliptic attributes are formed.

The flow structures associated with the V-notched group of nozzles, shown in Fig. 3.29(b), is very similar to what was shown for the A-notched geometry. However, due to the difference in between peak and trough sharpness, the manifestation of streamwise vortices is more evident. Similar to before, the main ring vortex initially follows the nozzle contour and thus has sharper troughs than peaks. Due to the vorticity filaments, which are located at the V-notch, being in close vicinity to each other, merging occurs. The trough sections of the main ring vortex become stretched and separate from it. The remaining main ring vortex re-connects and propagates downstream, with the smaller radii sections moving faster than the rest of the ring. In its final state the ring is eccentric with the major axis lying on the TT plane, similar to what was observed for the A-notch case. So similar to what Longmire *et al.*(1992a) documented, it has been shown that it is possible to produce jets with asymmetric cross-sections with the use of circular (axi-symmetric) IO nozzles.

An additional schematic was drawn which focuses on the flow structuring and movement within the braid region of the jet and is shown in Fig. 3.30. This plot was influenced by a representation published by Husain and Hussain, (1991) in which the flow evolution of an elliptic ring was explained. The schematic illustrates the braid vortex structuring along both streamwise and cross-stream planes. The lines used to draw the figure are consistent with the previous two figures (Figs. 3.29(a) and (b)),with the addition of an extra set of dashed arrows. The dashed arrows indicate the rotational sense of the main ring vortices, as they propagate downstream which help to identify the correct rotational sense of the braid vortices in the cross-stream plane.

Braid vortices initiate due to the induction of two sequential vortices, such as those shown in Fig 3.30. Due to the bending of the main ring vortices, an uneven shear rate is imposed on the fluid within the braid region. Sections of the main ring vortex that lie on the PP plane, are further downstream that the rest of the nozzle, as was clearly shown in the cross-stream LIF results (Figs. 3.25 and 3.27). Thus it follows that sections of the main ring vortex that lie on the TT-plane are further upstream or lag behind, also shown in Figs 3.25 and 3.27. The braid region is entrained in such a way that a vortex loop forms with opposite orientation to the main ring vortices of the jet. Due to the opposite orientation of the braid vortex, the

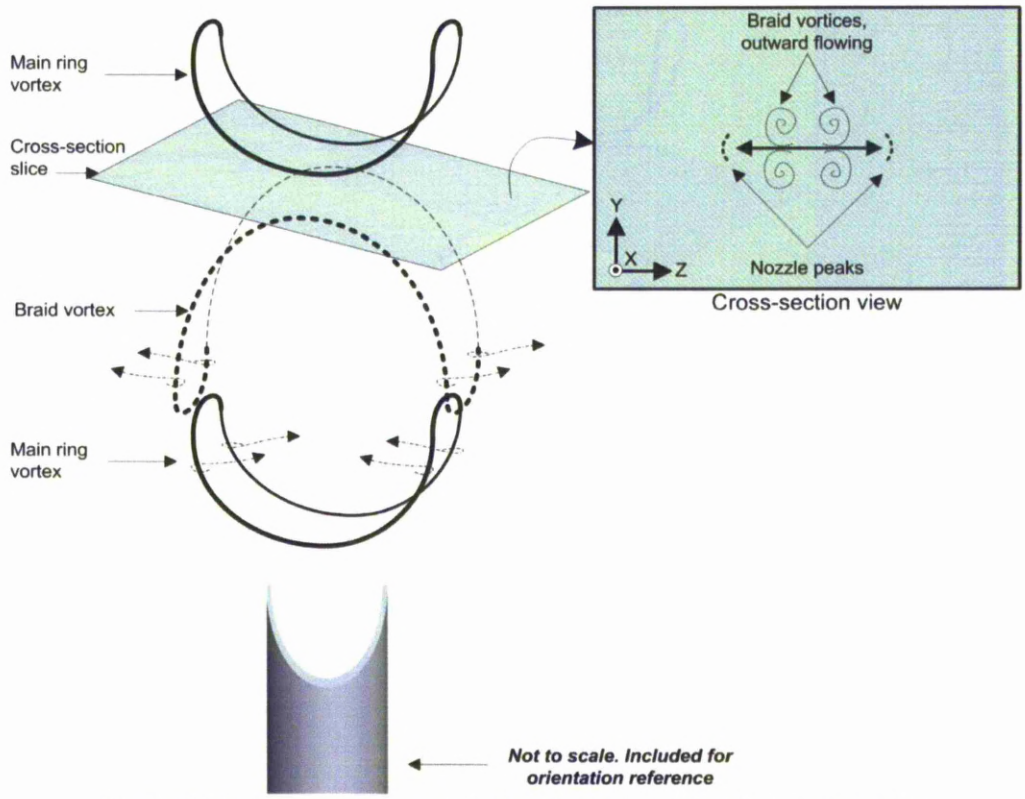

Figure 3.30 Braid vortex flow representation, viewed along PP and cross-stream views

filaments also rotate in an opposite sense to the main ring vortices, which is depicted by the dashed arrows. Note that the filaments of the main ring vortices produce inward flowing motion, while for the braid loop produce outward flowing motion. Thus, when a YZ cross section of the jet is taken, and viewed along the –X direction (orientation used for all cross-stream testing), the braid vortices appear as two vortex pairs, which along the PP, plane flow in a radially outward direction. This flow behaviour is consistent with results along streamwise and cross-stream directions for both A- and V-notched nozzle geometries.

3.2.3 Qualitative results (PIV)

a) Reference case

Streamwise results

Phase- and time-averaged results obtained along streamwise direction of the circular reference nozzle are shown in Figs. 3.31 and 3.32 while cross-stream testing results are shown in Figs. 3.33 and 3.34 respectively. The main ring vortices formed from the reference nozzle were shown to be well-defined azimuthal rings that propagate a large downstream distance before breaking down. This is also evident when looking at Fig 3.31(a), in which the discrete vortices are detected up to x/D=2.5. The potential core of the jet, which is defined as the region of the jet with a velocity magnitude of $0.9U_o$, is by far the longest

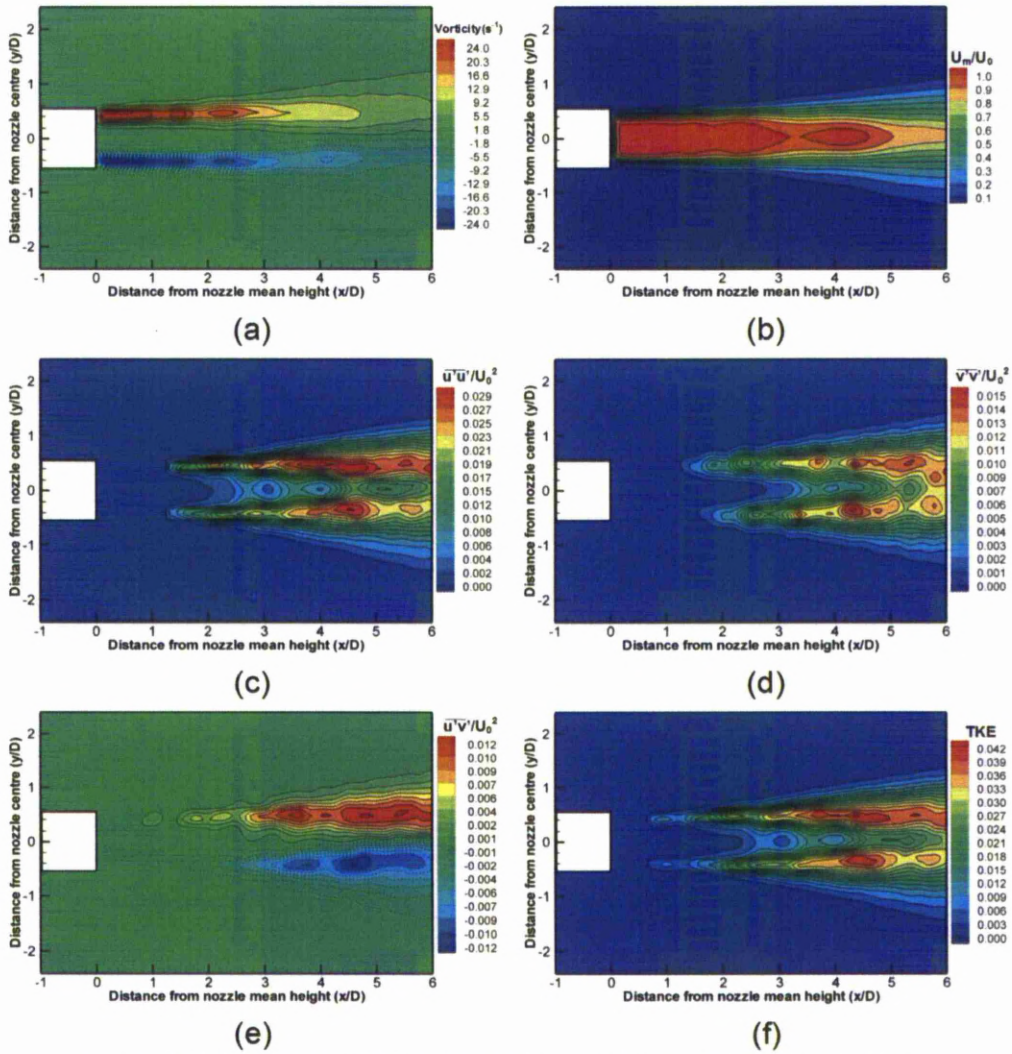

Figure 3.31 Phase averaged PIV results along streamwise direction for reference nozzle

between all the test cases and measures at approximately 6 diameters downstream of the nozzle exit, as shown in Fig. 3.32(b). Reduced interactions with the surrounding ambient fluid help to produce a more stable jet that takes longer to transist to turbulence. The jet is concentrated close to the nozzle centreline and thus a small amount of spreading is observed. This behaviour is noticed when looking at both phase and time-averaged graphs, but in particular, the time-averaged normalised velocity contour plot shown in Fig. 3.32(b) highlights the reduced spread. Regions of high vorticity, turbulent kinetic energy and Reynolds stress values are contained at the periphery of the jet because most of the mixing, for the reference case, is achieved by the main ring vortices. Vorticity dissipation is higher in the near-field region of the jet (x/D< 2), while TKE and Reynolds shear and normal stress are concentrated from 3 to 5 diameters downstream from the nozzle exit as shown in the time-averaged results. The increase in flow activity coincides with the instability region of the main ring vortices. As the main ring vortices break down, due to the formation of

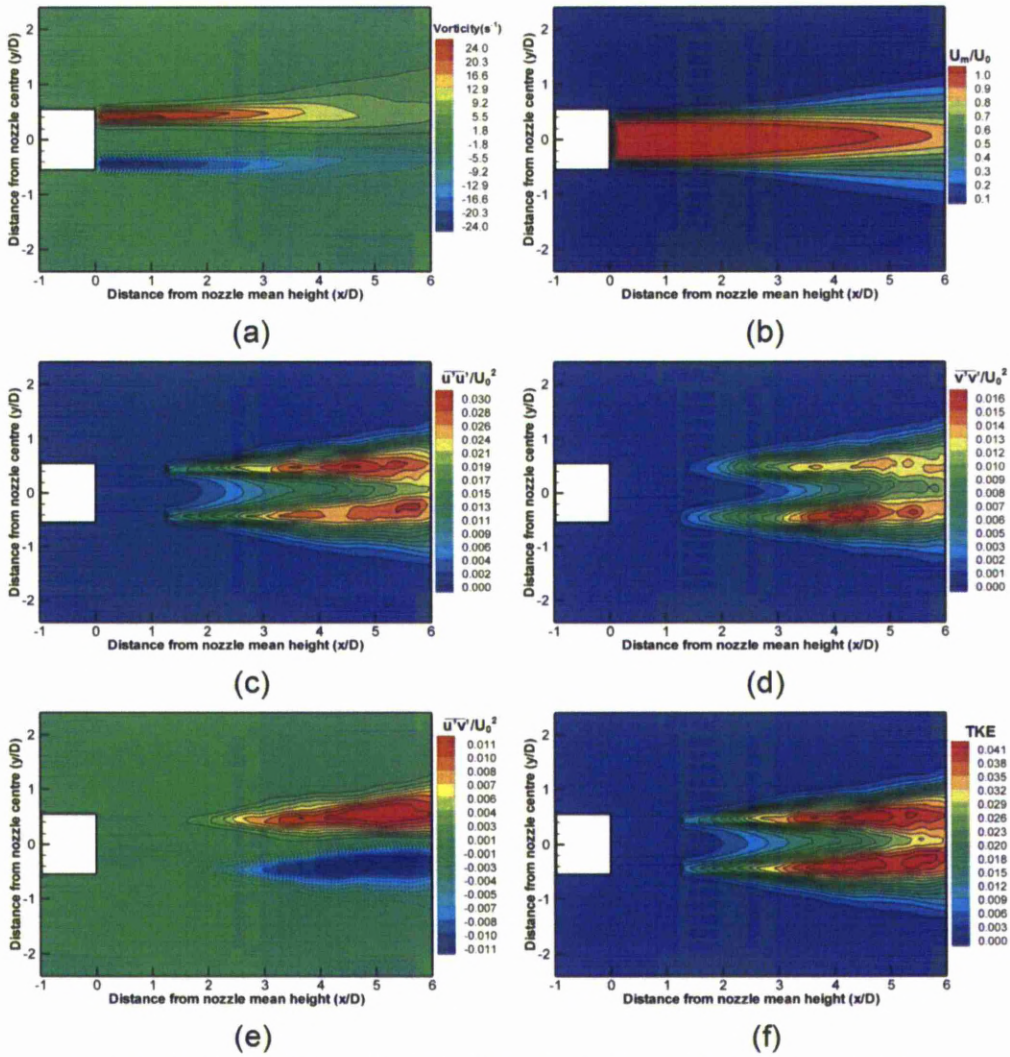

Figure 3.32 Time averaged PIV results along streamwise direction for reference nozzle

Widnall instabilities (Widnall *et al.*, 1974; Longmire *et al.*, 1992a), streamwise vortices and viscous effects, increased jet to ambient fluid interaction is achieved and small-scale eddies form which cause flow fluctuations and therefore increase flow stresses. It is also known that, mean velocity gradients, found in the jet shear layer, produce regions of high Reynolds normal and shear stress. There is an intimate connection between turbulence production and sheared mean flows. When comparing the normal stress levels, in Figs. 3.32 and 3.34 respectively, u' contributes the most, at nearly $2\overline{v'^2}$ and $10\overline{w'^2}$. The fact that the fluctuating velocities are not equal implies that the turbulence structure is anisotropic within the measurement domain. Maximum vorticity values associated with the reference nozzle (time- and phase-averaged) are comparable to the other tested geometries.

Cross-stream results

Cross-stream experimental results have been arranged in a three-dimensional stack as this arrangement is more intuitive, easier to understand and conveys the information in a concise manner. Figures 3.33 and 3.34 depict the phase- and time-averaged cross-stream results for the reference test case. Jet spread and streamwise vorticity is axi-symmetric, indicating no favourable spreading direction. This can be seen for both phase- and time-averaged results and can be expected from the reference nozzle, as the lip geometry does not produce bent main ring vortex filaments. Similar to the streamwise results, the cross-stream symmetric flow field also reinforces the notion of good initial experimental conditions.

Comparing the velocity flow fields between the phase- and time-averaged results, large deviations are evident. At cross-stream location corresponding to x/D=2, an opposite radial direction of the velocity vectors has been captured. The vectors associated with the phase averaged testing are positioned in an outward direction, while the time-averaged testing shows an inward vector orientation, as seen in Figs. 3.33(a) and 3.34(a) respectively. The reason for such a discrepancy was mentioned in the section 3(b), but can quantitatively be proven here. The steady-state, time independent flow field, shows ambient fluid entrainment as the persistent, dominant flow behaviour. The phase-averaged flow field shows that during a flow cycle, jet fluid is also ejected into the ambient surrounding fluid, but depends upon the particular flow phase. It can be deduced, that the persistent formation of main ring vortices immediately upstream of the x/D=2 cross-stream plane will produce an outward spreading flow field. Once the ring has passed through the plane and is situated downstream of the measurement plane a large velocity inflow would be expected. This inflow is caused by the ring entrainment, but also due to the natural entrainment associated with jet flow, in which the slower moving surrounding fluid is entrained towards the faster moving jet body. This inflow can be seen at cross-stream location x/D=3 in Fig. 3.33(a). Care must be taken when analysing the flow fields to differentiate between time-dependant and time-independent flow features.

The vorticity measured along the cross-stream planes agrees well with the vorticity measured along the streamwise planes. The phase averaged results show high levels of streamwise vorticity at locations x/D=2 and 3. The measured streamwise vorticity is affected by the formation of ring vortices and the ambient fluid entrainment. The time-averaged results shown in Fig. 3.34(b) indicate a region of high vorticity from x/D=2 to 5 with a gradual spread of the vorticity contours. High streamwise vorticity values are detected at position x/D=4 due to the breakdown of the main ring vortices and the associated smaller scale eddy flows which mix the ambient fluid with the jet body.

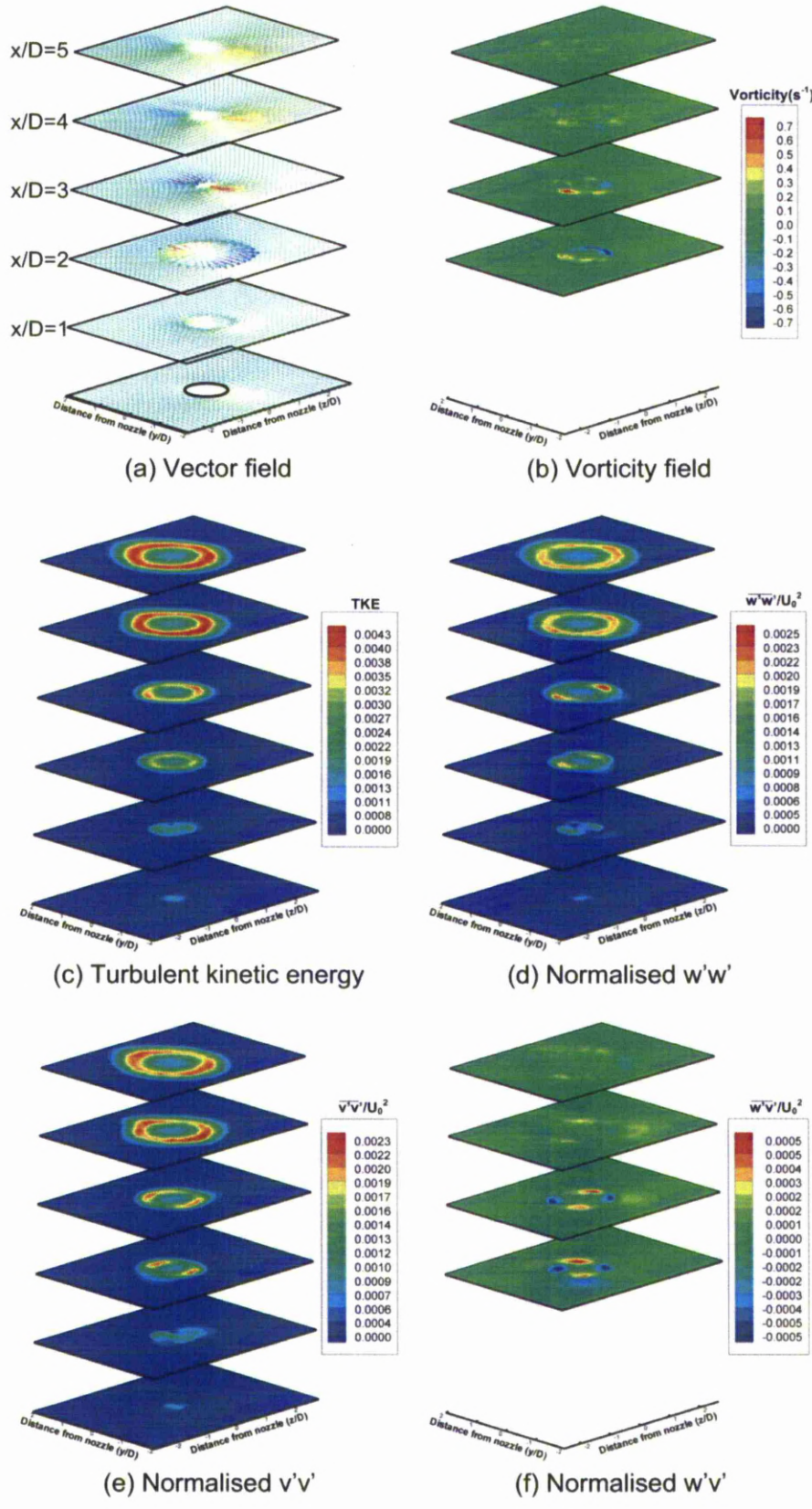

Figure 3.33 Phase averaged PIV results along cross-stream direction for circular reference nozzle

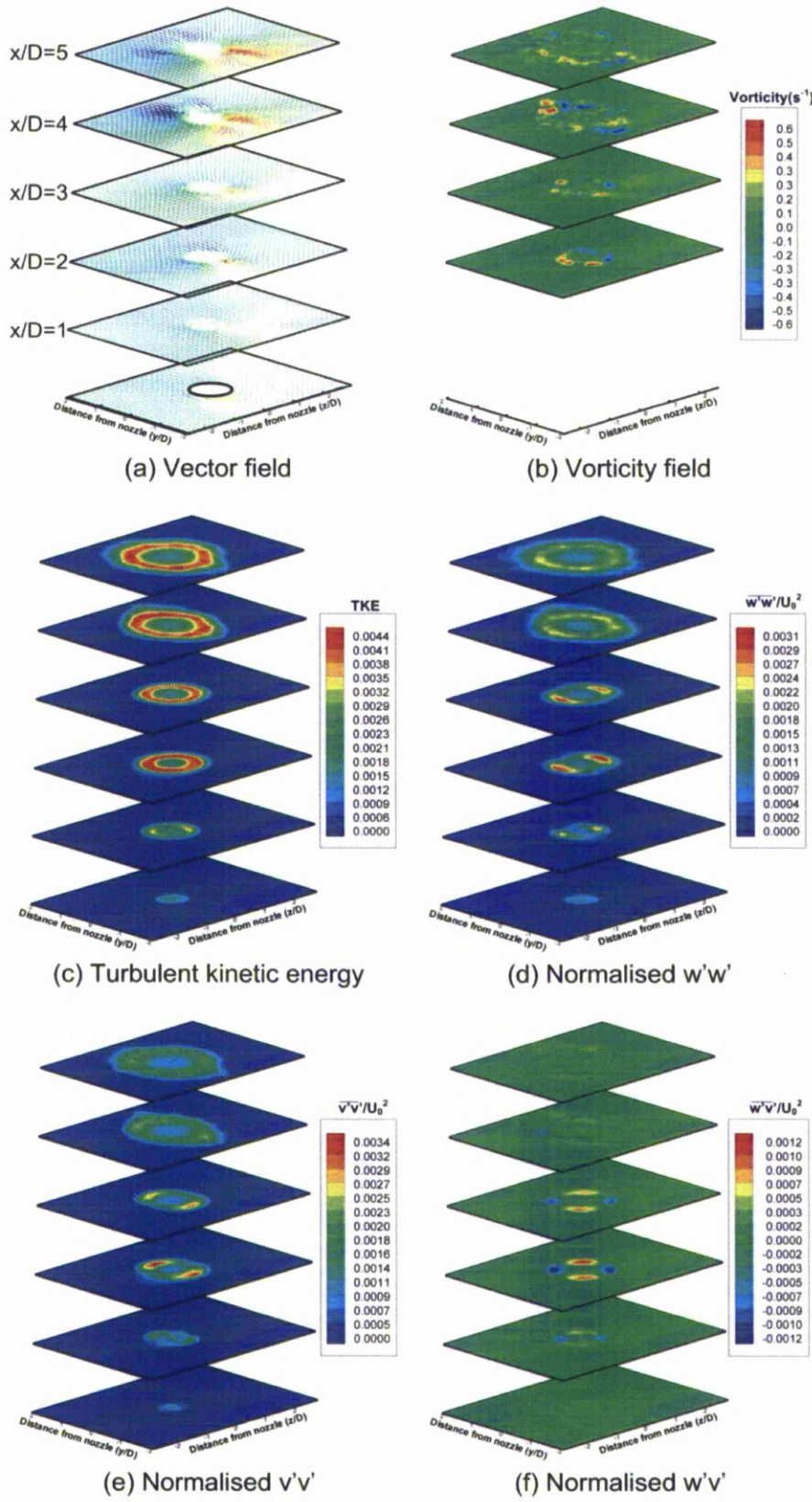

Figure 3.34 Time averaged PIV results along streamwise direction for circular reference nozzle

The TKE values measured along the cross-stream planes agree well with values presented earlier along the streamwise plane. The cross-stream phase-averaged results also show increased TKE values at locations x/D=3 to 5, which may be due to the influence of the particular flow pulsing phase. This can be explained by going back and looking at the streamwise results shown in Fig. 3.31. The influence of flow forcing is seen on the potential core of the jet. Two high speed regions exist, one that extends from the nozzle exit until x/D=3 and one from x/D=3.5 to 5. Between these region the TKE and stress values will be affected. The time-averaged cross-stream TKE values on the other hand are not affected by the phase of the flow perturbation and it can be seen, in Fig. 3.34(c), that the high TKE values start from x/D=2 until the end of the measurement window. Similarly to before, when compared to the results along the streamwise view, in Fig. 3.32(b), there is an agreement, albeit with a slight difference in the starting position. Focusing on the time-averaged normalised velocity plot in Fig 3.32(b), an increase of the jet-spread is evident at approximately x/D=2.5, which should lead to an increase in the shear layer and an increase in the flow interactions and flow fluctuations. For this reason the TKE values viewed along the cross-stream slices grow in diameter and exist up to the end of the measurement window.

Finally the Reynolds stresses viewed along the cross-stream plane for both phase- and time-averaged experiments are discussed. The Reynolds shear stress magnitude for the phase averaged case is approximately half of what was measured for the time-averaged case, shown in Figs. 3.33(f) and 3.34(f)) respectively, but both have circular contour lines indicating isotropic turbulence structuring. The same can also be noticed when observing the Reynolds normal stresses. In both, phase- and time-averaged cases, the u and w Reynolds normal stress components were similar in magnitude. This behaviour is typical of an axi-symmetric jet and was expected.

b) AR2 A-notched nozzle geometry

Streamwise results

Comparing the AR2 A-notched nozzle with the reference case presented above, differences in the flow fields arise. These differences have also been highlighted in the Flow visualisation section (3.2.1) but will be qualitatively substantiated in this chapter. Concentrating on the streamwise results first, the influence of the sharp peaks can be observed along the PP-plane in Figs. 3.35 and 3.36. It is immediately clear that the width of the region of influence along the PP-plane extends further. The time-averaged normalised velocity contours (Fig. 3.36(b)) show an increase in jet-spread and a reduction of the jet potential core. The reduction of the potential core could be due to the increased jet spread

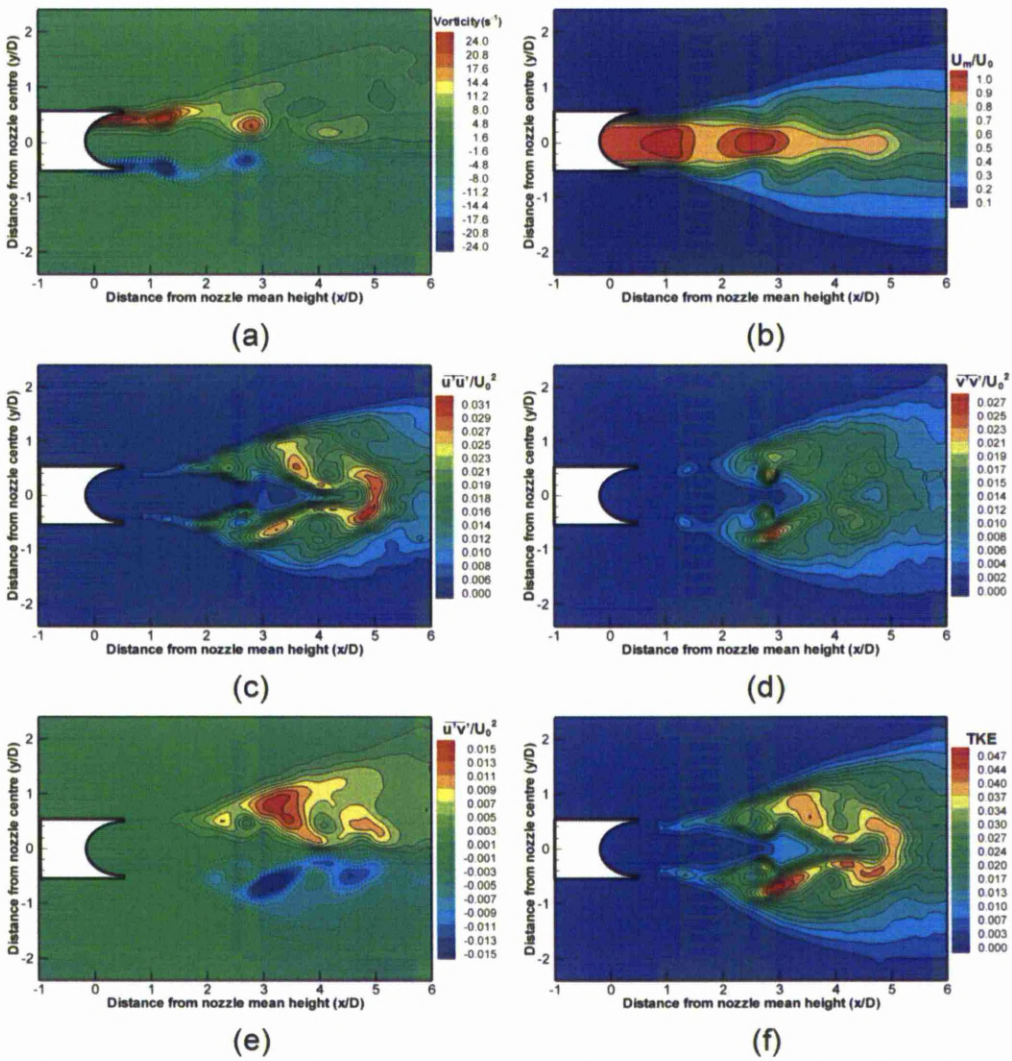

Figure 3.35 Phase averaged PIV results along streamwise direction for AR2 A-notched nozzle, PP view

and entrainment process. It is possible that the increased spreading will transfer a large amount of jet momentum to the surrounding ambient fluid thus causing a larger reduction within the jet.

Comparing jet-spreads along both views, it is evident that the jet-spread along the TT-plane is reduced, noticed in Figs. 3.37(a),(b) and 3.38(a),(b). This agrees well with previous observations in section 3.2.1. The lack of streamwise vortices could possibly restrict the spreading of the jet along the TT-plane.

The maximum jet vorticity between phase- and time- averaged experiments is comparable but is also similar to the reference case. Focusing on the main ring vortex formation in Fig. 3.35(a), movement towards the nozzle centreline is apparent. The evolution of the main ring vortices is visible in the figure shown. Although it shows favourable spreading along the PP-

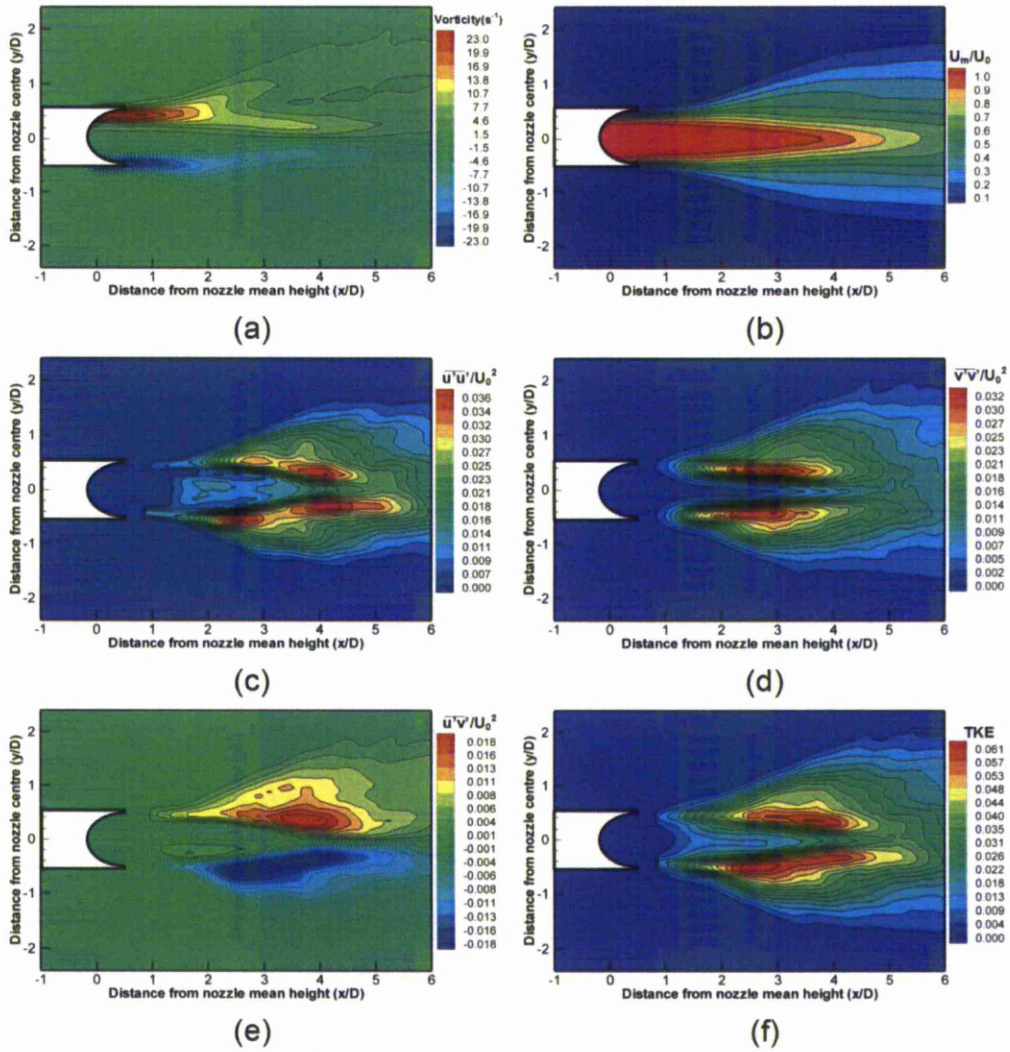

Figure 3.36 Time averaged PIV results along streamwise direction for AR2 A-notched nozzle, PP view

plane, the main ring vortex cores do not diverge but gradually move towards the nozzle centreline as they propagate downstream. This behaviour is indicative of axis-switching which can be found in nozzles of elliptic cross-section. Axis switching can be proven quantitatively when measuring the jet half-width. Half-jet width plots indicating such behaviour are analysed in section 3.2.4. The time-averaged vorticity results, in Fig. 3.36(a), are also in agreement with phase-average results and show a tendency of the vorticity to concentrate along the centreline of the jet. A small amount of branching can be observed. The branching is caused by the interaction of outward-flowing streamwise vortices with the jet body.

Along the TT-plane different flow behaviour is observed. The vorticity distribution is retained at the periphery region of the jet, and the main vortex rings do not move towards the nozzle centreline, similar to the reference nozzle. Phase- and time-averaged vorticity

distributions are depicted in Figs. 3.37(a) and 3.38(a). Time-averaged vorticity levels are reduced compared to the PP-plane indicating that the troughs do not intensify the flow field as much as the peaks do. It is interesting that along the PP-plane the jet undergoes behaviour that resembles the axis-switching phenomenon, found primarily in elliptic jets, while along the TT-plane the jet structures behave similar to the reference case.

Reynolds normal and shear stresses are presented in Figs. 3.35(c)-(e) to 3.38(c)-(e). The main stress contribution for all test geometries comes from the Reynolds normal streamwise stress. Focusing on the phase-averaged Reynolds normal streamwise stress, and comparing between PP- and TT-planes, a higher magnitude is attained from the latter (Figs.3.35(c) and 3.37(c)). The same observation can be made for the time-averaged results, showing that the difference is persistent and not caused by the particular flow phase. The flow structures, which can be viewed more clearly in the phase averaged plots, are also different. There is a correlation between the vorticity and the stresses, as high stress values are also measured at positions where main ring vortices exist. Regions containing high stress magnitudes are further upstream along the TT-plane (x/D=2.5) and also manifest at approximately x/D=4.5. Other differences are found in the region of influence. A larger area containing high stress levels is measured for the PP-plane which is due to the increased jet-spread because of the formation and interaction between the streamwise vortices and the jet body. The stresses associated with the PP-plane are approximately 10 -12% higher than the TT-plane. The stress difference is smaller when viewing the time-averaged results, but the flow differences are similar. The PP-plane stresses are concentrated closer to the centreline and further downstream, owing to the main ring vortex movement, while the TT-plane stress region, initiates upstream, dissipates faster and is situated along the periphery of the jet.

Moving on to the Reynolds normal cross-stream stresses, interesting differences between the two planes are highlighted. Examining the phase averaged results along the TT-plane first, regions of high cross-stream stress correlate well with the vorticity map shown in Figs. Fig.3.37(d) and 3.37(a) respectively. There are three distinct regions containing high stress, first at x/D=2.5, second at x/D=3.5 and the third at x/D=5. The region of influence is, as expected, smaller with respect to the PP-plane results. Focusing on the time-averaged results in Fig. 3.38(d), it is shown that for location x/D=3, a persistent high stress region exists. Additionally, comparing stress magnitudes between the two planes a difference of approximately 38% is calculated in favour of the PP-plane, Figs 3.35(d) and 3.36(d) respectively. The stress structuring along the PP-plane is more complex and is not only driven by the main ring vortex rollup. If only a relation with the main ring vortices existed then the region containing stress values would be similar to the TT-plane or even more

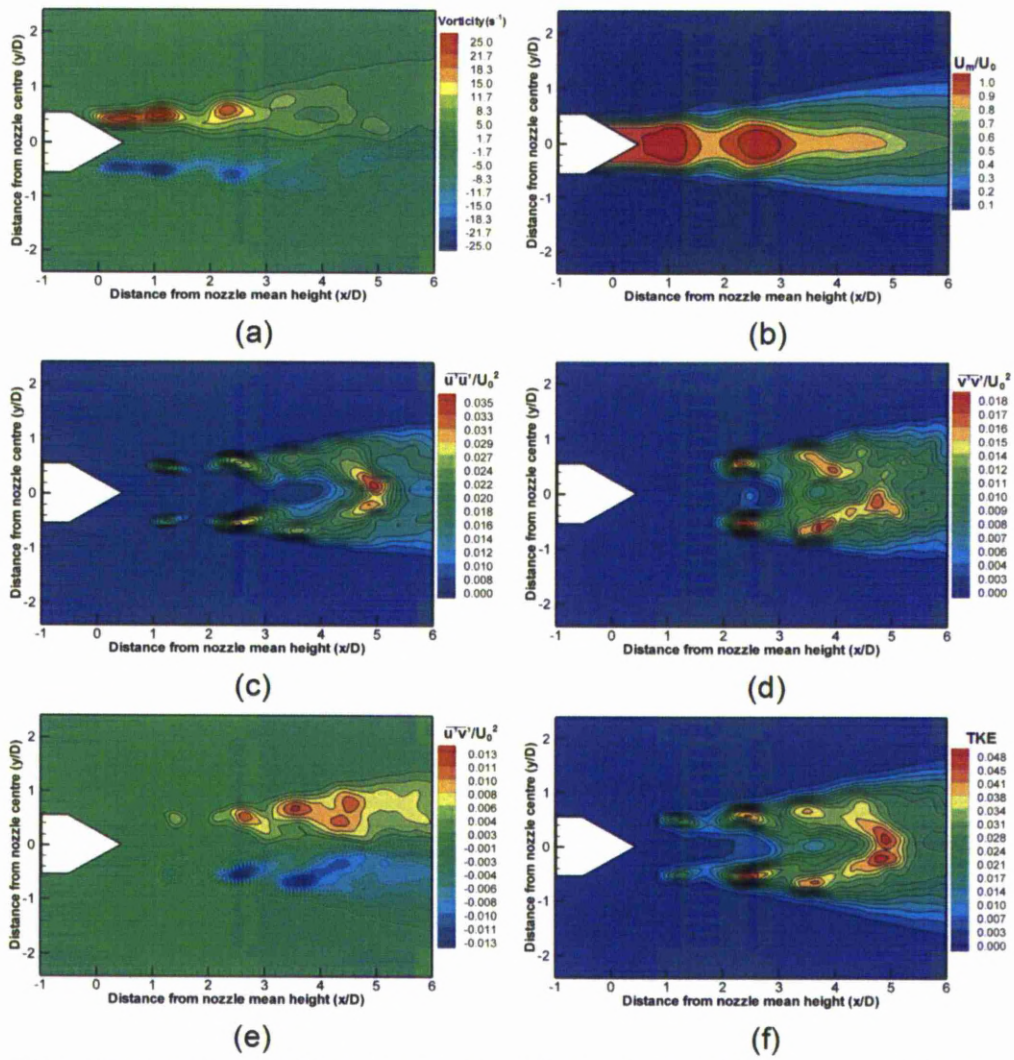

Figure 3.37 Phase averaged PIV results along streamwise direction for AR2 A-notched nozzle, TT view

concentrated along the nozzle centreline. For this reason, an additional influence must exist and is most probably caused by the streamwise vortices formed at the nozzle peaks. The highest cross-stream stress values, however, are attained at locations where vortices exist, as shown clearly in Figs. 3.35(a) and 3.35(d). The persistent inward motion of the main ring vortices possibly increases the ambient fluid entrainment and stress levels as shown in the time-averaged results in Fig. 3.36(d). The high stress region extends from approximately x/D=1.5 to 3.5D which coincides with the locations at which most of the inward main ring vortex motion occurs. Ho and Gutmark (1987) showed that the entrainment associated with an elliptic jet is three to eight times greater compared to a circular jet. This increase in entrainment was attributed to the axis-switching phenomenon. Since the PP-plane also shows axis-switching behaviour, an increase in the entrainment and cross stream flow stresses is expected.

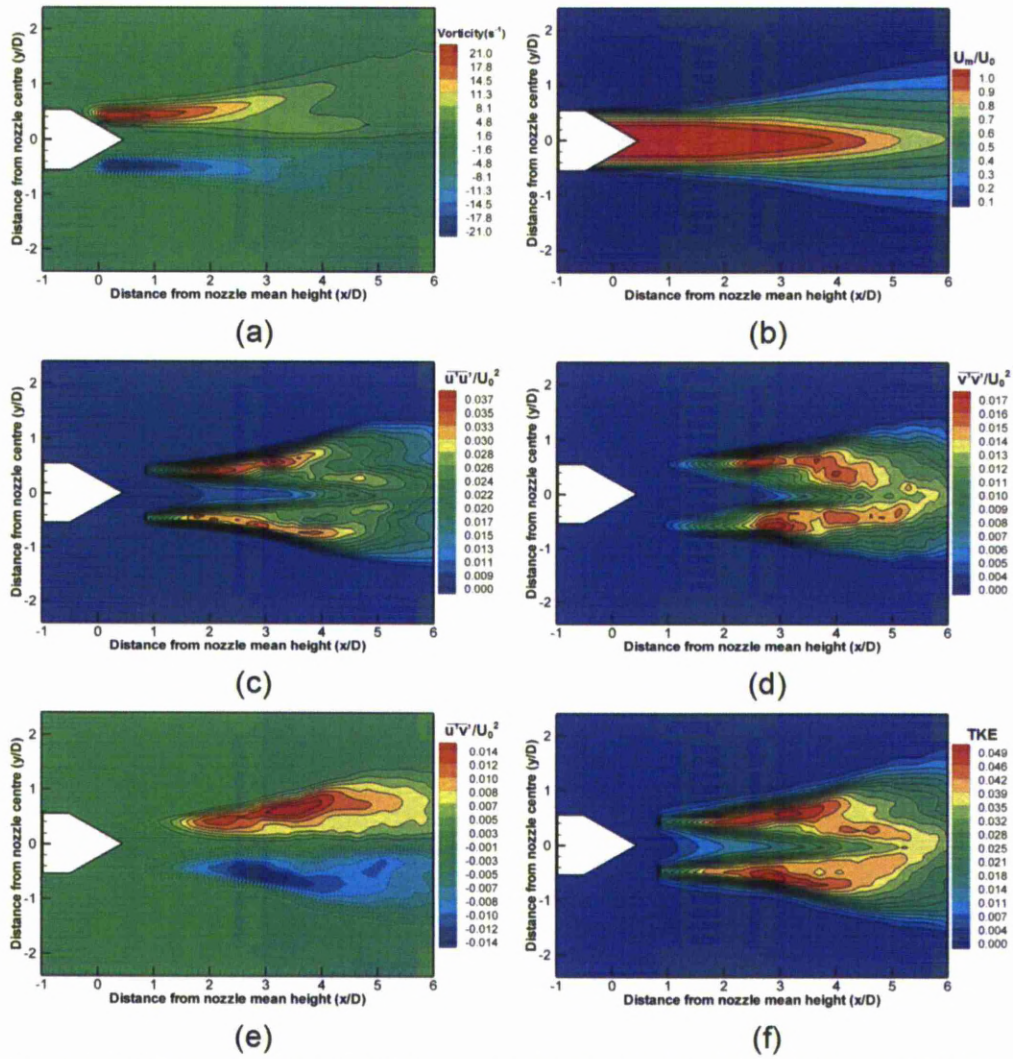

Figure 3.38 Time averaged PIV results along streamwise direction for AR2 A-notched nozzle, TT view

Evaluating the maximum Reynolds shear stress values, in Figs. 3.35(e) and 3.37(e), reveals that there is an approximate increase between the two planes by 30% in favour of the PP-plane. Since the Reynolds shear stress contains the product of the u' and v' velocity fluctuations, it can be understood that the findings will be similar to what has been shown previously for the Reynolds normal stresses. For the sake of brevity, a concise description will be made. Along the PP-plane the highest stress levels are concentrated along the nozzle centreline in similar locations to where the main ring vortices start to converge. This is seen in the phase- and time-averaged plots, in Figs. 3.35(e) and 3.36(e). Along the TT-plane the Reynolds shear stress structuring is influenced more by the cross stream component which in turn is driven primarily by the ambient fluid entrainment of the main ring vortices (Figs. 3.37(a) and 3.37(e)). A good correlation between the phase-averaged Reynolds shear stress and the vorticity can be seen. In the time-averaged results of Fig. 3.38, localised vortices are

not present, and the Reynolds shear stress diverges away from the nozzle centreline similar to what was observed by the dominant streamwise normal Reynolds stress component.

Turbulent kinetic energy values calculated along the streamwise view are shown in Figs. 3.35(f) to 3.38(f). The structuring is similar to the streamwise Reynolds normal stress described earlier and will not be discussed here in detail. This occurrence is caused by the dominance of the streamwise velocity fluctuation (u'^2). In contrast to the stress value, the maximum TKE magnitude attained from the time-averaged experiments is along the PP-plane. Similar to what was seen in the flow visualisation section, peaks intensify the flow and increase TKE approximately 24% with respect to the TT-plane, evident when comparing Figs. 3.36(f) and 3.38(f). The phase-averaged TKE plot do not show major differences in magnitude, but these values are phase-dependant and should be interpreted with care.

Cross-stream results

Figures 3.39 and 3.40 show results obtained from the cross-stream testing of the AR2 A-notched nozzle. For these cross-stream measurements, the nozzle was orientated such that the nozzle troughs were located near the top and bottom regions of the measurement windows, while the peaks were located on the left and right regions as indicated in Fig. 3.39(a).

Continuing the TKE analysis, some interesting points can be made when looking at the values calculated along the cross-stream direction, in Figs 3.39(c) and 3.40(c). In the vicinity of the nozzle exit, peak locations can be associated with an increase in cross-stream TKE. A difference of one jet-diameter along the x-direction can be found when comparing the influence of the peaks ($\overline{w'^2}$) between phase- and time-averaged plots. The location of the fully formed main ring vortices, measured during the phase-averaged experiments, explains this discrepancy. The first fully formed main ring vortex is captured at approximately x/D=1 as shown previously by Figs. 3.35(a) and 3.37(a). This location is further downstream than the high vorticity region associated with the time-averaged plots in Figs. 3.36(a) and 3.38(a).

Similarly, the cross-stream TKE component values associated with the peaks ($\overline{w'^2}$) are located further downstream for the phase-averaged experiments. After x/D=2, cross-stream TKE magnitudes and structuring are similar for both time-and phase-averaged test cases.

Inward ambient fluid motion can be seen in the velocity vector plot in Figs. 3.39(a) and 3.40(a)). The cross-stream velocity vectors ($\vec{w}, \vec{v}$) are coloured according to the magnitude of the $\vec{v}$ velocity component. Colouring the velocity vectors helps to distinguish inward flowing fluid and infer ambient fluid entrainment. Similar to all colour bands used throughout this thesis, blue coloured vectors move in the negative direction (downwards and left with

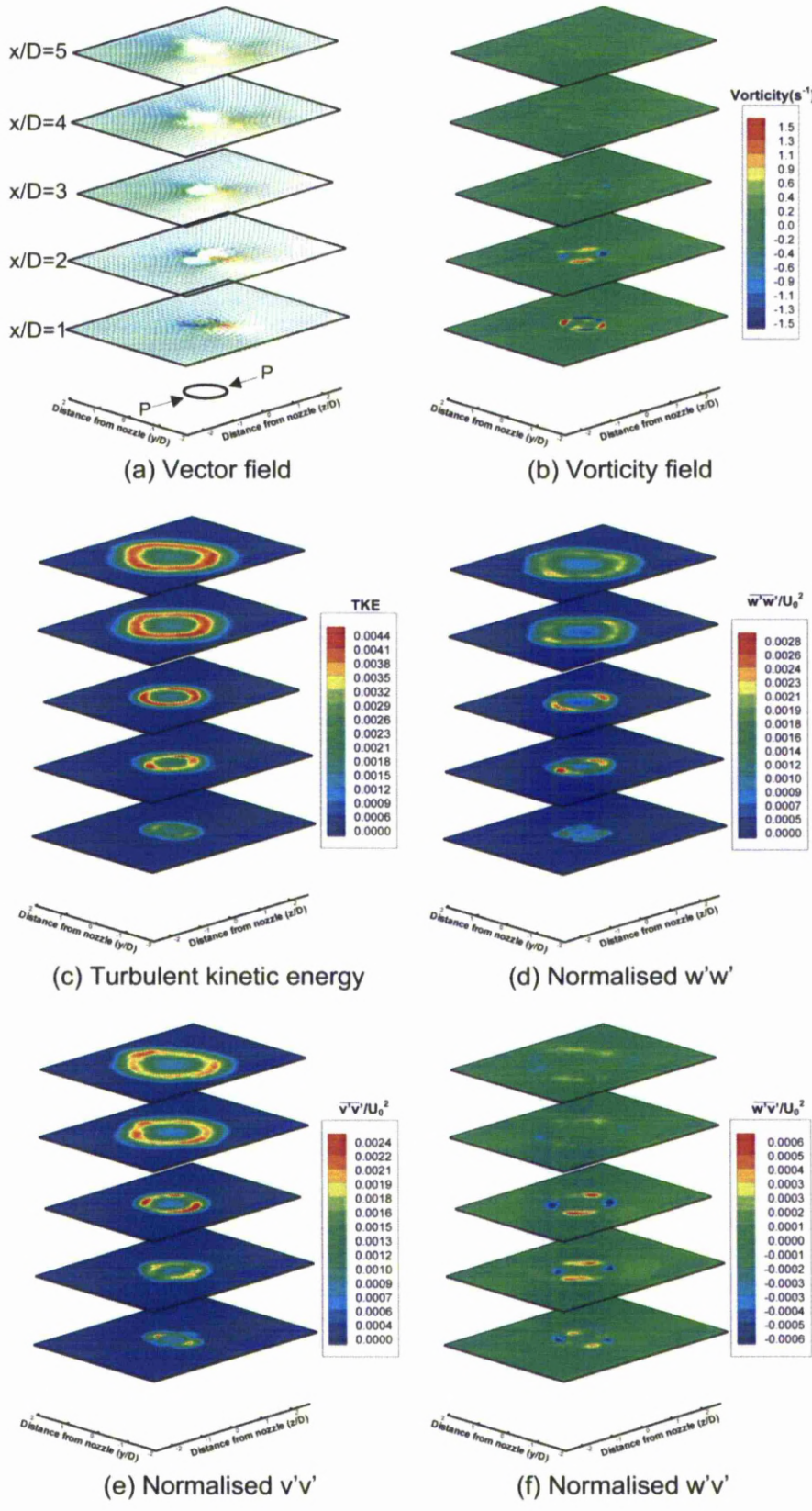

Figure 3.39 Phase averaged PIV results along cross-stream direction for AR2 A-notched nozzle

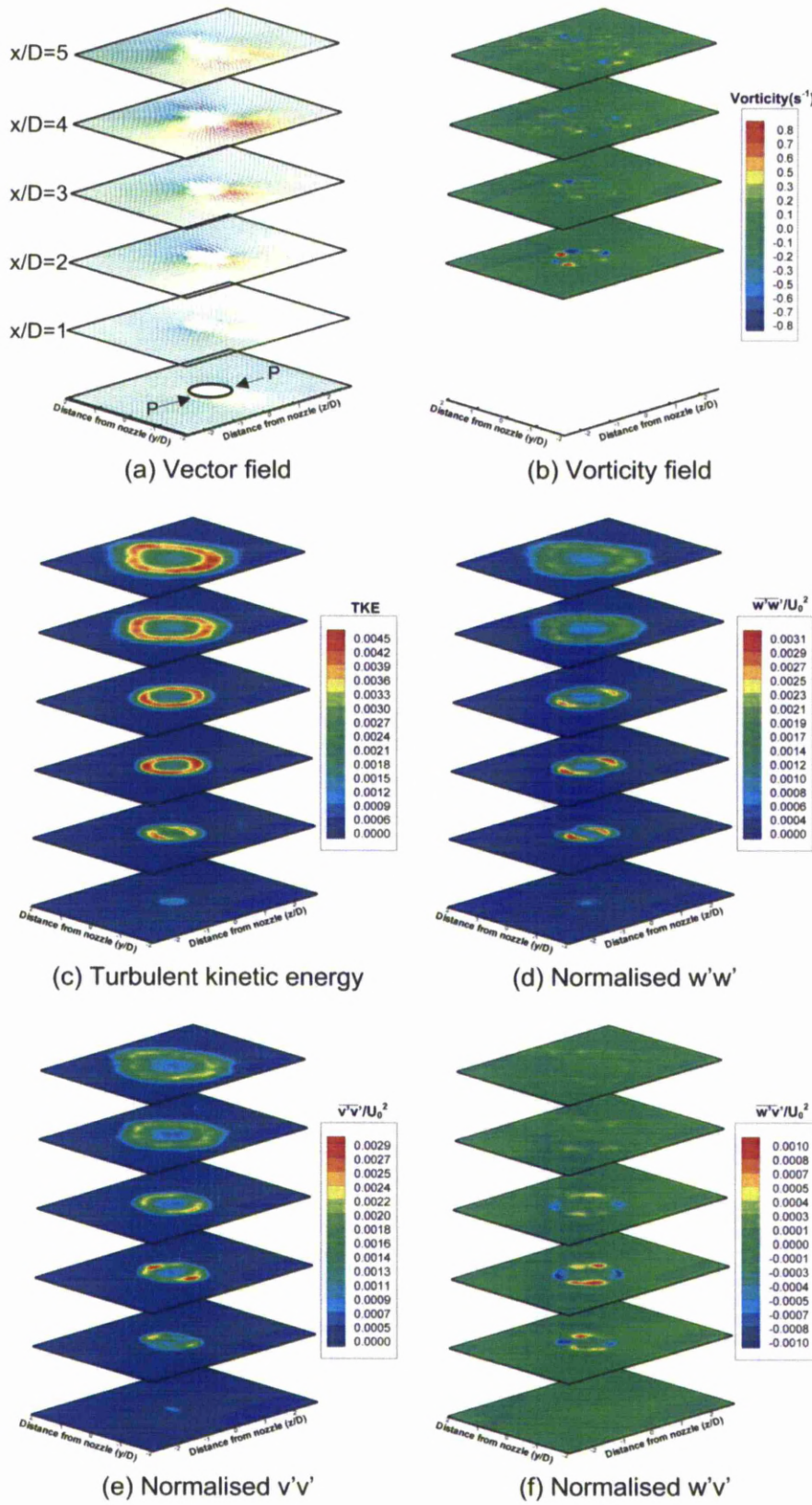

Figure 3.40 Time averaged PIV results along cross-stream direction for AR2 A-notched nozzle

respect to the paper), red coloured vectors move in the positive direction (upwards and right with respect to the paper) and green coloured vectors indicate a $\vec{v}$ magnitude close to zero, meaning that they can move along the z-axis ($\vec{w}$). Both phase- and time-averaged experiments result in similar flow fields. The jet body diverges as it propagates downstream and fluid inflow is the dominant flow behaviour. The phase-averaged flow field shows and increased velocity activity near the nozzle exit (x/D=2), indicated by the inward flowing vectors at the trough locations (orange and blue coloured). This behaviour is similar to what Longmire discovered when testing a nozzle with two peaks and two troughs (Longmire *et al.*, 1992a). When focusing on the time-averaged results through, higher flow activity is seen further downstream, between x/D=3 to 5. The increase in flow activity coincides with the breakdown of the main ring vortices and the formation of smaller scale eddies, similar to the reference case, presented earlier in Fig. 3.34(a). Comparing the two procedures it is evident that the cross-stream flow direction and magnitude is phase dependant. For phase-averaged results, the position of the main ring vortex in relation to the measurement plane is important. Inflow or outflow along the nozzle troughs can be affected. At this point it is worth noting that the dominant flow direction is outward-flowing at the trough locations, according to the time-averaged results.

The velocity plots correlate well with the vorticity plots shown in Figs. 3.39(b) and 3.40(b), although the latter provide more information about the streamwise vortices and their rotational sense. To further reinforce the notion that the particular flow phase influences the flow field result, a comparison between phase- and time-averaged vorticity results reveals a discrepancy in the rotational sense of the streamwise vortices. At location x/D=1of the phase-averaged results, the rotational sense of the streamwise vorticity suggests that there is ejection of fluid from the trough locations and inflow of fluid at the peak locations. The rotational sense of the counter-rotating vortices changes in the next fluid slice (x/D=2) and it is suggested that fluid is ejected from the peaks and entrained through the nozzle troughs. This behaviour coincides with the cross-stream velocity vector plot in Fig. 3.39(a), in which large $\vec{v}$ components are pointing inwards at trough locations and $\vec{w}$ components are pointing outwards at peak locations. The jet body is elongated along the PP-plane which also indicates spreading along the peaks.

The time-averaged results show a more coherent flow field in which there are no changes to the rotational sense of the streamwise vorticity. Looking at Fig. 3.40(b), it can clearly be seen that the streamwise vorticity orientation is such that promotes outward spreading at both trough and peak locations, similar to what was presented in section 32.2.

c) AR2 V-notched geometry

Streamwise

Similar to the A-notched nozzle, the jet associated with the V-notched geometry shows a similar trend. Along the PP-plane, shown in Fig 3.41(a), the main ring vortices move towards the nozzle centreline as they propagate downstream similar to the behaviour expected from an elliptic ring. The main rings form at the nozzle lip but start to converge at a downstream distance of approximately two jet-diameters downstream of the mean height. In contrast to the main ring vortices, the rib-structures diverge away from the nozzle centreline and spread the jet. This behaviour can be seen clearly in the time-averaged result shown in Fig. 3.42(a). A "fork-like" shape similar to a critical point (saddle point) is formed in the vorticity plot, possibly caused by the main ring movement towards the nozzle centreline and also by the streamwise vortex (rib-like structure) spreading. Although the

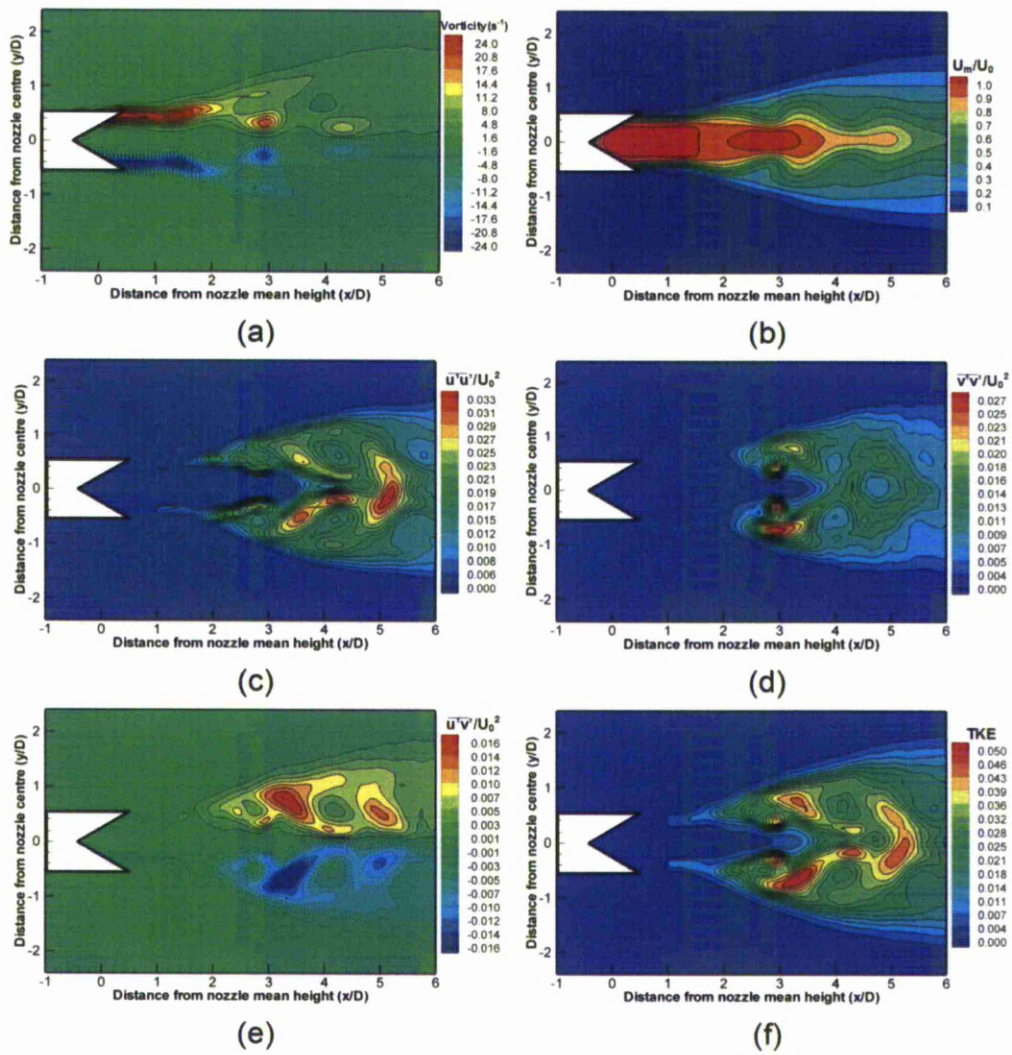

Figure 3.41 Phase averaged PIV results along streamwise direction for AR2 V-notched nozzle, PP view

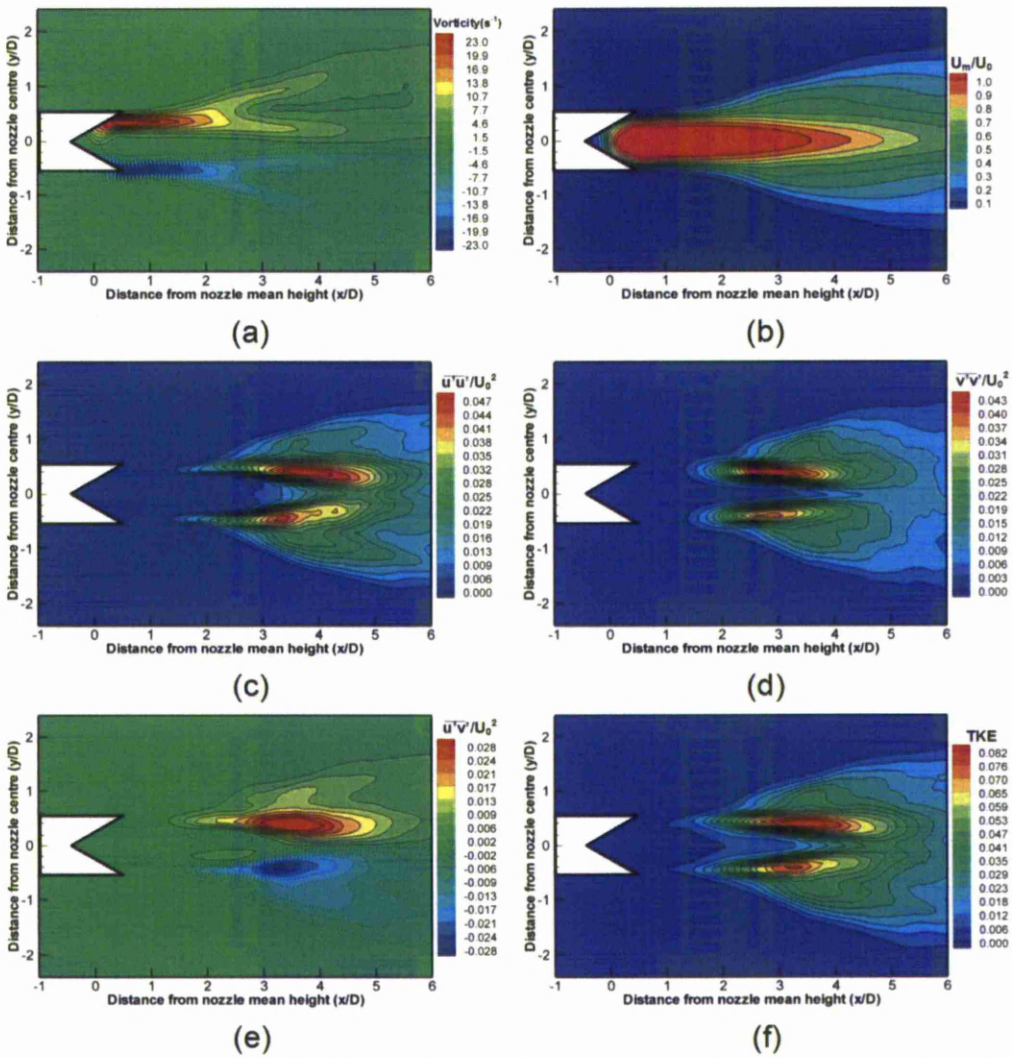

Figure 3.42 Time averaged PIV results along streamwise direction for AR2 V-notched nozzle, PP view

actual vorticity of the streamwise vortices cannot be measured along the streamwise direction, the region of influence caused by these vortices is measurable and coincides with the flow visualisation results presented in earlier chapters. Both phase-and time-averaged main ring vorticity levels are comparable to the reference case and to the A-notched nozzle along the same view (PP-plane).

The jet potential core, depicted in Fig. 3.42(b), extends to approximately 4.2 jet-diameters downstream of the mean height, similar to the A-notched nozzle. Spreading of the jet along the PP-plane is evident, especially downstream of x/D=2.5. The spreading was also seen in the flow visualisation section and is caused by the streamwise vortices (rib-structures). Similar to the A-notched case presented earlier, the peaks augment the generation of streamwise vortices which intensify mixing between the jet and its surroundings and cause the spreading of the jet. Comparing the spreading achieved by both A-and V-notched

nozzles along the PP-plane at the end of the measurement window, one can determine that they are similar by examining Figs. 3.36(b) and 3.42(b). Both nozzles would perform well in applications where asymmetric spreading and mixing between PP and TT-planes was required (asymmetric properties around the azimuth of the jet). The symmetric nature of the flow pulsing and the resultant flowfield can be observed when looking at the phase-averaged normalised velocity contours in Fig. 3.41(b), thus further reinforcing the notion of consistent experimental testing.

Comparing the results obtained along the PP-plane to the TT-plane, vortex structuring is more complex and is shown in Fig. 3.43(a). Along the TT-plane, the jet-spread is reduced promoting a thinner jet. Apart from the usual main ring vortices mentioned earlier, another set of secondary vortices are present in a consistent manner. While the main ring vortices move away from the nozzle centreline as expected, these secondary vortices tend to move toward the centreline. This movement is also captured in the time-averaged results and can be seen from the branching shown in Fig. 3.44(a). The movement of the main ring vortices is due to the bending orientation of the filaments as explained in the flow visualisation section presented earlier. On the other hand, the movement of the secondary vortices is not fully understood. Further investigations could shed some light on the formation and interaction of these vortical structures.

The Reynolds streamwise, normal and shear stresses associated with the V-notched nozzle of AR2 are presented in Figs. 3.41(c)-(e) to 3.44(c)-(e). The stress distributions are good indications of the mixing process and will help explain how the peak and trough configurations affect jet-mixing. By comparing the results obtained by the two measurement planes, it is clear that the stress levels and mixing mechanisms are significantly different.

Regions of maximum streamwise Reynolds normal stress levels along the PP-planes, in Figs. 3.41(c) and 3.43(c) respectively, are associated with more convoluted flow activities further downstream, as compared to the corresponding stress levels along TT-planes, shown in Figs. 3.42(c) and 3.44(c). The contour outlines suggest that the production of streamwise Reynolds normal stresses along the PP-planes is heavily associated with the vortex-bending and axis-switching behaviour. On the other hand, those along the TT-plane are thought to be associated more with the production of the large-scale vortex roll-ups than downstream flow activities.

Flow stresses are in good agreement with the vortex behaviour depicted in the flow visualisation images presented earlier, where different vortex-bending behaviours are observed along the two visualisation planes. Comparing with Figs. 3.4 and 3.5 where flow images along the PP-and TT-planes are shown, it can be deduced that the streamwise

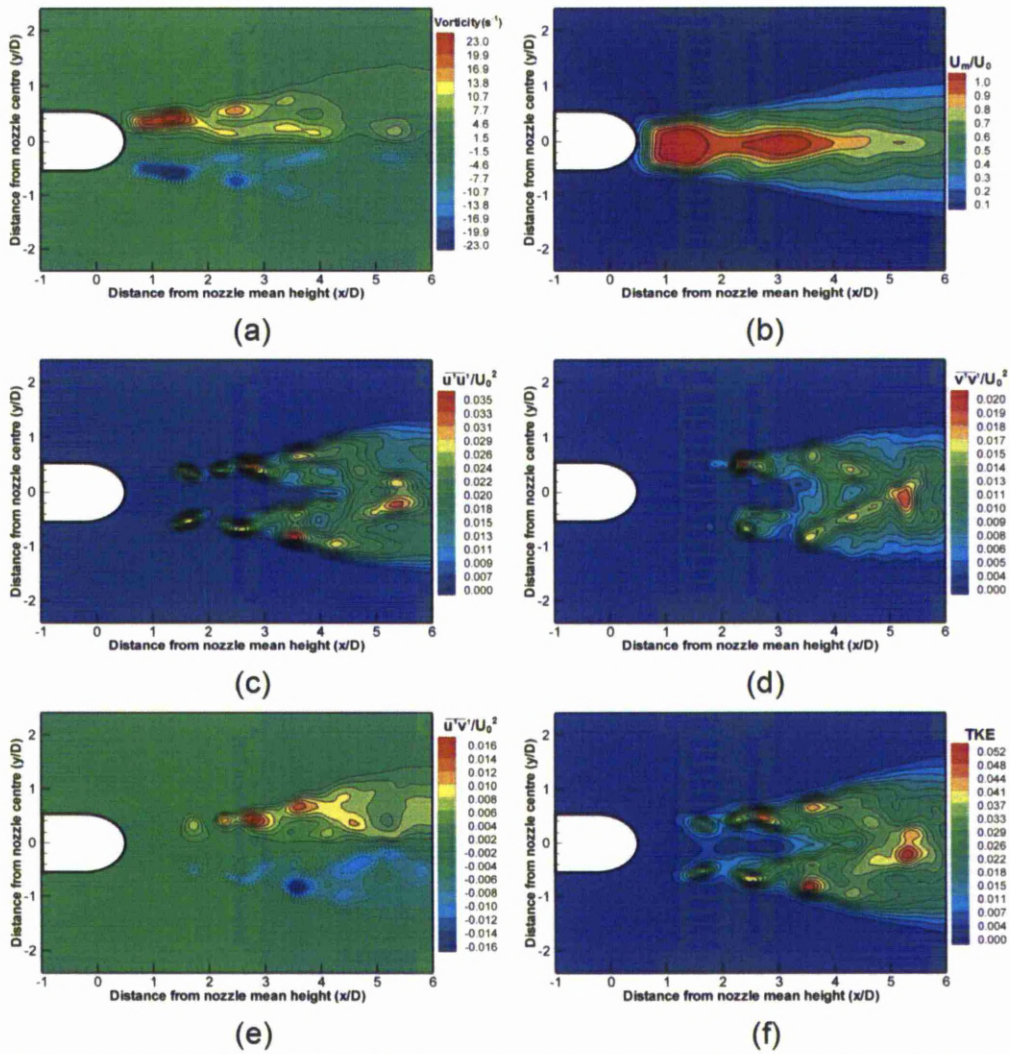

Figure 3.43 Phase averaged PIV results along streamwise direction for AR2 V-notched nozzle, TT view

Reynolds normal and shear stress distributions shown in Figs 3.41(c),(e) and 3.42(c),(e) are dominated by the downstream axis-switching behaviour (as indicated by the organised production of high flow stress regions) where the vortex roll-ups are bending in the downstream direction, rather than in the immediate vicinity of the nozzle exit. Higher self-induced velocities toward the jet centre line as well as in the streamwise direction introduced by the axis-switching behaviour will explain the observed stress distributions.

On the other hand, the distributions of streamwise Reynolds normal and shear stresses are largely driven by the large-scale vortex roll-ups forming off the nozzle lips along the TT-planes as shown in Figs 3.43(c),(e) and 3.44(c),(e). Although vortex-bending behaviour have been observed along these planes as well, they are toward the upstream direction and the vortex filament portions at the through locations do not move toward the jet centreline. Hence, the regions of high flow stress remain along the periphery of the jet shear layer.

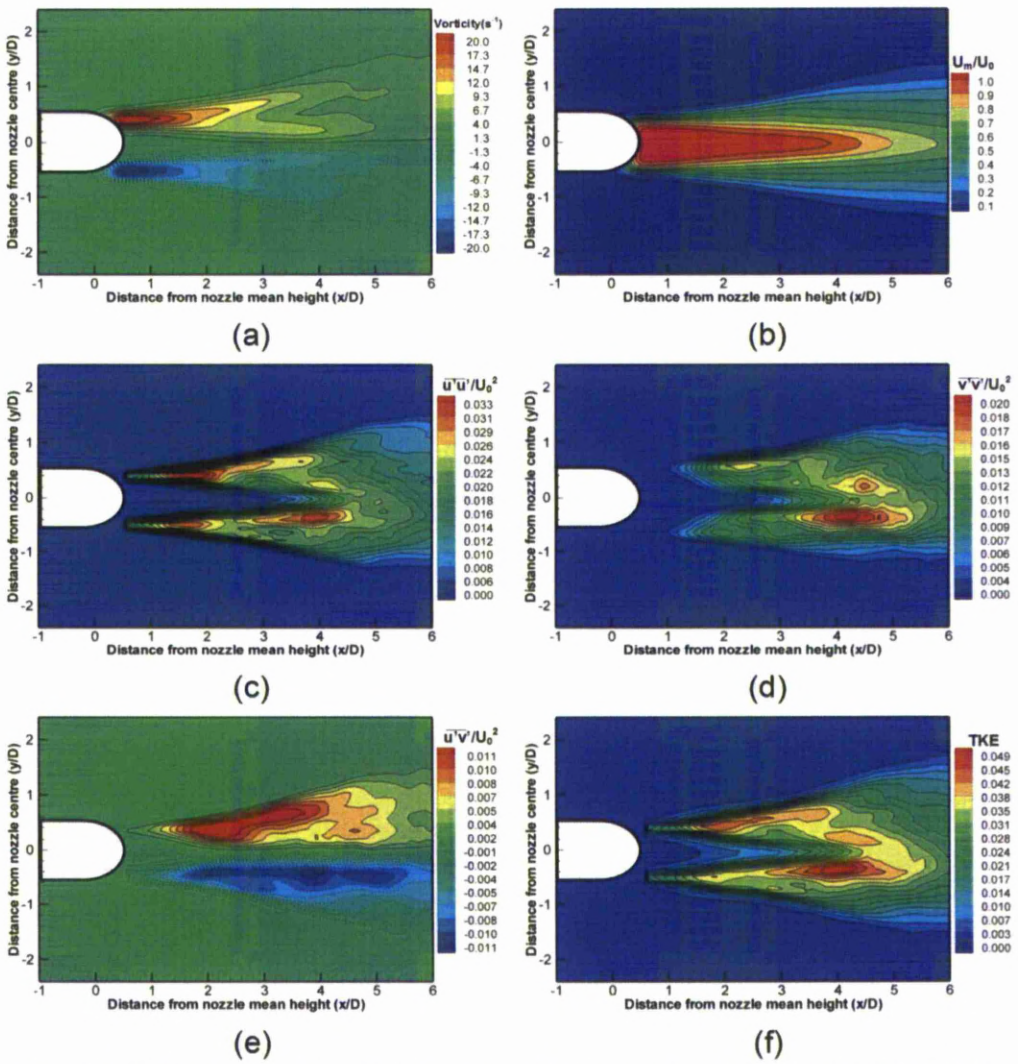

Figure 3.44 Time averaged PIV results along streamwise direction for AR2 V-notched nozzle, TT view

The cross-stream Reynolds normal stress which relates closely to jet entrainment levels follows a similar trend. Along the PP-plane, high stress regions are linked to the vortex roll-ups while along the TT-plane the breakdown of the main ring vortices at the end of the potential core promotes cross-stream stress production.

The turbulent kinetic energy distributions are related to the main ring vortices which is clearly demonstrated when comparing the phase-averaged results in Figs. 3.41(a),(f) and 3.43(a),(f). Along both measurement planes, maximum TKE magnitudes are attained at the locations where main ring vortices exist. It is worth noting that the secondary vertical structures found along the TT-plane do not influence the formation of high TKE magnitudes, in the vicinity of the nozzle exit. However, further downstream (x/D=5) both PP- and TT-planes have a region close to the nozzle centreline which contains high TKE values. This can be expected for the PP-plane as the main ring vortices are concentrated around the nozzle

centreline. However, the jet main ring vortices move away from the nozzle centreline along the TT-plane, which means that the secondary vortices must interact and cause an increase in TKE at downstream locations. It can thus be inferred that the flow stress distribution can be suitably manipulated by controlling the vortex-bending behaviour, which in turn is dependent on the lip modification applied to the nozzle.

Cross-stream results

To better understand and explain the presence of both the PP and TT streamwise vortices, phase- and time-averaged cross-stream PIV measurements were conducted, and are presented in Figs. 3.45 and 3.46. Similar to the cross-stream plots presented earlier the nozzle was orientated such that the nozzle troughs are located near the top and button regions of the measurement windows, while the peaks are located on the left and right regions.

Focusing initially on the flow behaviour or the jet, the time-averaged velocity and vorticity results reveal that there are four pairs of outward-spreading counter-rotating vortex-pairs associated with the streamwise vortices which are formed around the peripheral region of the jets at all peak and though locations. The peak streamwise vortices have a larger region of influence when compared to the trough streamwise vortices. This finding correlates well with observations made in the flow visualisation chapter in section 3.2.1. Interestingly, the rotational sense of the peak and though streamwise vortices cause fluid to be ejected radially outward from the jet core. However, between successive peak and trough locations on the nozzle periphery namely: Northeast, Southeast, Southwest and Northwest locations, the streamwise vortex orientation is such that there is an inflow of ambient fluid. This inflow and outflow of fluid could explain the association between streamwise vortices and the gross momentum exchange between the jet and the surrounding fluid as reported by Longmire *et al,.*(1992a). This behaviour cannot be seen in the phase-averaged vorticity results, in Figs. 3.45(a) and 3.45(b), where only evidence of peak streamwise vortices are present. The discrepancy may seem unintuitive initially, but again it should be noted that the particular flow phase will produce a unique flow-field result. For this reason greater attention will be given to the time-averaged results during the flow analysis.

Regardless of their size, strength and location, peak and trough streamwise vortices lose flow coherency very rapidly as they convect downstream. This can be clearly appreciated in the cross-stream development of the streamwise vortices cross-stream from x/D=1 to 4, as shown in Figs 3.45(b) and 3.46(b).

Comparing the finding of this study with findings published by other authors,

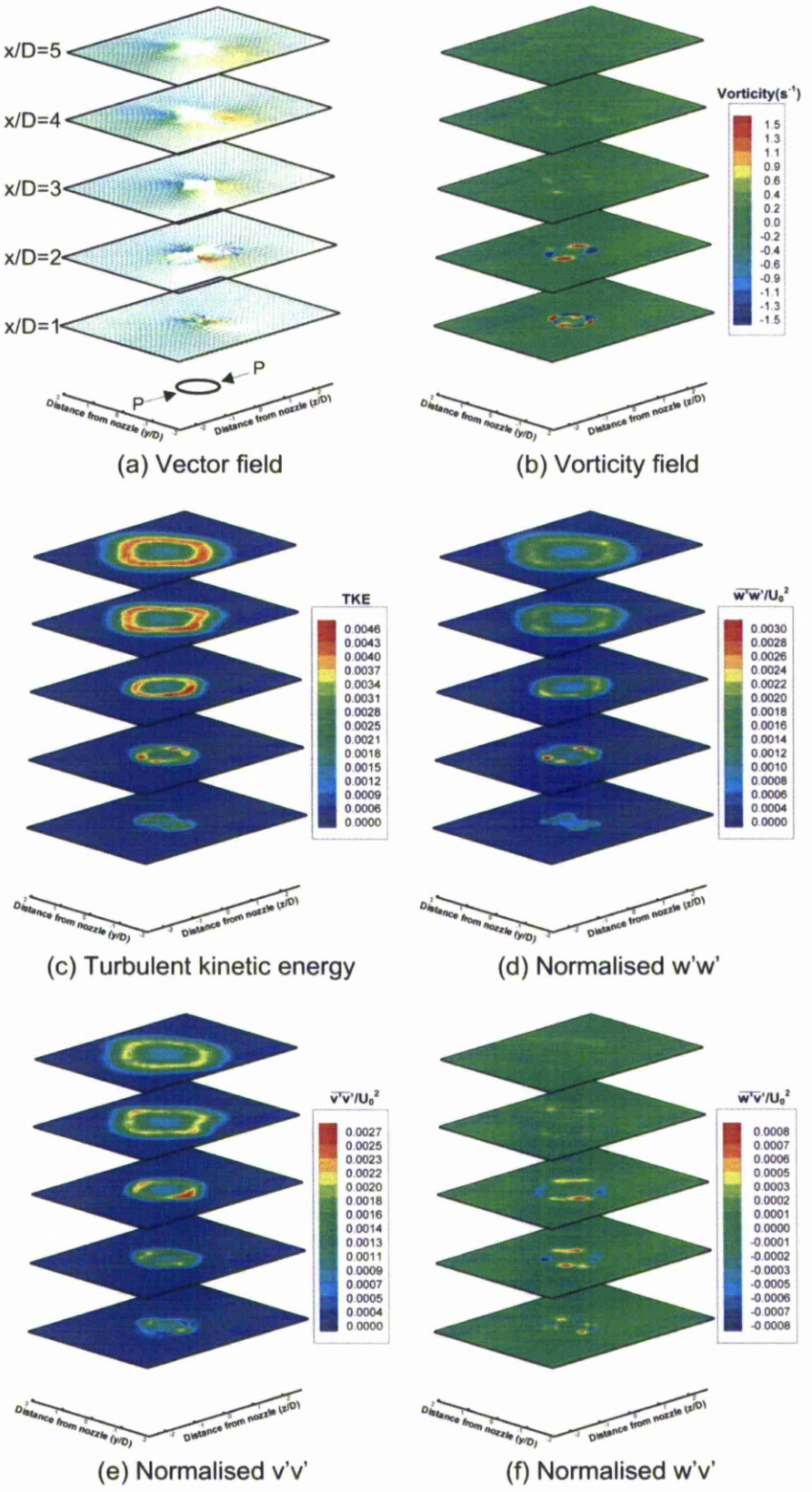

Figure 3.45 Phase averaged PIV results along cross-stream direction for AR2 V-notched nozzle

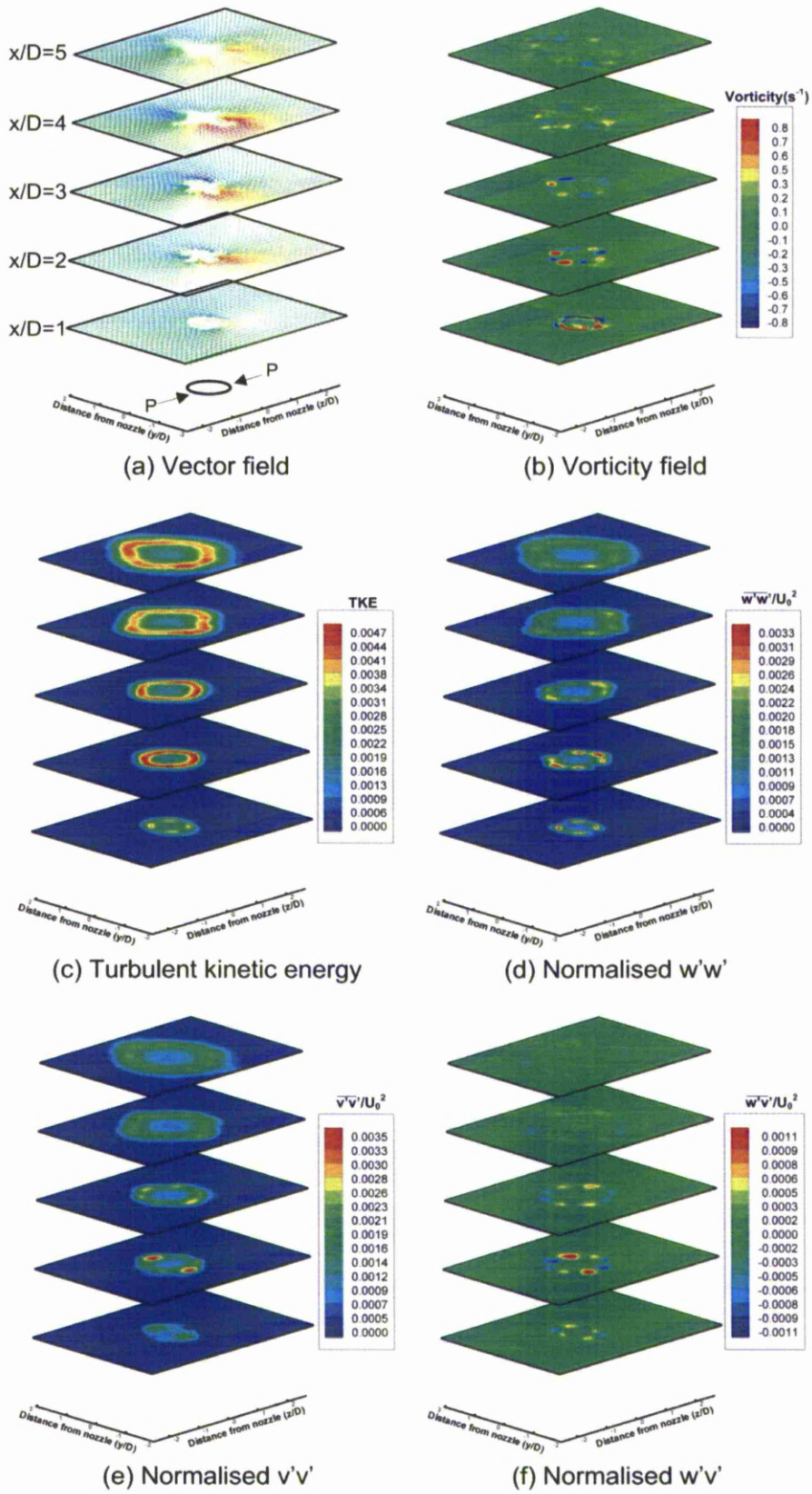

Figure 3.46 Time averaged PIV results along cross-stream direction for AR2 V-notched nozzle

(Longmire *et al.*, 1992a; Hu *et al.*, 2001a; Shu *et al.*, 2005) differences in the rotational sense of the streamwise vortices, depending on whether they are formed along the peak or though locations can be seen. For instance, while outward-spreading streamwise vortices were observed to form along peak locations in all these studies, inward-spreading streamwise vortices were formed along trough locations only in (Longmire *et al.*, 1992a; Shu *et al.*, 2005; Shu, 2005). However, the rotational sense of the streamwise vortices observed in (New *et al.*, 2005; New and Tsai, 2007) were similar to the present study. Although the exact reason for the discrepancy remains unknown to the authors at this point, it is worthwhile to mention here that the nozzle design rules used in (New *et al.*, 2005; New and Tsai, 2007) and the present study are quite similar and thus suggests that the specific geometry of the lip modification could be responsible for the discrepancy. Additionally, it is also possible that differing initial flow conditions of the jet flows between the studies led to the discrepancy. For example, the shear layer vorticity thickness of the circular reference jet flow using in Longmire *et al.*(1992a) measured approximately 0.03D, while the corresponding circular reference jet momentum thickness in(Shu *et al.*, 2005) was slightly above 0.02 D. On the other hand, momentum thickness of the circular reference jet flow in the present study as measured at the nozzle exit, measured approximately 0.05D. Furthermore, the Reynolds numbers were Re=19000 for Longmire *et al.*,.(1992a) and 5000 for Shu *et al.*(2005) respectively, as well as compared to Re=2000 for New *et al.*(2005) and the flow visualisation section in New and Tsai,(2007), while Re=2100 was used for the present study. This points out that significantly thicker jet shear layer emanating from the nozzles and the difference in the Reynolds number used within the present study may have played a role in affecting the resultant rotational sense of the streamwise vortices. It is also possible, that the transient nature and the added complexity associated with the highly three-dimensional flow may have obscured flow features indicating inward-spreading streamwise vortices.

High TKE values are achieved, as expected, along the shear layer of the jet where velocity gradients and fluctuations exist that enhance mixing. Close to the nozzle exit, regions of high TKE activity coincide with the nozzle peak locations which indicates that the peak streamwise vortices increase mixing at these locations. This effect extends to x/D=2 for the phase averaged case (Fig. 3.45(c)) and x/D=1 for the time-averaged case (Fig. 3.46(c)). Similarly, the major flow stress activity (Reynolds shear, normal streamwise and normal cross-stream) is found close to the nozzle exit, at approximately x/D=2 for both phase- and time-averaged.

d) Influence of nozzle sharpness along streamwise plane

In the following sections the nozzles with an aspect-ratio of four will be presented. Although the main flow properties are expected to be similar to the less sharp AR2 case, some interesting differences will be highlighted. As seen from the flow visualisation results, the resultant flow field was more intense and the vortex dynamics were more convoluted. The main ring vortices transist to turbulence faster and so a higher flow activity can be expected which could also increase the flow stresses. The effects of increasing the sharpness of the A- and V-notched nozzles along both planes will also be shown.

A-notched design

Starting the AR4 nozzle analysis with phase-averaged vorticity plot along the PP view, a familiar flow field is seen in Fig. 3.47(a). Although the main ring vortices move toward the nozzle centreline similar to the less-sharp AR2 case, thus showing similar overall flow behaviour, there are small differences worth mentioning. It can be seen that the exact vortex behaviour is influenced by the nozzle configuration. For instance, the use of a higher nozzle design aspect ratio results in a small (approximately 0.5D) upstream shift in the meet-up location of the vortex roll-ups along the PP-plane. Hence, it can be seen that increasing nozzle aspect ratio serves to accentuate the vortex dynamics and does not alter the general jet behaviour. The symmetric nature of the velocity flow field shown in Fig. 3.47(b) indicates an un-biased flow pulsing of the jet.

The phase-averaged streamwise flow stress distribution is shown in Fig. 3.47(c). Similar to the AR2 case, the location of the high magnitude streamwise stress is concentrated in the downstream region of the jet correlating well with the movement of the main ring vortices. Due to the faster movement of the main ring vortices, there is an upstream shift detected in the stress field of approximately 0.8D. The streamwise stress magnitudes between the two nozzles are similar. The cross-stream flow stress field in Fig. 3.47(d) shows small difference to the AR2 case. Increasing the aspect ratio of the nozzle for both PP and TT-planes (presented next) does not correspond to an increase of the cross-stream stress component. In fact, the maximum magnitudes observed for both TT- and PP-planes of the AR4 nozzle are slightly lower than that along the PP-plane for the AR2 nozzle. Interestingly, the Reynolds stress along both PP- and TT-planes, shown in Figs. 3.47(e) and 3.49(e), increases by 13% and 11% respectively when the aspect ratio is increased, and finally, the TKE values obtained from the AR4 nozzle are slightly reduced with respect to the lower aspect ratio nozzle.

An unexpected observation is noticed in the time averaged vorticity plot in Fig. 3.48(a). It was shown in the flow visualisation section that the increased aspect ratio of the nozzle

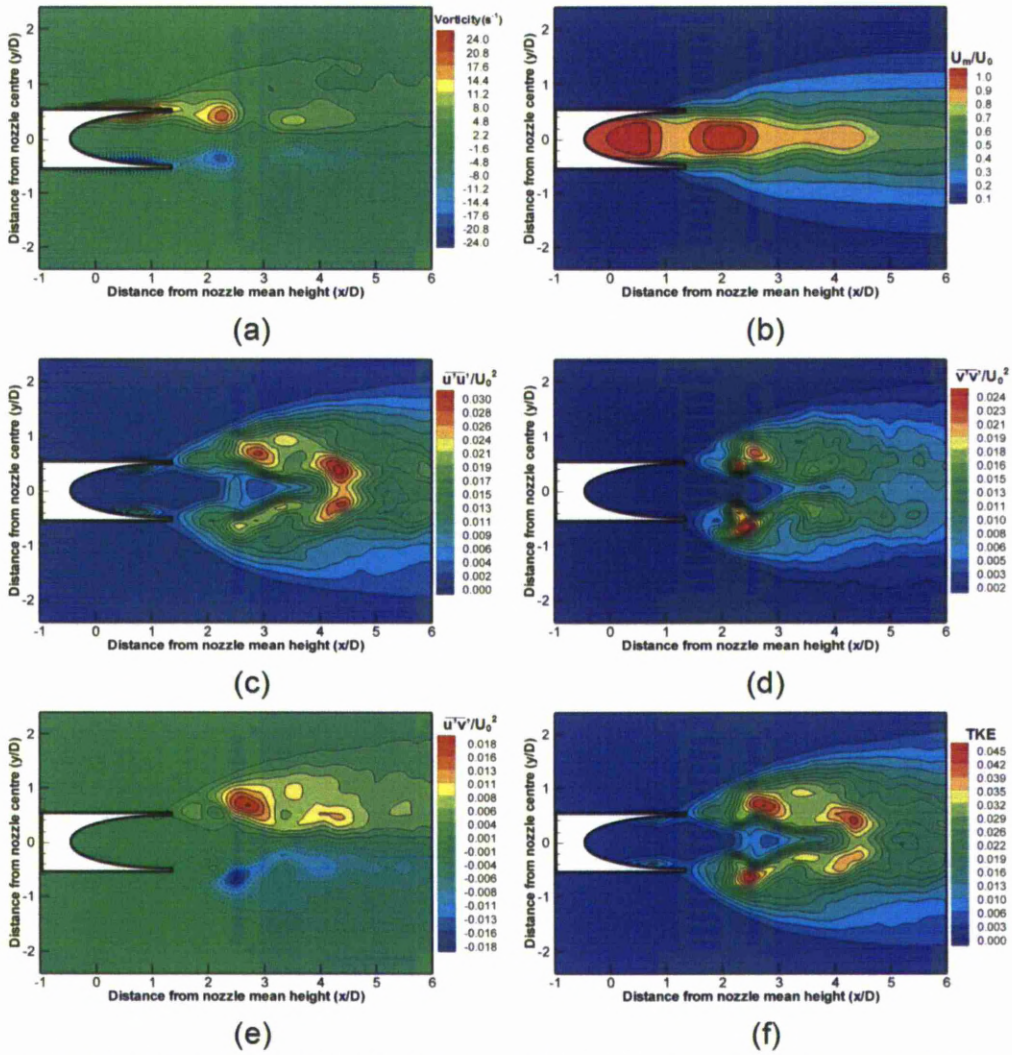

Figure 3.47 Phase averaged PIV results along streamwise direction for AR4 A-notched nozzle, PP view

intensified the flow and produced streamwise vortices that affect the main ring to a larger extent when compared to the AR2 nozzle. However, looking at the time-averaged vorticity there does not seem to any evidence of "forking" as seen for the lower aspect ratio case. This means that visually, the main rings are deformed more by an increase aspect ratio, but an increased interaction with the jet main body which would assist the jet spread along the PP-plane is not occurring.

Focusing on the normalised velocity plot in Fig. 3.48(b), the resultant jet spread along the PP-plane is shown. Similar to the less sharp case, the jet spread along the PP-plane is increased compared to the TT-plane plot in Fig. 3.50(b). However, comparing between nozzles of different aspect ratio a relatively small difference exists as seen in Figs. 3.48(b) and 3.36(b). Hence, the figures indicate that appreciably greater changes to the jet spreading

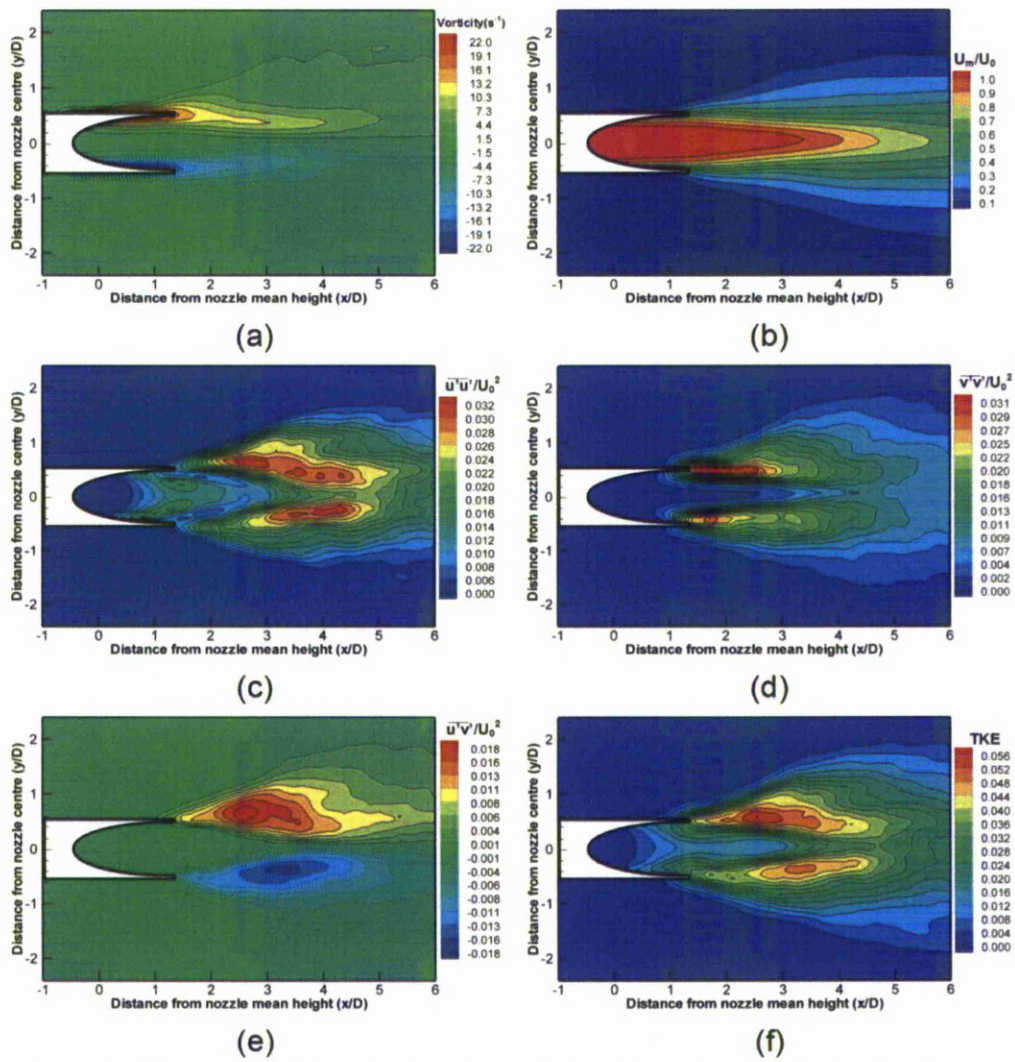

Figure 3.48 Time averaged PIV results along streamwise direction for AR4 A-notched nozzle, PP view

will result simply from the use of either peaks or troughs, rather that the use of sharper nozzles of similar configuration; at least regarding the A-notched design. On the other hand, increasing the aspect ratio assists marginally towards the erosion of the jet potential core. A small decrease of the jet potential core of approximately 0.3D is noticed when comparing time-averaged velocity plots in Figs. 3.36(b) and 3.48(b).

For the sake of completeness, phase- and time-averaged results along the TT-plane are presented in Figs. 3.49 and 3.50 respectively. The overall flow field is similar to the lower aspect ratio case and in particular it can be noticed that the vorticity remains close to the nozzle centreline and evidence of secondary vortical structures also exist in Fig. 3.49(a). The jet-spread is lower than that achieved along the PP-plane and comparable to the AR2 case as shown in Fig. 3.50(b). Due to the distinct similarity between the results obtained by the AR4 and AR2 nozzle, an in depth analysis will be repetitive. However, in the following section an

extensive study covering the half jet-width and momentum thickness of all nozzles will quantify the jet spreading and analyse the differences found between them.

V-notched design

In the following paragraphs, the effects of increasing the sharpness of the V-notched nozzles will be documented. Figures 3.51 and 3.52 depict results obtained by testing the AR4 V-notched nozzle, along the PP view under phase- and time-averaged conditions respectively, while Figs. 3.53 and 3.54 convey the results obtained along the TT view. Similar to the A-notched high aspect-ratio nozzles, the overall flow behaviour is governed by the same vortex flow model as proposed in section 3.2.2 and thus the resultant flow fields for both V-notched nozzles will be comparable, albeit with an expected increase in flow intensification as was shown in the flow visualisation chapter.

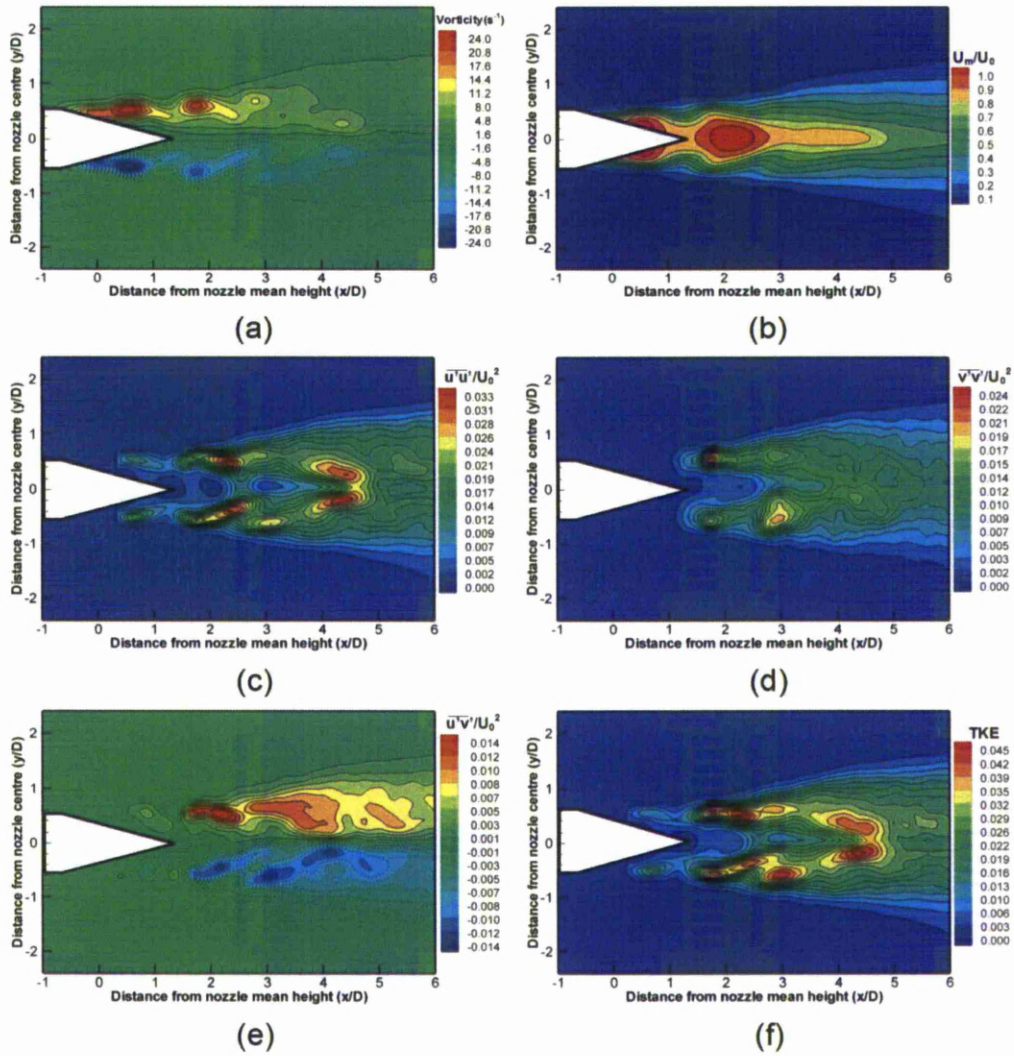

Figure 3.49 Phase averaged PIV results along streamwise direction for AR4 A-notched nozzle, TT view

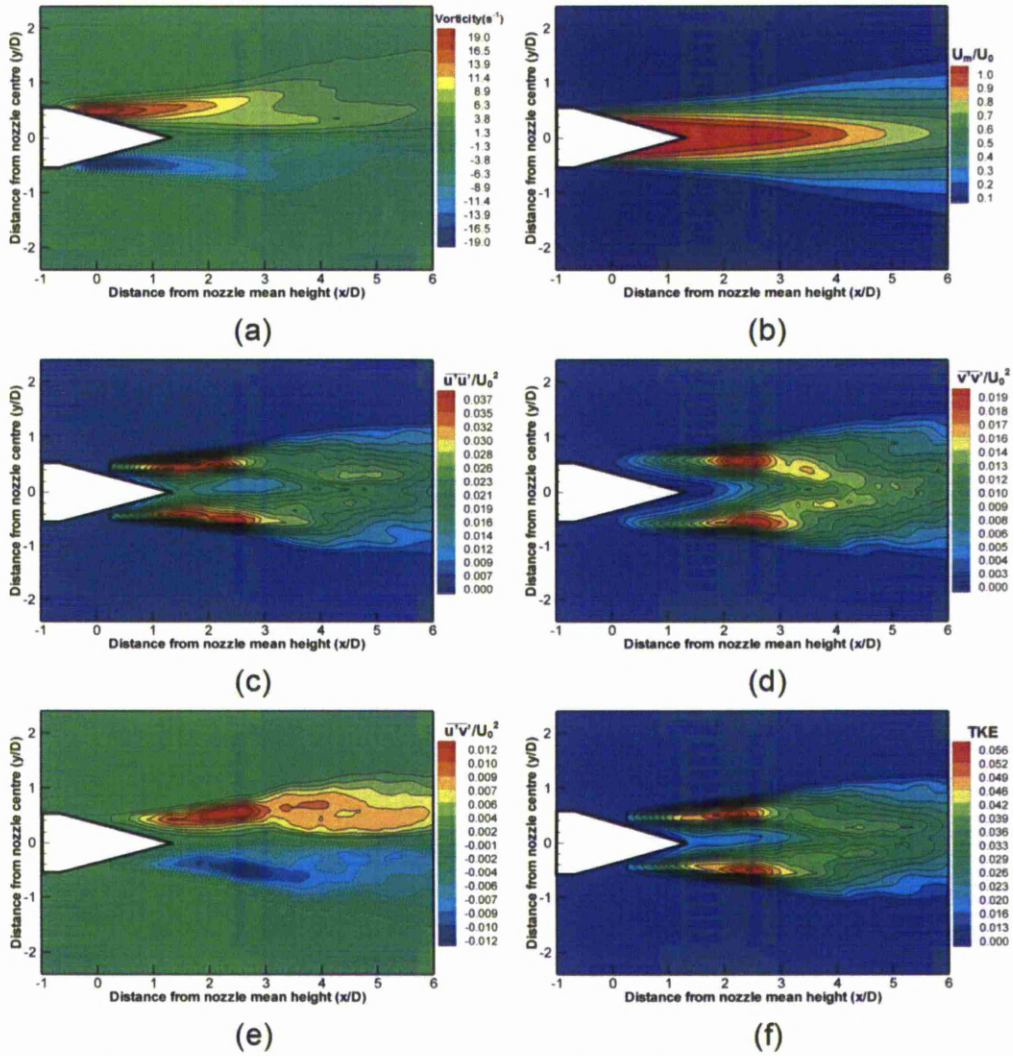

Figure 3.50 Time averaged PIV results along streamwise direction for AR4 A-notched nozzle, TT view

Evidence of similar flow structuring between AR2 and AR4 V-notched nozzles along the PP view can be seen in the vorticity plot, shown in Fig. 3.51(a). Similar to the AR2 case, the main ring vortices form and move towards the nozzle centreline as they propagate downstream. However formation and flow development is faster for the AR4 case, as the large scale coherent structures undergo an upstream shift of approximately 0.5D, compared to the AR2 V-notched case. Additionally, It can be seen that the cross-stream Reynolds stress component along with the TKE are predominantly influenced by the first set of main ring vortices, which are situated close to the nozzle exit, as shown in Figs 51(d) and (f). From this, the link between the main ring vortices and jet-to-ambient fluid interaction is demonstrated. On the other hand, regions containing high magnitude Reynolds shear stress, extend from the nozzle exit to approximately four jet-diameters downstream with respect to the mean height. It can be therefore said, that regions of high velocity fluctuation exist throughout the measurement window. However the underlying driving factor which causes

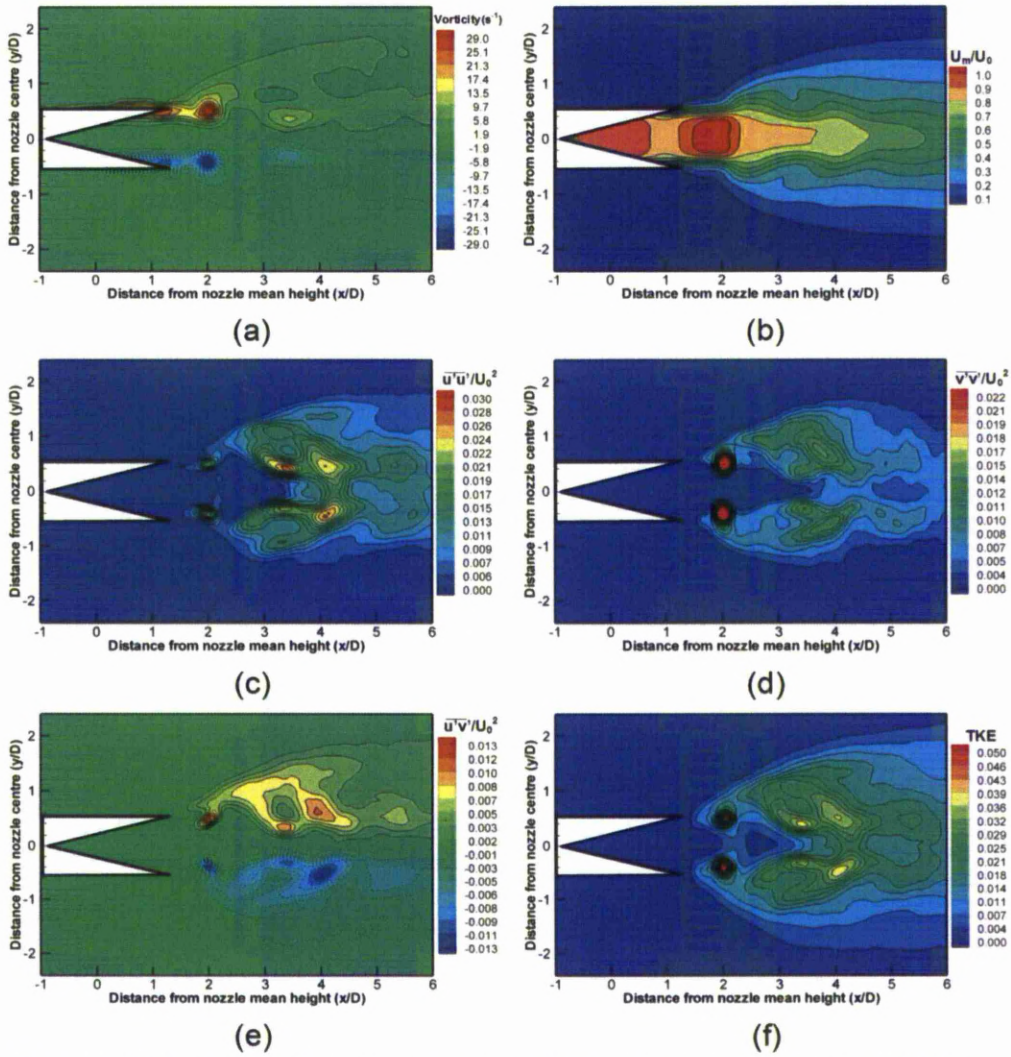

Figure 3.51 Phase averaged PIV results along streamwise direction for AR4 V-notched nozzle, PP view

these fluctuations is still the formation and development of the main ring vortices.

The time-averaged results of the AR4 V-notched nozzle along the PP view are shown in Fig. 3.52. Focusing initially on the velocity contour plot, shown in Fig. 3.52(b), a reduction of the jet potential core is noticed and a favourable spreading along the PP view is observed. The time-averaged vorticity plot is shown in Fig. 3.52(a) and compared to the AR2 case, some differences can be highlighted. Branching of the shear layer is not so obvious for the AR4 case, but some weak forking can nonetheless be detected in the bottom half of the shear layer. Apparently in the AR4 case, the region of influence of the streamwise vortices is not strong or persistent enough to be detected during the experiments. The intense interactions of the PP streamwise vortices with the ambient fluid as well as their rapid viscous dissipation shortly after they are formed, could be responsible for this observation. In contrast, the

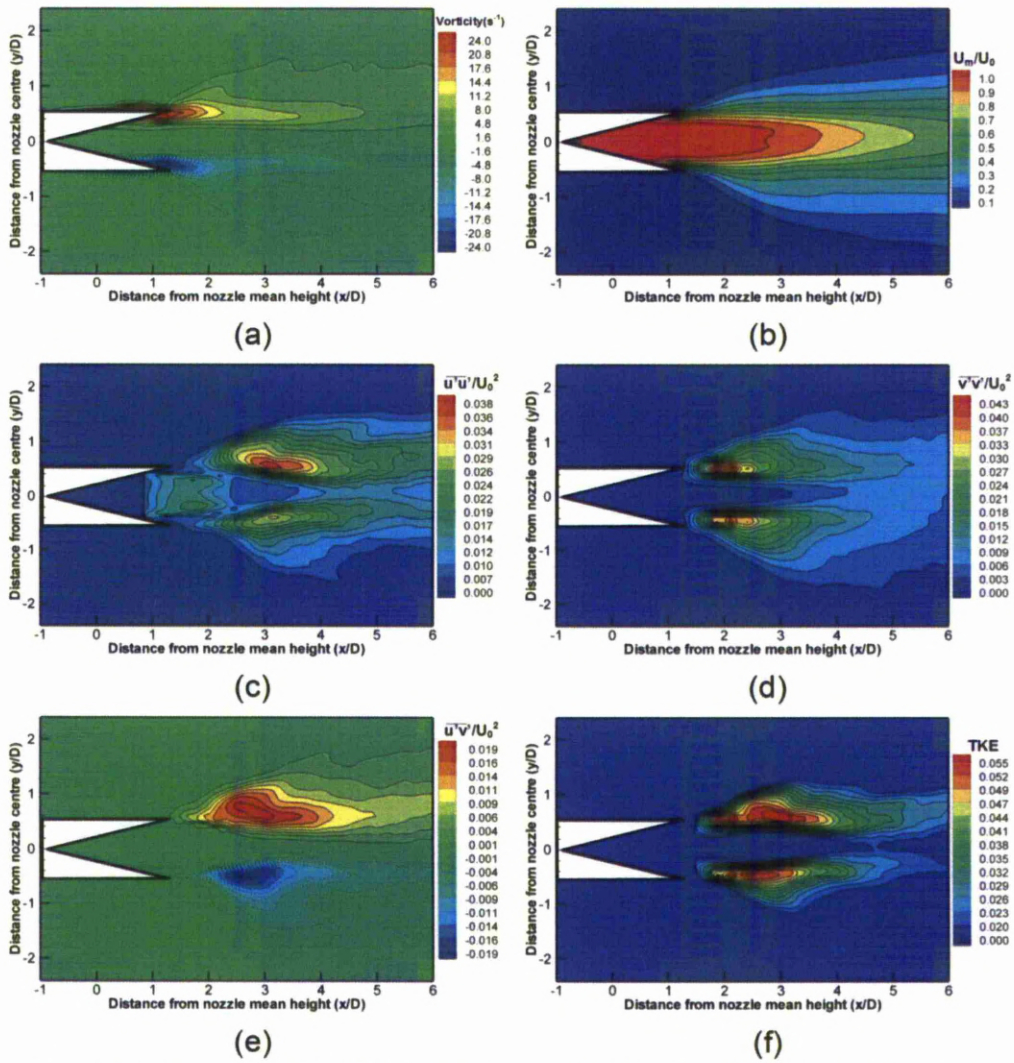

Figure 3.52 Time averaged PIV results along streamwise direction for AR4 V-notched nozzle, PP view

formation and flow developments of PP streamwise vortices is more gradual for the AR2 nozzle, which means that they will leave behind a more persistent trace on the time-averaged results. Interesting differences arise when the two nozzles are compared quantitatively. The vorticity is not affected greatly by the increase in peak aspect-ratio, but a modest 4% increase is achieved. However looking at the flow stresses, it can be seen that both streamwise and Reynolds shear stress components, as well as TKE are reduced substantially as shown in Figs. 3.52(c),(e) and (f) respectively. Additionally, a reduction of approximately 30% is noticed between the maximum measured TKE. These differences infer that the increase in aspect-ratio does not necessarily correspond to an increase in mixing performance of the jet. It can be seen that although large scale structures lose coherency and break down faster when using the AR4 nozzle, an increase in maximum TKE and Reynolds shear stress is not observed as one would expect. The absence of large scale structures must

be the dominant factor for the reduction in interactions between the jet and the ambient fluid, along the PP view.

The phase-averaged results for the AR4 V-notched nozzle along the TT view are presented in Fig. 3.53. Focusing initially on the vorticity plot, it can be seen that the flow structuring is similar to AR2 V-notched case. The main ring vortices form faster along the TT view and as they progress downstream they move laterally away from the nozzle centreline. Similar to the AR2 V-notched case, an interesting feature is observed at approximately three diameters from the nozzle mean height. Secondary vortices are detected close to the nozzle centreline, but how they occur is a question which remains unanswered at the present time. One plausible explanation is that these regions are not vortices but high strain regions, formed due to the increased ambient fluid entrainment by the main ring vortices, which are located on the periphery of the jet. Looking at the normalised velocity plot in Fig. 3.53. (b), the high velocity region ends at x/D=3 which could help accentuate the stain in that particular section of the flow. It can also be seen that the discrepancy between the vortex strengths associated with the peaks and troughs also increases when the nozzle aspect-ratio changes from AR2 to AR4, caused by an increasingly uneven azimuthal vortex strength distribution along the vortex roll-up filaments. This is in agreement with flow visualisation results, where AR4 nozzle leads to more intense vortex formations and interactions, which can be attributed to higher levels of dissimilar self-induced velocities along the vortex filaments. Another explanation could be that these secondary vortices are in fact the braid vortices presented in Fig. 3.30.

Figure 3.54 shows the time-averaged results obtained along the TT view for the AR4 V-notched nozzle. Comparing the jet spreading caused by the troughs between the AR4 and AR2 nozzles, shown in Figs. 3.54(b) and 3.44(b) respectively, it can be seen that the AR2 case produces a larger spread. Thus increasing the trough sharpness does not lead an increase in jet spread, which is detrimental to mixing. In fact, results suggest that as a V-notched nozzle becomes relatively sharper, jet spreads will increase in the near-nozzle region long the PP view but decrease along the TT view. Comparing Figs. 3.54(b) to 3.44(b) also shows the extent of reduction in potential core length when the nozzle sharpness is increased. For instance, the potential core length of the AR2 nozzle is approximately 3.5D, whereas that of the AR4 nozzle is estimated to be 2D. This calculates to approximately 42% reduction in potential core length due to a doubling of the nozzle design aspect ratio. Comparing the flow stress and vorticity magnitudes between the AR2 and AR4 nozzles for the time-averaged results, a different trend to the PP view is shown. The streamwise Reynolds stress component, as well as the Reynolds shear stress are comparable between both nozzles, however a decrease occurs for the cross-stream Reynolds stress component

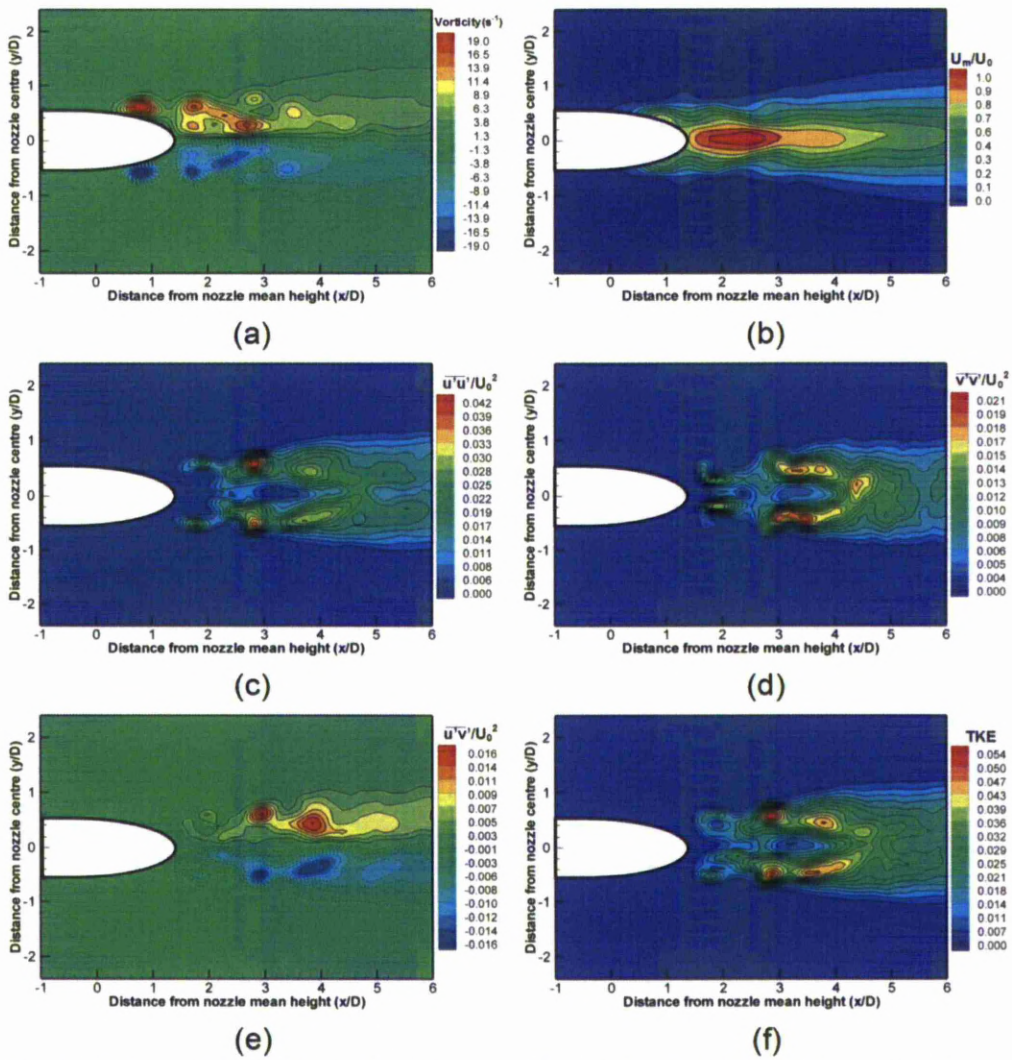

Figure 3.53 Phase averaged PIV results along streamwise direction for AR4 V-notched nozzle, TT view

and for the TKE, are shown in Figs 54(c)-(f) and 44(c)-(f). The reduction was calculated to approximately 25% and 20% respectively, which is lower than the reduction observed along the PP view, for the same increase in nozzle aspect-ratio. Interestingly though, when comparing the maximum vorticity magnitudes, it can be seen that the difference is substantial. The vorticity attained along the TT view, for the AR4 V-notched nozzle is the lowest or all nozzle configurations, indicating that increasing the trough sharpness does not promote more vorticity. This could be attributed to the faster breakdown of the main ring vortices and thus a negative influence on the vorticity magnitude. The vorticity decrease was calculated at approximately 40%.

Finally, comparing time-averaged results along PP and TT views of the AR4 V-notched nozzle, it can be seen that a large difference between the stress and vorticity level exists.

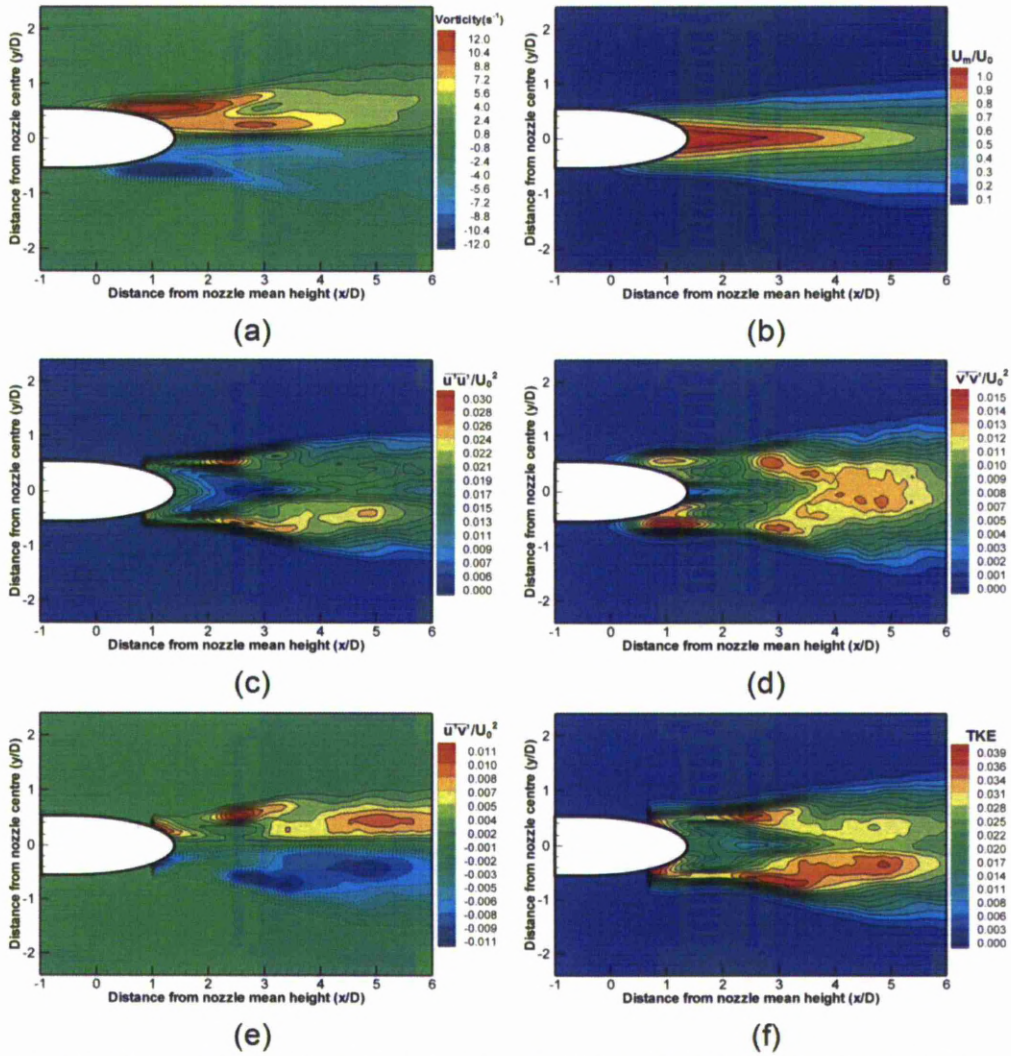

Figure 3.54 Time averaged PIV results along streamwise direction for AR4 V-notched nozzle, TT view

Although it was shown that in most cases both views have reduced stress and vorticity compared to the less sharp AR2 case, differences still exist between the two planes for the AR4 nozzle. Along the TT view vorticity levels as well as TKE and all Reynolds stresses are considerably lower than along the PP view. Vorticity is reduced by 50%, while the largest Reynolds stress decrease was found along the cross-stream component and was calculated to approximately 65%. Due to the particular nozzle design, a dissimilar induced velocity distribution exists between the two views of the jet. This shows that the peaks, once again, enhance flow interactions especially in the near-nozzle region, which could possibly benefit jet mixing. Ultimately, flow stress distributions may be suitably manipulated by controlling the vortex-bending behaviour, which in turn is dependent on the aspect ratio of the nozzles.

e) Influence of nozzle sharpness along cross-stream planes

A-notched geometry

Figures 3.55 and 3.56 show phase- and time-averaged results for the AR4 A-notched nozzle, along several cross-stream planes. Focusing initially on the phase-averaged results it can be seen that the cross-stream structures are more discernible compared to the less sharp AR2 A-notched case. Specifically, when looking at the vorticity plot, shown in Fig. 3.55(b), it can be seen that the streamwise vortices initiate at x/D=2 and maintain the same rotational sense as the AR2 case, but reduce in magnitude. Similar to what was observed with results along the streamwise direction, almost all measure flow parameters decrease as the nozzle aspect-ratio increases. Interestingly though, comparing the cross-stream Reynolds component along the v-direction, as shown in Figs. 3.39(d) and 3.55(d), it can be seen that the AR4 case achieves an increase of approximately 38%.This indicates an increase in trough sharpness is more beneficial to flow mixing than an increase to peak sharpness, especially in the near-nozzle region of the jet.

The time-averaged results of the AR4 A-notched nozzle are presented in Fig. 3.56. Similar to the phase-averaged results presented before the formation of streamwise vorticity is observed at x/D=2. This shows that the particular occurrence is not transient in nature and does not depend on the particular pulsing phase. After their formation, the streamwise vortices dissipate and loose coherency and strength rapidly, as they are not easily discerned in the next measurement plane (x/D=3). The rotational sense of the streamwise vortices and bent main ring vortices is consistent with the flow representation shown in Fig. 3.29(a) and 3.30. Two outward-spreading pairs of streamwise vortices are formed along the PP plane of the nozzle, while the four inner vortices measured by the PIV system correspond to the bent main ring vortex. As shown in the flow representation, the main ring vortex bends towards the downstream direction when viewed along the PP view, and thus when viewed in cross-section forms four distinct vortices. The rotational sense of these four vortices is consistent with the cross-stream PIV measurement. Increasing the nozzle aspect-ratio does not promote vorticity intensification and thus time-averaged vorticity magnitudes for AR2 and AR4 A-notched nozzles are comparable. Similarly, high magnitude Reynolds stresses regions mostly appear at the x/D=2 plane and differences between peak and trough locations are marginal. High TKE values are concentrated within the periphery of the jet (shear layer) and extend throughout the measurement window. Comparing time-averaged results between PP and TT planes, no preferable spreading is noticed.

V-notched geometry

Out of all test nozzles, the AR4 V-notched nozzle shows the best formation of streamwise structures, as shown in Fig. 3.57. Both the bent main ring vortex and streamwise vortices are clearly shown in phase- and time-averaged results. The results presented in this section agree

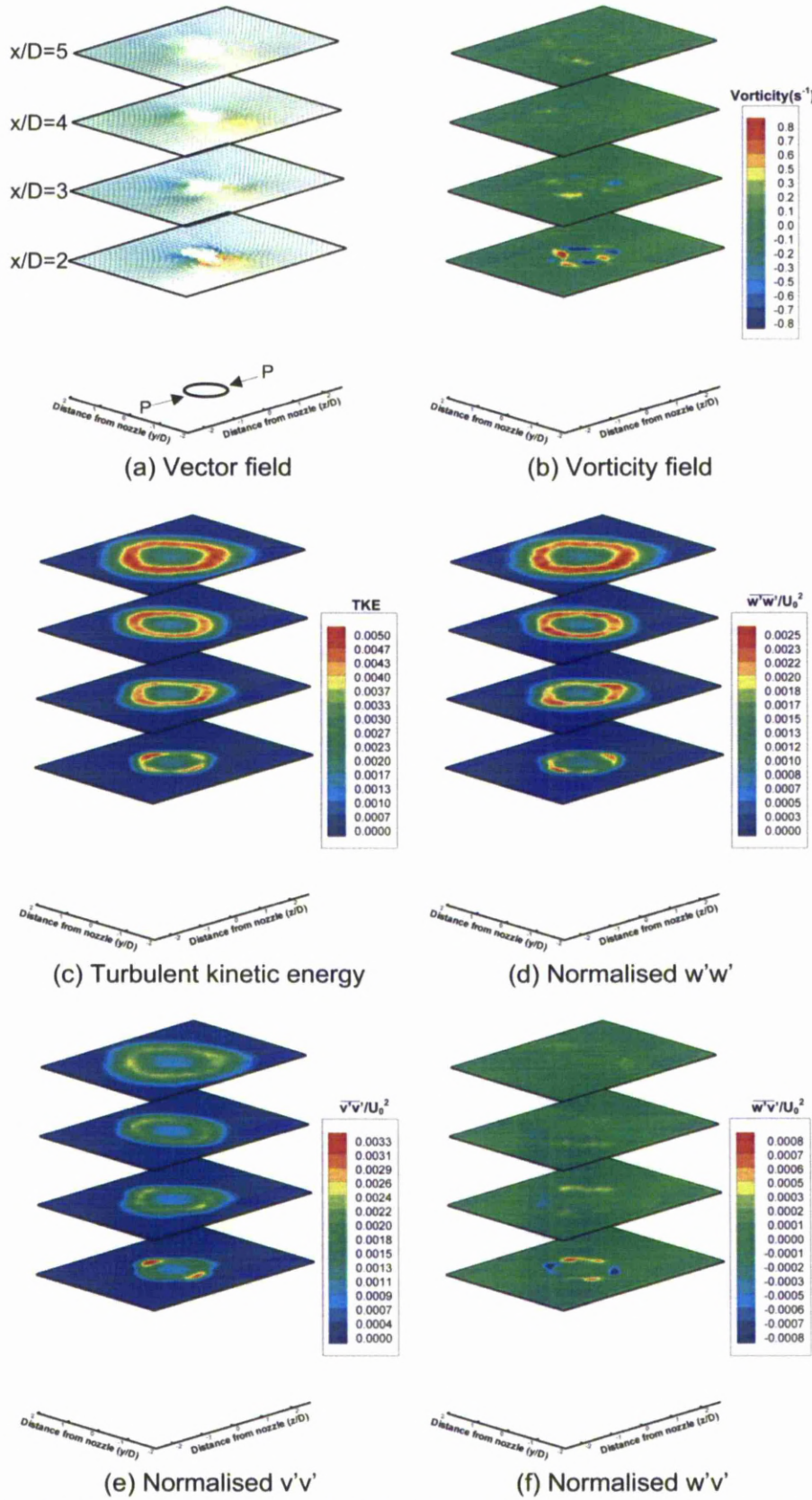

Figure 3.55 Phase averaged PIV results along cross-stream direction for AR4 A-notched nozzle

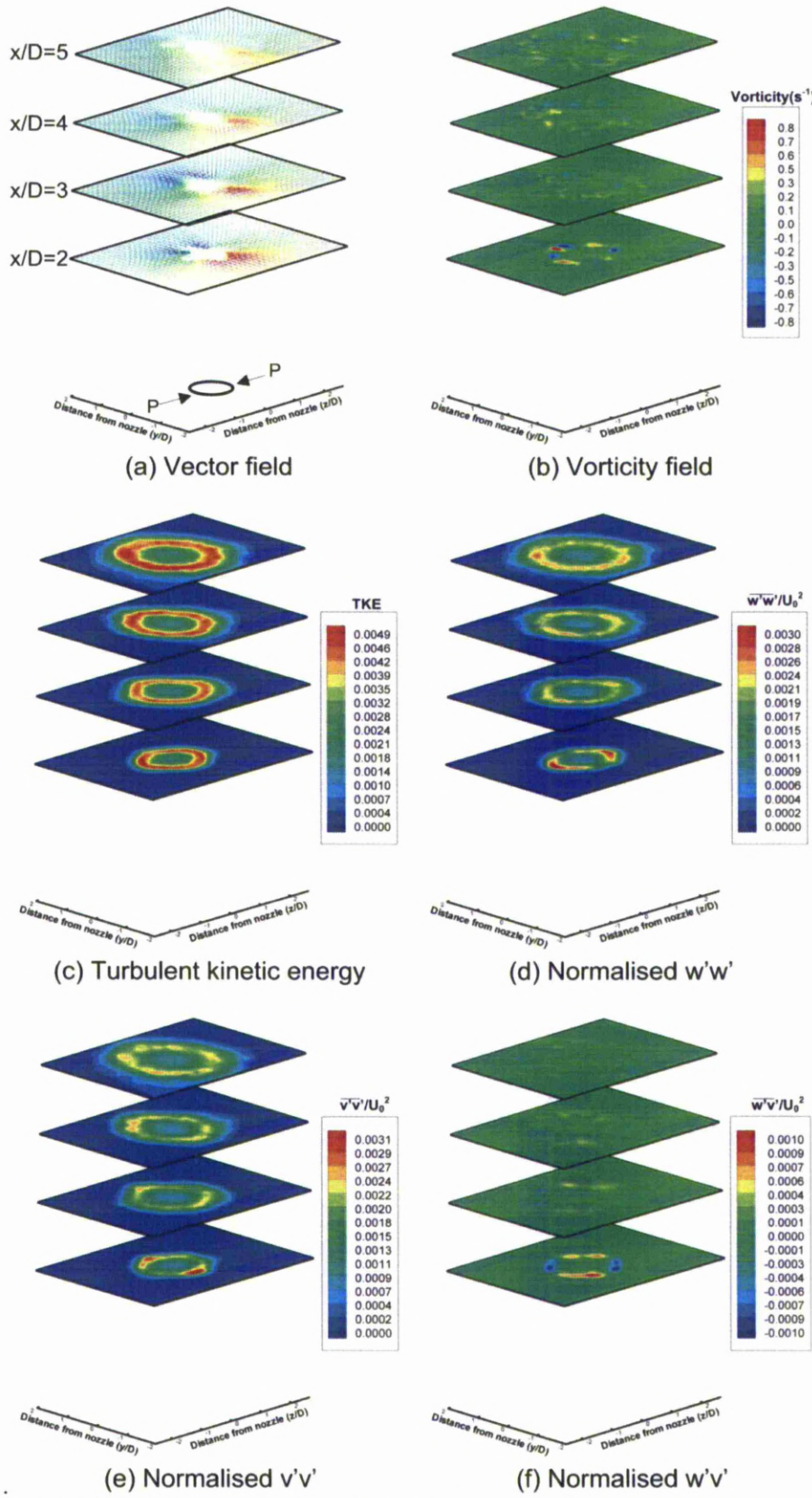

Figure 3.56 Time averaged PIV results along cross-stream direction for AR4 A-notched nozzle

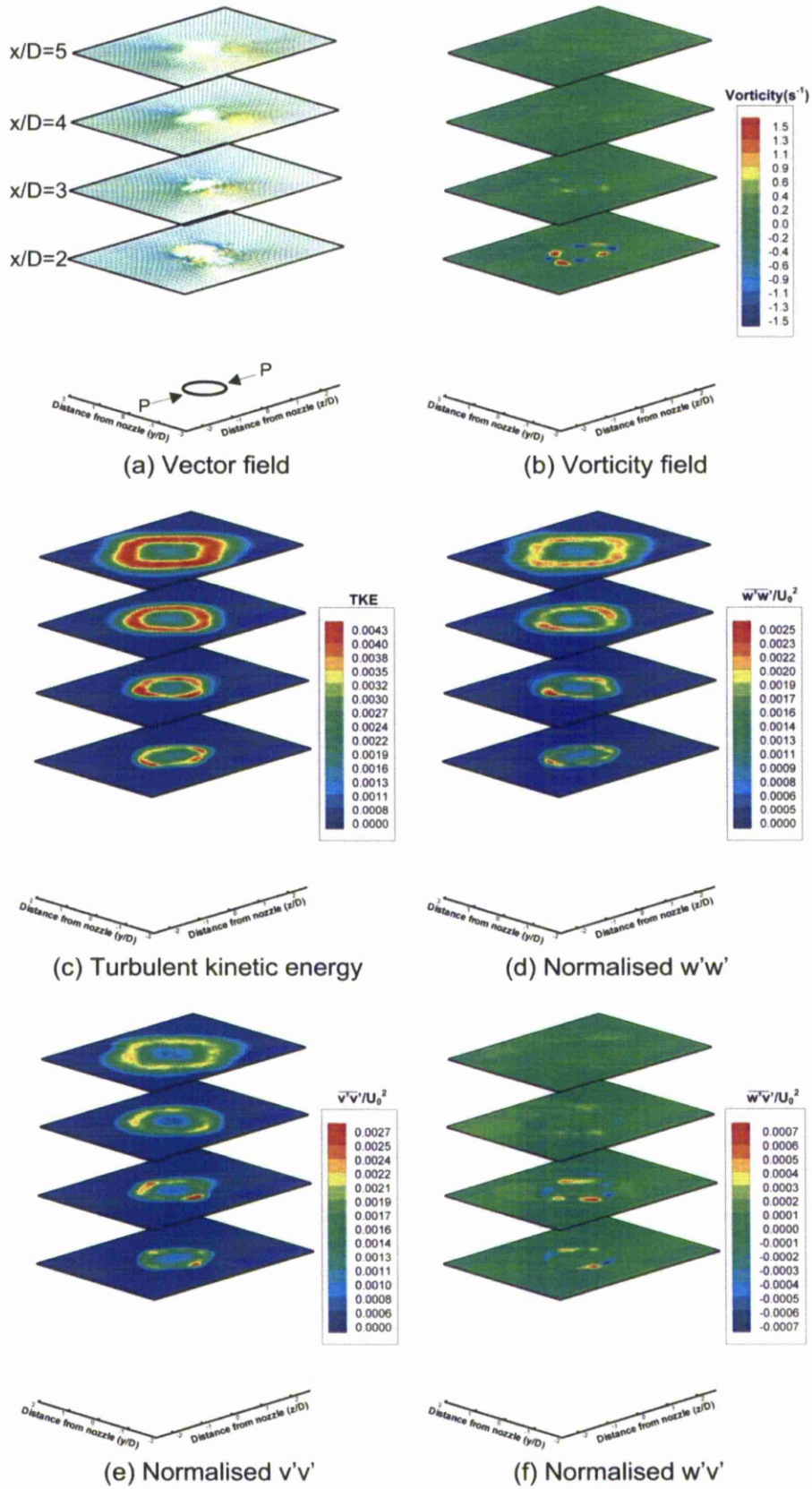

Figure 3.57 Phase averaged PIV results along cross-stream direction for AR4 V-notched nozzle

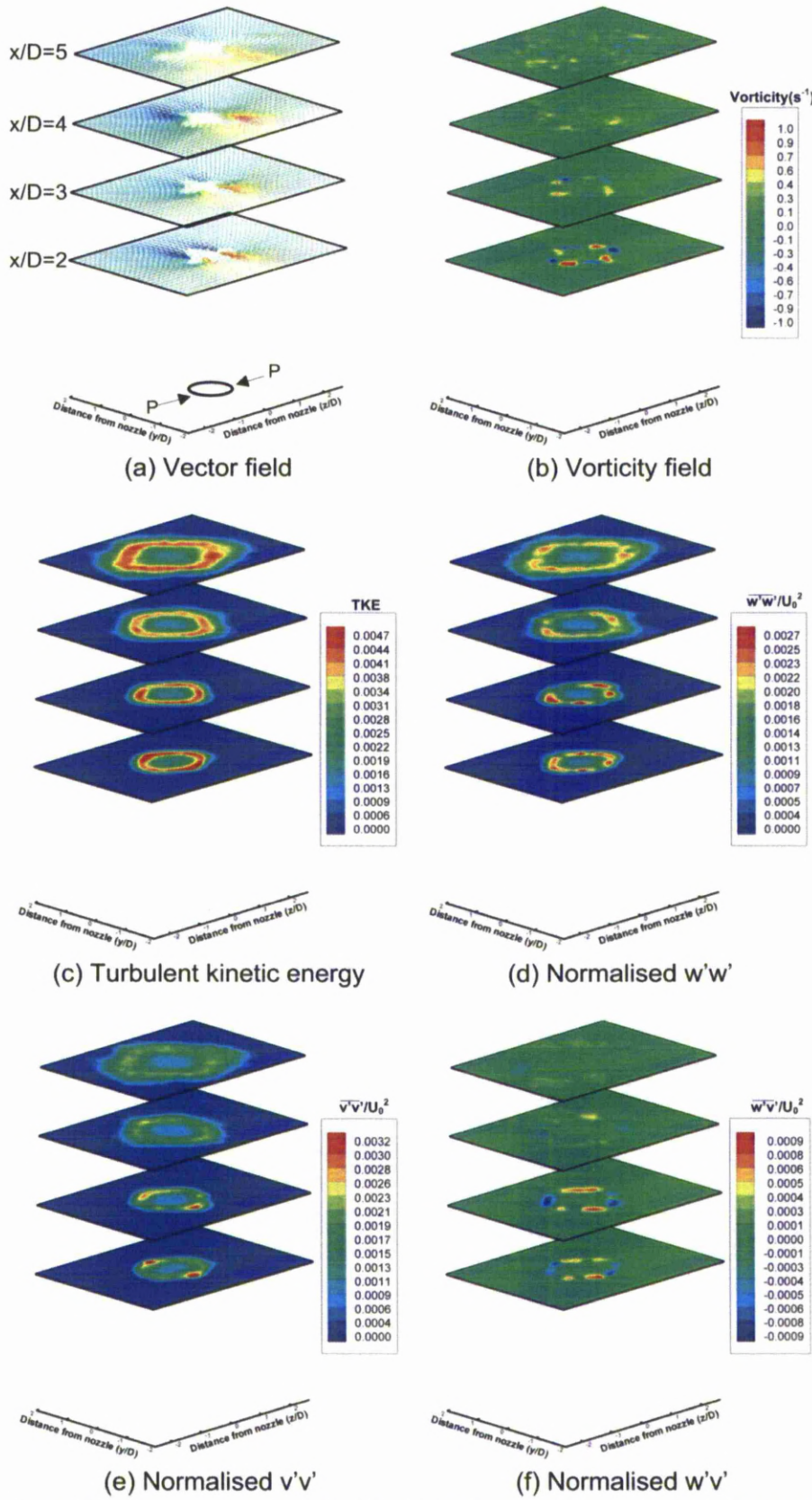

Figure 3.58 Time averaged PIV results along cross-stream direction for AR4 V-notched nozzle

well with the cross-stream LIF flow visualisation results presented earlier. Comparing between the two nozzles, the AR4 nozzle produces stronger streamwise vortices that those associated with the AR2 nozzle during the early formation stages. The Reynolds cross-stream stress component along the w-direction shows that the influence of the peaks is detected throughout the measurement window, as shown in Fig 3.57(d), while the high magnitude Reynolds cross-stream stress component along the v-direction manifests at x/D=2 and 3. Additionally, the regions of high TKE indicate a favourable spreading along the PP plane, shown in Fig. 3.57(c). Therefore in contrast to the A-notched design, the smooth peaks outperform the sharp troughs even at high aspect-ratios.

The time-averaged results agree well with the phase-averaged results. Focusing on the phase-averaged vorticity plot in Fig. 3.58(b), the clear formation of streamwise vortices is evident, which agrees well with flow visualisation results along both streamwise and especially cross-stream results, presented earlier. The two pairs of outward flowing streamwise vortices are located on the periphery of the jet along the PP plane. This is

consistent with the cross-stream LIF visualisation results in which streamwise vortices formed and moved radialy outward along the same plane. As the main ring vortex bends towards the downstream direction (along PP view), it causes the formation of four inner vortices. This flow behaviour is expected and the cross-stream rotational sense of both streamwise vortices and bent main ring vortices is consistent with the flow representations shown in Figs. 3.29(b) and 3.30. Independent of nozzle aspect-ratio, the underlying vortex dynamics associated with the V-notch geometry are similar. Finally, comparing the vorticity values between the A-notched and V-notched nozzles it can be seen that the latter case achieves the best results.

3.2.4 Half jet-width and momentum thickness

In the following section the half jet-width and momentum thickness calculated for the A- and V-notched nozzles are analysed. In all plots the time-averaged results were used. Figs. 3.59(a) and 3.59(b) show the half jet-width and momentum thickness associated with the A-notched nozzles, while Figs. 3.60(a) and 3.60(b) present the results associated to the V-notched nozzles. All AR4 data plotting starts at x/D=1 to avoid erroneous data from being presented. Data upstream of x/D=1will contain errors due to the presence of the nozzle in the measurement area. Blue coloured points were used to represent the less sharp AR2 case, while red points represent the AR4 geometry. Filled points show measurements along the PP-plane, while empty points were used for the TT-plane results. To assist the reader, this colour-scheme is consistent for all plots.

a) A-notched geometry

Focusing on the half jet-width initially, in Fig. 3.59(a), it can be seen that the TT-plane is initially wider that the PP-plane for both AR2 and AR4 nozzles. There are two regions however in the AR2 case, where the PP-plane half jet-width is larger than the TT-plane; namely between x/D=1.7 to 2.4 and most importantly from x/D=4.6 to the end of the measurement window. This distinct crossover point at which the half jet-width profiles along the PP- and TT-planes intersect resembles the axis-switching phenomenon found in noncircular jets. These findings show that the jet body of the A-notched nozzle does not diverge in an axi-symmetric manner similar to the reference case, but changes shape from circular to elliptic along its length. Initially the longer axis of the jet cross-section is aligned along the TT-plane, but after x/D=4.6 the jet body changes shape and the longer axis of the jet cross-section is then aligned along the PP-plane. The jet body cross-section remains elongated along the PP-plane up to the end of the measurement window. The AR4 A-notched nozzle follows the same characteristic axis switching behaviour, but does so in a faster manner. The cross over point is further upstream at approximately x/D=4. Interestingly though, the AR4 nozzle leads to smaller half jet-width after the crossover point as compared to the AR2 nozzle.

Similar to what was noticed for the half jet-width, the momentum thickness associated with the TT-plane in the vicinity of the nozzle exit, is initially greater when compared to the PP-plane. However the momentum thickness of the A-notched nozzle, regardless of orientation and aspect ratio is greater throughout the measurement window when compared to the reference case. As the jet progresses downstream the momentum thickness along the PP-plane grows faster and thus another crossover point exists. For the AR2 nozzle, the crossover occurs at x/D=1.4, whereas for the AR4 nozzle, it occurs at approximately x/D=1.7. Again faster flow development is associated with the sharper AR4 case. It is interesting, that in the latter stages of the flow development (x/D=2.3 onwards) the AR4 nozzle results in a smaller momentum thickness along the PP-plane when compared to the

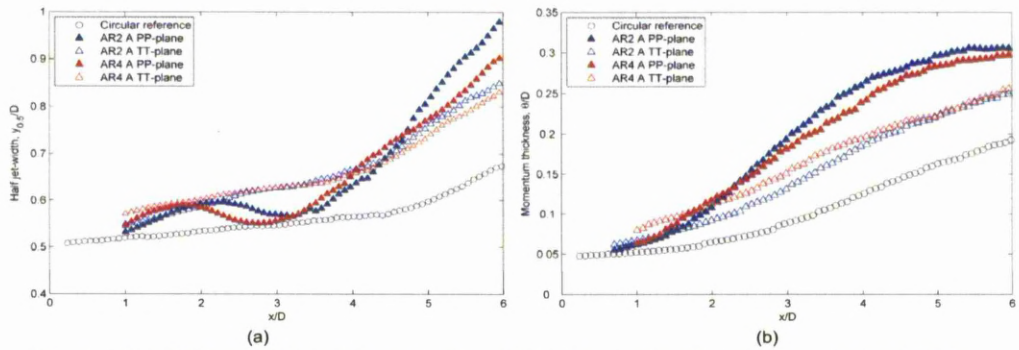

Figure 3.59 Half jet-width (a) and momentum thickness (b) profiles for reference, AR2 and AR4 A-notched nozzles along PP- and TT-planes

AR2. The growth rate of the momentum thickness especially along the PP-planes of both notched A-notched nozzles can be observed to be gradually reduced with increase in the streamwise distance. For the TT-plane, although the AR4 nozzle is initially larger in the vicinity of the nozzle, as downstream distance increases both nozzles seem to converge and from x/D=5 onwards the nozzles have the same thickness.

Increasing the aspect ratio promotes faster flow development but does not increase the mixing. Effectively an upstream shift of the AR2 graphs occurs. An AR2 A-notched nozzle should therefore be preferred over the reference and AR4 A-notched in applications where mixing is important, thus saving costs by the use of less material.

b) V-notched geometry

Some interesting conclusions can be drawn when studying the V-notched results in Figs. 3.60(a) and 3.60(b). Initially Half jet-width and momentum thickness along TT-plane is higher for both nozzles, similar to A-notched case. The half jet-width crossover point for the AR2 nozzle is at x/D=2. Indications of a second cross-over point at the end of the measurement window can be inferred for the AR2 V-notched nozzle, showing that the axis-switching mechanism is quite robust. After x/D=4 PP- and TT-plane half jet-widths converge and by x/D=6 the half jet-width difference between the PP and TT-plane is very small which leads to the conclusion of a near circular jet body cross-section. This behaviour is different from the rest of the A and V-notched nozzles. The particular nozzle could be suited for an application where axis-switching is required through the whole length of the measurement window.

As the nozzle sharpness is increased to AR4, an upstream shift in the plots is present. The crossover point moves upstream to approximately x/D=1.4, which indicates stronger vortex dynamics and faster flow evolution. However a second crossover point is not detected for the AR4 case. After the crossover point, the TT-plane half jet-width remains substantially lower that the PP-plane and at its local minimum point it is below the circular reference case. The range within which the TT-plane half jet-width is thinner than the reference case is approximately between x/D=2.5 and 3.3. At the end of the measurement window an asymmetric jet body cross-section with elongated sides along the PP-plane can be expected.

Regardless of aspect ratio, there is a distinct trend regarding the initial momentum thickness profiles. For both nozzles, the initial (x/D=1) momentum thickness along the TT-plane is substantially higher than for the PP-plane. However, the effect of the peaks on the flow field become clearly visible shortly after and the growth rate of the PP-plane surpasses the rate of the TT-plane. Inevitably as crossover point exists. The sharper nozzle reaches this crossover point further upstream than its less sharp counterpart which fits well with the findings

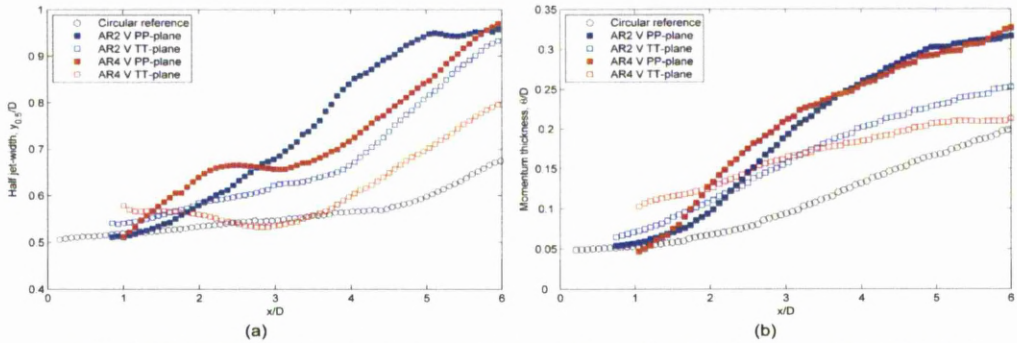

Figure 3.60 Half jet-width (a) and momentum thickness (b) profiles for reference, AR2 and AR4 V-notched nozzles along PP- and TT-planes

presented throughout this chapter. Faster flow activity associated with the sharper nozzle is similar to what was seen for the A-notched nozzle. The crossover point for the AR2 case is found at x/D=2.4, while for the AR4 case the crossover point is situated at x/D=1.9. However similar to the A-notched case, increasing the nozzle aspect ratio does not result in an increase of jet mixing. Focusing at the end of the measurement window in Fig. 3.60(b), the momentum thickness of both nozzles along the PP-plane is comparable, while along the TT-plane, the momentum thickness of the sharper nozzle is drastically reduced. This shows that the sharp nozzle results in a thinner momentum thickness. Another interesting point is that, although the initial momentum thickness of the sharper AR4 nozzle along the TT-plane is higher than the AR2 case, at the end of the measurement window the momentum thickness of the sharper nozzle is reduced to the extent where it can be comparable to the reference case. Clearly an increase in aspect ratio of the V-notched nozzle is not beneficial to jet mixing.

3.3 Chapter summary and conclusions

Throughout this chapter, the notion that circular IO nozzles can produce jets with elliptic attributes has been supported. With systematic placement of peaks and troughs around the periphery of the nozzle, axis-switching, which is a fundamental behaviour in elliptic jets, can be achieved and manipulated. Understanding and controlling axis-switching is interesting for scientific purposes as well as beneficial in applications where flow control and jet mixing are important. Manipulation of the axis-switching phenomenon opens up another set of parameters when designing a nozzle for a particular application. It has been shown that elliptic jets increase entrainment compared to axi-symmetric jets (Ho and Gutmark, 1987), thus controlling the cross-sectional shape of the jet body could be beneficial to applications such as injectors for internal combustion engines or cooling jets in a manufacturing plant. In applications where high mixing is required, out of all configurations, the AR2 notched nozzles should be chosen. Apart from better performance, the manufacturing cost of an AR2

nozzle would also be less. If however a nozzle is intended for use in a particular application where the jet temperature is elevated, such as an aeroengine nozzle, between the A- and V-notched nozzles, the latter should be chosen. The higher surface area at the peak location should reduce the thermal concentration and increase creep resistance and the life cycle of the component.

4 FLOW CHARACTERISTICS OF V-NOTCHED ELLIPTIC NOZZLES[2,3]

4.1 Chapter overview

In this section, the results associated with the IO elliptic nozzles will be presented. The purpose of this study is to combine IO principles into elliptic nozzles and to investigate the influence of nozzle lip-modifications on the resultant elliptic jet behaviour and comment on the influence made to the axis-switching behaviour of the jet.

Consistent with the layout of the previous chapter, flow visualisation results will be presented first, followed by quantitative PIV results. This chapter is split into sections to assist the reader and promote a better understanding of the differences between each configuration. The first section will consist of blue dye visualisation followed by LIF along streamwise and cross-stream directions. The second and third sections will delve into the quantitative aspect of the testing. Specifically, in the second section, PIV measurements along streamwise and cross-stream directions will be presented, while finally in the third, half jet-width and momentum thickness parameters will be discussed.

4.2 Results and discussion

4.2.1 Flow visualisation

a) Shear layer visualisation technique

Figures 4.1 and 4.2 highlight the evolution of the elliptic jet issued from the reference nozzle, along both major- and minor-planes respectively. Nozzle geometries similar to the reference case have been studied and documented extensively in the past and the associated flow fields have been explained (Oshima, 1972; Dhanak and Debernardinis, 1981; Ho and Gutmark, 1987; Morris, 1988). However for the sake of completeness, the flow field and vortex dynamics will be explained briefly. Along the major-plane, the main ring vortex rolls up and has the tendency to bend towards the downstream location, as shown in Fig. 4.1. This bending has been shown to deform the jet and effectively change the jet cross-section with respect to the downstream distance. When viewing the jet along the minor-plane, the

[2] Sections of this chapter were accepted and presented at the 39th AIAA Fluid Dynamics Conference, San Antonio, USA, 22-25 June, 2009

[3] Sections of this chapter have been accepted and will be presented at the 15th International Symposium on Application of Lasers Techniques to Fluid Mechanics, Lisbon, Portugal, 05-08 July, 2010

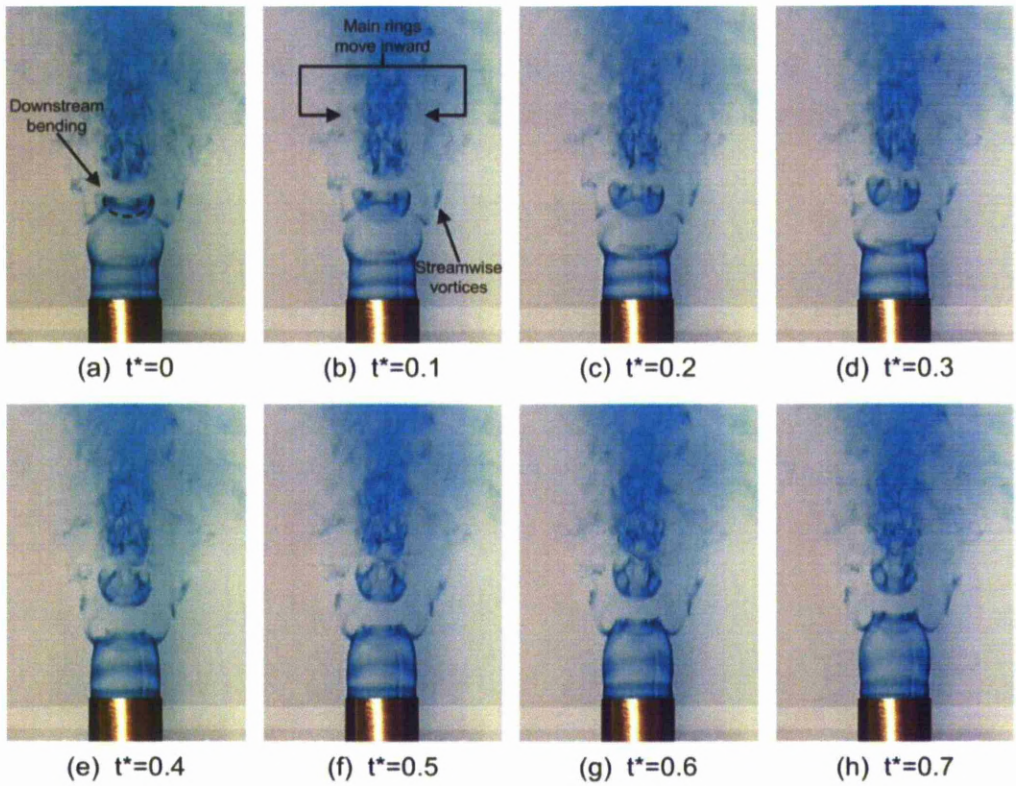

Figure 4.1 Flow visualisation of elliptic reference nozzle, major plane view

opposite effect is obvious, as shown in Fig. 4.2; the main ring vortices bend, but do so towards the upstream direction. Apart from main ring vortex bending, movement of the vortex cores is also evident. Along the major plane, the jet converges with the main ring vortices moving towards the nozzle centreline, while along the minor plane, the jet diverges with the main ring vortices moving away from the nozzle centreline ((Oshima, 1972; Dhanak and Debernardinis, 1981; Husain and Hussain, 1983). This behaviour leads to what is called axis-switching, and is responsible for the unique and inherent flow field produced by elliptic nozzles of moderate aspect ratio such as the ones being tested here. The important question is what causes the main ring vortices to bend in the first place. This was addressed by Arms and Hama (1965) who used the local induction approximation (LIA) and it was attributed to the geometric form of the main ring vortices. The main ring vortices issued from elliptic rings follow the nozzle lip contour and thus do not have a constant curvature. This difference in curvature is related to the self-induced velocity of the main ring vortex section. Curvatures with smaller radii move faster than curvatures with larger radii and thus the end sections of the main ring vortices in Fig. 4.1 move faster downstream than the rest of the vortex. This is also apparent in Fig. 4.2 where the middle section of the ring vortex, which has the smaller radius, moves downstream faster, thus causing the bending of the

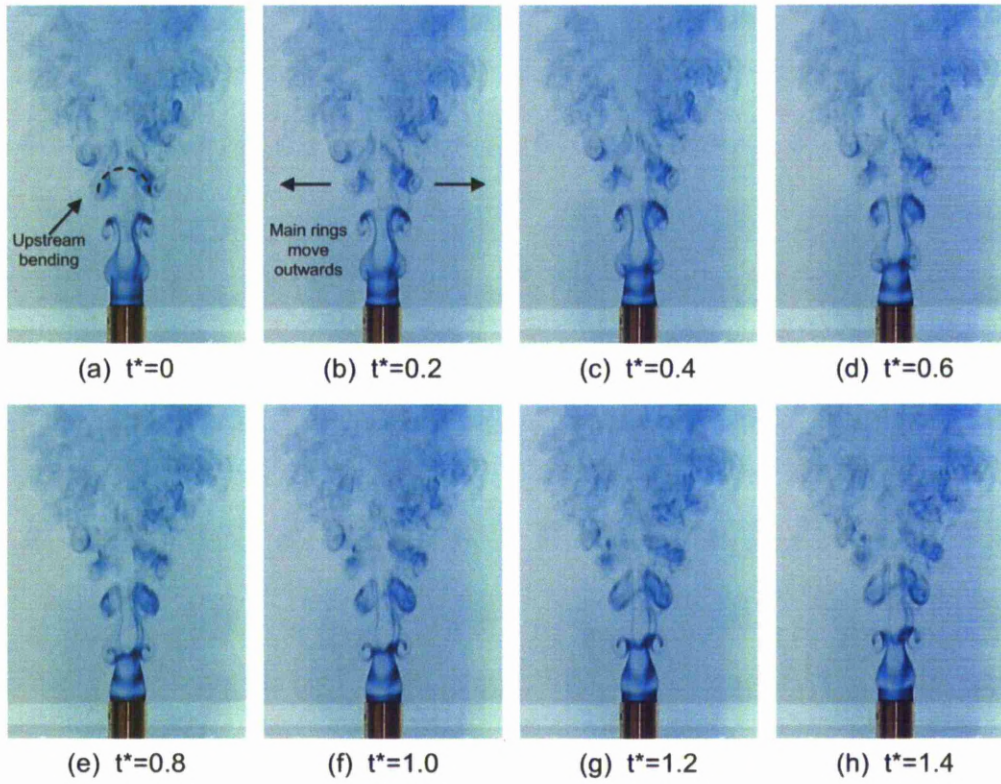

Figure 4.2 Flow visualisation of elliptic reference nozzle, minor plane view

filament. Studying the flow field from both planes it can be seen, in a purely visual and qualitative sense, that the jet undergoes axis-switching only once within the viewing window. After the axis-switching point, viscous effects become more dominant than the main ring vortex dynamics and break the coherent structures down into smaller, less-organised eddies which cannot be resolved in this study.

Figures 4.3 and 4.4 show the flow visualisation results for the 120° V-major nozzle along the major and minor planes respectively. Compared to the reference case, the flow field is more intense. The main ring vortices can be detected, but transit to turbulence much faster. Mixing between the jet and the surrounding ambient fluid as well as jet-spreading will be augmented due to the generation of streamwise vortices located at the nozzle peaks. Along the major plane, shown in Fig. 4.3, the flow development is quite different to the reference case. The V-shaped notch causes the formation of visually small streamwise vortices at both peak and trough locations. Another effect of the notches is that the main ring vortices follow the nozzle contour as they form and thus appear pre-bent in the direction of the notch (downstream). As the ring propagates downstream, the bending becomes greater but not to the extent seen for the reference case. The reason behind the limited amount of bending is due to the instability of the vortex ring which losses coherency due to pairing, as shown in

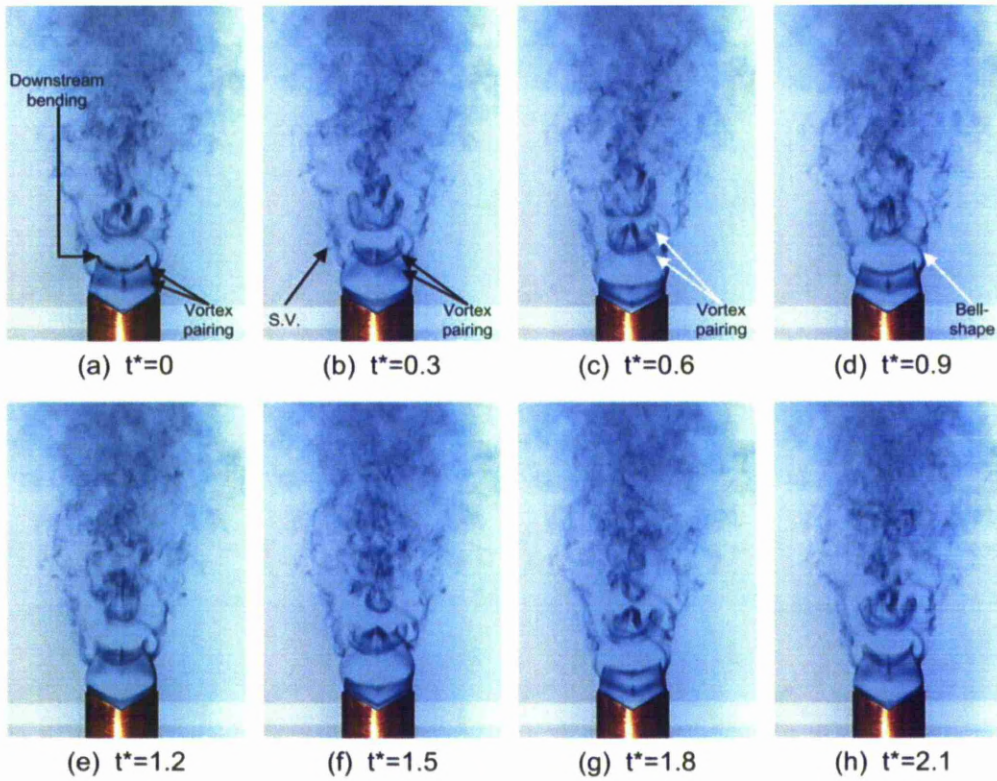

Figure 4.3 Flow visualisation of 120° V-major nozzle, major plane view

Fig. 4.3. When observing the flow sequence carefully, vortex pairing can be detected in Figs. 4.3(a)-(c). As the filament pair is formed and propagates downstream, the first filament starts to roll-up as expected. The second filament which follows, is entrained through the first one (where first and second refers to the formation of the filaments in a temporal and not a spatial frame of reference) forming a distinct "bell-shaped" pattern. The pairing effects are twofold; in the first case, main vortex ring development is restricted and loss of coherency is increased, while in the second instance, the rotation imposed to the second filament, due to entrainment from the first, causes sections of it to align with the nozzle centreline thus causing the formation of streamwise vortices. These structures are similar to the "rib-structures" described by Hussain and Husain (1989). Streamwise vortices improve the momentum exchange between the jet and the surrounding ambient fluid (Longmire *et al.*, 1992a). An observation worth mentioning can be made when comparing the flow field along major-axis plane of the reference to the 120° V-major nozzle, shown in Figs. 4.1 and 4.3 respectively. Visually, the jet spread of the 120° V-major nozzle is seen to increase, opposite to the traditional axis-switching behaviour of an elliptic jet along the major-axis plane. This behaviour is similar to what Zaman (1996) found when using a rectangular nozzle with tabs situated along the long side of the nozzle that protruded into the flow. In his study, it was

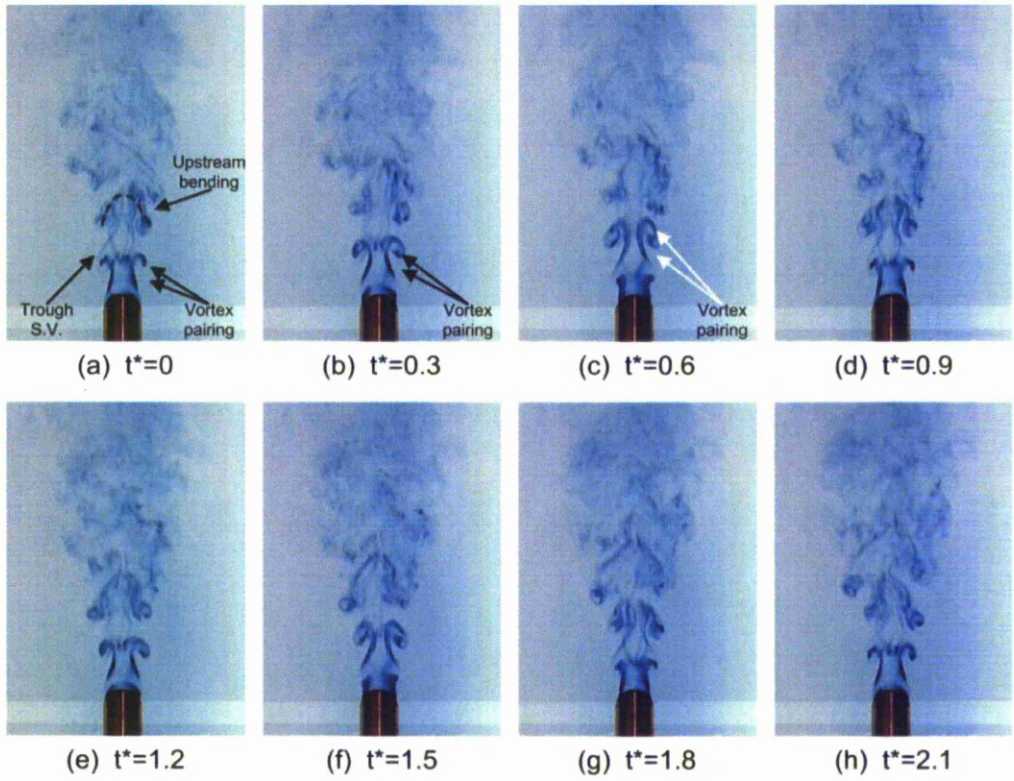

Figure 4.4 Flow visualisation of 120° V-major nozzle, minor plane view

shown that the re-distribution of streamwise vortices, when in a favourable rotational sense, can disrupt axis-switching. Effectively, the azimuthal and streamwise dynamics cancelled each other out and it was documented that the jet continued to diverge along the major-axis.

Along the minor view, the flow field is not significantly different to the reference case, as show in Fig. 4.4. The main ring bending orientation is toward the upstream direction and movement away from the nozzle centreline is apparent, however the main vortices break-down faster. Effects of the pairing mechanism, that was explained earlier, are evident in the time sequence Figs. 4.4(a) to (c). The entrainment and stretching of the centre portion of the filament is clear although unfortunately the minor-plane view does not elucidate the vortex dynamics any further. The influence of the sharp-trough streamwise vortices on the jet-spread cannot be detected, probably due to the large V-notch included angle used which produced subtle geometric differences when compared to the reference nozzle.

Figures 4.5 and 4.6 show time-sequenced images showing the evolution of the main flow structures associated with the 120 V-minor nozzle along both major and minor planes respectively. Comparing the present flow fields to the ones presented earlier, less turbulent features emerge. The main ring vortices remain coherent further downstream and movement

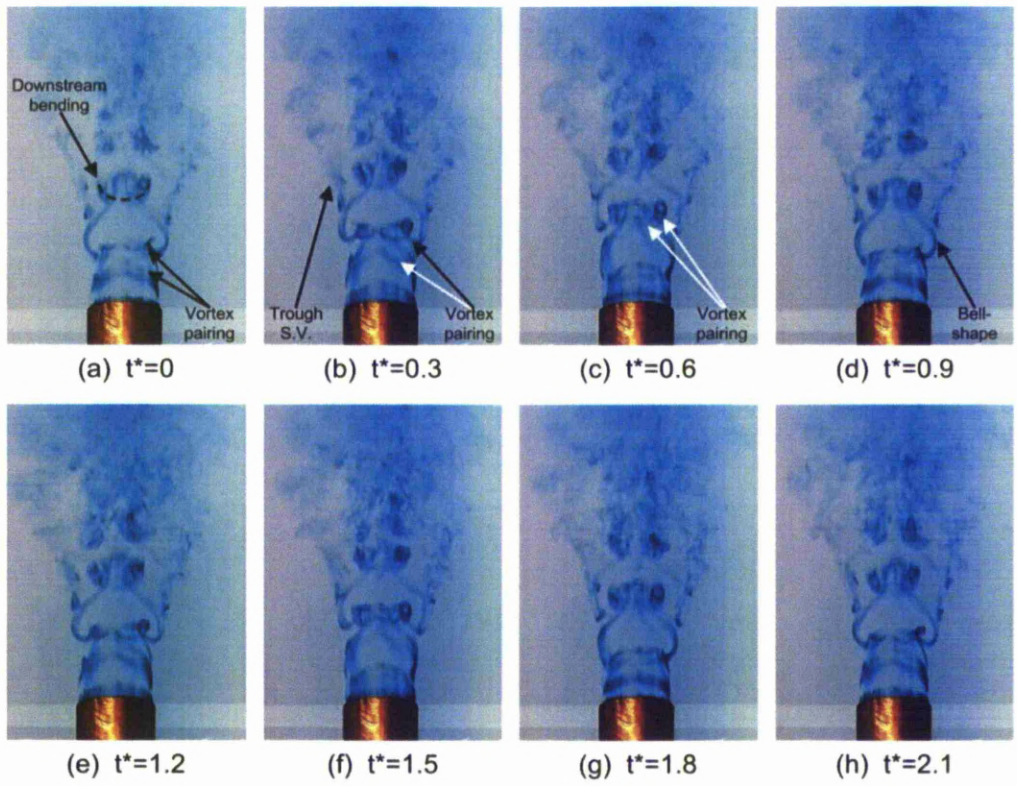

Figure 4.5 Flow visualisation of 120° V-minor nozzle, major plane view

of the vortex cores coincides with that associated to the reference case. Due to the less turbulent nature of the flow, reduced interactions between the jet and the surrounding fluid can be expected from this nozzle, as well as a potential core that extends further downstream than the 120 V-major case. Axis-switching appears to be present, since along the major plane, main ring vortices move towards the nozzle centreline, while along the minor plane the vortex cores move away from the nozzle centreline, thus increasing the jet-spread. However, compared to the reference case, a slight delay in the movement of the main ring vortices is present, thus delaying axis-switching. Interestingly, the ring vortices undergo bending toward the downstream direction by a reduced amount when viewed along the major plane, while along the minor plane the ring vortices bend by a similar amount and in similar direction to the reference case. "Bell-shaped" structures which help produce streamwise-oriented vortices are evident in Fig. 4.5. Similar to the 120 V-major nozzle, between successive rollups, within the braid region of the jet, fluid gets entrained and accelerated towards the downstream direction. This fluid entrainment process is helped by the movement of the main ring vortices. As the main ring vortices move towards the nozzle centreline any fluid being entrained will be accelerated due to the higher shear rate between

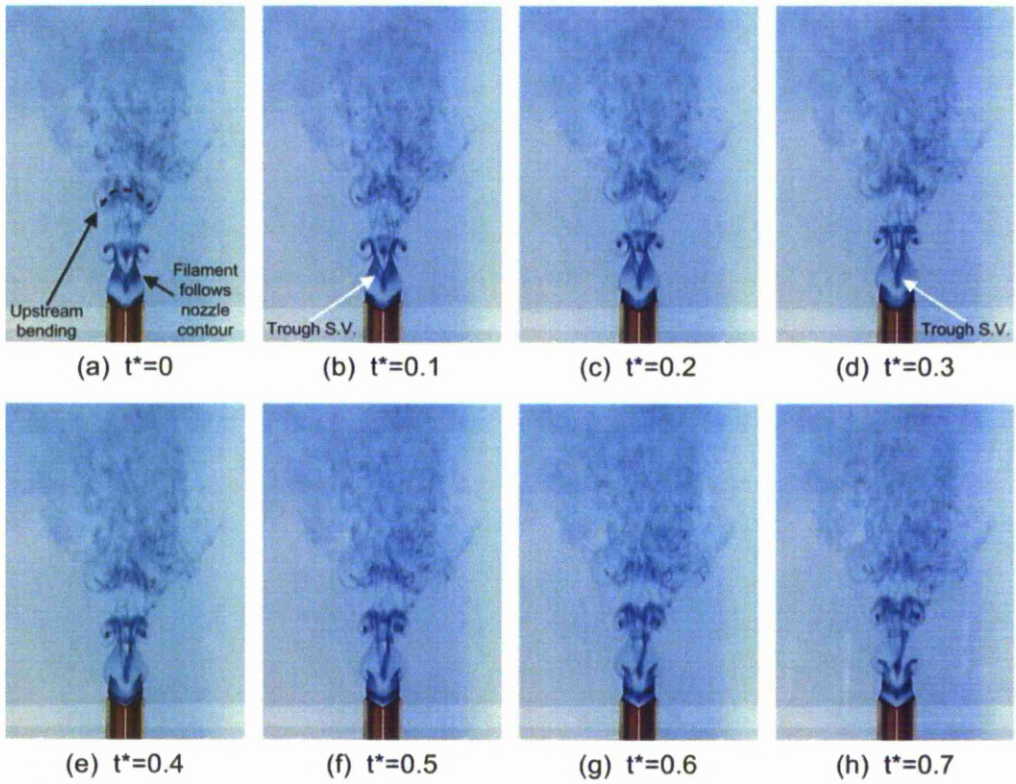

Figure 4.6 Flow visualisation of 120° V-minor nozzle, minor plane view

the vortex cores. As a result, stretching occurs within the braid region of the jet, between successive rollups (Liepmann and Gharib, 1992).

Finally, effects of the sharp troughs are visible along the minor plane, shown in Fig. 4.6. As the main ring filament exits the nozzle, it follows the nozzle contour. The distinct discontinuity found at the trough causes a "kink" in the filament as it propagates downstream. Due to the orientation of the V-notched cut portions of the filament are rotated and aligned with the nozzle centreline, thus creating visually weak streamwise vortices. The smooth peaks do not seem to influence the flow field in the same way and streamwise vortices do not form at the peak locations. Studying the flow visualisation images of this nozzle, results in the notion that streamwise vortices favour sharp discontinuous troughs, while on the other hand smooth peaks with large radii do not augment the generation of such structures.

The flow visualization images acquired for the 60° major nozzle are shown in Fig. 4.7. Comparing them to those of the reference and 120 V-major case, the differences in the general flow structures can be seen readily. The jet behaviour is more intense and coherent structures cannot be discerned after approximately one diameter downstream of the nozzle

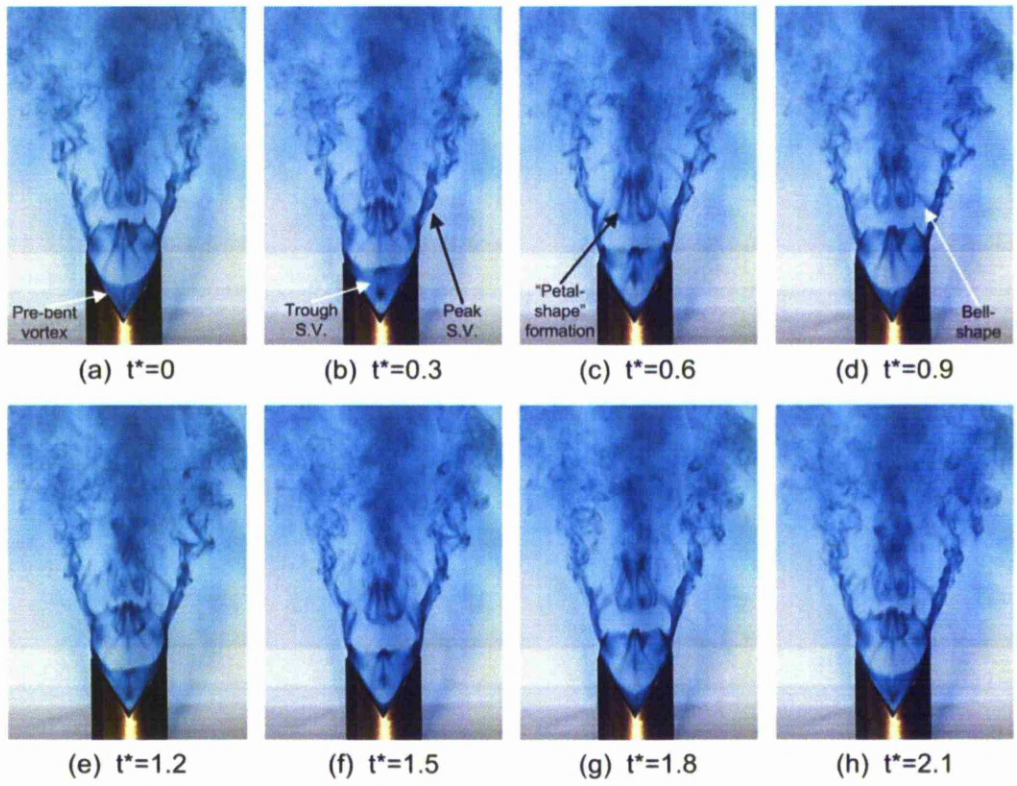

Figure 4.7 Flow visualisation of 60° V-major nozzle, major plane view

mean height. The ring vortices emanating from the nozzle follow its contour which resembles a pre-bent elliptic vortex ring entering its first cycle of axis-switching.

The ring therefore continues to bend but reaches its final bent position within a shorter axial distance from mean height compared to the reference case. A "petal-shaped" formation occurring at the centre of the nozzle is intriguing; however the exact reason for the occurrence is not fully understood. Severe bending of the main ring vortices in conjunction with stretching due to entrainment caused by the previous flow cycle, as seen in the other nozzle cases, may attribute to the formation of "petal-shaped" filaments. Along both major and minor-planes, visually large streamwise vortices are evident. These streamwise vortices form at the smooth peaks as well as at the sharp troughs of the nozzle as shown in Figs. 4.7 and 4.8. A large difference to the flow structures is observed, compared to the 120 V-major nozzle. As the nozzle sharpness increases a change in the streamwise vortex structuring takes place. The increased sharpness of the V-cut causes a larger rotation to the main ring filament, which in turn, aligns it with the jet centreline. Effectively, more of the main ring vortex contributes to the generation of streamwise vorticity. Streamwise vortices forming off the smooth peaks have a significant destabilising effect, similar to what Shu *et al.*(2005) found for a four-point tapered crown nozzle. The interaction of the streamwise vortices with

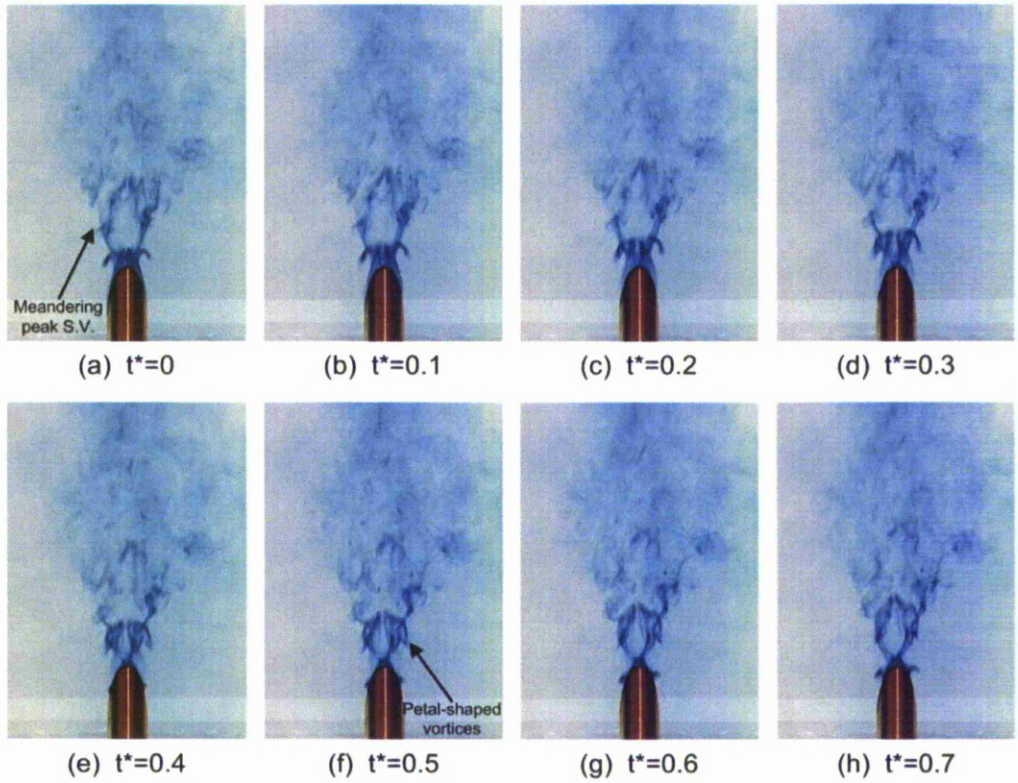

Figure 4.8 Flow visualisation of 60° V-major nozzle, minor plane view

the main ring vortices promotes their faster breakdown. For instance, looking at the minor-axis plane in Fig. 4.8, it can be seen that the streamwise vortices forming at the smooth peaks are not consistently being produced in the same manner, and occasionally meander about the peripheral region of the jet. The opposite is seen along the major-axis view, where streamwise vortices form regularly and consistently at the troughs and convect downstream without any observable distortions.

Figures 4.9 and 4.10 show the flow visualization results for the 60° V-minor nozzle along major and minor plane view. As with the less sharp nozzle (120 V-minor), looking at the flow developments along both views, the ring vortices that form follow the nozzle lip contours.

Along the major plane view, the jet body does not appear to narrow significantly as would be expected by an elliptic nozzle of similar aspect-ratio that undergoes axis-switching and movement of the main ring vortices is delayed when compared to the 120 V-minor nozzle. The coherency of the ring-vortices issuing from the nozzle is similar to the reference case, indicating that the flow field is less intense. Flow coherency is reduced at approximately x/D=5 thereafter. Streamwise-oriented vortices are observed in Fig. 4.9 and it is believed that they have been created by the re-arrangement of the main ring vortices along the

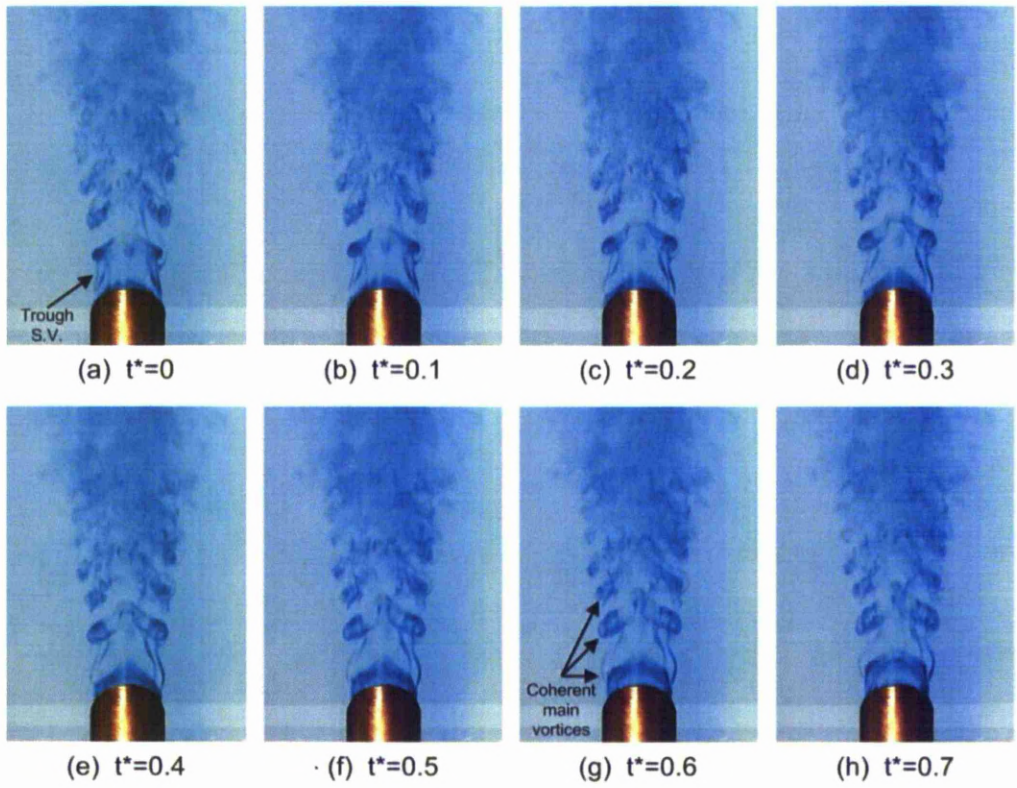

Figure 4.9 Flow visualisation of 60° V-minor nozzle, major plane view

streamwise axis due to vortex bending. They are not as intense as those produced by the peaks of the 120° V-minor nozzle which may be due to, amongst other factors, the increased curvature of the peak. If that is the case, then it may be possible that there is an optimum peak curvature associated with the promotion of streamwise vorticity production.

Looking at the minor plane view in Fig. 4.10, another interesting flow feature can be observed. Unlike what was seen for the reference and 120° V-minor case, the 60°V-minor nozzle does not behave as expected. The vortex filaments initially follow the nozzle exit contour and bend downstream, but do not change their orientation as they propagate downstream. The main ring vortices remain close to the nozzle centreline which is not expected from an elliptic nozzle undergoing axis-switching when viewed from the minor-axis. Streamwise vortices are produced by the sharp discontinuities located at the nozzle troughs. Similar to what was shown for the previous nozzles (V-minor and V-major groups), the streamwise vortices produced at the sharp troughs are robust and form in a very consistent and well organised manner.

In contrast to what was found for the V-major group of nozzles, increasing the sharpness of the V-minor did not intensify the flow. The flow field associated with the 60 V-minor nozzle

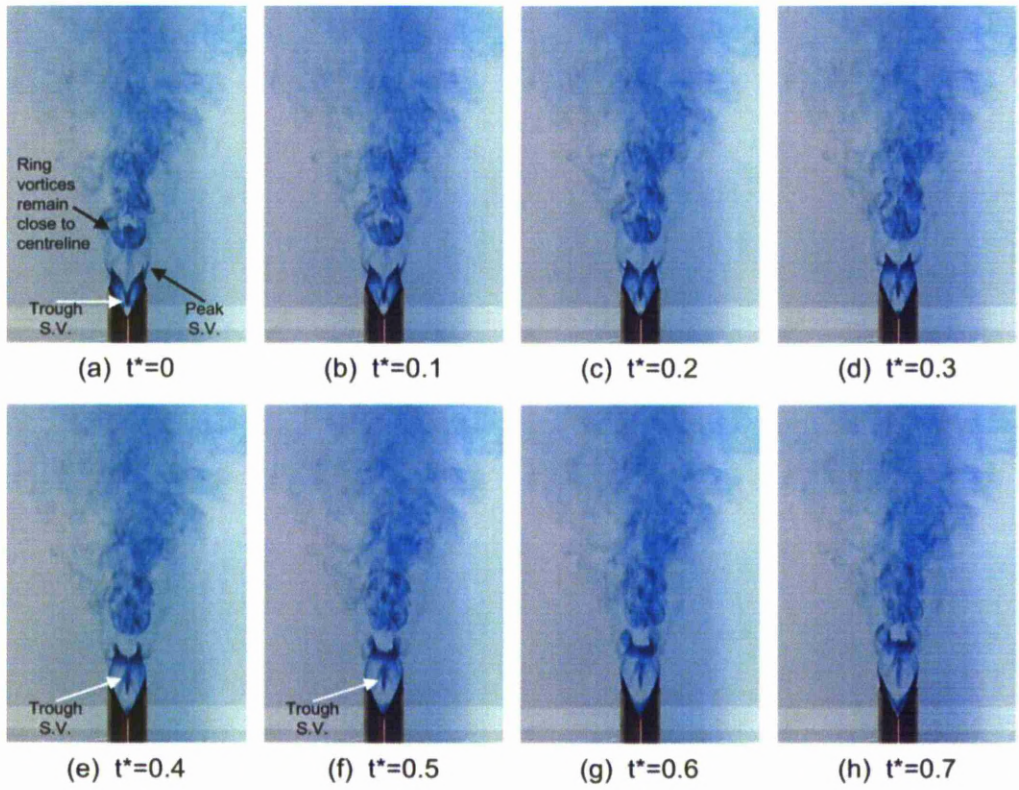

Figure 4.10 Flow visualisation of 60° V-minor nozzle, minor plane view

was more coherent and more organised. There seems to be a limit at which any further increase to the sharpness of the nozzle does not lead to an increase in flow activity.

b) LIF streamwise

With the use of the LIF technique, movement of the main ring vortices as well as the entrainment of ambient fluid is easily distinguished. However, since the laser sheet is aligned with the jet centre, most of the information regarding the periphery of the jet, such as the direction of the main ring vortex bending, is reduced.

The flow evolution of the reference jet along major and minor-plane is shown in Figs. 4.11 and 4.12 respectively. Initially studying the major-axis plane in Fig. 4.11, reduced flow activity is noticed. The jet column is very stable, especially in the vicinity of the nozzle exit, indicating that there is not much interaction between the jet column and ambient fluid. Following the formation of the main ring vortices, entrainment due to the rollups is noticed approximately 2.5D downstream of the nozzle exit. The rollups form within the shear layer of the jet and are initially positioned at the periphery of the jet. Movement towards the nozzle centreline, due to axis switching, initiates immediately after the vortex formation. Formation of "rib" structures are apparent between successive rollups (within the braid

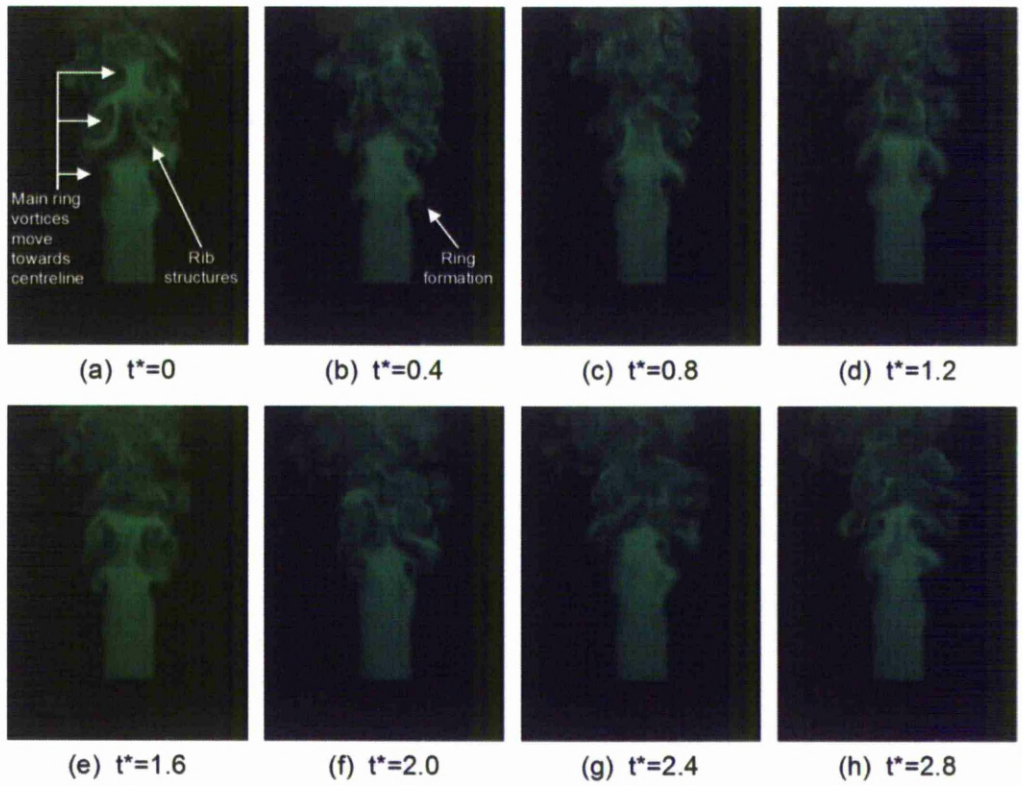

Figure 4.11 Streamwise LIF visualisation of elliptic reference nozzle, major plane view

region). Entrainment caused by vortices from the previous flow cycle help the generation of such structures.

Along the minor plane view, shown in Fig. 4.12, the movement direction of the main ring vortices is clearly discernible. Upon rollup, the vortices move outwards, away from the nozzle centreline thus completing the axis-switching phenomenon. A larger amount of jet column erosion due to ambient fluid entrainment can be seen by the black areas penetrating the green dye. Another flow feature worth noting that is highlighted along the minor-axis plane is the entrainment of jet fluid by vortices from the previous flow cycle. In Fig. 4.12 there are two instances where this flow characteristic can be seen, namely in Figs. 4.12(a) and 4.12(h). This behaviour is most likely caused by the movement of the main ring vortices along the major-axis plane but the effects are more noticeable along the minor-axis plane due to the clearer flow field. Effectively, when the main ring vortices bend downstream, the ends of the vortex move closer to each other causing a region of high entrainment between them. This entrainment causes following jet fluid to be propelled towards the downstream location. This jet fluid is detected by a distinct green patch of fluid approximately 6 jet-diameters downstream of the nozzle exit (or nozzle mean height). The vibrant green colour

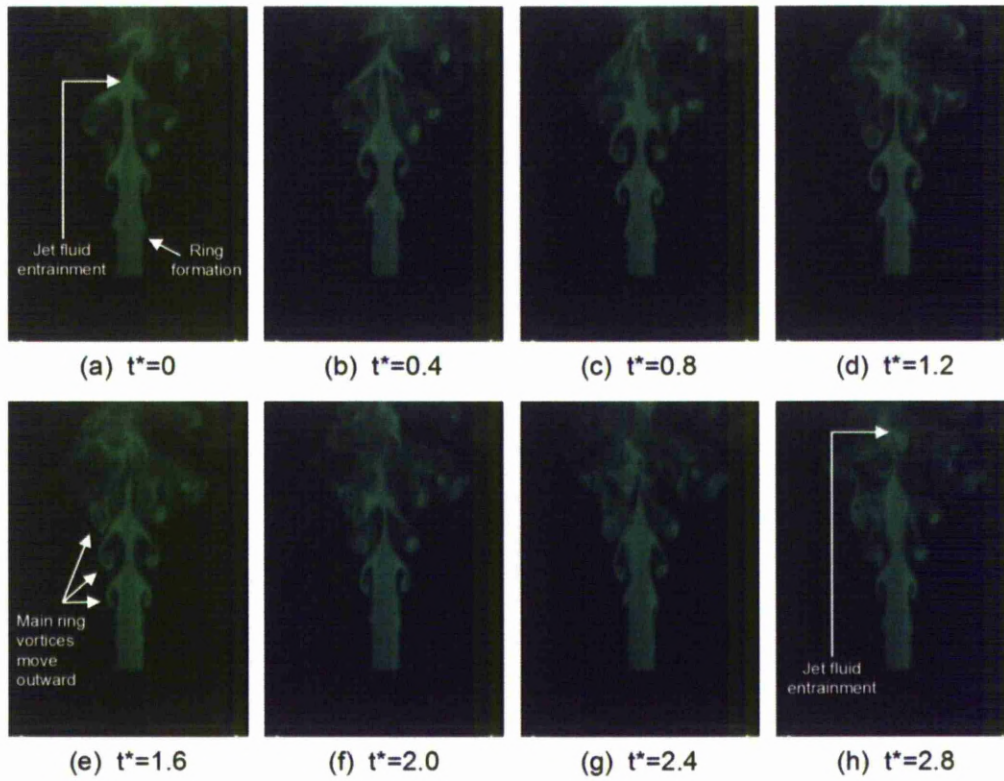

Figure 4.12 Streamwise LIF visualisation of elliptic reference nozzle, minor plane view

indicates that this fluid region containing jet fluid has not mixed well with the surrounding ambient fluid.

Imposing a lip modification in the form of a V-shaped cut with an included angle of 120° along the major axis of the nozzle, leads to a flow field captured in Figs. 4.13 and 4.14. As expected from the dye visualisation results presented in the previous section, compared to the reference case, the 120° V-major nozzle produces a more intense flow field and the point at which the jet transists to turbulence is further upstream. An increased jet spread along the major plane view is also noticed when comparing Fig. 4.11 with Fig. 4.13. Since the increase in jet-spread is also noticed using the LIF technique, it therefore indicates that the peaks are responsible for the particular flow behaviour. Along the major-axis plane, the illuminating laser sheet was aligned with the nozzle peaks. As explained in the previous section, peaks intensify the generation of streamwise vortices which in turn increase the interaction between the jet and the surrounding fluid, thus increasing the jet-spread. Situating peaks instead of troughs at the end of the major-axis of the nozzle enhances mixing but also may reduce the axis-switching ability of the jet. It has to be noted that axis-switching in elliptic jets of moderate aspect ratio increases the entrainment (Ho and Gutmark, 1987). Finding the optimising balance between these two parameters will increase mixing. Due to

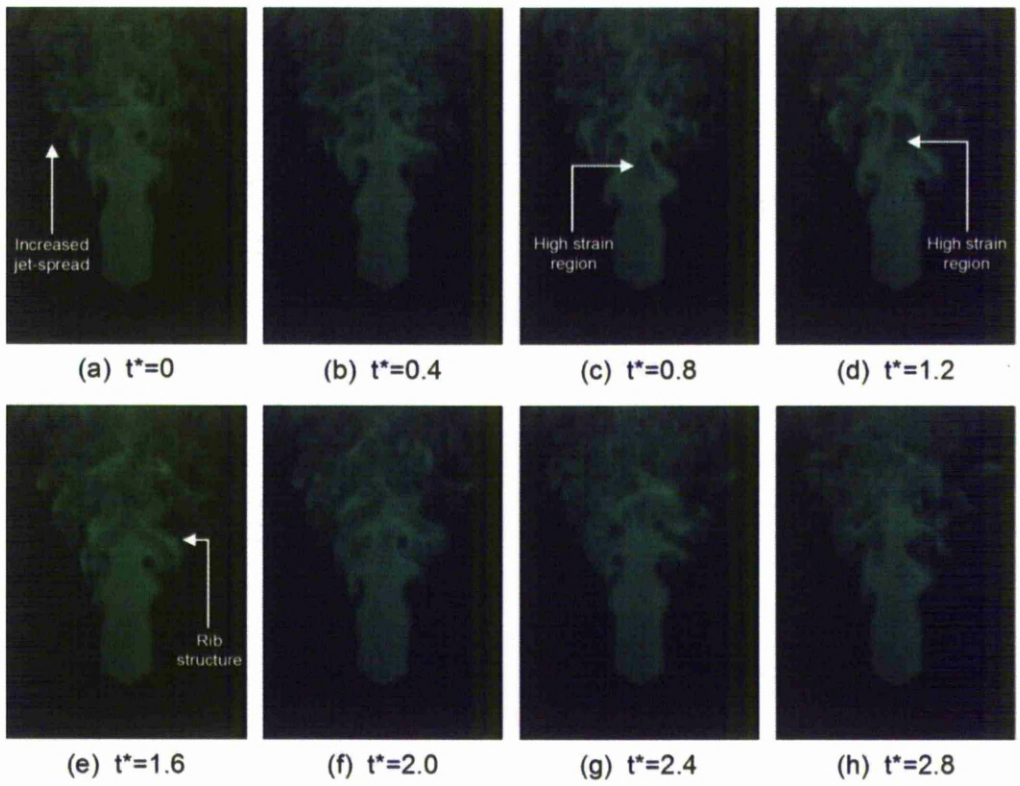

Figure 4.13 Streamwise LIF visualisation of 120° V-major nozzle, major plane view

the reduced movement of the main ring vortices towards the nozzle centreline, the axis-switching capability of the jet may also be reduced, however along the nozzle centreline at approximately 3 jet-diameters there is still evidence of high strain regions as seen in the reference case. These regions are created by the dominant effects caused by the lateral (cross-stream) movement of the main ring vortices. They contain entrained ambient fluid, indicated by the darker areas, and are expected to have high flow activity levels.

Examining the minor-axis plane results presented in Fig. 4.14 and comparing the captured flow field to the reference case, subtle differences exist. The visually weak trough streamwise vortices presented in the "dye visualisation" section do not seem to manifest and affect the jet structuring. Having sharp troughs with an included angle of 120° along the major axis of an elliptic nozzle do not have a great effect towards flow manipulation, at least in a flow visualisation sense. Contrary to the major-axis plane, lateral (cross-stream) movement of the main ring vortices is similar to the reference case. An observable difference between the current nozzle and the reference case is that, green patches containing high dye concentrations cannot be discerned at downstream locations (x/D>4). This indicates that most large-scale coherent structures have broken down into smaller eddies within the measurement window thus possibly resulting in better mixing.

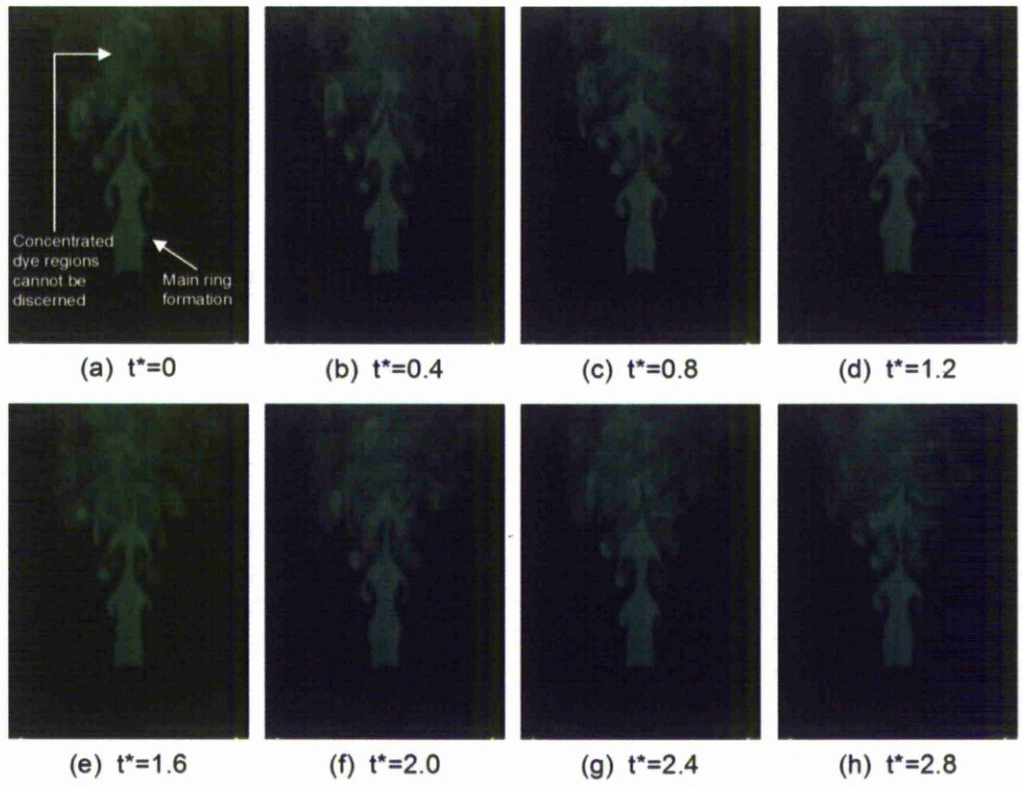

Figure 4.14 Streamwise LIF visualisation of 120° V-major nozzle, minor plane view

Switching the orientation of the V-notched cut, the effects of having a smooth peak and a sharp trough along the major and minor-axis respectively can be assessed. Figures 4.15 and 4.16 show the 120° V-minor nozzle along both major- and minor-axis measurement planes. Compared to the V-major nozzle of similar sharpness, the flow field is more coherent not only along the periphery of the jet as seen in the dye visualisation section earlier, but also within the jet column (Figs. 4.13 and. 4.15). Main ring lateral (cross-stream) movement is similar to the reference case, albeit delayed slightly with respect to downstream distance. The movement of the ring vortices is complete, meaning that the vortices start at the edge of the jet (shear layer) and at approximately x/D=2.5 start to move towards the jet centreline and continue to do so until both ends of the bent ring vortex nearly meet, thus axis-switching behaviour is still maintained. The effects from the sharp troughs situated at the ends of the nozzle major-axis, are minimal. The large-scale flow structures are largely unaffected by the lip modification. Again the subtle disturbance, if any, caused by the V-shaped trough on the flow field is shown.

The effects of the smooth peaks are better understood when viewed along the minor-axis plane. Visually weak streamwise vortices form at the smooth peaks and help to spread the jet. Peaks along major-axis of the elliptic nozzle interact with the jet to a greater extent than

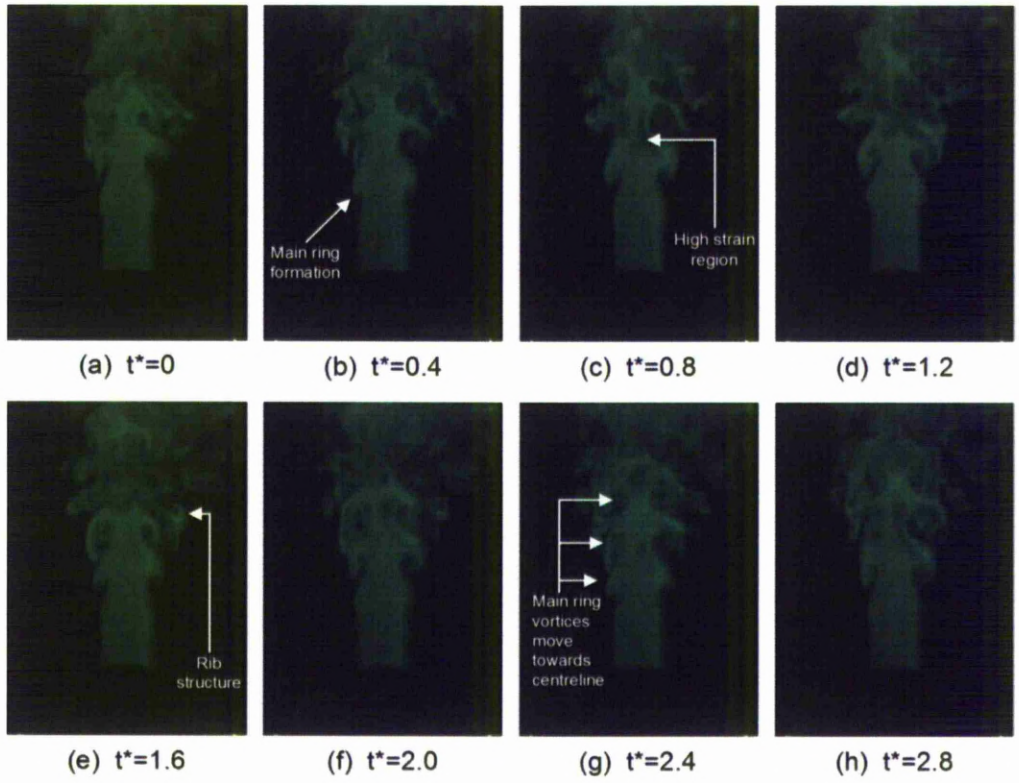

Figure 4.15 Streamwise LIF visualisation of 120° V-minor nozzle, major plane view

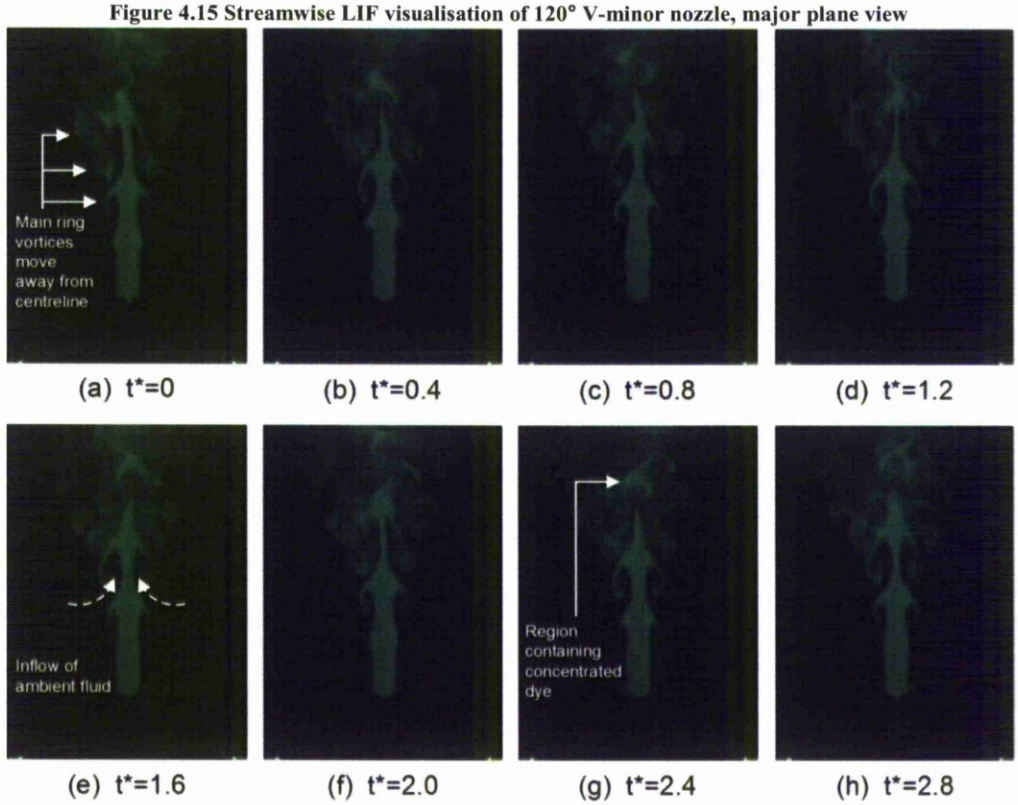

Figure 4.16 Streamwise LIF visualisation of 120° V-minor nozzle, minor plane view

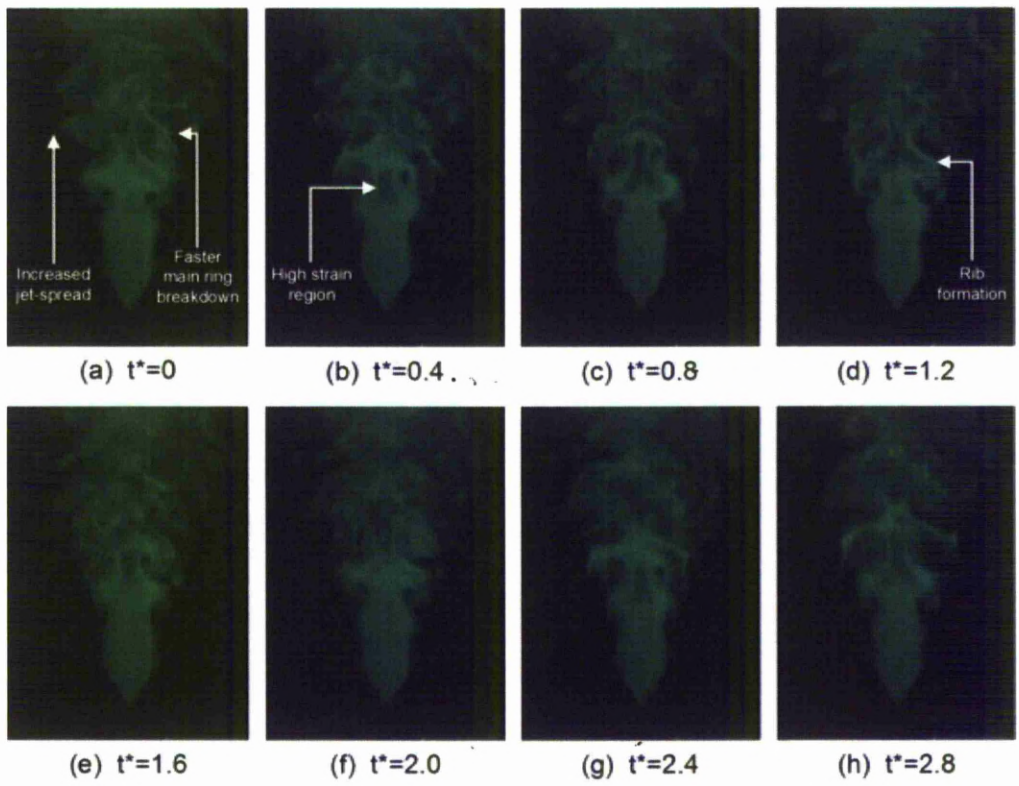

Figure 4.17 Streamwise LIF visualisation of 60° V-major nozzle, major plane view

troughs as shown when investigating the 120 V-major nozzle. The main ring vortices move outwards nearly to the extent of the reference case, which in conjunction to the movement along the major-axis plane, allows the expectation of axis-switching. As with most of the nozzles along the minor-axis plane, penetration of ambient fluid within the jet body is detected, however not to the extent observed for the 120° V-major case. A thick streak of high green dye concentration extends to the far downstream section of the jet, indicating the reduced interactions associated with this nozzle. The amount of concentrated green dye, although not quantifiable, is similar to the reference case.

Increasing the sharpness of the V-major nozzle has a further destabilising effect on the flow field as shown in Figs. 4.17. Flow coherency is lost within a shorter downstream distance from the mean height. Main ring vortices form and move towards the jet centreline but break down much faster than when issued from the less sharp 120° V-major case. The jet spread is increased mostly due to the formation of stronger peak streamwise vortices with an outward rotational sense. These streamwise vortices interact with the main ring vortices promoting a faster breakdown of the latter.

Viewing the jet along the minor-axis plane, shown in Fig. 4.18, as expected, an increase in flow intensity is apparent. The flow field is very turbulent and coherent structures do not

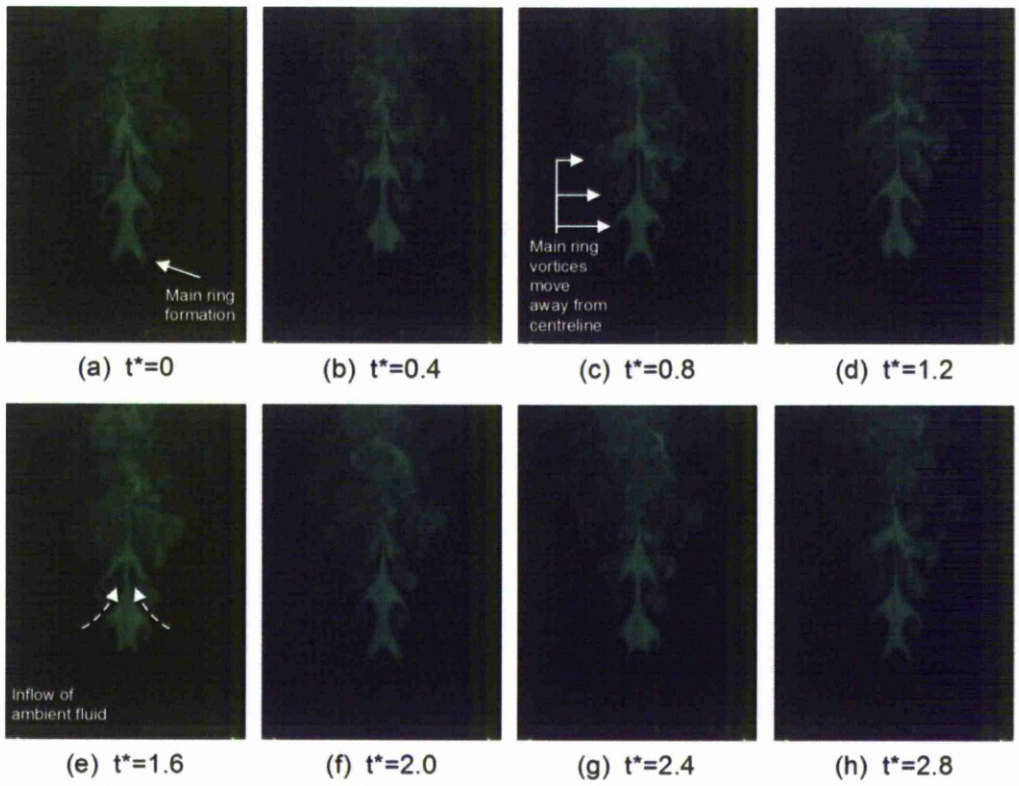

Figure 4.18 Streamwise LIF visualisation of 60° V-major nozzle, minor plane view

propagate far downstream. The jet shear layer rolls-up to form main ring vortices much earlier compared to the major-axis plane due to the lower momentum thickness associated along the minor-axis, (1989). Lateral movement of the ring vortices is similar to the reference case but jet column erosion in this case is much greater. Large entrainment of ambient fluid, noticed by black regions in jet column, indicates that more interactions take place with the current configuration that the rest of the nozzle geometries, especially in the near field region of the jet $x/D<3.5$. Interestingly, it seems that only after the trough sharpness has been increased above a certain level, is more flow activity observed. Clearly the streamwise vortices formed at the sharp troughs interact with the jet and cause a larger amount of jet spreading especially in the near-field region of the nozzle, compared to the less sharp 120° V-major case.

Increasing the V-notched sharpness along the minor-axis does not have the expected influence of the jet. The major plane view of the 60° V-minor nozzle is shown in Fig. 4.19. Comparing the 60° V-minor to the 120° V-minor presented earlier in Figs. 4.15 and 4.19 respectively, a more coherent flow field can be observed. Increasing the nozzle sharpness reduces the jet structures and results in a more stable jet. The main ring vortices form further downstream and their lateral movement is slower compared to the reference and 120° V-

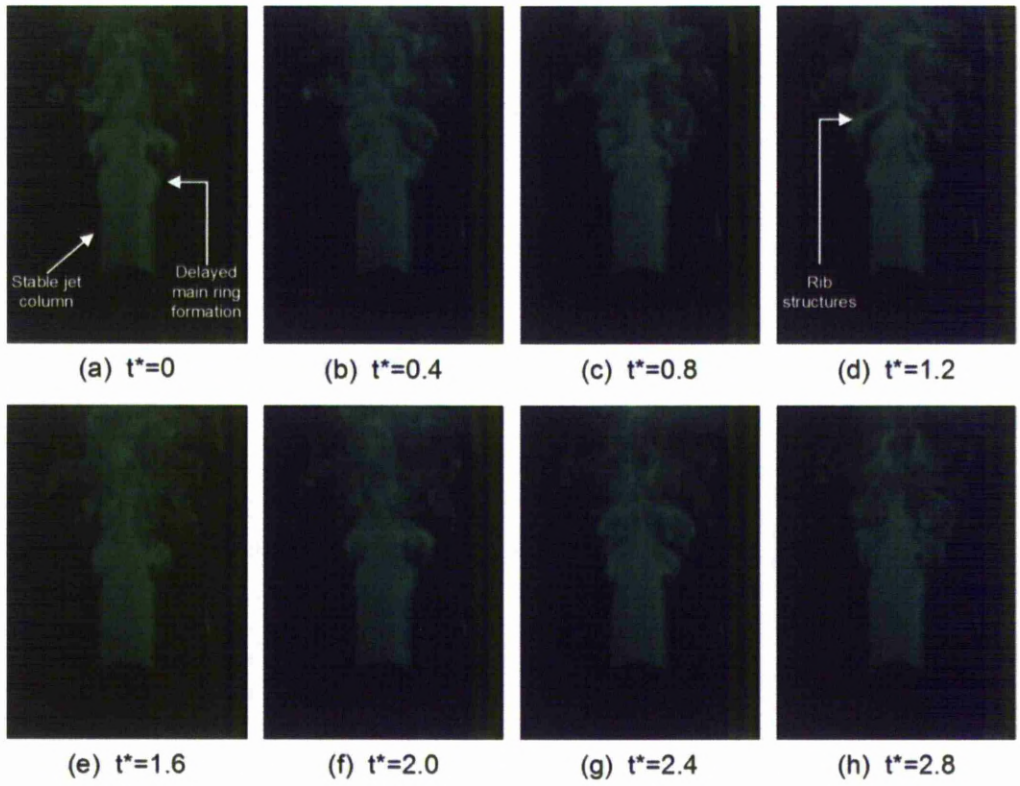

Figure 4.19 Streamwise LIF visualisation of 60° V-minor nozzle, major plane view

minor case. Any streamwise vortices formed at the sharp troughs do not show up in the captured image sequence, indicating that their area of influence is minimal. The conclusion that can be drawn from both V-minor nozzles is that a sharp trough does not help the production of extraneous streamwise structures. Additionally, when the trough sharpness is increased this effect becomes more apparent, resulting in even less interactions between the streamwise structures and the jet.

The increased sharpness of the smooth peaks along the minor-axis plane, promote more interactions, as seen in Fig. 4.20. A wider jet spread is observed, caused by the interactions between the better-developed vortices formed at the peak locations or the nozzle and the jet. Compared to the 60° V-major and reference cases, a delay in the shear layer rollup is detected. The delay is expected as the shear layer (it is strictly a boundary layer as the fluid has not left the nozzle cavity) is within the nozzle for a larger downstream distance compared to the rest of the nozzles. Within that distance, the jet boundary layer and momentum thickness is expected to grow and thus when exiting the nozzle has less tendency to roll up, as shown by Hussain and Husain, (1989) who used an elliptic nozzle of moderate aspect ratio (AR=2), carefully contoured to manipulate the momentum thickness. After the shear layer rollup, a reduced amount of main ring vortex lateral movement is detected. The

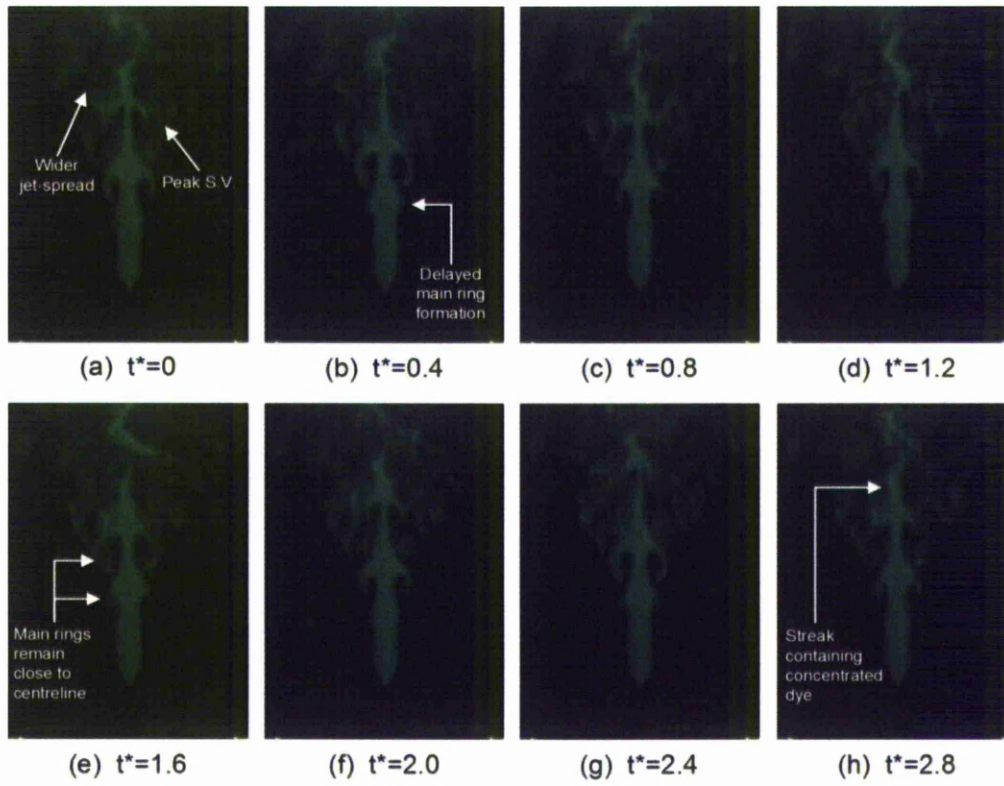

Figure 4.20 Streamwise LIF visualisation of 60° V-minor nozzle, minor plane view

ring vortices remain close to the nozzle centreline as they propagate downstream. The reduction in movement along both planes will inevitably reduce the axis-switching ability of the jet. Even though a large jet spread is noticed along the minor-axis plane, these disturbances do not affect the jet core. A steady streak of highly concentrated green dye is apparent along the nozzle centreline, which extends throughout the measurement widow. Minimal amounts of ambient fluid entrainment along both major- and minor-axis due to delayed axis-switching and weak streamwise vortex generation are responsible for this phenomenon. As a result of the previous findings it can be said that low mixing and a large potential core are the main attributes/characteristics of this particular nozzle configuration.

c) LIF cross-stream

Cross-stream LIF results of all elliptic IO nozzles are shown in Figs. 4.21 to 4.30. Flow development and other features such as the shape and formation of main ring vortices and streamwise vortices will be shown at several cross-stream slices, downstream of the mean height.

Figure 4.21 depicts the flow associated with the reference nozzle. Unlike the rest of the test cases, eight cross sectional cuts of the flow field are presented. As shown from earlier

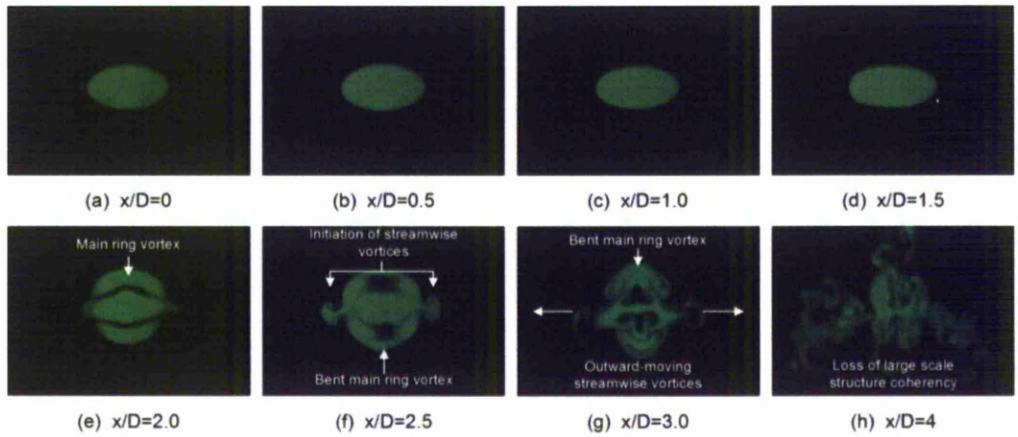

Figure 4.21 Cross-stream LIF visualisation of elliptic reference nozzle

results, the reference case produces one of the most stable flow fields and thus the shear layer rollup occurs at a later (downstream) stage,($1.5<x/D<2$) Main ring bending is expected when consulting the previous results and previous research work (Arms and Hama, 1965; Dhanak and Debernardinis, 1981; Husain and Hussain, 1983), and can be seen in Fig. 4.21(e). The top and bottom sections of the main ring vortex are highlighted by the laser because of the downstream bending of the ring as explained in previous sections. As the shear layer rolls up, portions of the main ring that are situated at the ends of the major-axis of the elliptic nozzle move faster (due to higher induced velocity caused by the reduced radius) and thus downstream before the rest of the ring can catch up. For this reason only the top and bottom portions of the ring are highlighted in Fig. 4.21(e). These are the portions that have been "left behind", following the rest of the ring. On the contrary, left and right sections of the ring have already cut across the laser sheet and thus are not captured by the camera. As the flow develops, more interesting flow features such as streamwise vortices emerge. In Fig. 4.21(f), outward spreading streamwise vortices are clearly visible. The flow field should be symmetric as the nozzle in test has a symmetric geometric design, however small experimental uncertainties accumulate and cause slight asymmetries to arise such as the ones seen between the two outward-spreading streamwise vortices in Fig. 4.21(f). Another feature worth mentioning is the gradual change in shape of the main ring vortex which eventually leads to axis-switching. The main ring vortex shape changes from an elliptic towards a more circular shape caused by the inward movement along the major-axis plane and outward movement along the minor-axis plane, when viewed along the streamwise orientation as presented eariler. The black sections situated on the top and bottom side of the main ring vortex filament are again caused by the shape of the ring. Due to downstream bending of the main ring vortices, the "left and ring" portions or the ring filament are ahead (more downstream) of the "top and bottom" sections. It follows that,

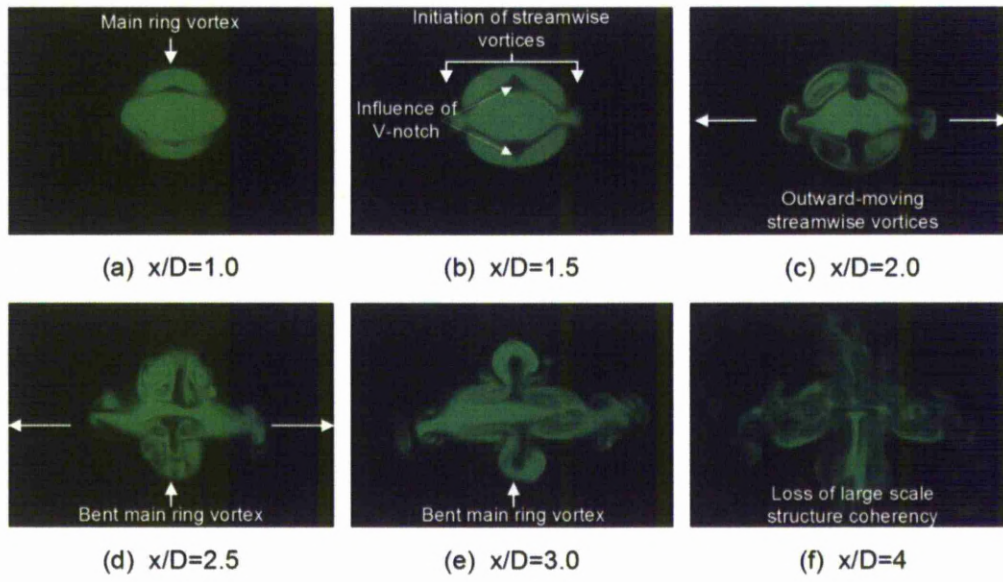

Figure 4.22 Cross-stream LIF visualisation of 120° V-major nozzle

when the left and right sections are illuminated, the top and bottom sections have not yet passed the illumination plane and thus cannot be captured by the camera. In the next downstream slice, at x/D=3 location, it can be inferred that axis-switching has taken place since the main ring vortex has switched the minor- and major-axis. The new major-axis is now orientated along the "top-bottom" direction. Further development of the streamwise vortices is also evident, showing an increase in size while still maintaining the same outward orientation. Finally, as expected, by x/D=4 most flow coherence is lost and large spreading is detected along both initial major- and minor-axis mainly due to the outward spreading streamwise vortices.

The main ring vortex development is different when observing the 120° V-major nozzle shown in Fig. 4.22. Initially, the ring forms much faster compared to the reference case, but the bending orientation is similar, towards the downstream direction as can be seen in Fig. 4.22(a). At the next downstream location, x/D=1.5, the ring has a distinct shape that resembles the V-notch cut of the nozzle. This feature must be attributed to the V-notch as the reference case does not show this behaviour. The subtle formation of streamwise vortices takes place but not until further downstream do the vortices form fully. At x/D=2 the main ring vortex has thickened by entraining ambient fluid and has changed shape towards a more circular one. The streamwise vortices are now apparent and have an outward spreading direction. As the downstream distance increases the size and region of influence of the streamwise vortices become much greater until x/D=4 by which most of the flow features are not discernible. The main ring vortex continues to bend and at locations x/D=2.5 and 3 can be seen to have changed orientation. More specifically at x/D=3, the ring filament is

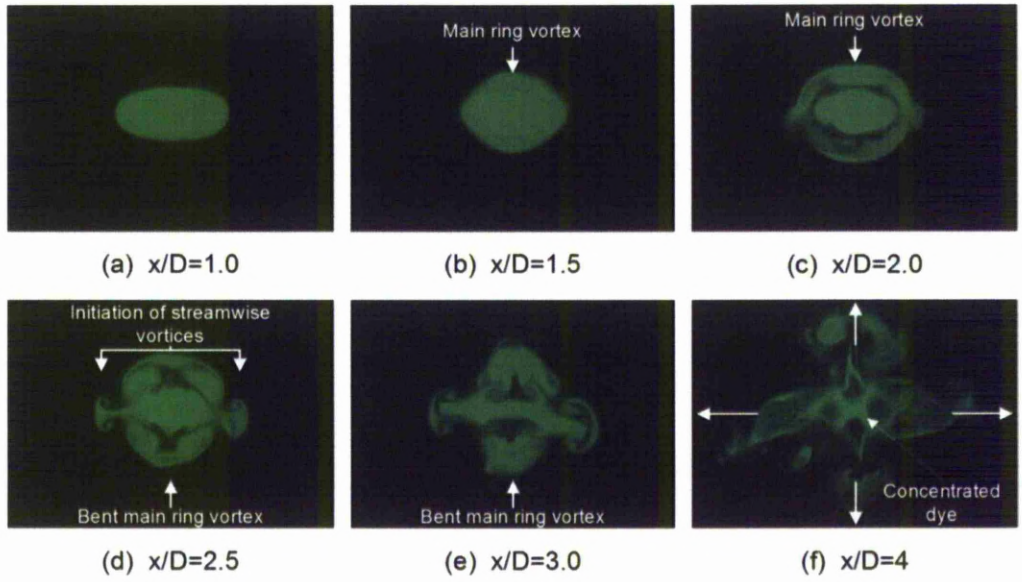

Figure 4.23 Cross-stream LIF visualisation of 120° V-minor nozzle

aligned along the "top-bottom" direction and is very slender which is different compared to the reference case. By x/D=4 all main ring vortices have been broken down. Although the main ring vortices do bend and thus change orientation, it cannot be said with certainty that the whole jet undergoes axis-switching. The large outward flowing streamwise vortices generated at the smooth peaks of the nozzle increase jet spread along that plane (along major plane view) thus retaining the original jet orientation.

Studying the cross-stream flow images of the 120° V-minor nozzle shown in Fig. 4.23, immediately a reduction in flow field intensity is detected. This fits well with the streamwise results. Specifically, when viewing Fig. 4.23(f), flow features such as streamwise vortices and main ring vortices can still be detected. Interestingly in the centre of the jet a rhomboid shape exists which agrees well with the "concentrated green dye patch" observed in the streamwise results. This shows again that the jet potential core is comparable to the reference case and much larger compared to the 120° V-major case. Going back to the start of the image sequence, a delay in shear layer rollup is apparent. The formation of main ring vortices is initiated between x/D=1.5 and 2, thus being comparable to the reference case. Such a delay is expected as the boundary layer of the jet will be thicker due to the longer, major-axis section, of the nozzle. Compared to the reference case, a reduction of main ring vortex bending exists and can be seen when looking x/D=2. The whole ring is illuminated by the laser sheet indicating that each section (point) of the ring is on the same plane. Further downstream (D>2), the shape of the vortex ring changes and eventually switches axis, aligning along the "top-bottom" direction. Streamwise vortex generation initiates at x/D=2, but fully formed outward-flowing vortices are observed for x/D>2. However, compared to

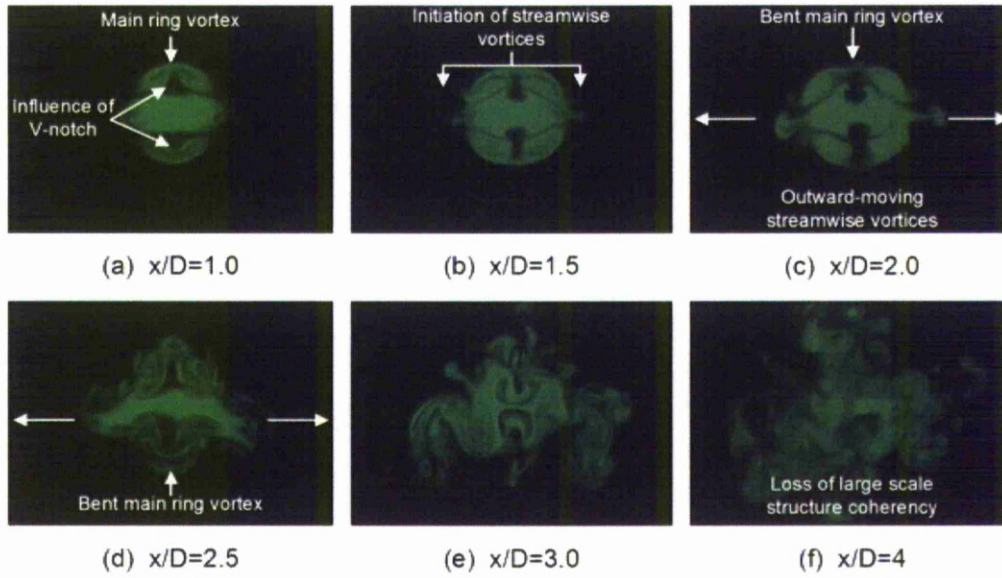

Figure 4.24 Cross-stream LIF visualisation of 60° V-major nozzle

the streamwise vortices of the 120° V-major nozzle, they are less intense. As shown earlier, smooth peaks seem to produce more flow structuring than sharp troughs. Favourable spreading along both major- and minor-axes caused by the influence of streamwise and main ring vortices is shown in Fig. 4.23(f).

Increasing the sharpness of the V-cut along the major axis intensifies the flow field even further compared to the 120° V-major. A further reduction of the potential core is noted as most flow coherence is lost by x/D=3. The distinct V-shaped notch is apparent in the main ring vortex, however the effects of the trough are noticed further upstream when compared to the less sharp nozzle. At x/D=1 in Fig. 4.24, the main ring vortex has already started to bend and incorporates flow features caused by the sharp troughs. With increasing downstream distance the main ring bending continues until x/D=2.5, after which the ring vortices cannot be discerned. Increasing the V-notch angle to such high sharpness has a detrimental effect on the propagation of the main ring vortices. However mixing can be expected to increase, due to the reduction of the potential core. Streamwise vortices start to form and continue to grow from x/D=1.5 but are most dominant with the region of $2.5<x/D<3$. From just looking at the flow visualisation results, streamwise and cross-stream the jet does not seem to axis-switch, however a more detailed quantitative analysis will explain whether or not the flow visualisation data correlates well with the PIV results.

Similar to the 120° V-minor case, the flow field produced by the sharper 60° V-minor nozzle is very stable. Comparing between the two nozzles it can be shown that the sharper nozzle produces less flow activity than its counterpart. The streamwise vortices as well as the main ring vortices can be distinguished even at the last cross-sectional plane (x/D=4) which means

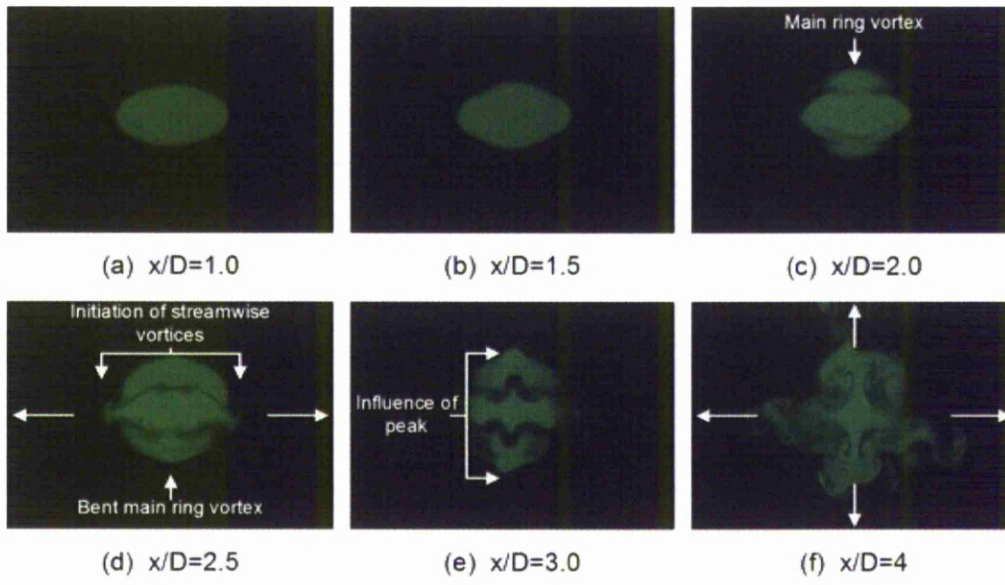

Figure 4.25 Cross-stream LIF visualisation of 60° V-minor nozzle

that mixing between the jet and the surrounding fluid is reduced when compared to all other test nozzles. An interesting flow feature is seen in Fig. 4.25(e), in which the main ring vortex has changed orientation and is now aligned along the "top-bottom" direction. The top and bottom ring vortex filaments have a "kink" in the centre. This kink is towards the outward direction and is possibly caused by the formation of streamwise vortices at the peak locations (top and bottom) as seen previously in Fig. 4.20 when presenting the LIF streamwise results. Another interesting flow feature worth pointing out is the clear axis-switching behaviour seen at x/D=4. In Fig. 4.25(f) the jet body is has a preferential spreading along the "top-bottom" direction, perpendicular to the initial state of jet. The fact that the jet body is visible, correlates well with the streamwise results in which, a steady green dye streak was shown to extend to the end of the measurement window presented earlier in Fig.4.20. Finally, incorporating V-notches at the end of the major axis of an elliptic ring does not help to produce energetic streamwise vortices. Looking at Figs. 4.25(d) and (f), only at locations x/D=2.5 and 4 do the streamwise vortices seem strong enough to interact with the main ring vortices and cause a large momentum exchange between the jet and the surrounding fluid. It must be noted, that a discrepancy regarding the bending orientation of the main ring vortices between the shear layer injection and the cross-stream LIF results exists. However the next section will address this inconsistency in more compelling way through the use of flow evolution image sequences.

d) Evolution of coherent flow structures

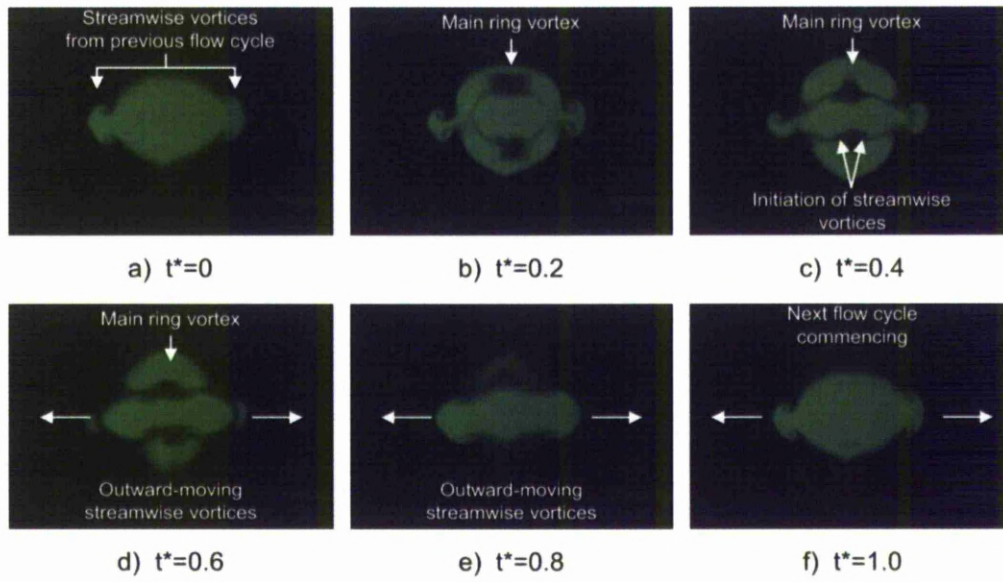

Figure 4.26 Flow evolution of reference nozzle, taken at x/D=2.5

To aid the understanding of the development of the main ring vortices and the streamwise vortices, a series of consecutive image-sequences which covered a complete forcing cycle, were used. For the sake of brevity, image-sequences from only one cross-stream location were chosen. A cross-stream location which highlighted the most representative flow features was chosen for each nozzle.

The reference case is presented in Fig. 4.26 and was captured at a cross-stream distance of x/D=2.5 from the nozzle exit. The evolution of an elliptic jet of moderate aspect-ratio (AR=2) has previously been studied in great detail by Husain and Hussain,(1993) and thus only a brief description highlighting the main points of the flow evolution will be given. Starting with the first image in the figure, the streamwise-aligned vortices or "rib-structures" formed from the previous flow cycle are clearly visible. The important point is that the rib structures are created between two successive main ring vortices (or "rolls" as named by Husain and Hussain) and that the downstream section of the streamwise vortices is entrained by the downstream main ring vortex (as shown in the flow visualisation section earlier), but the upstream section passes over the outside of the upstream (or following in a time sense) main ring vortex. For this reason the streamwise-aligned vortices apparent in Fig. 4.26(a) are situated on the periphery of the jet at the ends of the major-axis. The rest of the flow sequence shows the formation of the main ring vortex and the bending associated with it. Sections of the ring-vortex situated at the ends of the major-axis move faster and thus in Fig. 4.26(b) there is a distinct black patch along the minor-axis of the jet. The minor-axis side of the ring is trailing behind and thus is highlighted in the next time sequence, Fig. 4.26(c).

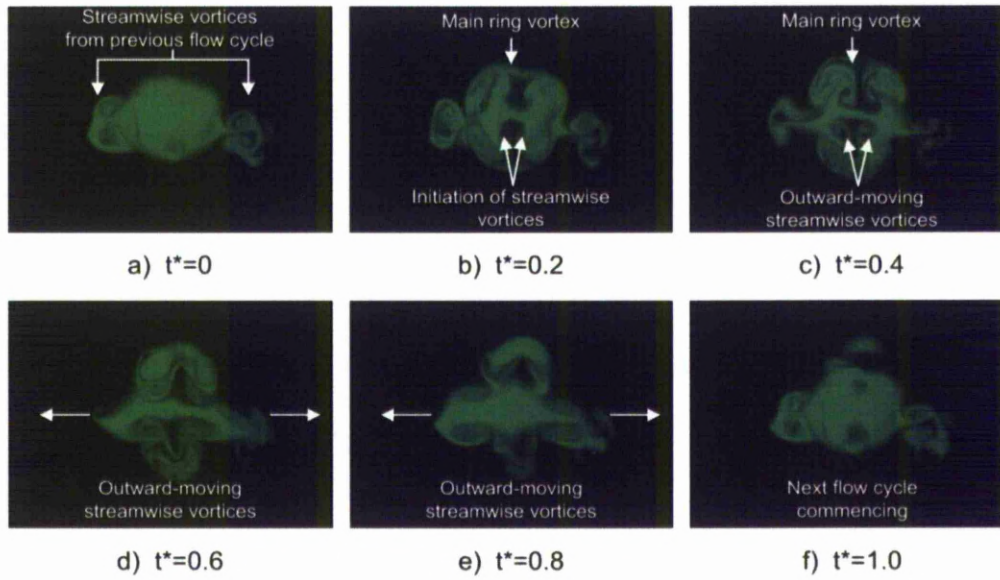

Figure 4.27 Flow evolution of 120° V-major nozzle, taken at x/D=2.5

Finally, the initiation of streamwise-aligned structures within the braid region of the jet, can also be seen. Viewed from the camera line of sight, a dominant outward motion is detected, but in reality if viewed isometrically, the streamwise aligned structures are cone-like shaped. As the flow cycle completes itself, the streamwise structures continue to spread and a new main ring vortex starts to form as show in Figs. 4.26(d),(e) and (f).

Figure 4.27 depicts the flow evolution of the 120° V-major nozzle. Looking at the first and last images of the flow cycle it can be seen that the streamwise structuring associated with this nozzle is larger compared to the reference case. This was also mentioned in the previous sections when analysing the streamwise LIF results. Smooth peaks seem to intensify the formation of streamwise vortices. A slight difference to the reference case can be observed when focusing on the evolution of the main ring vortex shown in Fig. 4.27(b)–(e). Although the general bending orientation is toward the downstream direction which is similar to the reference case, the influence of the V-notch produces an extra curvature to the ring-vortex. The streamwise-aligned vortical structures initiate rapidly within the braid region of the jet (t*=0.4) and move outward similar to the reference case.

The cross-stream flow cycle associated with the 120° V-minor nozzle is shown in Fig. 4.28. Looking at the image sequence downstream bending of the main ring filament is noticed. Even though the V-notch cut orientation is different, the resultant ring vortex is similar to the 120° V-major nozzle case. Another similarity is that the rib structures associated with this nozzle are comparable to the 120° V-major case, which was not easily observable when analysing the dye injection results. Once some portion of the main ring vortex has passed the

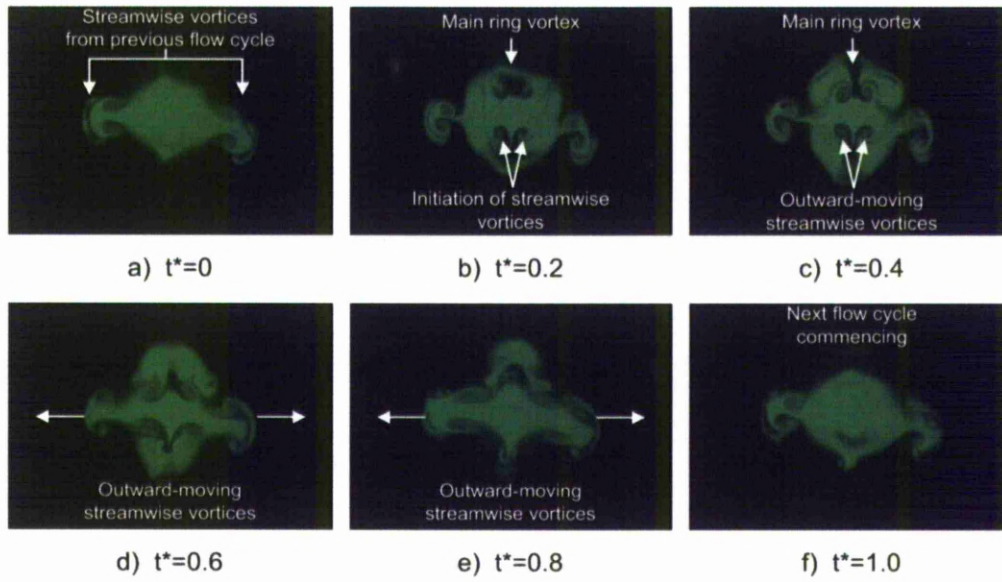

Figure 4.28 Flow evolution of 120° V-minor nozzle, taken at x/D=3

illumination plane, the rib structures start to form and along with their formation ambient fluid is seen to enter the jet body and is engulfed. The ambient fluid is distinguished by the absence of fluorescent dye. Upon forming, and influenced initially by the downstream main ring vortex, the streamwise structures move radially outwards similar to the reference case. It seems that both 120° V-notched cases introduce stronger and more coherent generation of rib-like structures in the braid region of the jet. Also due to the favourable orientation of the rib structures an increase in ambient fluid engulfment is observed. This is in accordance with the rest of the flow visualisation results presented in earlier sections.

Increasing the sharpness has the effect of distorting the main ring vortex to a greater extend. Apart from promoting a faster transition to turbulence and a faster break-down of the main ring vortex, some extra flow features emerge. It is interesting to see that the streamwise vortices are visually reduced compared to the less sharp, 120° V-major case. In Fig. 4.29(a) the initiation of the main ring vortex rollup is shown. As the main ring vortex is formed, extraneous features at the edge of the major-axis are noticed. Effectively the top side of the main ring vortex coupled with the extra features resembles a "moustache-like" shape. Although the particular effect caused by these features on the main ring vortices remains unknown, their formation could be caused the presence of the peak. Comparing to the dye visualisation results presented earlier (Fig. 4.7) and taking into account the similarity in downstream location, the extra flow features noticed could possibly be the intriguing "petal-shaped" filaments which were pointed out when analysing the dye visualisation results. Although the author is not in the position to estimate the importance of these flow features,

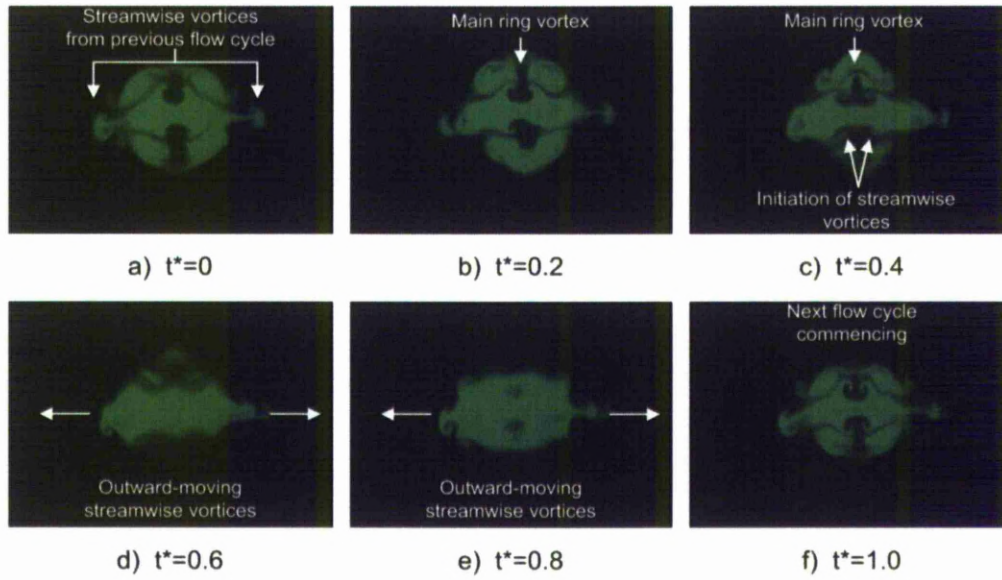

Figure 4.29 Flow evolution of 60° V-major nozzle, taken at x/D=2

their robustness however proves that they are an essential step in the flow evolution of the particular nozzle. As the time progresses, portions of the highly bent main ring vortex pass through the illumination sheet and streamwise vortices start to form. Similar to the reference case and to the flow model proposed by Husain and Hussain,(1993) their orientation is outward spreading along the major-axis of the jet. However, a larger amount of ambient fluid, detected by the lack of fluorescent dye, is drawn-in which could lead to higher entrainment within the braid region of the jet.

As expected, the cross-stream flow evolution of the 60° V-minor, shown in Fig. 4.30, reveals

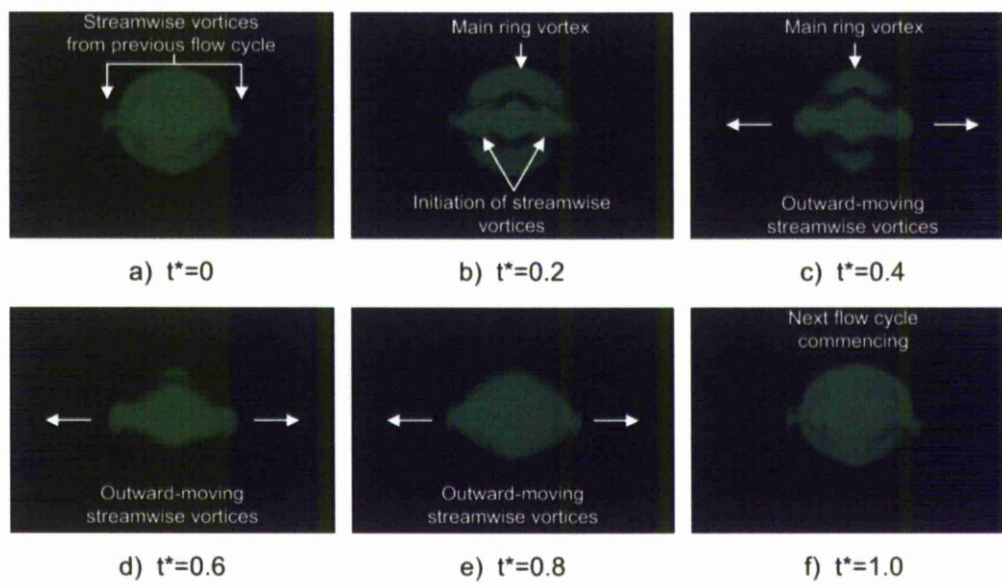

Figure 4.30 Flow evolution of 60° V-minor nozzle, taken at x/D=2.5

minor flow features. However, contrary to the indications given when analysing the dye injection visualisation results, the main ring vortices do not bend in the opposite sense with respect to the reference case. Downstream bending of the ring vortices is clearly visible. A decrease in the size of the streamwise structures as well as a decrease in the interactions between the main jet body and ambient fluid are noticed. Due to the reduced interactions, as explained earlier, the jet is more stable and the breakdown of the large-scale coherent structures takes place further downstream.

4.2.2 Vortex flow model

Considering the flow visualisation results presented so far, a schematic representation of the evolution of the main ring vortices is shown in Fig. 4.31. The purpose of the schematic is to highlight the main flow features and provide an easier way of interpreting the results. The solid black coloured lines depict sections of the rolled-up shear layer. Since the underlying gross flow behaviour between the 60° and 120° V-notched nozzles is quite similar, for the sake of brevity only one nozzle per category is illustrated.

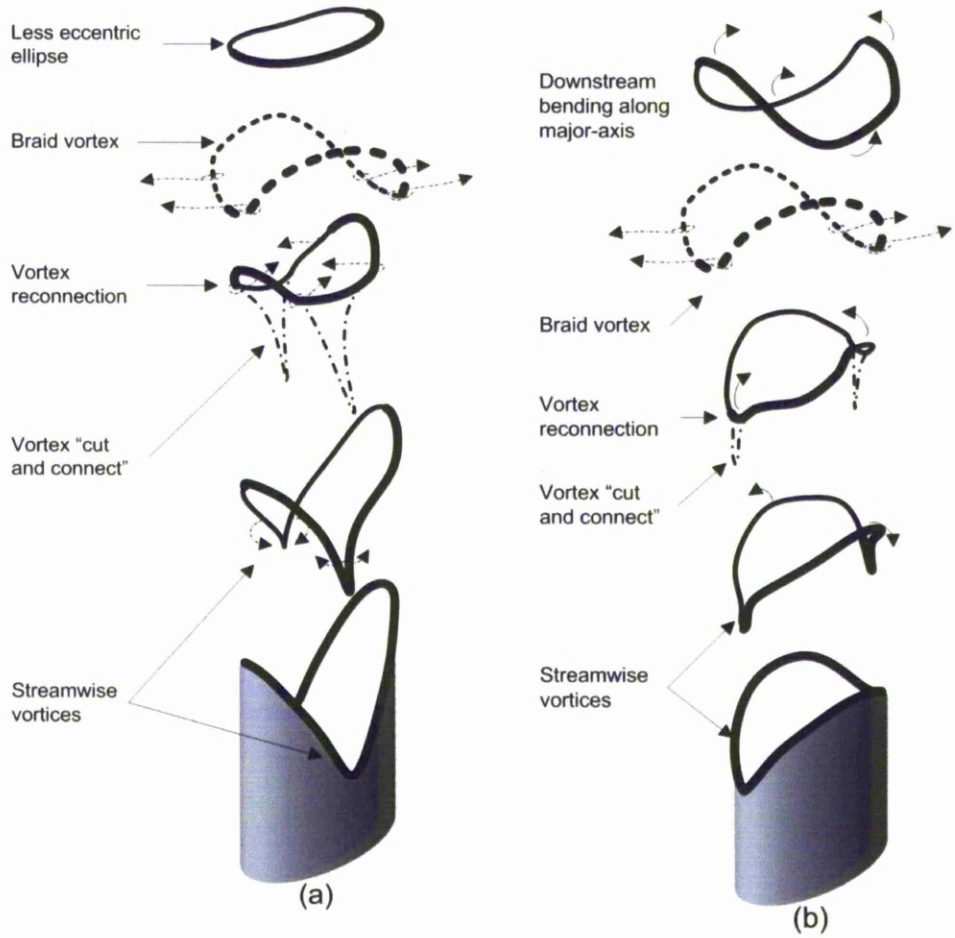

Figure 4.31 Flow representation for indeterminate-origin elliptic jets, (a) V-Major nozzle and (b) V-Minor nozzle

The V-major nozzle flow interpretation will be analysed first. Past studies have shown that for elliptic jets of aspect-ration two, Initially the shear layer rollup is faster along the major plane view, due to the smaller momentum thickness (Hussain and Zedan, 1978; Husain and Hussain, 1991). The presence of the notch exposes the shear layer earlier and thus exaggerates the effect. The opposite can be noticed along the peak plane. Due to the large momentum thickness associated with elliptic nozzles at the ends of the major plane and the additional peak length caused by the lip contour, the shear layer rollup will occur further downstream. This has the effect of the shear layer rollup following the contour of the nozzle lip, which is highlighted in the flow development illustration, in Fig 4.31(a). As the main ring forms, due to the dissimilar curvature along the periphery, sections with smaller radii will move ahead of the rest. The trough V-notch parts, due to their reduced curvature, move faster forward. This was also noticed in the cross-stream LIF results in for both V-major nozzles, in Figs. 4.27 and 4.29. However due to the closeness of the V-notched segments and vortex stretching, merging occurs. The two sections break away from the main ring vortex and "cut and connect" occurs similar to what was observed by Hussain (1986).This merging effectively causes the main ring vortex to lose its elliptic planform and become more circular. The two elliptic ends have merged forming a less eccentric ellipse, similar to the effect caused by one "retarding the ends of a rubber band". This has the effect of reducing the difference in radii around the periphery of the ring vortex, thus reducing the tendency to axis-switch. This behaviour is consistent with the growth of the half jet width, which will be presented in the next section. Effectively, when the major and minor half jet widths become equal, they do not cross-over but continue to grow equally, similar to the behaviour of a jet not undergoing axis-switching. These sections of the shear layer rollup, that break apart from the main ring due to the V-notch geometry, are aligned predominantly towards the streamwise direction, thus forming the trough streamwise vortices. Their presence is short because of their disconnection from the main ring vortex when the merging occurs. Due to their minimal strength, the trough s.v. can only be seen in the dye injection, visualisation method.

The braid vortices are more pronounced. They can be clearly detected in both streamwise and cross-steam flow visualisation results as well as in the cross-stream PIV results. Caused by the induced flow between two successive main ring vortices, when observed in cross-stream, these braid vortices have opposite orientation to the main ring vortices. Their direction is radially outward and help spread the flow, as seen in the flow visualisation results. Due to their upstream bending, as they cross the laser sheet, they first appear in the middle section of the jet and gradually move towards the periphery. Finally, due to the

induction and orientation of the two successive vortex rings, the braid vortices are dominant along the peak plane.

The flow illustration of the V-minor nozzle is shown in Fig. 4.31(b). Similar to the process shown in Fig. 4.31(a), the rollup initially follows the nozzle contour. As the main ring vortex propagates downstream, sections of the ring corresponding to the trough plane lag behind. However, these sections stretch, and finally become detached from the main ring vortex. The "cut and connect" method takes place for the main ring vortex, which, contrary to the V-major case, results in the formation of a main ring vortex, with an elliptic planform. This ring then behaves according to observations made by Hussain and Husain (1989) and continues to axis-switch, albeit with some delay, due to the initial complications. This has been depicted in the flow illustration, as the main ring vortex begins to bend, with the sections laying on the trough plane moving forwards faster than the rest of the filament. When the V-notch is increased, this effect is amplified and the distance over which the cut-and-connect takes place must increase, thus giving rise to a spatially delayed switch- over point. Another plausible explanation, is that when the V-notch is increased, more of the main ring vortex is stretched and separated through the "cut and connect" method. This could result in a less eccentric main ring vortex, which in turn will reduce the axis-switching velocity due to the reduced main ring induced velocities.

The formation of braid vortices takes place in a similar way to an elliptic ring without lip-modifications and thus have a rotational sense resulting in radially outward flow. For the sake of brevity, the analysis will not be repeated.

4.2.3 Qualitative results (PIV)

The elliptic reference, 120° V-major and 120° V-minor nozzles will be presented initially. PIV results along both streamwise and cross-stream directions will be shown. Finally, another two sections will follow: The first one, investigating the flow field influences caused by increasing the nozzle sharpness along the streamwise direction and the second, focusing on the influences along the cross-stream direction.

a) Reference nozzle

Figures 4.32 to 4.36, show the PIV results for the reference nozzle along major- and minor-axis planes for both streamwise and cross-stream directions.

The phase-averaged results along the major-axis view, shown in Fig. 4.32, confirm that the findings presented in the flow visualisation were accurate. The main ring vortices initially form in the shear layer of the jet and as the downstream distance increases, the vortices

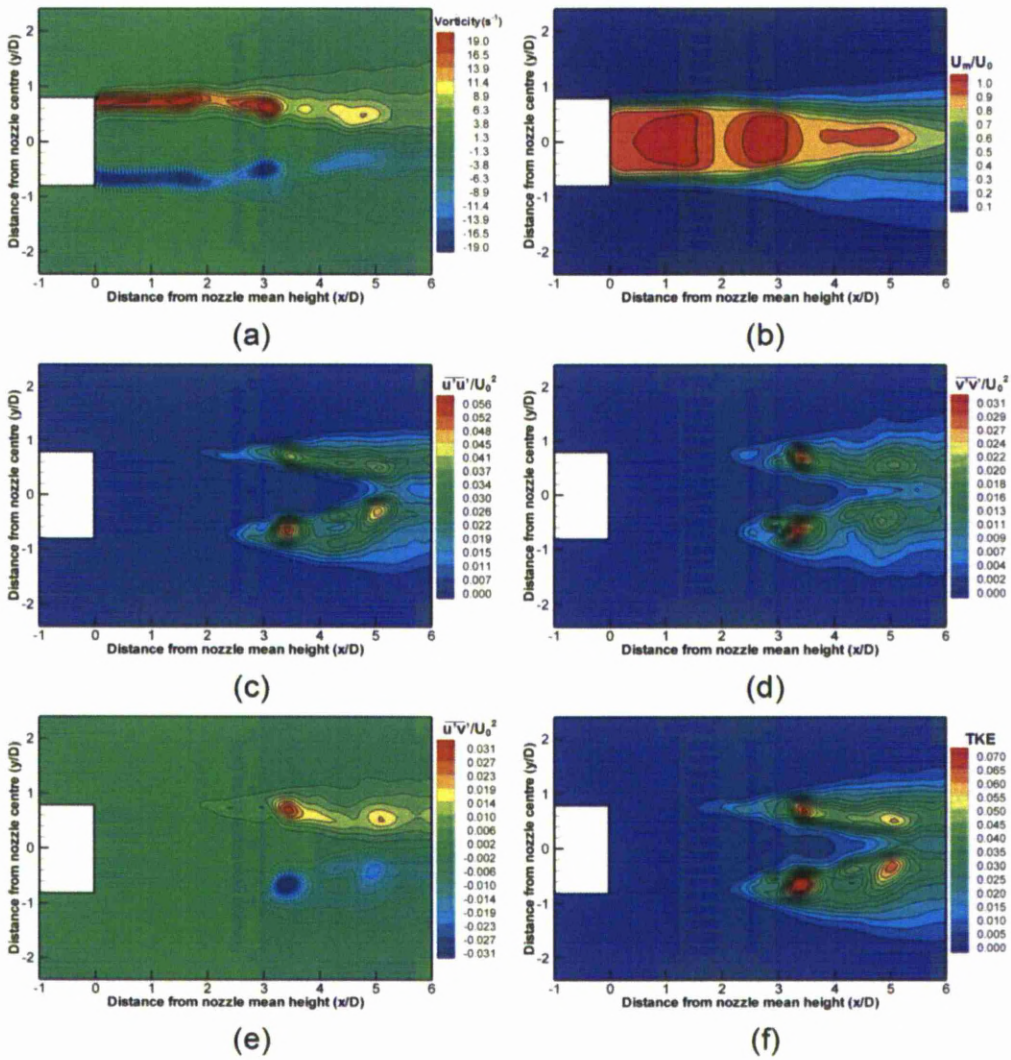

Figure 4.32 Phase averaged PIV results along streamwise direction for elliptic reference nozzle, major plane view

move laterally towards the nozzle centreline. This can be seen clearly when studying the vorticity field in Fig. 4.32(a). Regions of concentrated vorticity (vortex cores and jet shear layer) are depicted in bright red and blue. It is evident that that after approximately 2.5D, tapering-in of the jet occurs. A slight asymmetry exists in the flow field and can be seen by looking at the normalised velocity contours of Fig. 4.32(b). The bottom shear layer seems to be influenced more by the forcing than the top shear layer and thus an instability arises at 3.2D from the nozzle mean height. However when looking at the time-averaged velocity contours in Fig. 4.33(b) a symmetric flow field with no inconsistencies is show. Continuing with the phase-averaged analysis in Fig. 4.32, an interesting point can be made. Comparing Reynolds streamwise and cross-stream stresses found in Figs. 4.32(c) and 4.32(d) respectively, high levels of cross-stream Reynolds stress are located in the upstream region of the jet while high levels of streamwise Reynolds stress is also concentrated at the

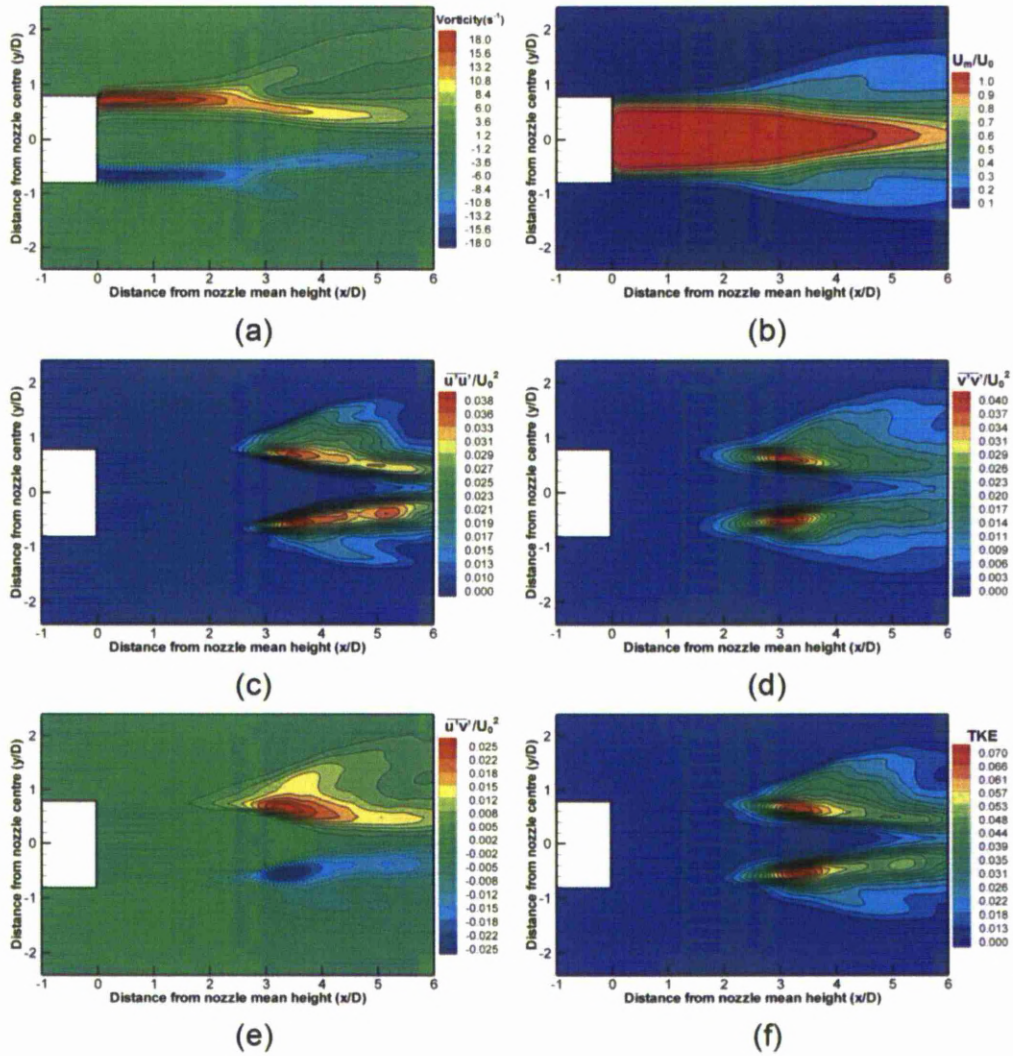

Figure 4.33 Time averaged PIV results along streamwise direction for elliptic reference nozzle, major plane view

downstream region of the jet. It therefore implies that the movement of the main ring vortices cause an increase in cross-stream stress. It has been shown that axis-switching increases the entrainment of a jet so the induced movement of the main ring vortices must also increase the velocity fluctuation and thus the flow stress. Regarding the magnitude of the two normal stresses, the streamwise component is substantial greater than the cross-stream component by approximately 55%, indicating that the direction of the main flow velocity is responsible for most of the stress generation. Influenced by the two normal components, the maximum Reynolds shear stress is found upstream at approximately 3.2D from the nozzle mean height. A second region of increased flow activity is at 5D from the nozzle mean height, which coincides with the streamwise stress component. For sake of completeness, TKE values have been plotted in Fig. 4.32(f).These values closely resemble

those of the Reynolds shear stress in which two areas of increased kinetic energy exist; one approximately 3.2D and the second 5D from the nozzle mean height.

The vorticity field shown in Fig. 4.33(a) highlights a distinguishable flow feature worth noting. As shown in the previous chapter when the A- and V-notched nozzles were presented, the top and bottom shear layers "fork" at approximately 3D from the nozzle mean height (or exit in this case). This can be attributed to the rib-structures and the combined movement of the main ring vortices. The inner part (towards the centreline) of the fork structure is caused by the inward movement of the main ring vortices along the major-axis plane while the outer section of the structure is caused by the diverging rib-structures. Although the streamwise vorticity cannot be calculated along the streamwise view, the area of influence due to the formation and interaction of the rib-structures with the jet, is detected. As stated earlier, the velocity field is symmetric and disturbances to the 0.4 contour are in the top and bottom half of the jet. These disturbances could be caused by the outward direction or the streamwise vortices. The stress field and TKE structuring are similar to what was described for the phase averaged results and for the sake of brevity will not be analysed further. A final point worth mentioning is that the stress values for both streamwise and cross-stream normal Reynolds components are reduced compared to the phase-averaged case. Also, in the time-averaged case both streamwise and cross-stream components have similar values. From the above it can be deduced that the high streamwise stress must be influenced by the individual vortices.

Viewing the phase-averaged vorticity field along the minor-axis plane also agrees well with the flow visualisation findings presented earlier. The main ring vortices diverge away from the nozzle centreline with increasing downstream distance. Comparing minor- and major-axis planes in Figs. 4.34(a) and 4.32(a) respectively, it can be shown that, at approximately three jet-diameters downstream from the nozzle mean height the jet undergoes axis-switching. The distance from the main ring vortices to the nozzle centreline is equal for both of the views. Reinforcing this analysis is the fact that in the downstream region of $2.5<x/D<3$ the LIF cross-stream results indicate a round jet as shown in Fig. 4.21 which was presented earlier. Of particular interest are the secondary vortices detected close to the centreline of the jet, approximately five jet-diameters downstream of the exit. The occurrence of these vortices does not fit the flow model proposed by Dhanak and Debernardinis,(1981). These regions of high shear are caused by jet fluid being entrained by the main ring vortices along the major-axis plane as described in the previous section and were identified as green patches close to the centreline of the nozzle in Fig. 4.12. The phase-averaged normalised velocity plot in Fig. 4.34(b) shows a symmetric flow field. Even the

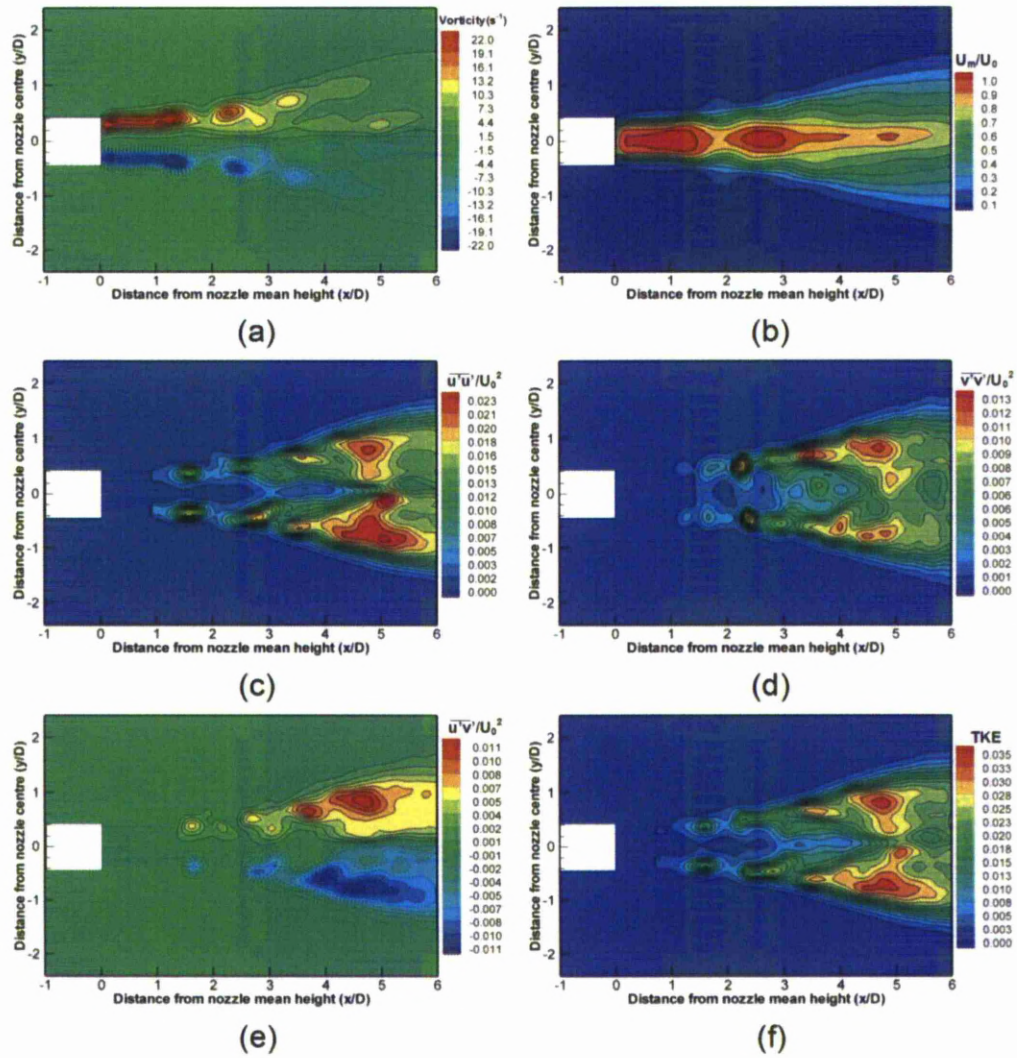

Figure 4.34 Phase averaged PIV results along streamwise direction for elliptic reference nozzle, minor plane view

shear layer disturbances are almost a mirror image with respect to the nozzle centreline. Regions of high flow activity for both Reynolds streamwise and cross-stream normal stress values are found in the downstream region of the jet ($4<x/D<5.5$). The streamwise stress component is excited by the main ring vortices, but also by the high shear region close to the nozzle centreline. Thus a region of high stress activity exists in the downstream region of the jet that extends laterally from the shear layer (caused by the main ring vortices) to the nozzle centreline (caused by entrained jet fluid). The cross-stream component is mostly affected by the entrainment of ambient fluid due to the rotation of the main ring vortices in the shear layer of the jet. The contribution of both streamwise and cross-stream stresses are shown in the Reynolds shear stress plot in Fig. 4.34(e). Most of the high stress region is located along the jet shear layer in the downstream region of $3.5<x/D<5$. The highly energised region of

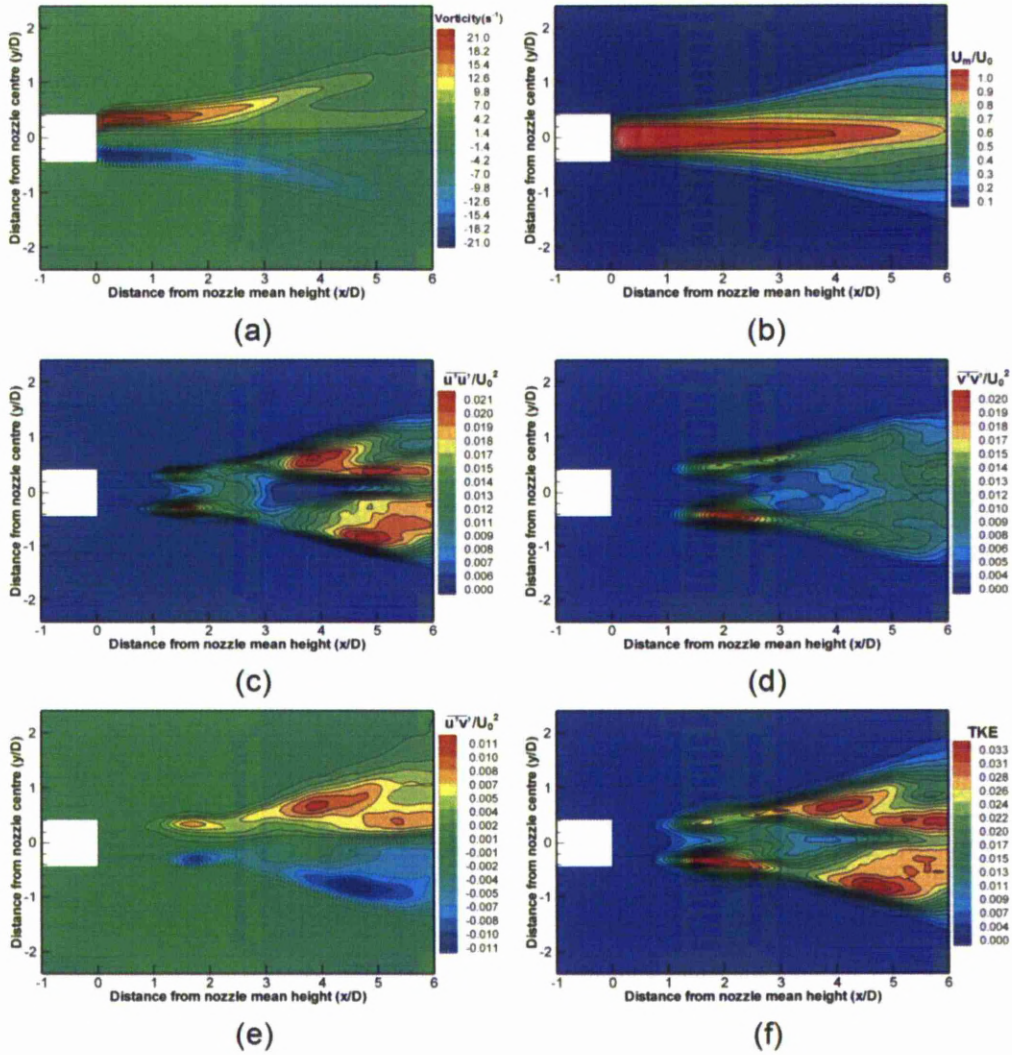

Figure 4.35 Time averaged PIV results along streamwise direction for elliptic reference nozzle, minor plane view

the flow however is in a narrow band between 4.2<x/D<5 that extends from the jet centreline to the shear layer, as shown in Fig. 4.34(f). Compared to the major-axis plane, all Reynolds stress and TKE values are reduced.

Similar to the major-axis plane, a "fork-like" shape is also seen along the minor-axis plane, in the time-averaged vorticity plot shown in Fig. 4.35(a). This forking, which is located in the shear layer of the jet, is caused by the conjunction of two parameters. The divergence of the main ring vortices away from the jet centreline and the persistent high shear found close to the nozzle centreline at downstream locations. Along this view the jet-spread increases drastically, due to axis-switching, and the final jet spread values are comparable between both planes. The potential core of the reference nozzle extends to approximately 5.2D downstream of the nozzle mean height. The time-averaged stress and TKE plots show a

slight difference compared to the phase-averaged results. The difference in maximum attainable stress levels between streamwise and cross-stream Reynolds normal stress is reduced, while Reynolds shear stress and TKE values are similar in magnitude. The streamwise stress has two distinct sections where high magnitudes are found, at x/D=1.2 and x/D=3.5-5, while on the other hand, the cross-stream stress regions have a noticeable upstream shift, albeit with an asymmetry between the top and bottom shear layer. This upstream shift shows that the cross-stream stress is driven by the ambient fluid entrainment caused by the main ring vortices. These vortices are stronger in the near-field of the jet as seen in Fig. 4.35(a) and thus have a larger effect on the near-nozzle flow entrainment. However, most of the contribution towards the Reynolds shear stress is made by the Reynolds normal streamwise stress component. It can be seen that the major flow activity is driven by the formation of the main ring vortices and the entrained jet fluid in the downstream region of the jet. Finally, an upstream shift of the TKE field also takes place. The time-averaged TKE plot closely resembles that of the Reynolds shear stress and thus could be driven by the same flow features.

Viewing both phase averaged and time-averaged cross-stream PIV results shown in Figs. 4.36 and 4.37 respectively, similar flow features can be distinguished. Gross flow features such as the evolution of the jet cross-sectional shape and axis-switching are evident in the velocity fields in both cases. Focusing on Fig. 4.36 initially, the effect that distinct vortices have on the jet cross-stream, vorticity and flow stresses is highlighted. Comparing velocity and vorticity plots shown in Figs. 4.36(a) and 4.36(b) as well as streamwise vorticity plots, a dominant main ring vortex exists in the region $1<x/D<2$. As expected, inward flowing velocity is captured upstream of the main ring vortex (x/D=1) and outward flowing velocity downstream of it (x/D=2). Interestingly though, at x/D=2 along the minor-axis plane (top-bottom) inflow is detected. As a consequence, the vorticity contours in Fig. 4.36(b) have a similar rotational sense, indicating outflow along the major-axis plane and inflow along the minor-axis plane. The TKE and flow stresses do not seem to be affected largely by the first dominant main ring vortex as regions of high flow activity are situated further downstream ($3<x/D<5$) where axis-switching, main ring vortex breakdown and streamwise vortices are dominant flow features.

The time-averaged cross-stream results shown in Fig. 4.37 compared to the phase-averaged results presented above, show small differences in the flow field due to the absence of localised flow disturbances in the form of main ring vortices. Changes in the cross-sectional shape on the jet body as well as evidence of axis-switching can be seen when looking at the velocity field in Fig. 4.37(a). Apart from the change in cross-sectional shape, evidence of

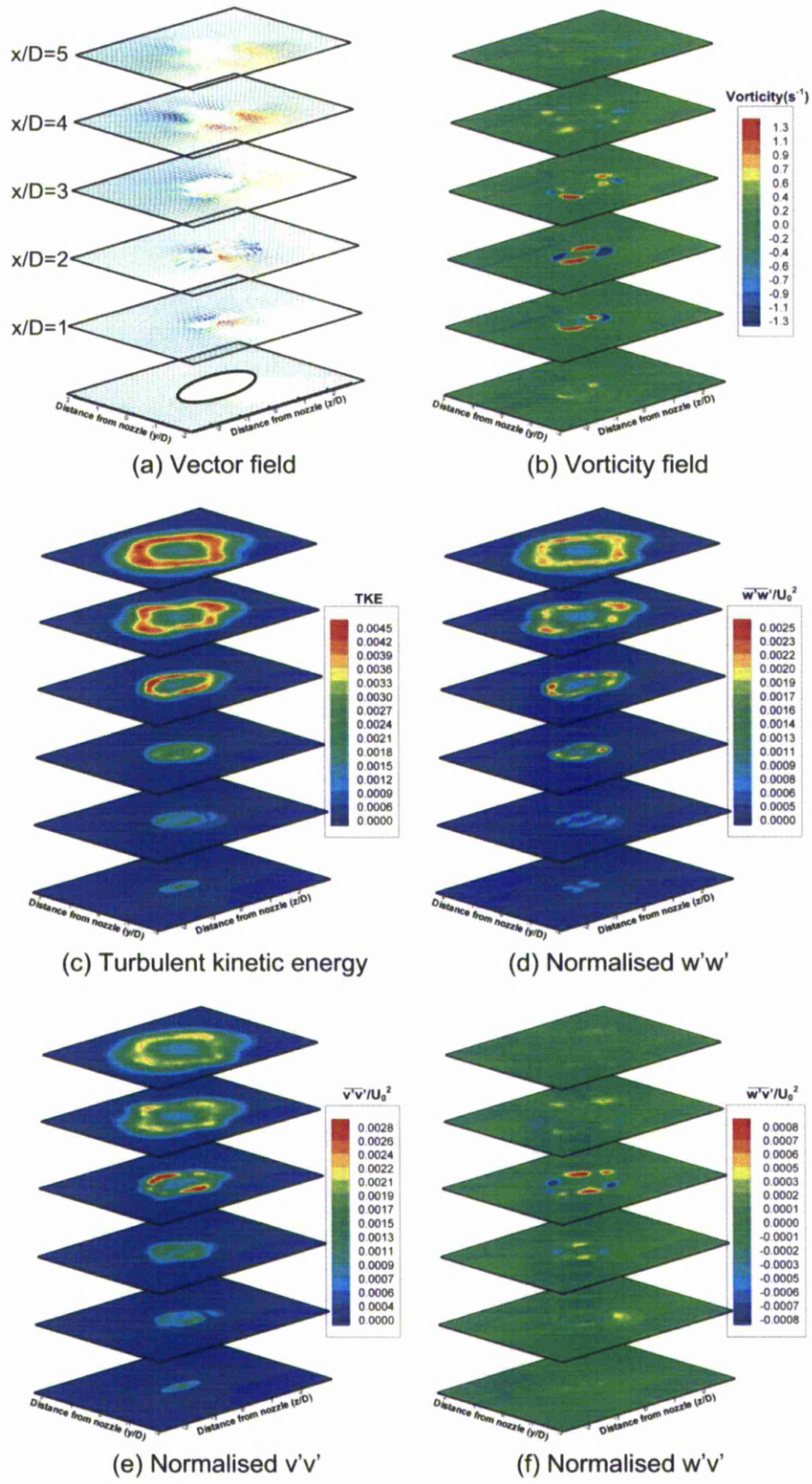

Figure 4.36 Phase averaged PIV results along cross-stream direction for elliptic reference nozzle

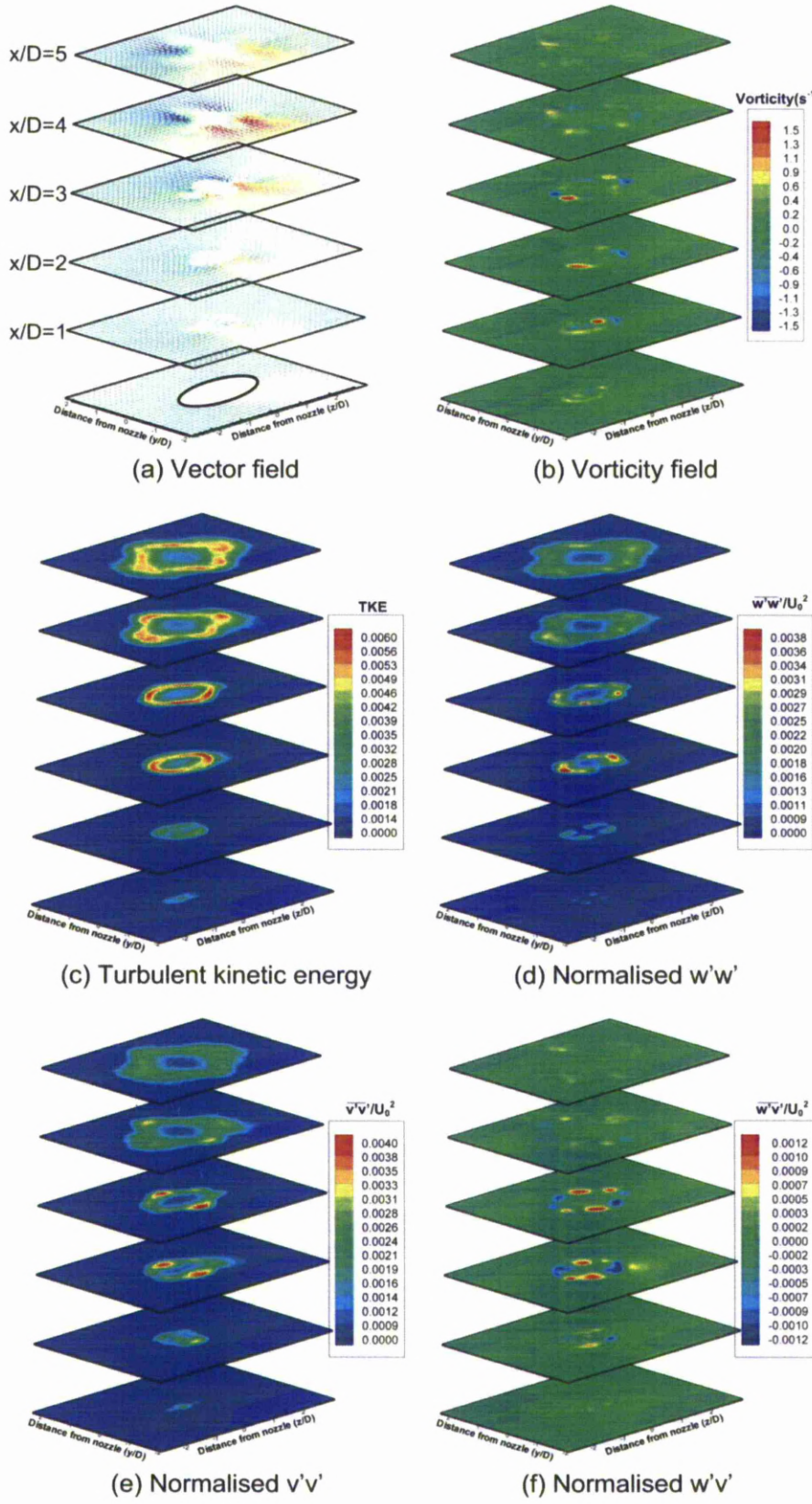

Figure 4.37 Time averaged PIV results along cross-stream direction for elliptic reference nozzle

outward-flowing streamwise vortices can be detected, especially at x/D=3. At the same cross-stream location the maximum vorticity is attained which is in agreement with streamwise and cross-stream LIF results presented earlier and shown in Figs. 4.20(a) and 4.21(g) respectively. Relatively weak streamwise vortices exist along the minor-axis plane but their rotational sense suggests outflow which is in accordance to the axis-switching phenomenon. As the cross-stream distance increases, the streamwise vortices reduce in magnitude and spread away from the nozzle centreline. Maximum attainable TKE values are found within the periphery (shear layer) of the jet and at a downstream distance of 2D from the nozzle exit. Relatively high TKE values (approximately 80% of maximum TKE value) are present throughout a wide region up to the last measurement plane (x/D=5). All maximum Reynolds stress regions on the other hand, are concentrated within a narrow distance (2<x/D<3) possibly affected dominantly by the main vortex ring motion.

b) 120 V-Major nozzle

Differences between reference and the 120° V-major PIV results, shown in Fig. 4.38, are not as drastic as one may think having previously seen the flow visualisation results. The main ring vortices form at similar locations and with similar magnitude to the reference case. The individual vortices do not move toward the nozzle centreline to the extent of the reference case, but movement in that direction is clearly evident. A small asymmetry between the top and bottom shear layer can be detected when observing the normalised velocity contours in Fig. 4.38(b). Similar to the reference case, the small asymmetry is more prone to manifest along the major-axis plane view. Two regions of high Reynolds shear stress exist; one located close to the periphery of the jet at approximately 3D from the nozzle mean height and another closer to the nozzle centreline at a downstream location of x/D=4.6. The first region achieves higher flow activity than the second due to the fact that both streamwise and cross-stream normal Reynolds stress components contribute to the formation of it as can be seen in Figs. 4.38(c) and 4.38(d) respectively. The second region is mainly influenced by the streamwise stress component, which is persistent even at downstream locations. Reynolds stresses and TKE are mainly driven and influenced by the position and strength of the main ring vortices.

A shorter potential core and a wider spreading is detected when comparing the time-averaged results of the 120° V-major to the reference case. The higher mixing associated with this particular nozzle causes a breakdown of the large-scale coherent structures as well as entrainment of ambient fluid which both contribute to spreading and shortening the potential core of a jet. A subtle "forking" takes place along the top and bottom shear layer which is caused by the combined movement of the main ring vortices towards the centreline

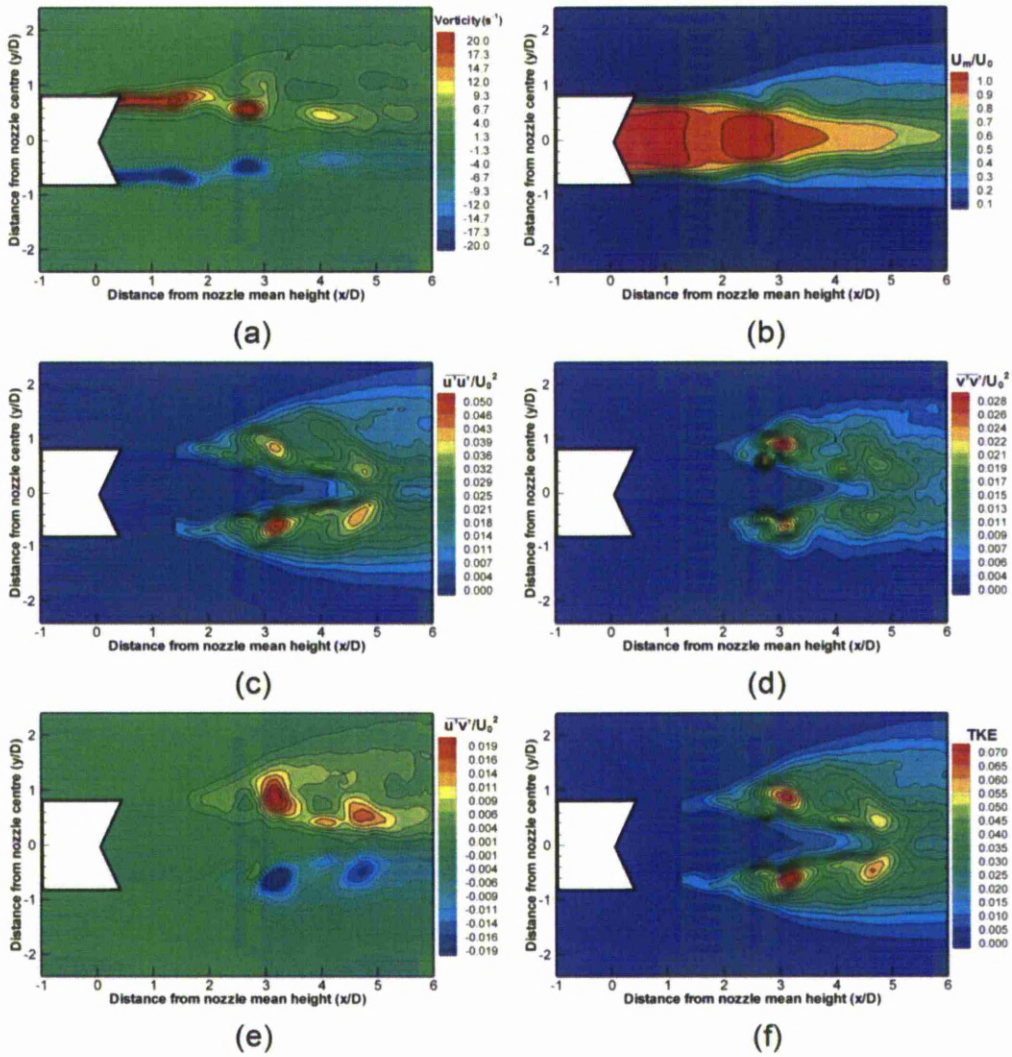

Figure 4.38 Phase averaged PIV results along streamwise direction for 120° V-major nozzle, major plane view

and the spreading of the streamwise vortices formed at the peaks of the nozzle. Most of the vorticity is dissipated in the near-field region of the jet and this also affects the Reynolds stress and TKE fields. Contrary to the reference case, only one region containing maximum streamwise and cross-stream components of the Reynolds stress is found. The location of this region is further upstream when compared to the reference case. The reason for the upstream shift of the streamwise stress component is due to the fact that most of the turbulence is generated at the end of the high vorticity region ($x / D \cong 3$) affected also by the formation of the peak streamwise vortices. Finally and more importantly, the jet centreline velocity drops rapidly after the end of the short potential core. As the jet velocity is the main contributor towards the streamwise Reynolds stress component, a reduction in the downstream region can be expected. It follows that most of the high magnitude Reynolds

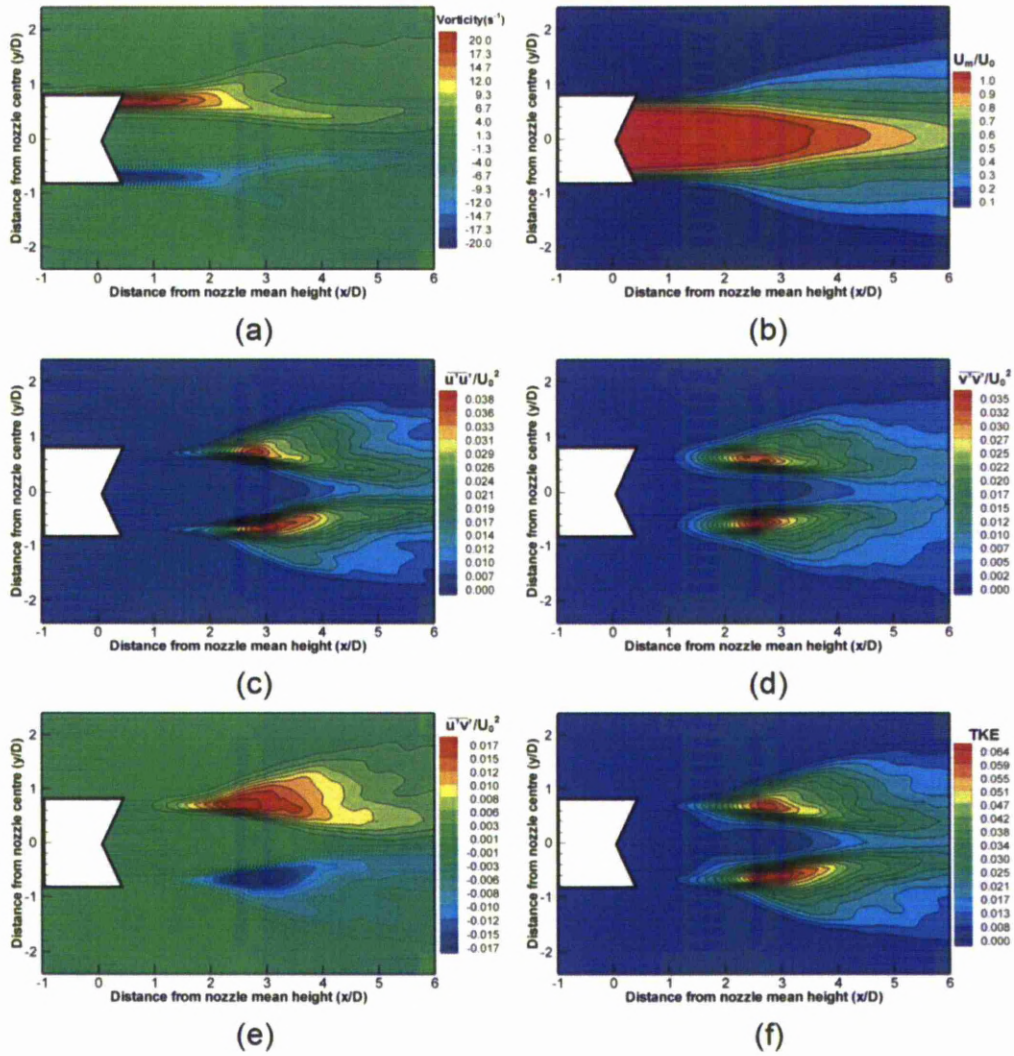

Figure 4.39 120 Time averaged PIV results along streamwise direction for 120° V-major nozzle, major plane view

shear stress is dissipated within the region (2<x/D<2.3), while the maximum TKE region is confined within (2.5<x/D<3.2).

Similarities between the reference and the 120° V-major nozzle are noticed when the resultant flow-fields are viewed along the minor-axis plane. The gross flow features such as movement of the main ring vortices and jet-spread are comparable. Viewing the phase-averaged vorticity field in Fig. 4.40(a), outward spreading of the main ring vortices and spreading of the jet is seen. The V-notched cut imposed on the nozzle does not affect the main ring vortex formation and movement greatly, while the vorticity field has similar magnitude values to the reference case. A set of secondary vortices is observed close to the nozzle centreline and approximately five diameters from the nozzle mean height. This finding, is in agreement with the LIF flow visualisation shown in Fig. 4.14, however with a

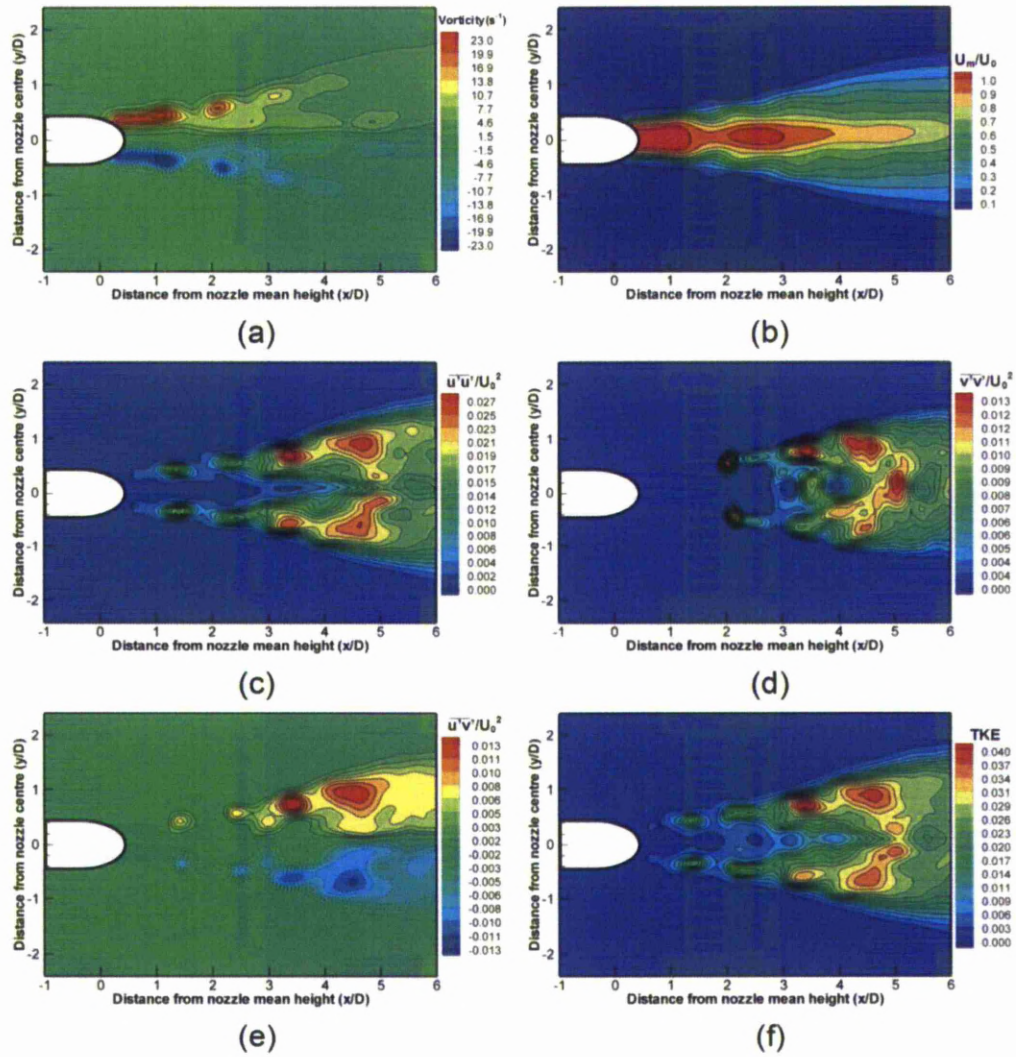

Figure 4.40 Phase averaged PIV results along streamwise direction for 120° V-major nozzle, minor plane view

small discrepancy in the downstream distance. The symmetricity of the forcing is shown in the normalised velocity plot in Fig. 4.40(b), where disturbances along the top shear layer are also present in the bottom. Similar to the vorticity field, the Reynolds stress and TKE structuring and magnitude levels are comparable to the reference case and thus a brief description in given. A good correlation between the individual vortex rollups and high stress levels is detected and thus high flow activity is observed close to the periphery of the jet (within the jet shear layer) and only manifests close to the nozzle centreline at the far downstream location.

Along the minor-axis plane, a high dissipation rate of vorticity is evident due to the fact that most of the high-magnitude vorticity has diffused by x/D=1.5 as seen from the time-averaged results in Fig. 4.41(a). Also, due to the combined movement of the main ring

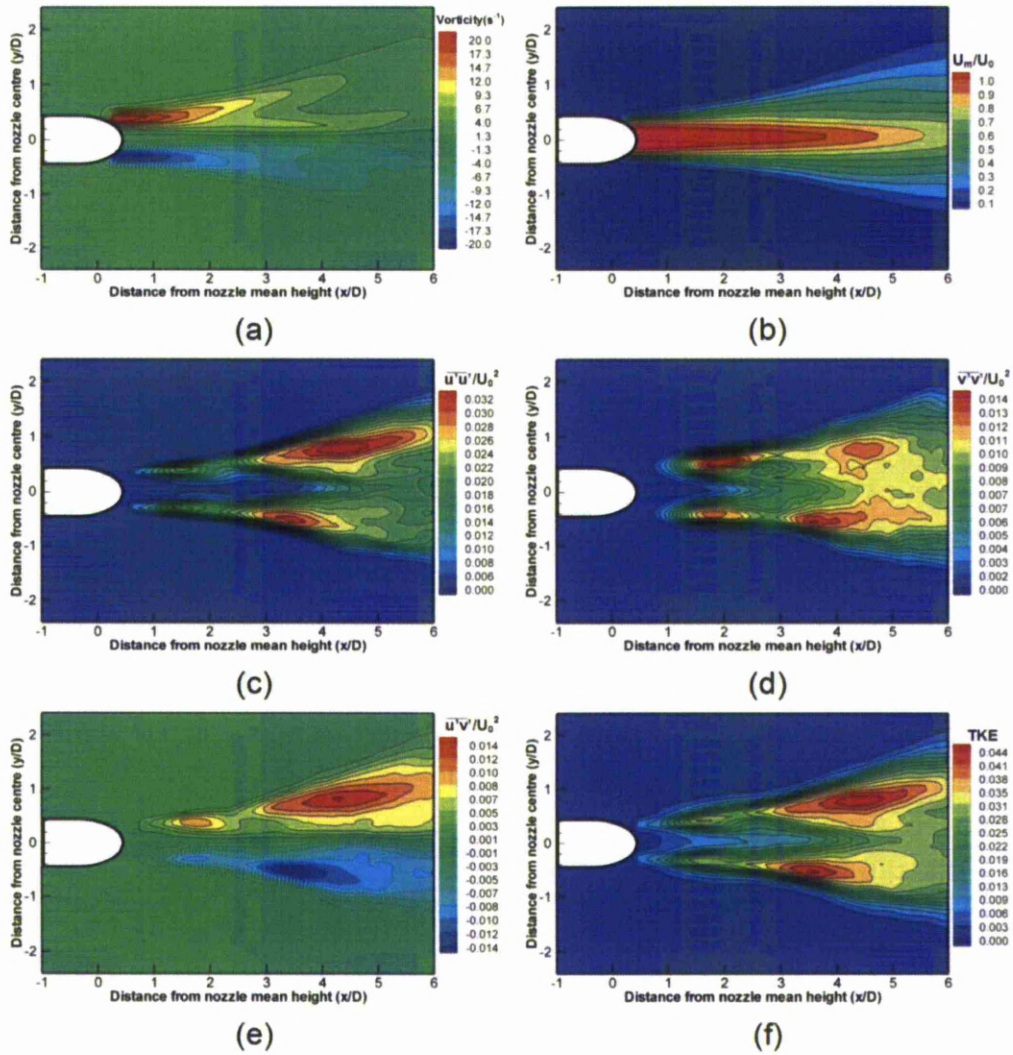

Figure 4.41 Time averaged PIV results along streamwise direction for 120° V-major nozzle, minor plane view

vortices and the entrained jet-fluid, a small amount of "forking" takes place within the jet shear layer. The jet spread growth rate is also comparable to the reference case although the potential core of the jet is reduced by approximately 0.5D thus only extending to 4.6D from the nozzle mean height. The time-averaged cross-stream Reynolds stress component as well as the TKE field, show different flow activity with respect to the reference case (Figs. 4.41(d) and 4.35(d) respectively). Two regions, as opposed to one in the reference case, exist where the cross-stream stress achieves maximum values; one in the near-field (x/D=1.7) and one in the far-field (x/D=4). The first region is possibly influenced by the formation of strong main ring vortices that entrain ambient fluid and the second region must generate turbulence due to the breakdown of the main ring vortices into smaller eddies. All of the high magnitude TKE regions are concentrated in the far-field region of the jet possibly

caused again by the influence due to the breakdown of the main ring vortices. Interestingly though, a region of high TKE activity in the vicinity of the nozzle exit does not exist. On the other hand the streamwise Reynolds stress component and the Reynolds shear stress component are similar in magnitude and formation to the reference case.

The notion of reduced axis-switching ability and higher flow turbulence generation within the near-field of the jet is observed in both phase- and time-averaged cross-stream plots, shown in Figs. 4.42 and 4.43 respectively. By comparing the streamwise to the cross-stream results, the formation of the first main ring vortex can be assumed to be situated in the region,$1<x/D<2$.The first cross-stream measurement plane ($x/D=1$) is dominated by inflow of ambient fluid due to the suction caused by the influence of the main ring vortex situated immediately downstream of the plane as seen in Fig. 4.42(a). However the second measurement plane ($x/D=2$) has evidence of inflow and outflow, again as a result of the main ring vortex situated upstream of the plane position. Inflow is present along the troughs of the nozzle, while outflow is seen at the peak locations. As the downstream distance increases this flow pattern continues exist, while the jet body changes shape towards a more circular shape. However, only the first main ring vortex is strong enough to produce effects that can be measured in the vorticity plot shown in Fig. 4.42(b). The forcing in conjunction with the subtle nozzle lip modifications produce strong flow field effects at the peak locations but not at the sharp troughs. Outward oriented streamwise vortex pairs form at the peak locations as shown in Fig. 4.42(b), however due to the rapid breakdown of the main ring vortices in the near-field region of the jet, streamwise vorticity is not detected in the far-field region this however could also be due to measurement resolution limitations. On the other hand, the TKE field is more active at the far-field regions of the jet as seen in Fig. 4.42(c). The faster breakdown of the large scale coherent structures is responsible for increasing the velocity fluctuations. A distinct difference between both cross-stream Reynolds stresses is seen when looking at Figs. 4.42(d) and 4.42(e). The v'v' stress component is driven by the main vortex rings but also by the streamwise vortices generated at peak locations as is clearly noticed when looking at the $x/D=3$ measurement plane. High stress levels are detected throughout the measurement domain. Similar stress levels are detected in the w'w' stress component however within a smaller the region in the near-field of the jet. Similarly the Reynolds shear stress activity is also contained in the near-field region $x/D<2$. Interestingly regions of high Reynolds shear stress coincide with peak and trough locations thus indicating that the sharp throughs augment the generation of turbulence.

The differences between phase- and time-averaged results highlight the effect that individual vortices have on the flow field. Figure 4.43 shows the resultant time-averaged fields

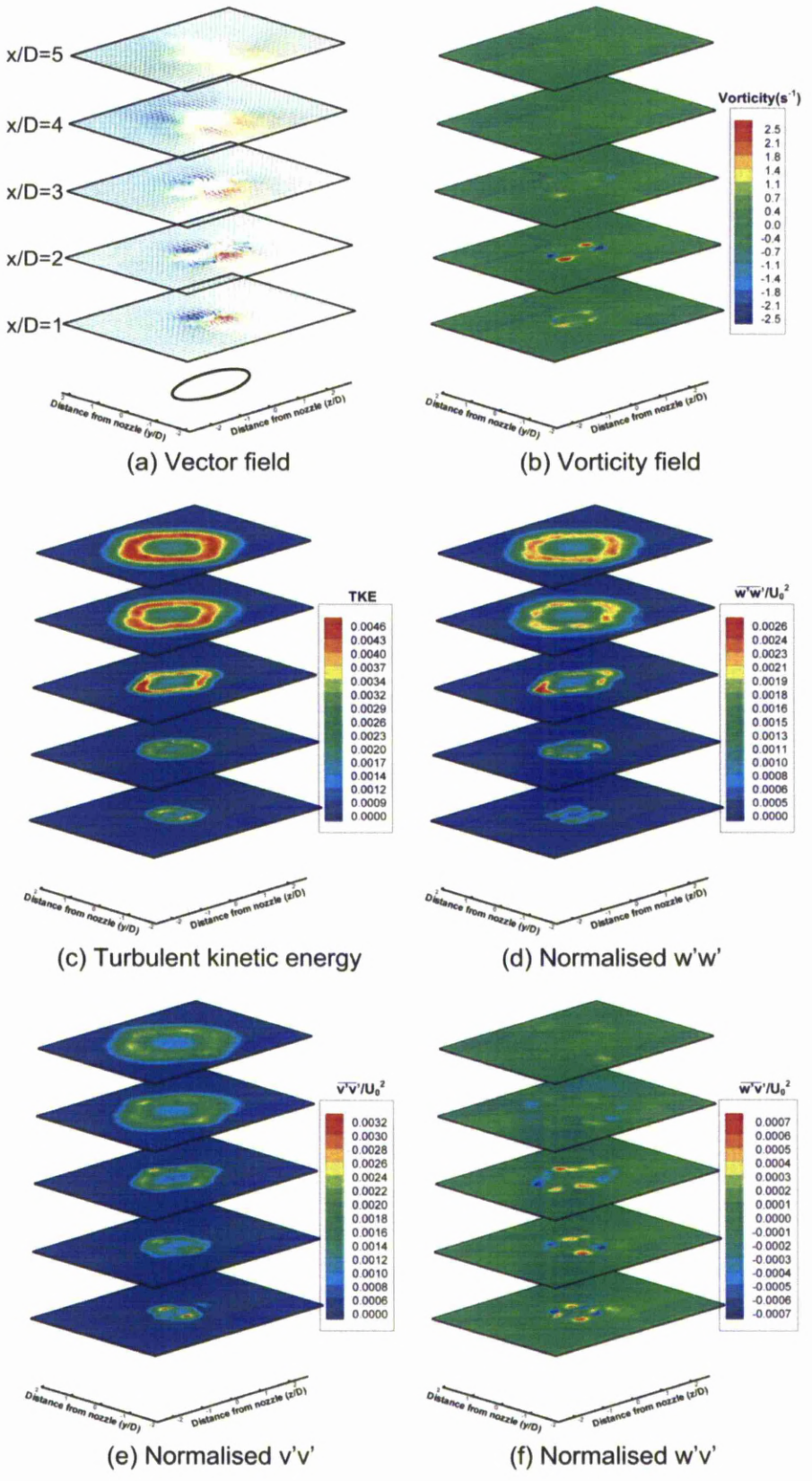

Figure 4.42 Phase averaged PIV results along cross-stream direction for 120° V-major nozzle

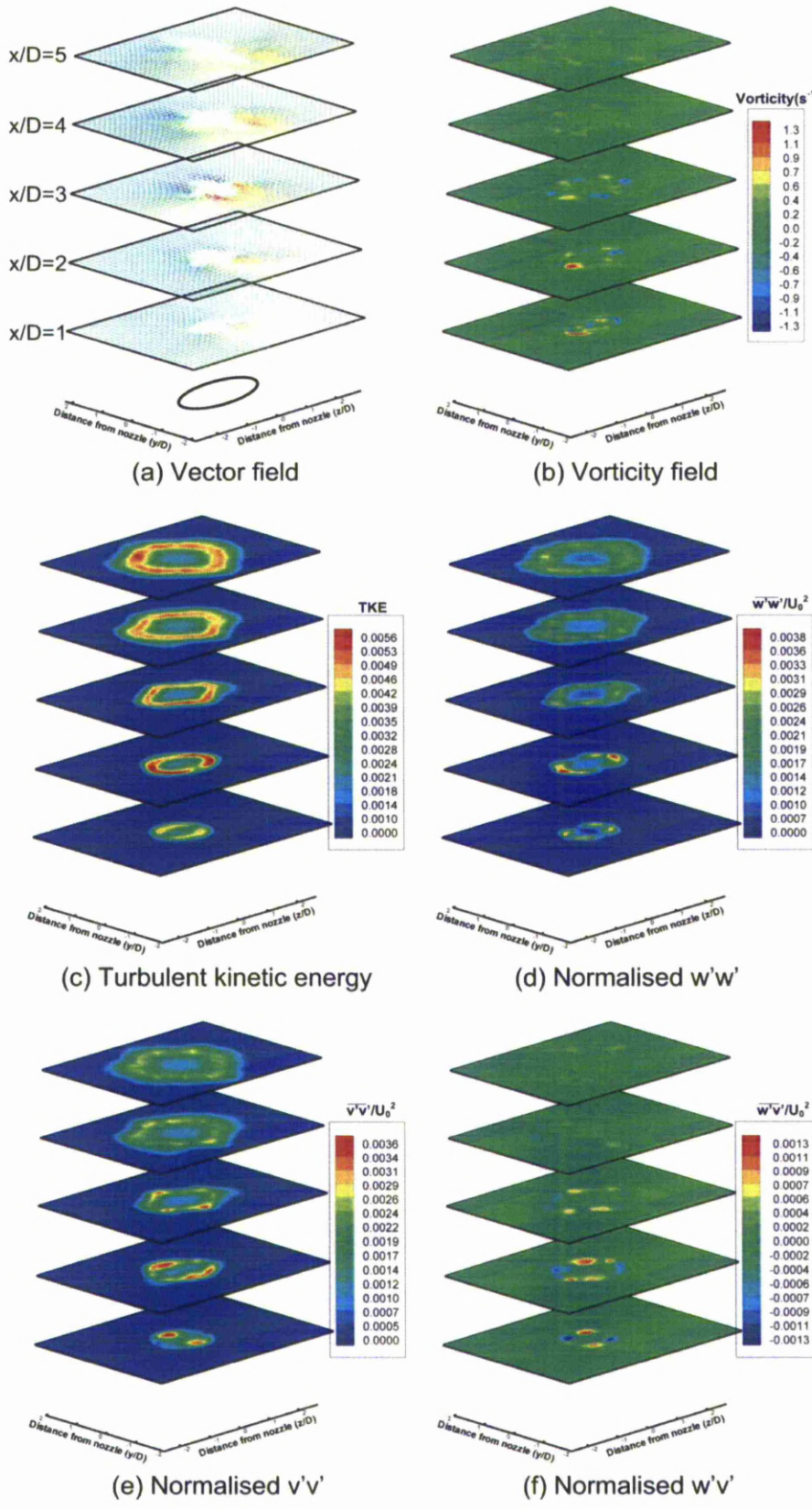

Figure 4.43 Time averaged PIV results along cross-stream direction for 120° V-major nozzle

obtained from testing the 120° V-major nozzle. Compared to the reference case, a general upstream shift of the flow activity is observed. As stated previously, this shift or faster flow development, may be due to the faster breakdown of the large scale structures (main ring vortices). Comparing the vorticity field to the reference case, high streamwise vorticity is achieved approximately one diameter further upstream. The peak in vorticity magnitude correlates well with the formation of streamwise vortices. As shown in the flow visualisation section, nozzle peaks promote faster development of streamwise vortices and thus visually they form in upstream locations compared to the reference case. Although in flow visualisation sections, visually larger vortices were captured, this does not result in stronger cores, but rather in a redistribution of the streamwise vorticity levels along the jet column (x-direction).

c) 120 V-minor nozzle

In this section, the 120° V-minor nozzle will be analysed. Figures 4.44 and 4.45, show the streamwise results along the major plane view, while Figs 4.46 and 4.47 show results obtained along the minor plane view. Figures 4.48 and 4.49 depict the phase-averaged and time-averaged cross-stream results.

Studying the vorticity plot of the phase averaged results along the streamwise direction, a delay in the formation of the main ring vortex is observed compared to the reference case. Additionally, a slight delay in the convergence of the main ring vortices is also apparent, indicating that a delay in axis-switching is likely. A small flow asymmetry can be seen in bottom shear layer of the jet at approximately three jet-diameters downstream from the mean height. This asymmetry, although persistent, does not cause concern as it is not present in the time-averaged results. Worth noting, are the high velocity regions which coincide with the main ring vortices. These regions are formed by the high induced velocity of the main ring vortices.

The stresses are mostly driven by the second set of vortices at location x/D=3. In particular, the cross-stream Reynolds stress component in Fig.4.44(d) is maximum at the same location, indicating that most of the exchange between the jet and ambient fluid takes place in the vicinity of the second vortex pair. As expected however, the dominant stress direction is along the flow direction and results show that the streamwise Reynolds stress component is 84% larger than the cross-stream component. The Reynolds shear stress and TKE shown in Figs. 4.44(e) and 4.44(f) respectively, indicate that the production of turbulence is dominant in the far-field region of the jet and is mainly influenced by the second and third pair of main ring vortices, found at locations x/D=3 and x/D=4.5 from the nozzle mean height. Magnitudes are slightly reduced compared to the reference case.

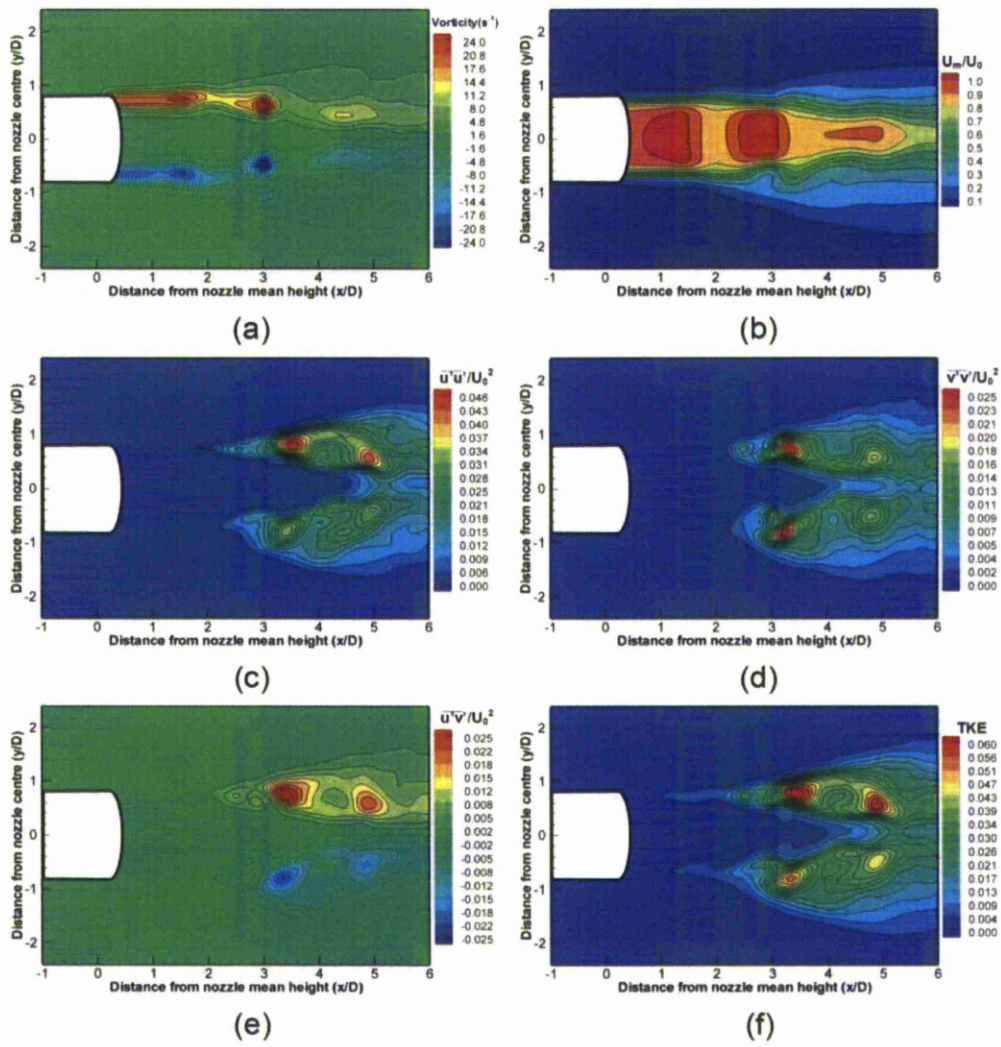

Figure 4.44 Phase averaged PIV results along streamwise direction for 120° V-minor nozzle, major plane view

The potential core of the jet can be measured from the normalised velocity contour plot in Fig. 4.45(b). Interestingly, the potential core extends nearly to the edge of the measurement

window at 5.5D from the mean height. Compared to the 120° V-major nozzle, the potential core is extended by nearly one diameter, which equals the reference case. The increased potential core is in agreement with the reduced interactions found when analysing the flow visualisation results. The flow visualisation showed that large-scale coherent structures did not break down rapidly. Increased spreading occurs at approximately x/D=2.5, which coincides with the location at which outward-spreading braid vortices form, as seen from the cross-stream LIF images presented in Fig. 4.23. The maximum vorticity levels are similar to the reference nozzle, however the range in which the vorticity dissipates is shorter. Although

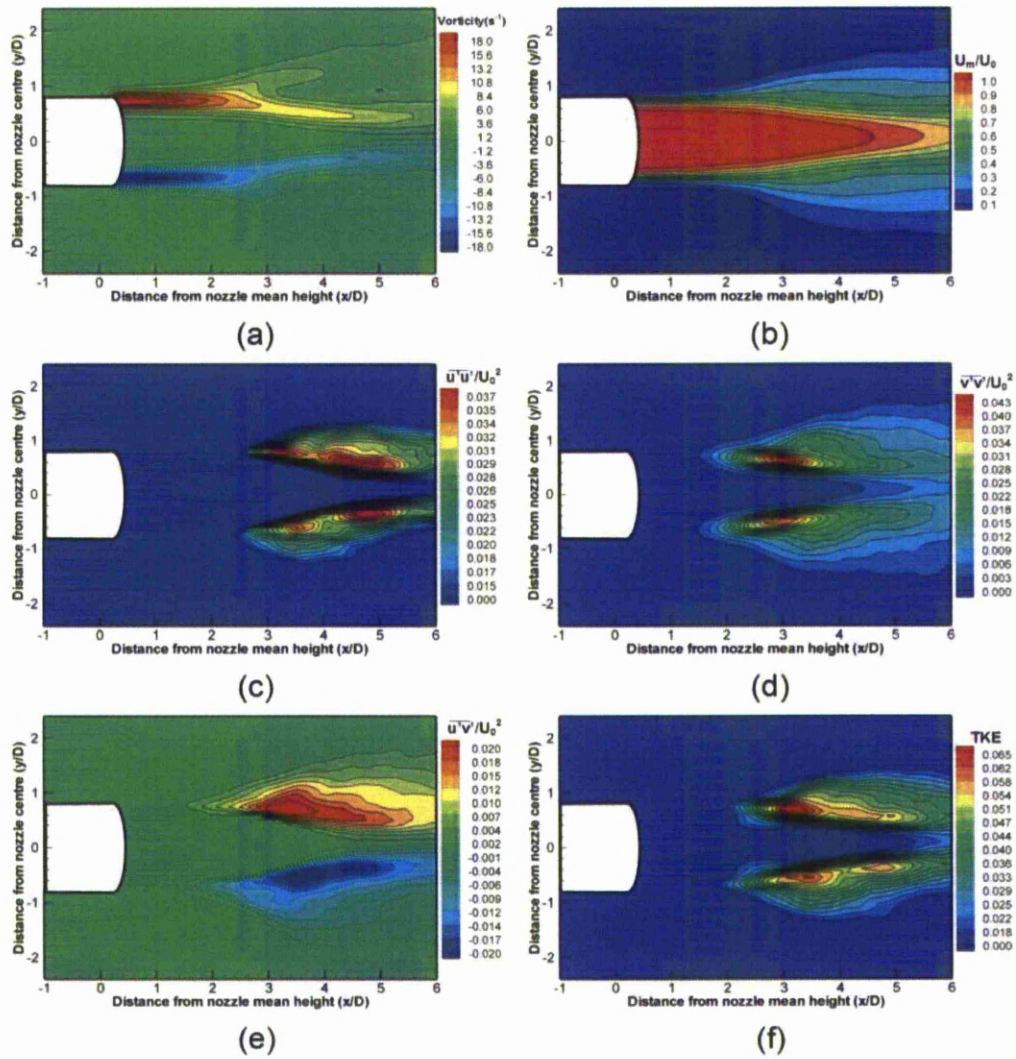

Figure 4.45 Time averaged PIV results along streamwise direction for 120° V-minor nozzle, major plane view

in the phase-averaged plots, the link between main ring vortices and stress levels was discerned, the time-averaged results help determine the range within which, maximum stress and TKE levels are found. These regions are responsible for the breakdown of large-scale structures and the generation of turbulence. Reynolds shear stress is shown in Fig. 4.45(e). In this graph, the total contribution of both cross-stream and streamwise Reynolds stress components are combined. It is shown that the range in which high stress regions exist is $3<x/D<5$, where the upstream part of the range is due to the cross-stream stress component, and the downstream part due to the streamwise stress component. A final observation, is that the maximum TKE is concentrated within a smaller range, $3<x/D<4$, which compared to both the reference and 120° V-major case, is located approximately half of a diameter further downstream, as shown in Fig. 4.45(f).

A spreading trend is noticed when looking at the phase-averaged vorticity contour plot, along the minor plane in Fig. 4.46(a). Compared to the major plane, the vorticity is higher, something that is true for all test cases. The thinner momentum thickness promotes a faster rollup and stronger main ring vortices. Along the minor plane view, maximum vorticity levels attained by the120° V-minor nozzle are higher that both reference and 120° V-major nozzle. Although the differences are not substantial, the presence of peaks in the 120° V-minor nozzle could be responsible for the discrepancy. Spreading of the vortices is apparent after the second set of the main ring vortices, after approximately 2.5D downstream, similar to the reference case. Although the main ring vortices spread away from the nozzle centreline, a region of increased shear is present at the end of the potential core, at five jet-diameters downstream of the nozzle mean height. This high-shear region is close to the nozzle centreline and could be caused by the entrainment of jet fluid, as was noticed in the streamwise LIF results shown in Fig. 4.16. Another plausible explanation is that the high shear region is caused by the convergence of the main ring vortices along the major plane view. This region however is associated with the production of large streamwise Reynolds stress levels as shown in Fig. 4.46 (c). Maximum levels of the cross-stream Reynolds stress component, on the other hand, are found further upstream, approximately at 3.5D, and are situated on the periphery of the jet. This location coincides with the location of the third row of main ring vortices. Both Reynolds shear stress and TKE maximum values are found in the downstream region of the jet, however Reynolds shear stress is mostly confined within the shear layer and the TKE is affected by the high-shear region found close to the nozzle centreline, just after the end of the potential core, at five jet-diameters from the nozzle mean height.

Similar to the phase-averaged results presented above, maximum time-averaged vorticity magnitude is also measured along the minor plane. Looking at the time-averaged vorticity plot in Fig. 4.47(a), the shear layer extends furtherer downstream that the major plane view. Forking within the shear layer is present, which as seen for other nozzles, usually occurs along the plane incorporating the nozzle peaks. The occurrence of forking corresponds to the downstream location at which the main ring vortices start to diverge away from the nozzle centreline. Additionally the streamwise vortices, although weak, may influence the shear layer formation and assist spreading. From the time-averaged velocity contour plot in Fig. 4.47(b), the symmetricity of the flow field evident. Spreading rate increases abruptly after approximately 3.5D from the mean height, which is delayed with respect to the major plane view, while the final spread is similar to the reference case. The streamwise Reynolds stress component is highest close to the nozzle centreline and in the downstream region, while the

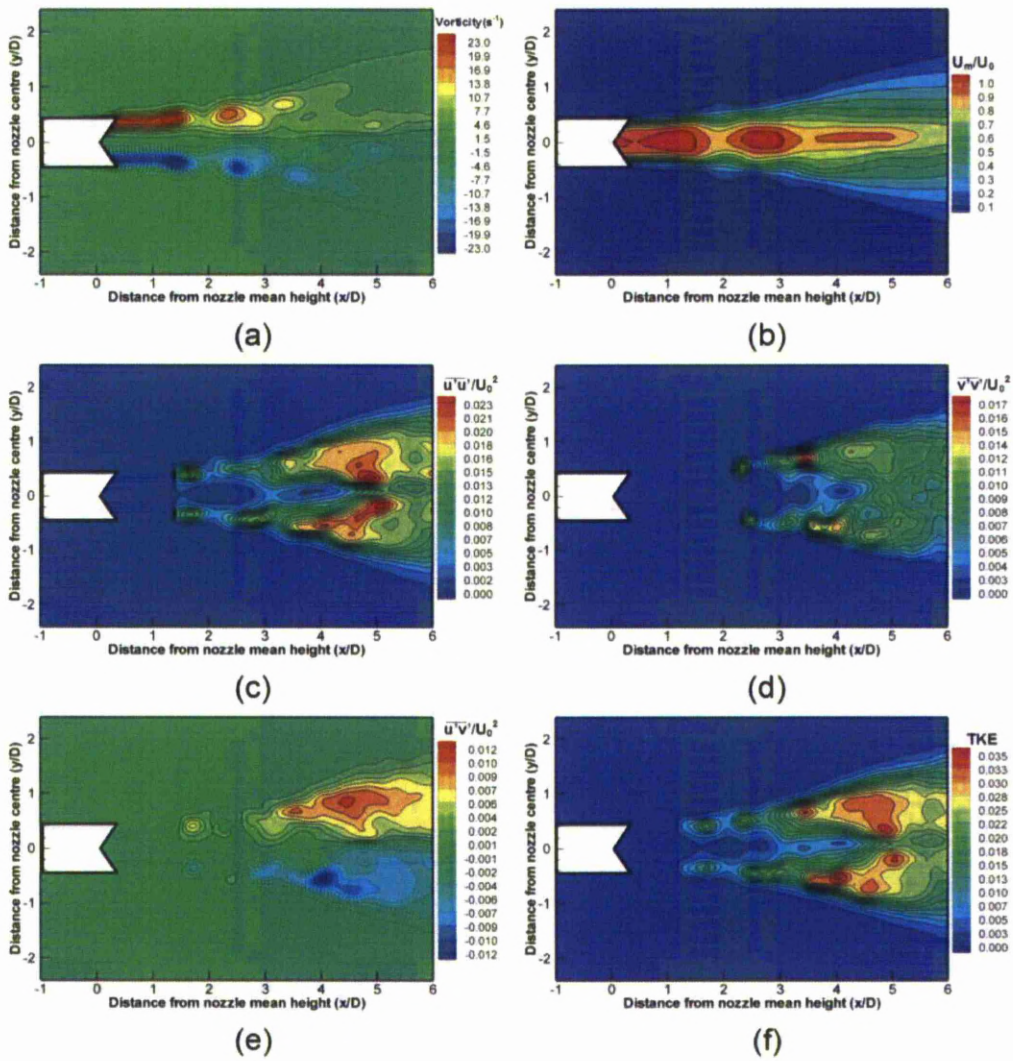

Figure 4.46 Phase averaged PIV results along streamwise direction for 120° V-minor nozzle, minor plane view

high magnitude Reynolds cross-stream stress component is situated on the periphery of the jet and further upstream, 2<x/D<3. As with all nozzles so far, along the minor plane the cross-stream stress is substantially reduced. Compared to the reference case though, relatively similar values are attained, while compared to 120° V-major nozzle, an increase of approximately 17.5% is measured. Geometries with peak along their major axis (V-minor) promote more interactions between the jet and the ambient fluid, possibly due to the generation of peak streamwise vortices. The regions within which the Reynolds shear stress and TKE plots are maximum are quite similar and develop in the downstream range, of 3.5<x/D<6. Initially Reynolds shear stress and TKE are driven by the main ring rollups found in the periphery of the jet, at approximately 3.5D. However, further downstream at 5.5D, the fluid interactions which take place close to the nozzle centreline play a major

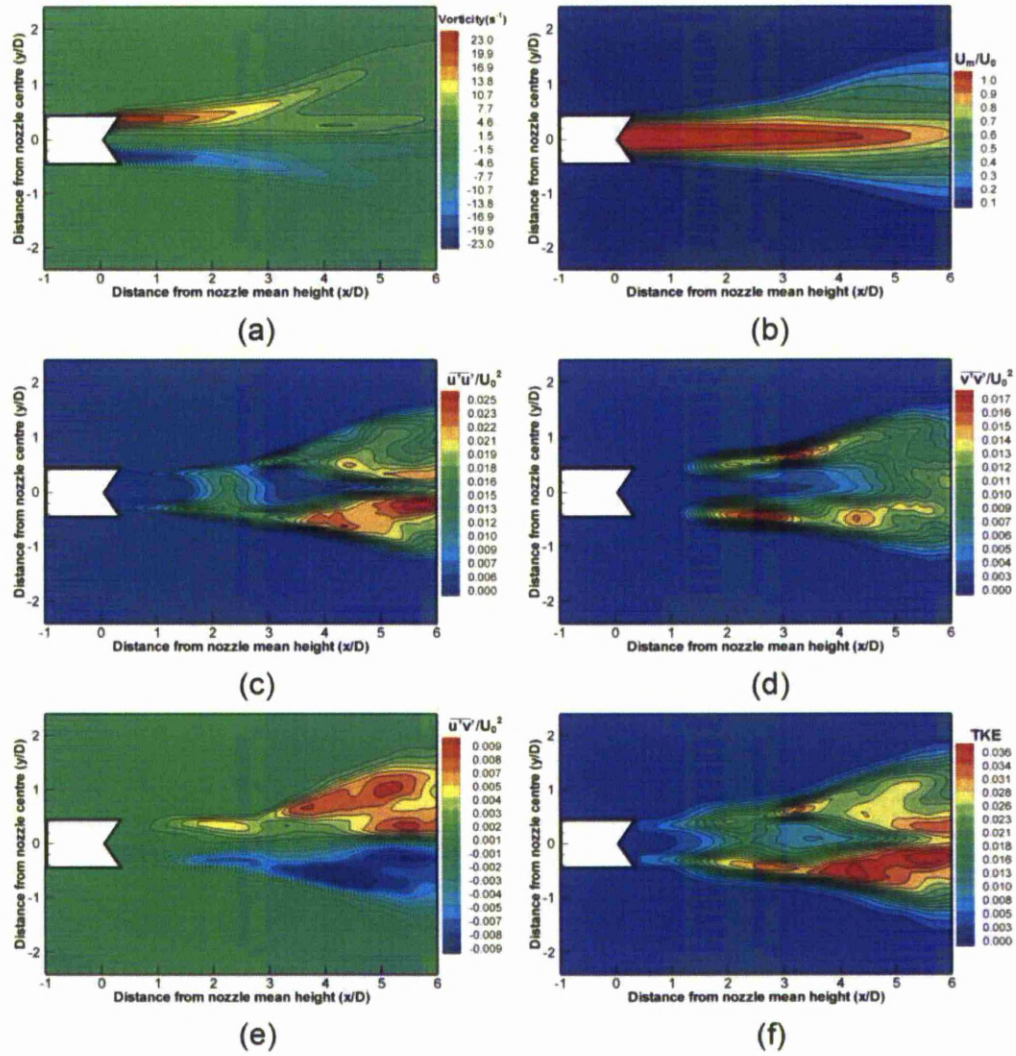

Figure 4.47 Time averaged PIV results along streamwise direction for 120° V-minor nozzle, minor plane view

factor towards turbulence generation. Worth noting is that apart from vorticity, the stress and TKE values along the minor plane view are reduced when compared to the major plane view.

Viewing the stacked velocity vector plots in Fig. 4.48(a) shows that, as the jet propagates downstream an increase in spreading along the minor plane is observed. This was also noticed during the presentation of the streamwise results. Moving on to the vorticity plot shown in Fig. 4.48(b), the streamwise vortices are clearly discernible at the third measurement plane, x/D=3. However, they might also exist further upstream, at x/D=2, as seen from the flow visualisation results presented earlier, but not appear on the measurement plane. The reason for them not appearing is that they might be obscured by the entrained fluid of the main ring vortex. As described in earlier sections, the position of the main ring

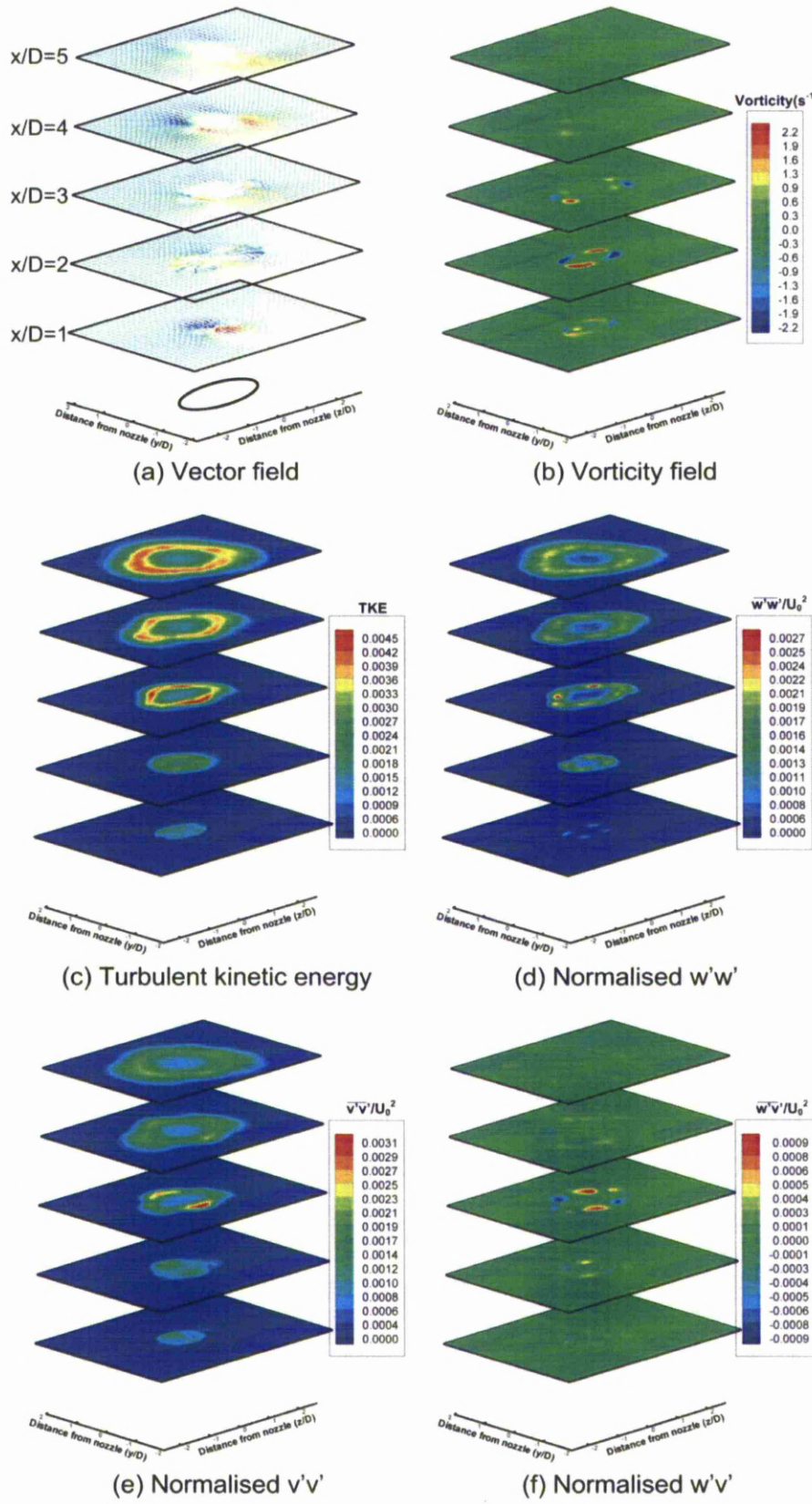

Figure 4.48 Phase averaged PIV results along cross-stream direction for 120° V-minor nozzle

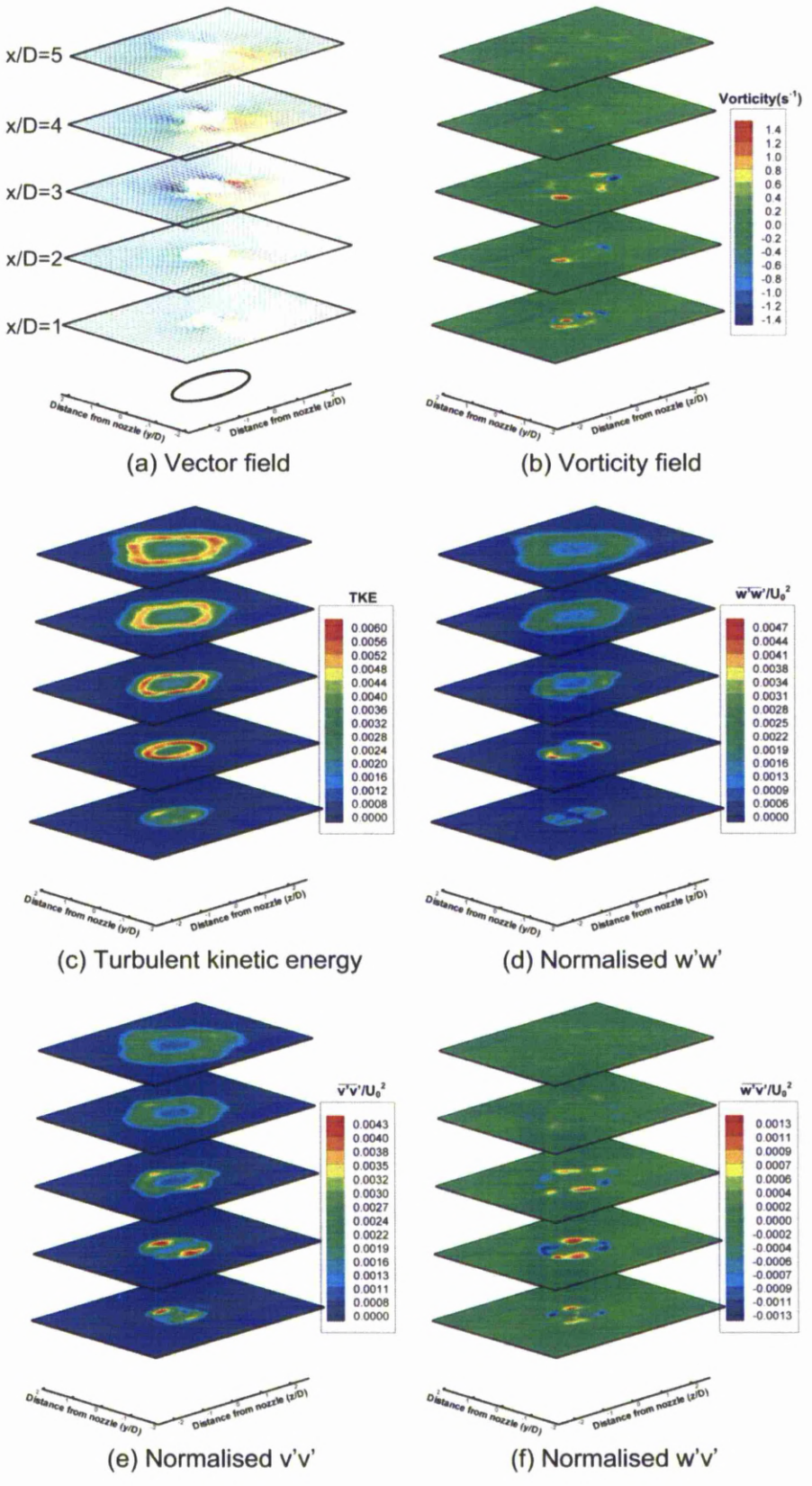

Figure 4.49 Time averaged PIV results along cross-stream direction for 120° V-minor nozzle

vortex is important when interpreting phase-averaged results. If the main ring vortex is just behind the laser sheet, the radial outflow of fluid will be more dominant and obscure the streamwise vortices. TKE and the v'v' Reynolds stress component are influenced by axis switching. Both terms have maximum values at three jet-diameters downstream of the nozzle mean height which coincides with the location as which the main ring vortices start to axis-switch. Comparing TKE and stress values between the two planes, it can be seen that the peak plane causes most of the high-stress flow intensification. However, the trough plane (major axis) shows a preferential spreading of TKE, which is possibly caused by the outward spreading braid vortices. Finally, the connection between peaks and regions of high stress is also shown in the Reynolds shear stress contour plot in Fig. 4.48(f). Compared to the reference case, the stress values are marginally increased.

From the time-averaged velocity plot in Fig. 4.49(a), axis-switching behaviour can be identified. By the end of the measurement window the elliptic jet appears to have rotated by 90°. The vorticity fields depicted in Fig. 4.49(b) show that streamwise vortices are evident from 2D onwards. The rotational sense of these structures, is such that fluid is ejected radially outward, which was also shown when the cross-stream LIF images were presented earlier. Specifically, at x/D=3, four pairs of vortices are observed. The outer pair consists of the braid vortices and has an outward rotational sense, while the inner pair is formed from the main ring vortex. As the vortex bends towards the downstream direction, which was highlighted in the flow visualisation section, the ends of the major axis pass through the laser plane first. Due to the orientation of the filaments, the induced velocity is not normal to the measurement plane and thus, a component of this velocity is measured by the PIV system. Effectively, the two inner vortex pairs correspond to the four sections of the bent main ring vortex. The downstream bending orientation of the ring, causes the formation of pairs with inward rotational sense. This phenomenon even is clearer when examining the sharper nozzle case (60° V-minor, presented later). Most of the high magnitude TKE is concentrated at x/D=2, possibly influenced by the streamwise vortices which are formed at the troughs as well as the outward spreading braid vortices which initiate at approximately the same downstream location. The trough and peak influences on the production of turbulence is contained within the near-nozzle region as seen in Figs 49(d),(e) and (f). The peak plane (major-axis for this nozzle configuration) however, does promote the production of small-scale structures more effectively. Similar with the phase-averaged results, TKE and Reynolds shear stress magnitudes are comparable to the reference case.

d) Influences of notch sharpness on flow field along the streamwise plane

Because of the similarity between jets of the same IO design, the following results will be presented in a concise manner to avoid repetition. Where applicable, differences will be shown and comparisons will be made.

The phase-averaged results of the 60° V-major nozzle along the major plane view are presented in Fig. 4.50. Analysing the vorticity plot, an upstream shift of the main ring vortices is evident. The flow development happens faster and the last discernible main ring vortex pair is at 3.5D downstream from the mean height. Within that region, lateral movement of the main ring vortices towards the nozzle centreline is also evident. The velocity field as well as the stress and TKE are affected by the main ring vortices, especially the second pair. Regions containing high velocity, stress and TKE values are noticed further upstream compared to the less sharp, 120° V-major case presented earlier.

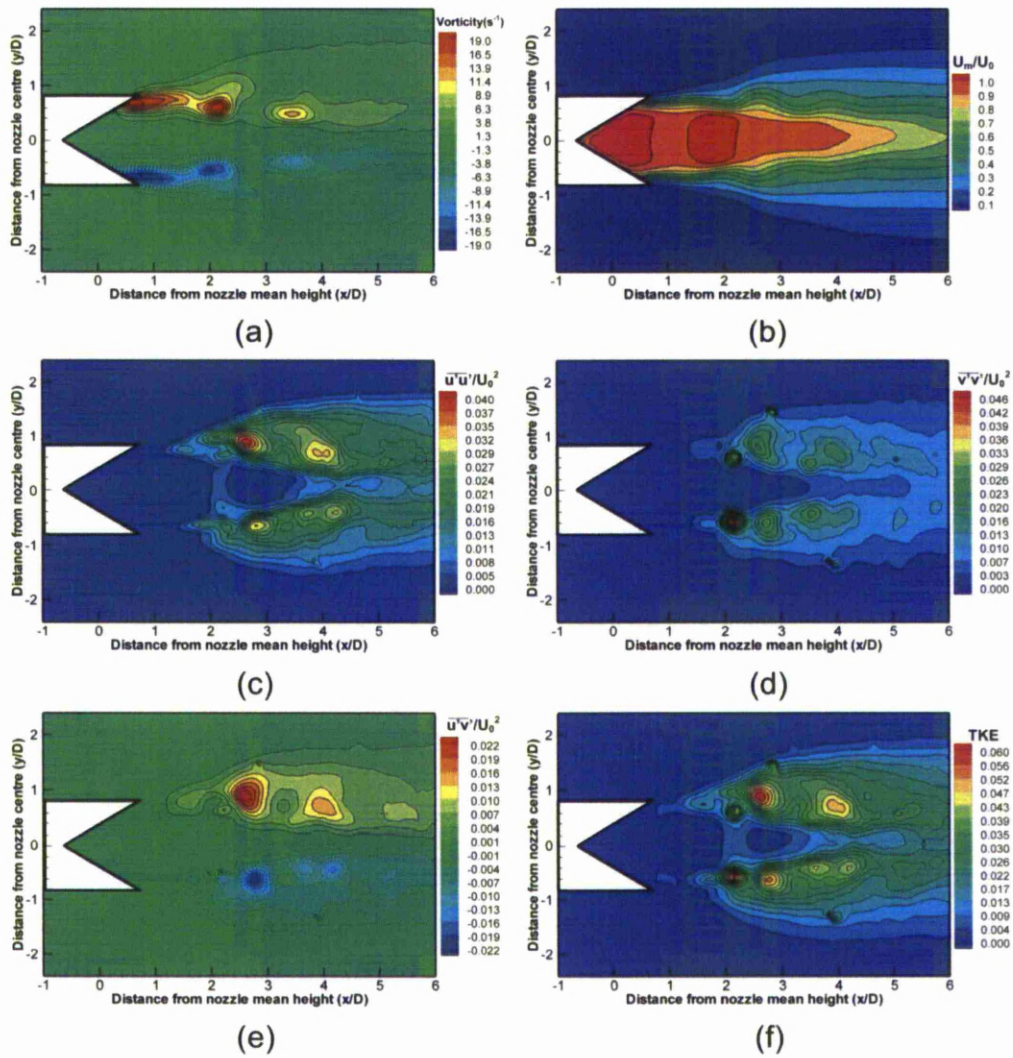

Figure 4.50 Phase averaged PIV results along streamwise direction for 60° V-major nozzle, major plane view

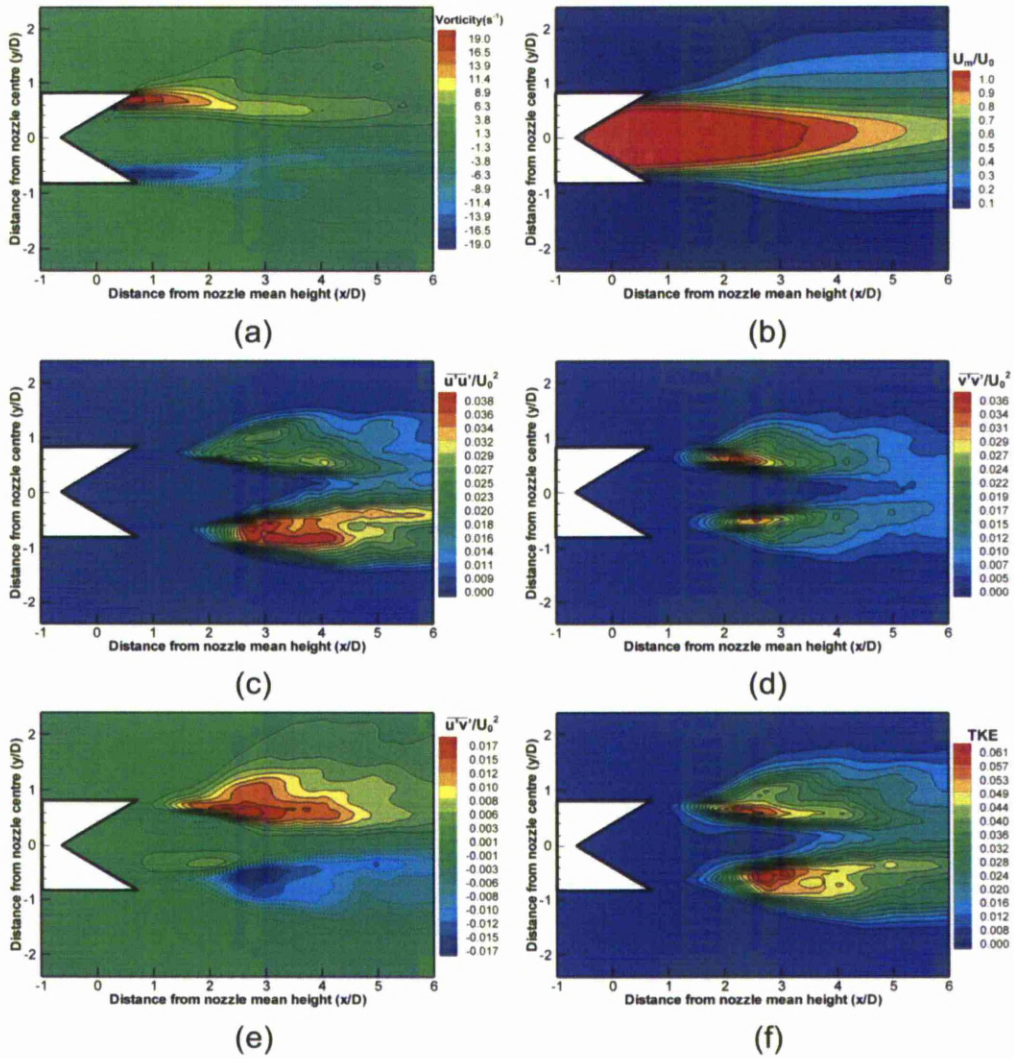

Figure 4.51 Time averaged PIV results along streamwise direction for 60° V-major nozzle, major plane view

In the time-averaged vorticity plot presented in Fig. 4.51(a), it can be seen that most of the vorticity is dissipated within the near-nozzle region. Main ring structuring and magnitudes are comparable to the less sharp, 120° V-major, nozzle geometry and thus it can be stated that increasing the peak sharpness does not affect the vorticity of the main ring vortices along the major plane. The following contour plot in Fig. 4.51(b) shows the normalised jet velocity. In this figure it can be noticed that the 60° V-major nozzle has the shortest potential core that all nozzles, extending only to approximately 4.2D from the nozzle mean height. Compared to the rest of the nozzles, it measures a half jet-diameter shorter than the 120° V-major nozzle and almost one jet-diameter shorter than the reference case. Due to the sharper nozzle contour, more intense stretching of the vortex filament takes place along with formation of stronger streamwise vortices (Longmire *et al.*, 1992a), which help breakdown the large-scale coherent structures and thus reduce the jet potential core. Additionally,

compared to the 120° V-major nozzle, more spreading takes place which initiates further upstream. This behaviour can be linked to the formation of more intense streamwise vortices formed at the nozzle peak locations. Similar to the phase-averaged results, regions containing high stress and TKE values are shifted upstream, compared to the 120° V-major case. However magnitudes are comparable between the two jets shown in Figs. 4.39(c)-(f) and 51(c)-(f).

Phase- and time-averaged results, obtained along the minor plane are shown in Figs. 4.52 and 4.53. Looking at the phase-averaged vorticity plot, a very fast shear layer rollup it noticed. This observation agrees well with results presented for the reference nozzle, and has also been studied extensively by Husain and Hussain (1993). A thin shear layer has the tendency to rollup faster, and the introduction of the V-notch exposes the shear layer earlier, thus accelerating the rollup process. Interestingly though, the vorticity magnitude is slightly reduced with respect to the 120° V-major and reference nozzle geometries. As the main ring vortices propagate downstream, movement away from the nozzle centreline is observed. This lateral movement however is drastically reduced compared to the reference nozzle.

Similar to the phase-averaged results, looking at both time-averaged vorticity and velocity plots, it can be seen that the flow field does not spread to such an extent as the 120° V-major case as shown in Figs. 4.53(a) and 4.53(b). Additionally, the spreading profile is almost linear and the spread rate does not increase after a certain downstream location, as seen for the 120° V-major nozzle. The spreading pattern of the 60° V-major nozzle is more similar to the reference case that the less sharp V-major case. Focusing on the vorticity contour plot, it can be observed that compared to its counterpart nozzle, the shear layer extends further downstream, indicating a lower dissipation rate. The vorticity magnitude measured along the minor plane, is substantially reduced compared to the major view. It is the lowest vorticity magnitude measured throughout all elliptic test cases. It seems that the increased trough

sharpness does not promote strong shear layer rollups. By comparing the corresponding stress values between the reference, 120° V-major and 60° V-major nozzle geometries, an interesting trend is discovered in Figs 4.35, 4.41 and 4.53 respectively; The reference case maximum streamwise and cross-stream Reynolds stress components were measured at 0.021 and 0.020 respectively. When the less sharp V-notch is introduced (120° V-major), the streamwise Reynolds stress component increases to 0.032, while the cross-stream decreases to 0.014, indicating that more turbulence is generated along the streamwise direction. However, when the V-notch sharpness is increased (60° V-major), the streamwise stress component decreases to its original reference value (0.021), and the cross-stream component remains unchanged (0.014). The resultant effect is that the highest maximum Reynolds shear

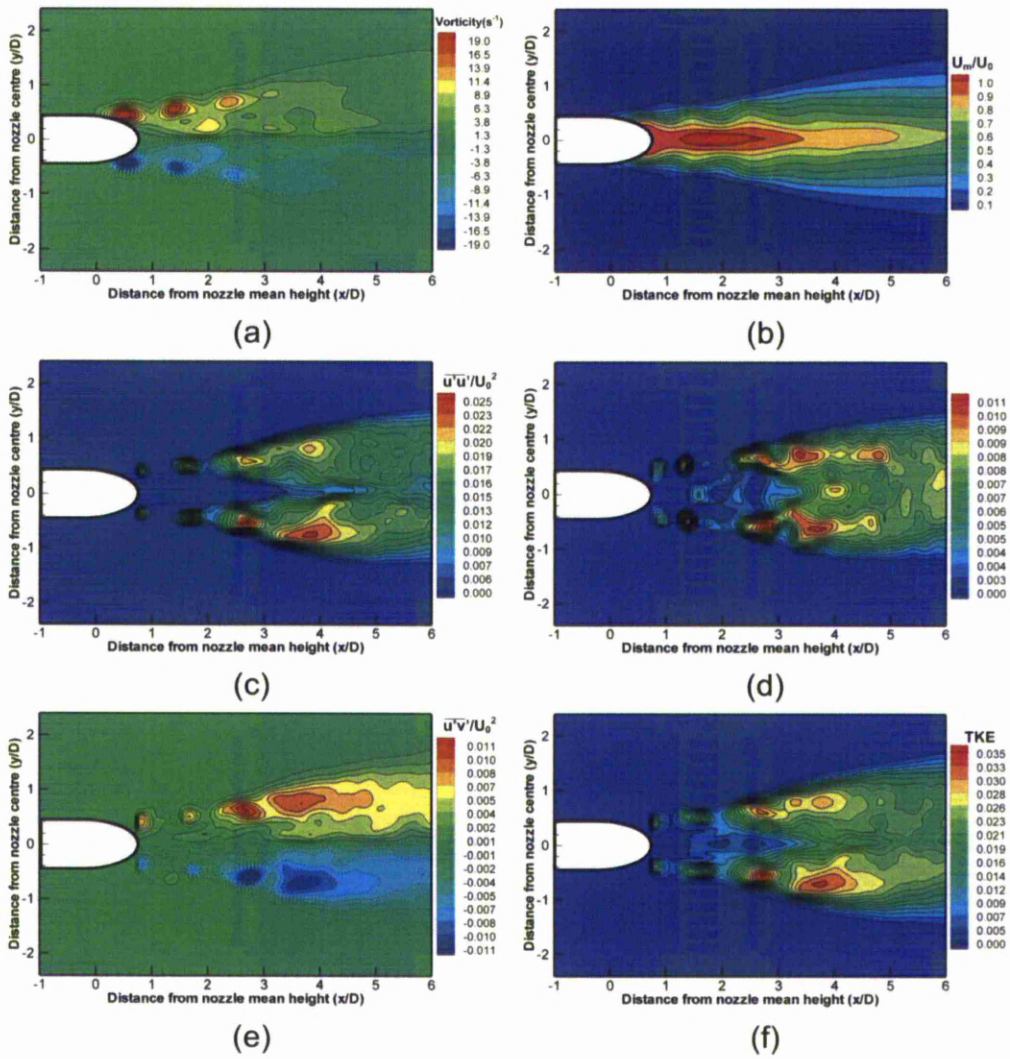

Figure 4.52 Phase averaged PIV results along streamwise direction for 60° V-major nozzle, minor plane view

stress and TKE is generated by the less sharp, 120° V-major nozzle geometry. It can therefore be appreciated, that between the two V-major nozzle configurations, the optimum nozzle geometry associated with maximum turbulence generation along the minor plane view, is the 120° V-major nozzle. However one question remains unanswered; why do both V-major nozzles attain low cross-stream Reynolds stress components compared to the reference case. One plausible explanation is that due to the reduced axis-switching behaviour associated with the nozzle, i.e. reduced spread rate, and a smaller induced velocity is attained along the lateral direction.

The 60° V-minor nozzle results, taken along the streamwise direction, are shown in Figs. 4.54 to 4.57. Starting off with the phase-averaged plots along the streamwise view, immediately a significant difference in the flow field can be observed. The shear layer is

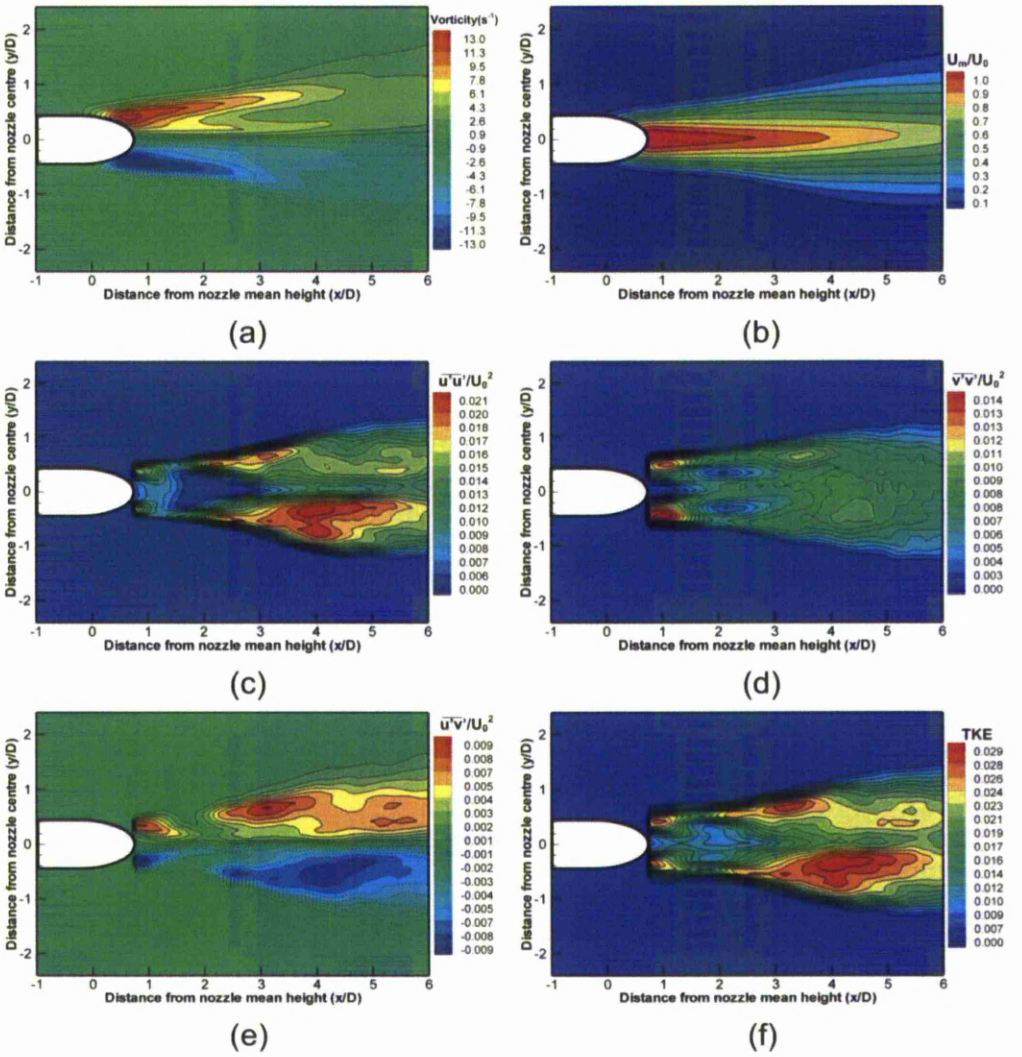

Figure 4.53 Time averaged PIV results along streamwise direction for 60° V-major nozzle, minor plane view

stable and the first discernible vortex rollup is at three jet-diameters downstream of the mean height. Additionally, the flow development is slow and lateral movement of the main ring, towards the nozzle centreline, vortices takes place after x/D=3. Comparing the vorticity magnitude with that of the 60° V-major and 120° V-minor nozzles, along the same major plane view, a slight reduction is noticed. Increasing the trough sharpness does not augment the generation of vorticity. The symmetricity of the flow field can be seen from the vorticity plot in Fig. 4.54(b). As seen with previous test cases, the correlation between the stresses and the main ring vortices is high, as the stresses are strongly driven by the main ring vortices. Since the main ring vortices and flow development is delayed for this particular nozzle geometry, it follows that the high stress regions are also delayed and thus are detected further downstream. The high magnitude TKE values are also found in the far-field region,

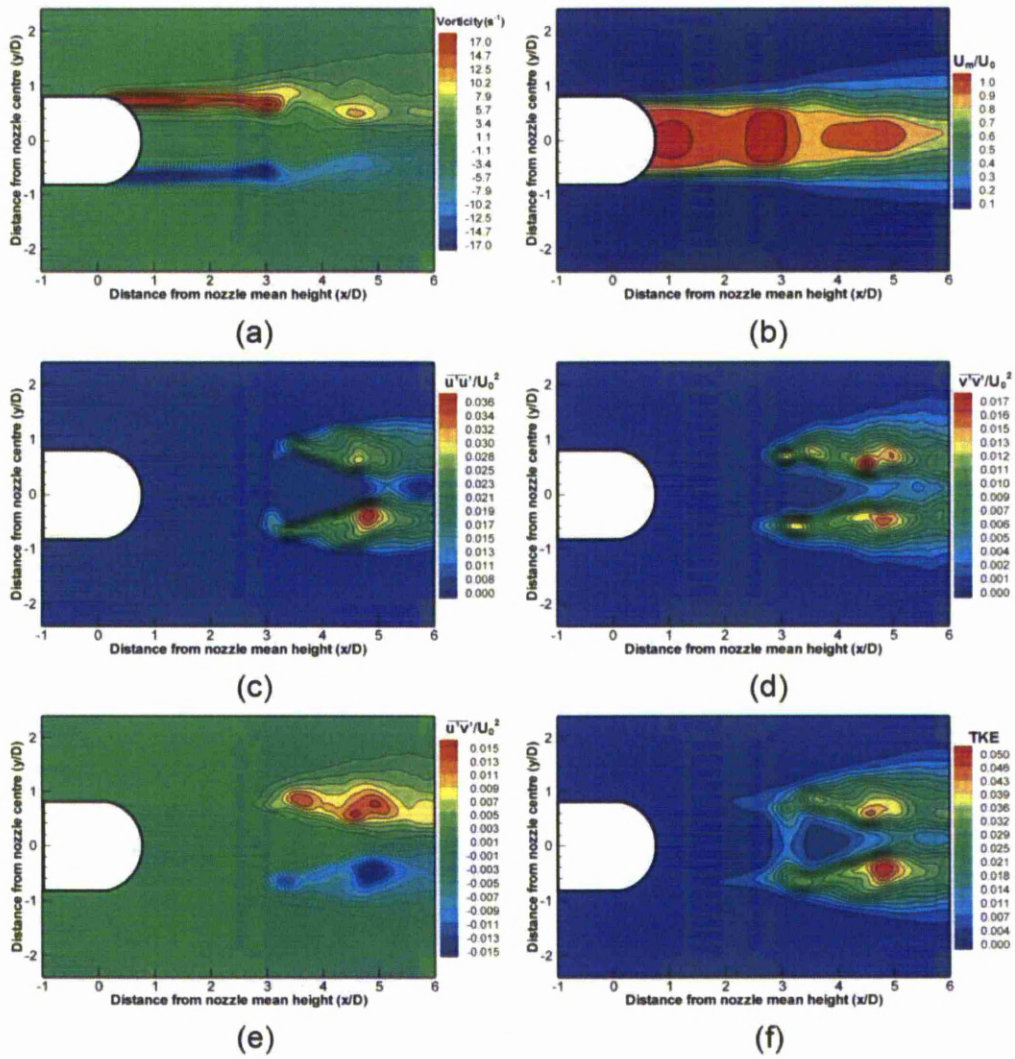

Figure 4.54 Phase averaged PIV results along streamwise direction for 60° V-minor nozzle, major plane view

possibly augmented by the breakdown of the large-scale main ring vortices at the end of the potential core.

Flow visualisation and phase-averaged PIV results have shown so far, that increasing the peak and trough sharpness of the V-minor geometry leads to a more stable elliptic. This notion is also confirmed when analysing the time-averaged results presented in Fig. 4.55. In Fig 4.55(b), the potential core of the jet extends to the end of the measurement window (6D), making it the longest of all tested nozzles, reaching even further than the reference case. This indicates that the interactions between the jet and the ambient fluid are minimal and that the large-scale coherent structures propagate the furthest before breaking down. Agreeing well with the phase-averaged results presented above, regions of high stress are concentrated in the downstream region, due to the delayed movement of main ring vortices,

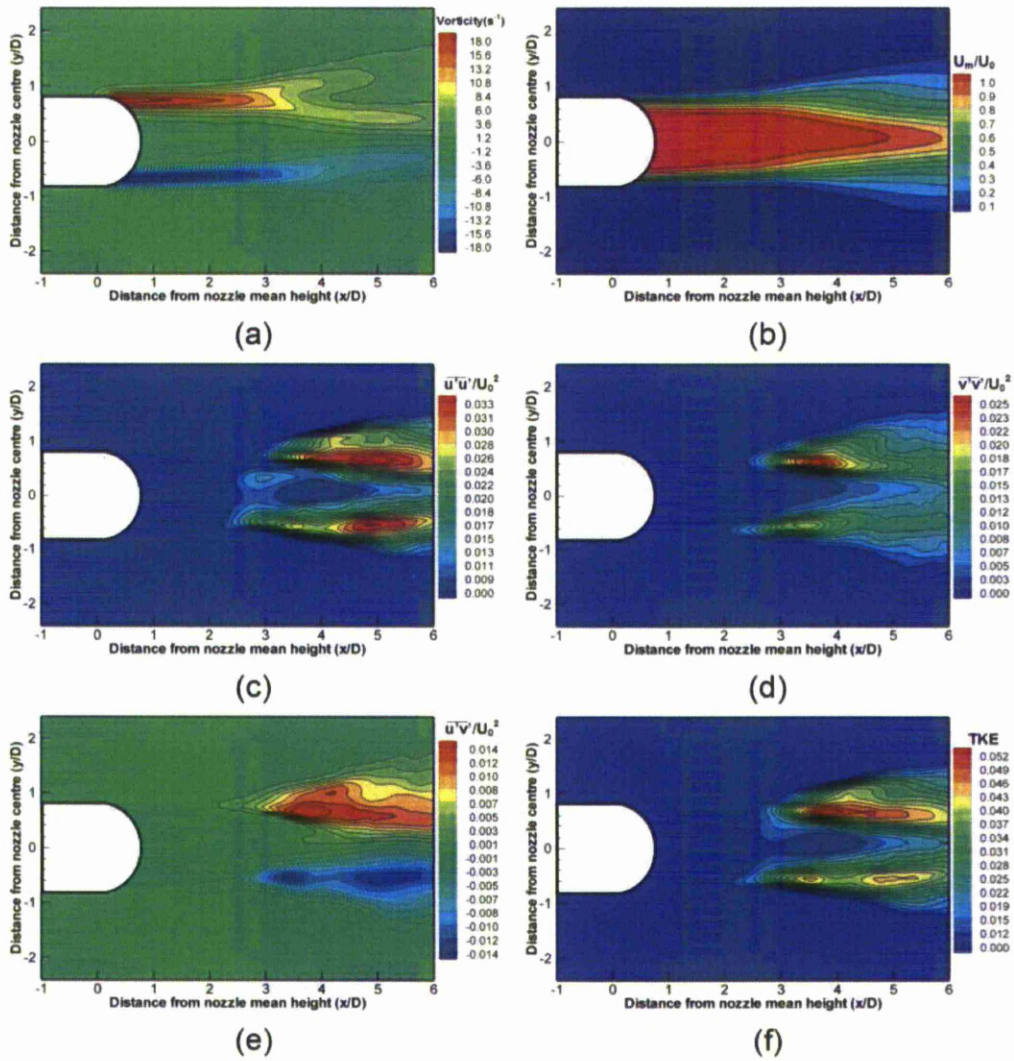

Figure 4.55 Time averaged PIV results along streamwise direction for 60° V-minor nozzle, major plane view

or delayed axis-switching. Compared to the reference and to the less sharp case (120° V-minor) the location of the high stress regions is similar, indicating that by increasing the notch sharpness not much difference is achieved. However, comparing to the V-major nozzles, which along the same view (major plane view) consist of peaks, a large discrepancy arises regarding the location of the high stress regions. This indicates that peaks, compared to troughs, are able to intensify the near-nozzle flow field. By comparing the stress levels of the reference, 120° V-minor and 60° V-minor nozzles the following trend is found in Figs. 4.33,4.45 and 4.55 respectively; The Reynolds shear stress decreases by 20% as a result of the introduction of the V-notch and decreases further by another 30% as a result of increasing the trough sharpness. Both cross-stream and streamwise Reynolds stress components associated with the 60° V-minor nozzle are reduced. Similarly TKE values also

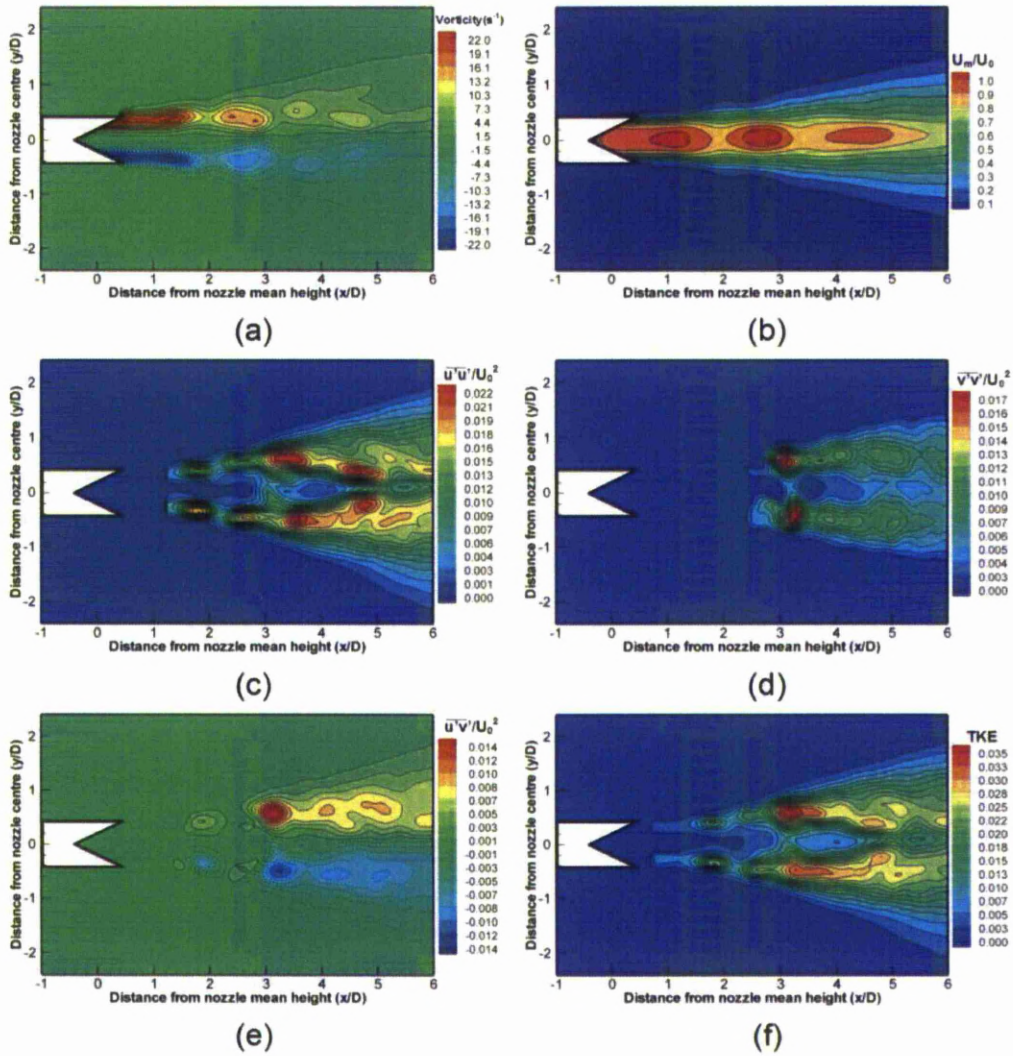

Figure 4.56 Phase averaged PIV results along streamwise direction for 60° V-minor nozzle, minor plane view

follow the trend with a 20% corresponding decrease between 120° and 60° V-minor nozzle configurations. These findings reinforce the flow visualisation results presented in earlier sections notion, and show in a quantitative way that reduced flow interactions exist.

Along the minor plane view, a similar behaviour can be seen in Fig. 4.56. Reduced flow interactions, reduced axis-switching behaviour and reduced spreading is observed. The main ring vortices form and as they propagate downstream, they stay concentrated close to the nozzle centreline. Compared to the less sharp nozzle case (120° V-minor), similar vorticity magnitudes are attained. As expected, faster rollup occurs along minor plane view. An interesting flow feature is noticed at approximately five jet-diameters downstream. The flow feature looks like the 4th set of main ring vortices, which cannot be possible since the main ring vortices spread, albeit with a slower rate compared to the reference case, and thus

should not be located close to the nozzle centreline. This flow feature is a high shear area also observed when analysing the streamwise LIF images in Fig. 4.20. Due to the reduced interactions and the larger potential core associated with the sharper 60° V-minor nozzle, more jet fluid propagates downstream and interacts with the main ring vortices at the end of the potential core. At that location, the main ring vortices forming along the major plane converge and interact with the jet fluid. Similar to less sharp case (120° V-minor), the streamwise Reynolds stress is concentrated in the periphery of the jet, driven by the main ring vortices. Most of the cross-stream, Reynolds shear stress as well as TKE are concentrated further upstream (at three jet-diameters from the nozzle mean height) compared to the major plane view, which was expected due to the faster rollup. Additionally with respect to the 120° V-minor case, more turbulence is generated in the upstream region. Possibly, the sharper peaks help to increase the generation of turbulence further upstream, in the near-nozzle region. Interestingly, although axis-switching behaviour is delayed and flow interactions are reduced, the sharper peaks do augment the generation of turbulence.

Moving on and looking at the time-averaged velocity plot in Fig. 4.57(b) a symmetric flow field is noticed. Also, compared to the reference and less sharp nozzle (120° V-minor) jets, slower and more gradual spreading is observed. The effect that the peaks have on the flow field can be demonstrated by comparing the vorticity values of the current nozzle, in Fig. 4.57(a), to the valued attained from the 60° V-major case in Fig. 4.53(a), along the same measurement plane (minor plane view). By comparing the two jets, a vorticity increase of approximately 70% is calculated, indicating that peaks promote stronger interactions and more energetic shear layers. In Figs. 4.57(c) and 4.57(d), both Reynolds streamwise and cross-stream stress plots show a small asymmetry between top and bottom shear layers.

However looking at the symmetricity of the velocity plot, the stress results must still be within the experimental uncertainty. By comparing the 60° V-minor nozzle to the reference and 120° V-minor cases, the effects of the peaks are discerned as shown in Figs 4.57, 4.35 and 4.47. When the peaks are introduced, the streamwise Reynolds stress component increases while the cross-stream component decreases. This trend continues as the peak sharpness in increased. However in the 60° V-minor nozzle, the increase in the Reynolds streamwise stress component is larger than the associated decrease in the cross-stream component, resulting in a higher Reynolds shear stress and TKE. Therefore, contrary to the troughs, sharp peaks are effective in the generation of turbulence an thus it can be inferred that they will be effective in applications requiring good mixing.

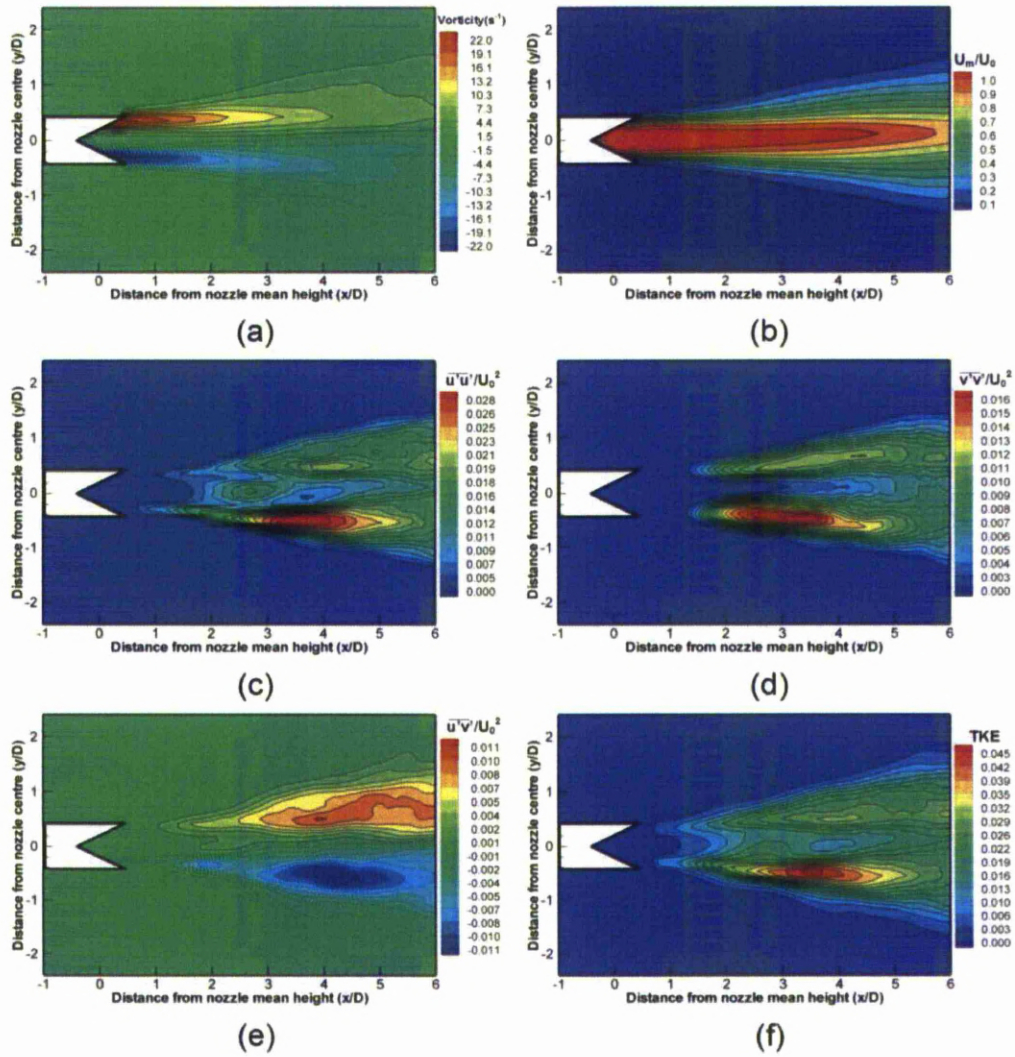

Figure 4.57 Time averaged PIV results along streamwise direction for 60° V-minor nozzle, minor plane view

e) Influences of notch sharpness on flow field along the cross-stream plane

To investigate further, phase-averaged cross-stream PIV measurements were carried out to clarify the flow differences between notches of 120 and 60. Figures 4.58 to 4.61 show the velocity vector fields, vorticity fields, turbulent kinetic energy and Reynolds stress distributions determined from PIV measurements for the 60° V-notched nozzles up to the x/D=5 location. Maintaining the same pattern as before, both phase- and time-averaged results will be presented and the major- and minor-planes of the nozzles have been aligned along the z and y axes of the plots respectively

Initiating the analysis by examining the phase-averaged vorticity distributions, of the 60° V-major nozzle shown in Fig. 4.58(b), it can be seen that the streamwise vortices produced by the nozzle are readily discernible in the near-field region of the jet. This agrees well with the

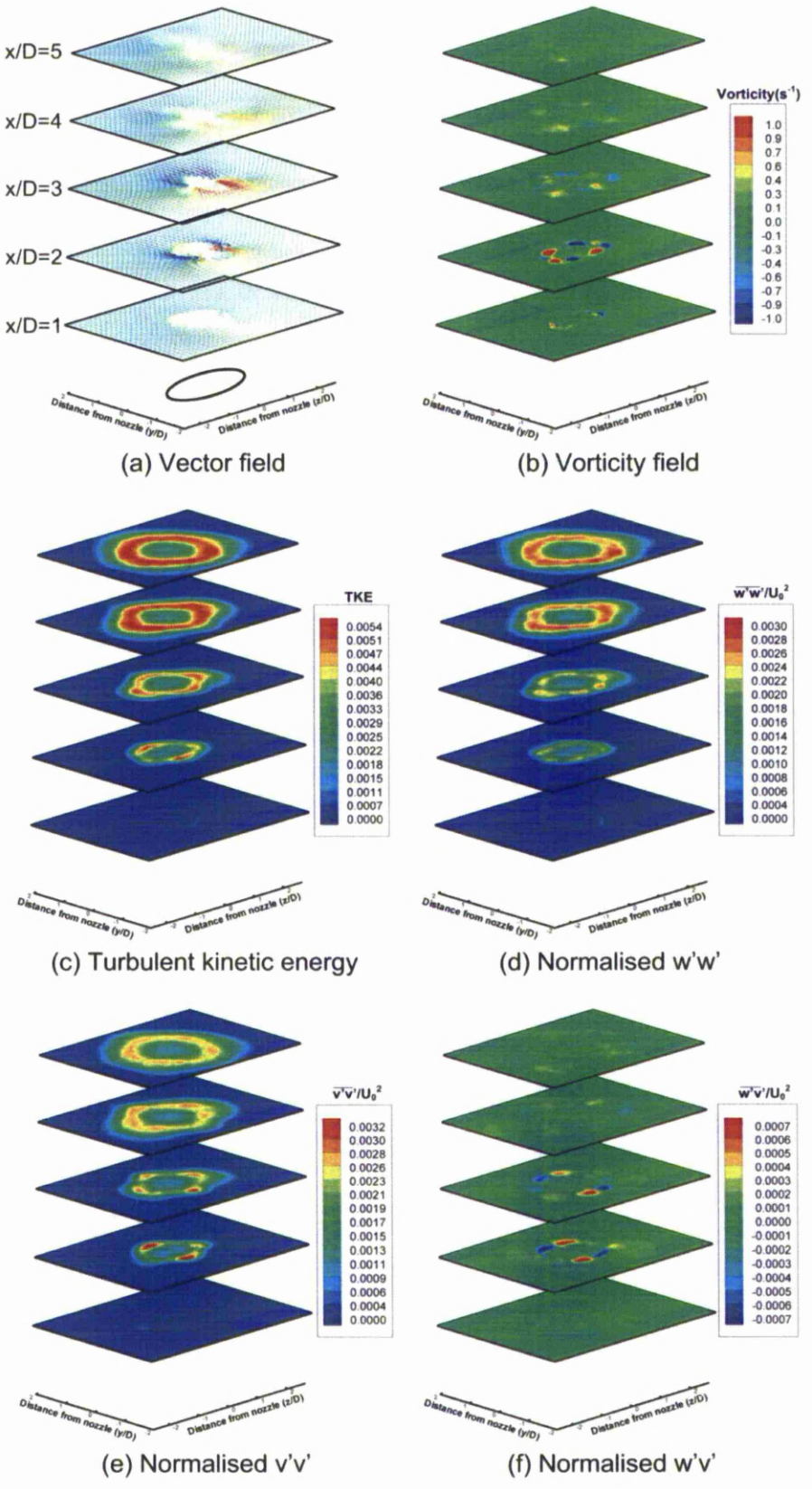

Figure 4.58 Phase averaged PIV results along cross-stream direction for 60° V-major nozzle

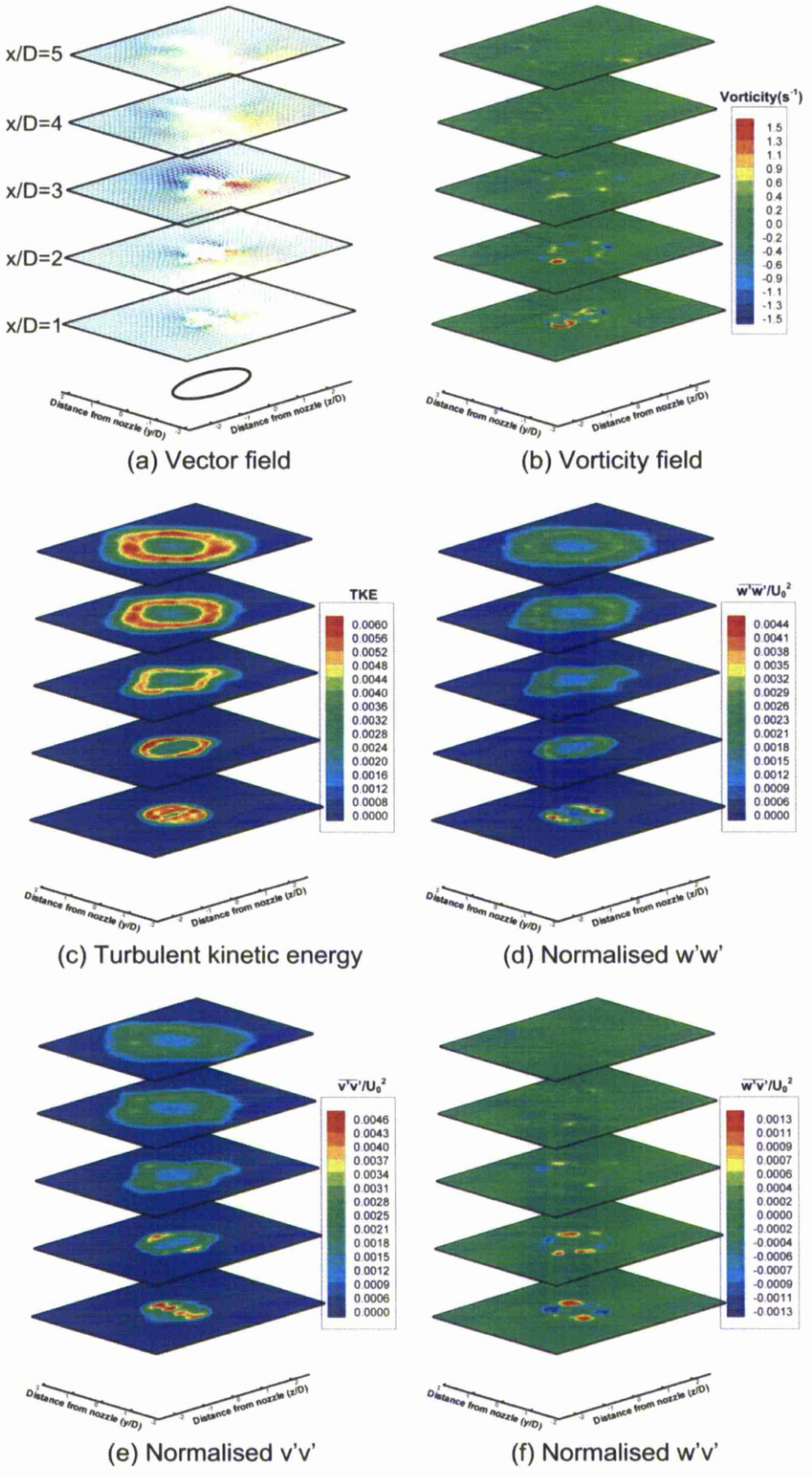

Figure 4.59 Time averaged PIV results along cross-stream direction for 60° V-major nozzle

earlier coloured-dye and LIF flow visualization images. Additionally, the rotational senses of the vortex structures in the figure are also in agreement with the flow visualization images. Specifically at x/D=2, a set of eight vortex cores are depicted. The inner four vortices depict the bent main ring vortex, while the outer four depict the streamwise vortices formed at the locations corresponding to the nozzle peaks. In particular, the former four vortices are captured when the main ring vortex is bending towards the downstream direction, with the ends of the major-axis of the elliptic ring crossing the laser sheet (measurement plane). Thus in the vorticity field, four corresponding distinct vortex cores will be formed, with a radially inward rotating orientation. The streamwise vortices on the other hand eject fluid from the jet core towards the surrounding ambient fluid. Hence, the vorticity field shown in Fig. 4.58(b) is consistent with the flow interpretations so far. Compared to the less sharp 120° V-major case, the flow features presented here are more pronounced and thus easily detected. This is due to the stronger streamwise vortices which promote increased interactions with the main ring vortices.

The effects of the peaks are addressed better when looking at the time-averaged plot shown in Fig. 4.59. Similar to what was observed for the phase-averaged results, the streamwise vortices of the 60° V-major nozzle are more pronounced and therefore can be detected easier. Comparing the maximum vorticity magnitudes attained by the two V-major nozzles, it can be seen that for the sharper nozzle geometry (60° V-major) the corresponding increase in vorticity is 15%, as shown in Figs 59(b) and 43(b) respectively. The flow stresses as well as the TKE also increase. It was calculated that the Reynolds cross-stream, w-component and v-component was increased by 15% and 27% respectively. Additionally, TKE increased by 7%. Both phase- and time-averaged results along streamwise and cross-stream directions show that increasing the sharpness of the V-major nozzle promotes faster breakdown of large-scale structures and increases flow intensity.

Comparing the cross-stream phase-averaged results of the 60° V-major to the 60° V-minor nozzle, shown in Figs. 4.58 and 4.60 respectively, it can be observed that the streamwise vortices initiate further downstream for the 60° V-minor nozzle. For instance, clear formation of the streamwise vortices is evident at x/D=3 cross-stream location shown in Fig. 4.60(b). It is worth noting that the orientation of both inner vortex cores, which correspond to the bent main ring vortex, and outer vortex cores, which correspond to the streamwise vortices formed at the trough locations, match the LIF flow visualisation results. It seems that although the lip modifications affect the formation of the streamwise vortices, the main ring vortex bending towards the downstream direction remains persistent. Due to the spatial delay in the formation of the streamwise vortices, regions containing increased flow stress and TKE activity are also shifted downstream. Apart from the downstream shift, maximum

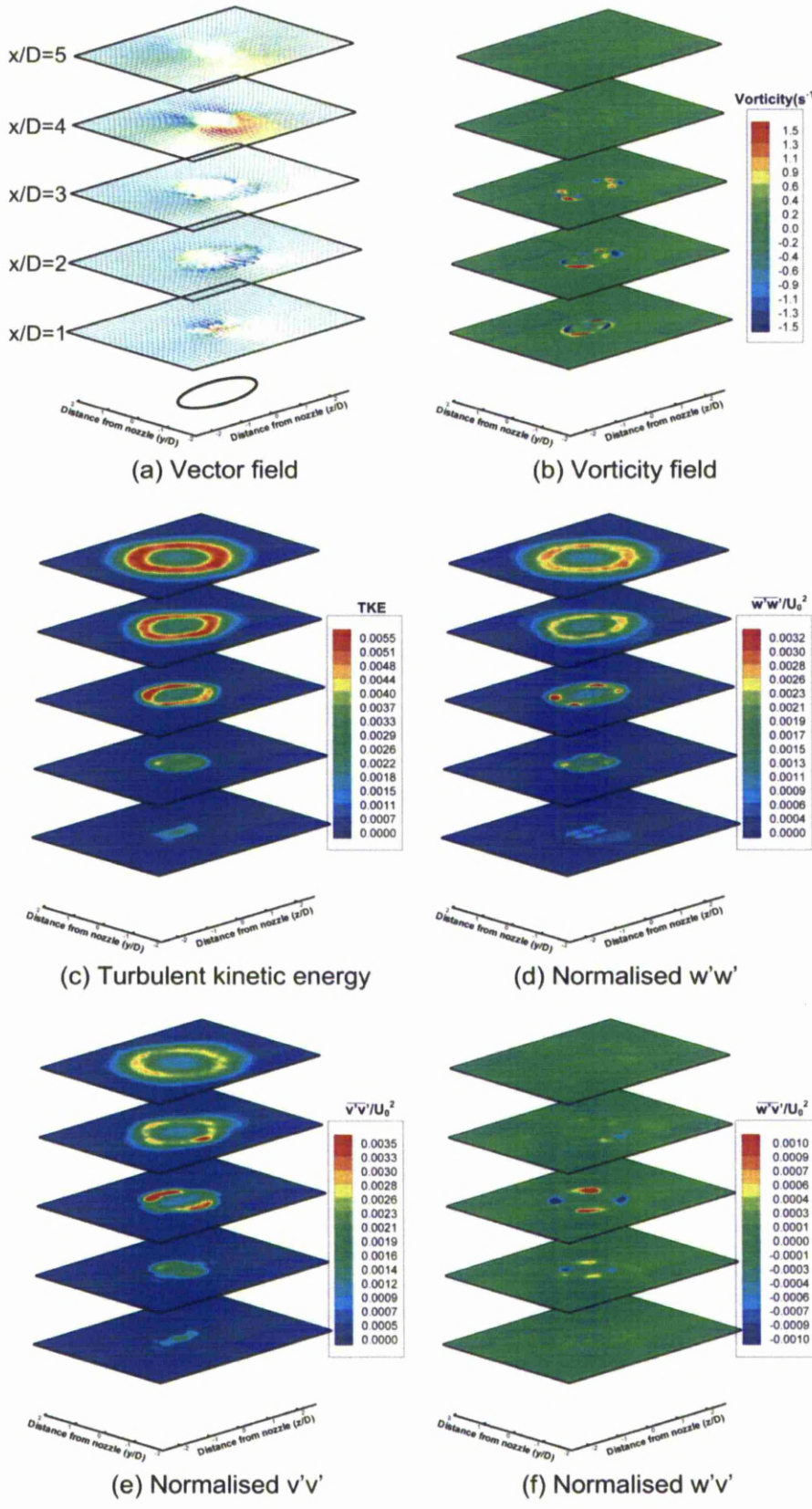

Figure 4.60 Phase averaged PIV results along cross-stream direction for 60° V-minor nozzle

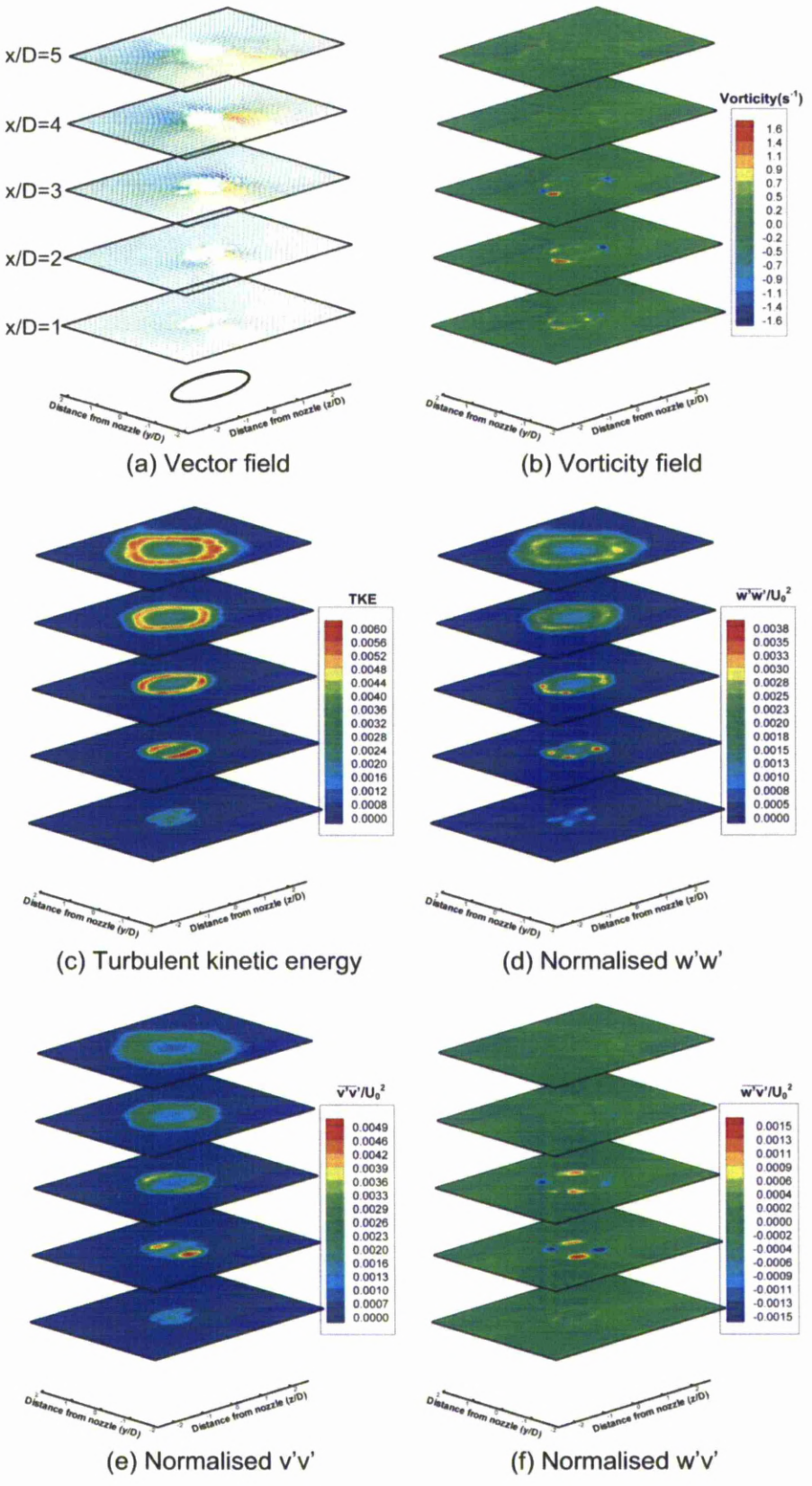

Figure 4.61 Time averaged PIV results along cross-stream direction for 60° V-minor nozzle

TKE magnitudes are similar for both nozzles. The effect that the peaks have on the flow field are highlighted when comparing both V-major and V-minor nozzles. The 60° V-major nozzle presents a favourable spreading of high stress along the peak plane. Similarly, the 60° V-minor nozzle attains high Reynolds normal stress along the peak plane in Fig. 4.60(e), indicating that the peaks prove beneficial towards turbulence generation. Finally, comparing the Reynolds shear stress plots of both nozzles, additional stress regions are noticed for the 60° V-major nozzle, possibly caused by the stronger influence of the outward-spreading streamwise vortices, as shown in Fig. 4.58(f). Since, they are closely related to the mixing characteristics of elliptic nozzles, these observations suggest that appropriate designs of V-notched elliptic nozzles may bring about improved control over flow-mixing levels.

The time-averaged vorticity results of the 60° V-minor nozzle, shown in Fig. 4.61(b), indicate that the streamwise vortices initiate at two jet-diameters from the nozzle mean height, but develop and become better formed by x/D=3. As stated in the previous paragraph, TKE and cross-stream Reynolds shear stress (w'v') are influenced by the peaks, especially in the near-nozzle region, as shown in Figs. 4.61(c)-(f). However when compared to the, less sharp, 120° V-minor nozzle, it can be seen that the increased sharpness only affects the maximum Reynolds shear stress. Maximum TKE remains unchanged, at $6x10^{-3}$, while the Reynolds shear stress is increased by 15%. Interestingly the sharper nozzle also promotes a lower w' but higher v' Reynolds stress components. The Reynolds stress reduction along the w-component is 19%, while the increase along the v-component is 14%. These comparisons reiterate the notion that peaks benefit more by the increase in sharpness over the troughs.

4.2.4 Influence of notch sharpness and position on half jet-width and momentum thickness

Figures 4.62 and 4.63 show the normalised half jet-width and normalised momentum thickness, for V-major and V-minor nozzle configurations respectively. The reason for categorising the results in such a way, is to highlight the effects of nozzle sharpness. Comparisons between the two categories have also been included, thus showing which nozzle geometry is best-suited for mixing applications. For ease of comparison, colouring and symbol selection were kept consistent. In all graphs the reference case is presented with black coloured points, while the 120° configuration is noted in blue and the 60° in red points respectively. The filled points depict results taken along the major plane view, while the empty points represent the minor plane view.

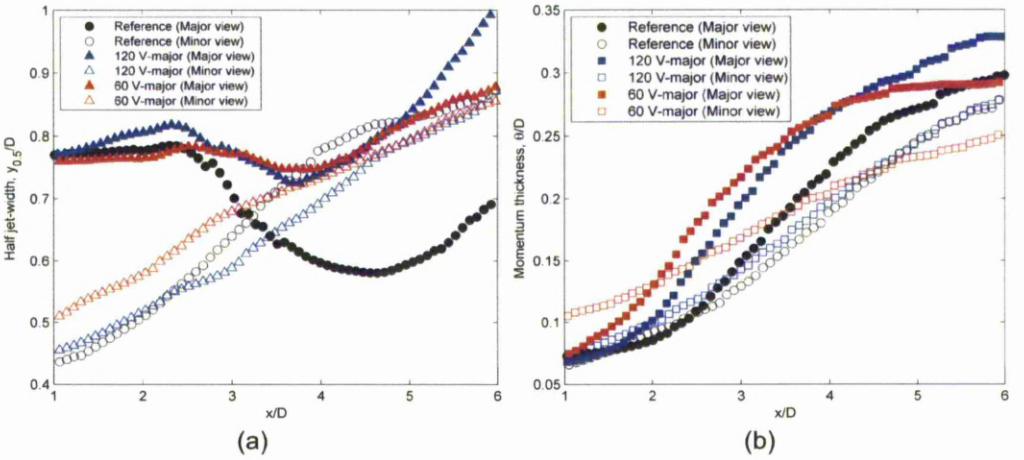

Figure 4.62 Graphs showing (a) half jet-width and (b) momentum thickness, for V-major nozzle configurations

Inspecting the normalised half jet-width of the V-major nozzle geometries in Fig. 4.62(a) initially, it can be seen that the elliptic reference nozzle undergoes axis-switching, as expected. The cross-over point, the point where the major and minor half jet-widths intersect, is located at approximately three jet-diameters from the nozzle exit (nozzle exit coincides with the mean height for the reference case). This compares well with the earlier study conducted by Hussain and Husain (1989). In their study a 2:1 elliptic nozzle was used and a forcing excitation level of 2.5% (based on the centreline jet exit velocity) was implemented, while the non-dimensional forcing frequency was set to a Strouhal number of 0.4. However compared to the current study, a discrepancy in the nozzle design exists. In their study, the nozzle was contoured in such a way in order to attain a constant initial momentum thickness along the nozzle circumference, something that has not been done in this study. Nevertheless, the location of the cross-over point was measured at 2.7D from the nozzle exit, which compares well with the results presented in the current study. It must be noted that in the Hussain and Husain paper the equivalent nozzle diameter was used to non-dimensionalise the downstream distance and not the hydraulic diameter, as done in this study. This factor has to be considered when comparing the results. Looking at the plots for the other two nozzles, it can be seen that the flow behaviour is substantially different. Although the top and bottom shear layers begin to merge, they do not cross. This shows that axis-switching for both 120° and 60 ° V-major nozzles is suppressed. This flow behaviour is similar to what was shown by Zaman *et al.* (1994). However, the benefit of the current nozzle design, is that blockage effects are eliminated as tabs do not impede the jet flow. Thus a reduced pressure drop can be expected which is beneficial in applications where high thrust is required. Compared to the reference case, the largest deviation is achieved along the major plane view, which is also the most dominant factor behind the suppression of axis-

switching. It can be seen that the introduction of a V-notch suppresses the lateral movement of the jet. Effectively along the major plane view, the jet does not taper in, and thus it's width is always larger or equal to the jet-width along the minor plane view The introduction of the V-notch does change the jet-width growth drastically. The main factor is that the growth becomes more linear and as the notch sharpness increases, the growth rate decreases.

From the normalised momentum thickness plot shown in Fig. 4.62(b), some interesting observations can be made. Starting off with the reference case, it can be seen that along the major plane, the momentum thickness is consistently higher than the minor plane. This was expected and has been highlighted throughout this study. It has also been reported in previous studies conducted on elliptic jets. Incorporating the V-notch does not change this fact, but does promote changes in the growth of the momentum thickness along both major and minor planes respectively. Specifically, the momentum thickness of the 120° V-major nozzle along the major plane increases throughout the measurement window, indicating that the addition of peaks does improve mixing substantially. Along the minor plane however, only a slight increase over the reference case is noticed, within the first four jet-diameters from the nozzle exit, which indicates that the 120° troughs do not promote better mixing. On the other hand, when the notch sharpness is increased (60° V-major), both major and minor planes benefit in the near-nozzle region but underperform in the far field. Compared to the 120° V-major case, an increase of the momentum thickness is noticed along the major plane until 3.5D downstream, while along the minor plane the increased momentum thickness extends to approximately four jet-downstream from the nozzle exit.

The V-minor group of nozzles exhibit significantly different flow behaviours. Focusing on the half jet-width plot, shown in Fig. 4.63(a), it is noticed that all nozzles undergo axis-switching. However, as the nozzle sharpness increases, the axis-switching point moves further downstream. As shown previously, the reference case axis-switches at approximately 3D, while the 120° V-minor and the 60° V-minor nozzles axis-switch at approximately 3.5D and 4.5D respectively, from the nozzle exit. So it can be seen that by modifying the elliptic nozzle to include V-minor notches, the cross-over point moves downstream by half a diameter. By subsequently doubling the notch sharpness, results in the cross-over point moving downstream by one more jet-diameter. It would be interesting to see what a larger range of cut angles would do to the location of the cross-over point and within what range of angles would the projection hold. Another interesting point that can be drawn from the half jet-width graph is that as the nozzle sharpness increases, it results in an equal reduction of the rate at which both major and minor planes axis-switch. Due to this, the normalised half jet-width of the jet at the cross-over point is similar to the reference case which means that the jet cross-section will be of the same size for the V-minor and reference nozzles. This is

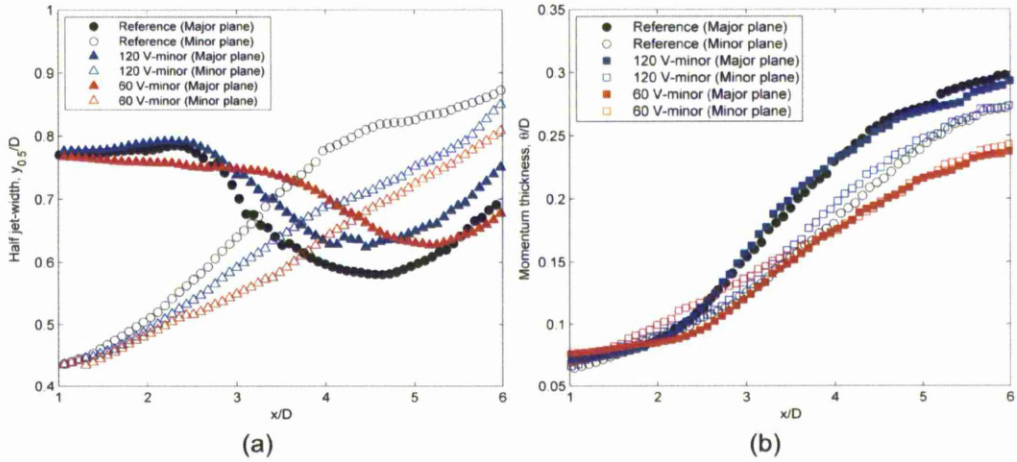

Figure 4.63 Graphs showing (a) half jet-width and (b) momentum thickness, for V-minor nozzle configurations

different to what was noticed for the V-major case, where the jet-spread rate along the minor plane was higher compared to the major plane. Due to the spread rate difference between the two shear layers, a jet with a larger cross-section at the cross-over point is expected.

The momentum thickness plots, in Fig. 4.63 (b), show that the sharpness of the V-minor notch alters the mixing characteristics of each jet. It is interesting to see that for most of the measurement range, the 60° V-minor nozzle has the lowest momentum thickness compared to the less sharp 120° V-minor and the reference case. This indicates that the increased sharpness does not necessarily equate to improved mixing throughout the whole measurement range. This finding agrees well with flow visualisation results along both streamwise and cross-stream directions. However it must be noted, that the peaks do marginally increase the momentum thickness in the near-nozzle region of the jet, when viewed along the minor plane view. So although the sharper nozzle design does not promote better mixing, the peaks on the other hand do perform better in the upstream region. Interestingly, the 120° V-minor nozzle and reference case produce nearly identical momentum thickness graphs. Subtle differences between the two plots are detected, within the downstream range of 3D to 5D. In this range, the 120° V-minor nozzle performs best along the minor plane, which is the plane that consists of the nozzle peaks. So although there are only marginal improvements, nevertheless it has been shown consistently that peaks, compared to troughs, produce beneficial mixing characteristics.

A comparison of the half jet-widths between V-major and V-minor nozzle designs is not worthwhile considering, since both nozzle designs produce drastically different flow behaviour. However it was shown that axis-switching was suppressed when peaks were added along the major plane of an elliptic nozzle and delayed, when added along the minor

plane of the ellipse. Thus the positioning of peaks and troughs is critical in the evolution of an IO elliptic jet.

The momentum thickness plots shown in Figs. 62(b) and 63(b) however do elucidate the mixing performance of each jet and are worth comparing. Viewing the plots of all nozzles along the major plane view, it can be seen that the V-major geometries always produce higher momentum thickness values, thus showing that peaks, instead of troughs are more beneficial. However it is also worth noting that increasing the sharpness of the peaks and troughs for both nozzles, leads to a change in the rate at which the momentum thickness grows but does not necessarily lead to an overall increase of the maximum attainable value. Along the minor plane view and interesting observation can be made in Figs. 62(b) and 63(b). For the less sharp nozzle geometries, both peaks and troughs seem to behave similarly. However when the sharpness is increased, it can be seen that the troughs benefits more that the peaks. This shows that depending on the positioning of the troughs, effective mixing can be achieved by using the sharper V-notch. This statement is demonstrated when one compares the momentum thickness associated with the 60° V-major nozzle to the 60° V-minor nozzle along the minor plane view. The former nozzle attains a higher momentum thickness than the corresponding momentum thickness of the latter nozzle, nearly throughout the measurement plane. This shows that along the minor plane view a trough of increased sharpness should be preferred for mixing applications.

Summarising the previous comparison, it was shown that the V-major nozzle geometry is better suited for mixing applications. However for a predictable manipulation of the axis-switching location of an elliptic jet of AR 2, the V-minor configuration performs best.

4.3 Chapter summary and conclusions

Experimental results showed that lip modifications in the form of V-notched cuts imposed on elliptic nozzles produced large differences in the resultant flow-field compared to a reference nozzle without such modifications.

The vortex dynamics associated with V-major nozzle were more convoluted compared to the reference and V-minor cases. A faster transition to turbulence and a reduced potential core length as well as the generation of streamwise vortices suggested an increased interaction between the jet and the surrounding ambient fluid. Additionally, increasing the sharpness of the V-notch resulted in an increase of the flow activity, especially in the near-nozzle region. Another important finding worth mentioning is that the use of the V-major nozzle geometry suppressed axis-switching.

The V-minor nozzle resulted in a stable shear layer with few interactions between the jet and the surrounding ambient fluid. Cross-stream PIV results measured weak streamwise vortices, possibly causing the interaction reduction. Contrary to the V-major case, as the V-notch sharpness increased, a resultant reduction in the flow interactions and flow stresses was measured. The use of this nozzle also affected axis-switching. It was shown that the location at which the jet undergoes axis-switching is found further downstream compared to the reference case. Additionally, when the nozzle sharpness is increased, the axis-switching location shifts further downstream.

5 CONCLUSIONS AND FUTURE WORK

a) Conclusions

Circular

Two experimental methods were implemented in order to understand the effects that A- and V-notched IO nozzles have on the jet flow field. The first method was flow visualisation which provided a qualitative comparison between the flow fields and helped identify the flow behaviour associated with each nozzle. Additionally, information indentifying flow attributes such as the formation of large scale coherent structures, streamwise vortices and braid vortices, as well as their interactions and how they transist to turbulence was presented. The second experimental method made use of the quantitative PIV measurement technique, in order to measure the velocity fields associated with each nozzle case and from that, calculate several flow parameters used for comparative purposes.

Both nozzles showed similar flow behaviour and the use of flow visualisation helped trace the movement of large scale structures. It was shown that when the main ring vortices were viewed along the PP view, they moved towards the nozzle centreline, while along the TT view a lateral movement away from the nozzle centreline was highlighted. This inferred that jets issued from A- and V-notched nozzles underwent axis-switching. Flow visualisation results showed that smoothly contoured peaks, such as those found on the AR2 and 4 V-notched nozzles, are more beneficial for the generation of extraneous flow structures, as well as the increase in jet spread. Additionally, the smooth peaks increased the generation of streamwise vortical structures, which have been shown to increase the momentum exchange between the jet and the surrounding fluid (Longmire *et al.*, 1992a). On the other hand troughs were not so sensitive to the exact geometry of lip contour, however smooth contoured troughs, such as those found on A-notched nozzles did influence the spreading of the jet, especially in the low aspect-ratio case. For both nozzle configurations, increasing the nozzle aspect-ratio led to flow field with less coherent structuring and more visually intense streamwise vortices. Large scale structures were observed to break down faster compared to the less sharp nozzle cases.

The use of PIV measurements along both streamwise and cross-stream directions reinforced the flow visualisation results. Movement, bending direction and rotational sense of the main ring vortices as well as streamwise vortices was consistent in both experimental techniques. Smooth peaks were shown to increase shear layer vorticity as well as Reynolds stress and TKE values, however in most cases, increasing the nozzle aspect-ratio did not invoke favourable changes to the magnitudes of the measurable flow quantities. However, the shortening of the jet potential core and an upstream shift of the high stress regions provides

preferential mixing in the near-nozzle region. Thus the choice of nozzle aspect-ratio should be carefully considered depending on the application it is intended for.

The half jet-width plots showed quantitatively, that circular A- and V-notched nozzles undergo axis-switching, thus verifying the flow visualisation observations. Since axis-switching is present in both nozzle configurations (A- and V-notched), it indicates that axis switching in notched nozzles is robust and not highly sensitive towards the exact configuration of the peaks and troughs. Although the AR2 V-notched nozzle did show preferential axis switching behaviour compared to the rest of the nozzles. Results presented compared well and reinforced previous work on notched nozzles (New and Tsai, 2007)

The momentum thickness plots suggested that increasing the nozzle aspect ratio did not necessarily lead to further significant increase in the momentum thickness. Collating with earlier observations from the half jet-width profiles, it has been shown that increasing the nozzle aspect ratio beyond AR2 confers little further favourable flow effects in terms of jet-widths and momentum thickness. Instead, increasing the aspect ratio mainly accentuates the underlying mechanisms responsible for the variations in the half jet-widths along the PP-plane, which lead to an upstream shift of the profile, thus increasing mixing in the near-nozzle region.

Elliptic

An experimental study has been performed on V-notched elliptic nozzles using flow visualisation techniques and PIV measurements to investigate their effects on the underlying vortex flow behaviour. Streamwise flow visualisation observations reveal that the flow interactions associated with elliptic ring-vortices produced by the V-major nozzles were more convoluted than those of the reference nozzle and V-minor nozzles. It was also shown that the V-major nozzles transited to turbulence faster due to the interactions between the visually intense streamwise vortices forming at the peaks and troughs and the elliptic main ring vortices. These effects were intensified as the included V-notch angle was reduced. Cross-stream LIF results confirmed that outward spreading streamwise vortices were persistently present along the major-planes of the reference and V-major nozzles, while the V-minor nozzles effectively suppressed their formation. Increasing the sharpness in the V-major nozzle produced a more convoluted flow field and promoted stronger streamwise vortices which assisted the faster breakdown of large-scale structures. The V-minor nozzles resulted in a stable shear layer with few interactions and weaker streamwise vortices. The increased sharpness reduced the flow interactions even further.

Quantitative results agreed well with the flow visualisations results. Along the streamwise direction, it was shown that between all nozzle geometries, the 60° V-minor nozzle produced

the largest potential core, inferring that reduced jet mixing takes place. On the other hand, the 60° V-major nozzle produced the shortest potential core, which showed an increased amount of interactions between the jet and ambient fluid. Additionally, it was demonstrated what in all nozzle cases, the planes consisting of peaks influenced the flow field more than the troughs. Experiments along the cross-stream also confirmed the influence of the nozzle peaks on the flow field. Results showed that peaks were linked to high stress regions and by increasing the peak sharpness, the flow activity was increased, especially in the near-nozzle region.

Finally the half jet-width and momentum thickness of all nozzles were assessed. It was found that the, V-minor geometry delays axis-switching in a predictable manner while the V-major notch suppresses axis-switching altogether. By increasing the sharpness of the nozzles both effects were exaggerated and it was observed that the cross-over point for the V-minor nozzle moved downstream by approximately one and a half diameters, compared to the reference nozzle. In terms of mixing, of the two nozzle geometries, the V-major geometry produced the larger momentum thickness, while the 60° V-minor produced the lowest, even lower than the reference case. Additionally when the sharpness of the V-major case was increased, the near field momentum thickness became dominant, but was reduced in the downstream region. Thus, depending on the application, the effective use of geometrical modifications on an elliptic nozzle of AR2, can result in significant alterations to the underlying jet behaviour.

b) Future work

An extensive experimental study was conducted on IO circular and elliptic nozzles, however some fundamental questions still remain unanswered. Due to time constraints, only low Reynolds number experiments were conducted and thus the effects that notches and flow forcing have on the flow field of high Re number turbulent jets has not been investigated. Due to the application of such nozzles in high Re and Mach number flows, increasing the Reynolds number at which the experiments are conducted would be beneficial as a future project. A study at a Reynolds number of Re$\cong 10^5$ would provide useful insight to the jet flow field properties, including compressibility effects. However, such a study would necessarily be conducted in air and thus the use of instantaneous flow visualisation capability would be lost. Thus flow visualisation of flow structures and effects caused by mechanisms such as pairing will not be possible. Additionally, the construction of a suitable test facility will be required which inevitably will increase the project cost substantially. An alternative solution would be to use computational fluid dynamics (CFD) to assist with the high Reynolds number study. CFD software packages such as Fluent and OpenFoam can be used. The former package is a commercial product available at the University of Liverpool,

while the latter is an open source software which can be downloaded and run without license fees. Additionally, OpenFoam incorporates a wide range of flow solvers for applications in compressible and incompressible fluids as well as large eddy simulation (LES) and direct numerical simulation (DNS) numerical techniques.

Apart from the high Re number study, a supplementary experimental or computational study of small duration could be conducted to elucidate the relationship between nozzle notch location and size with main ring vortex bending and how this influences the braid region of the jet. As stated in earlier sections, the exact flow development is not completely understood. For example, the link between the elliptic 60° V-major nozzle and the formation of "moustache-shaped" main ring vortices, observed during cross-stream LIF flow visualisation, cannot be conclusively explained due to experimental limitations. Possibly the use of smaller downstream intervals during cross-stream testing would highlight this behaviour. Alternatively, with the use of more advanced PIV setups, such as volume mapping tomographic PIV or a volumetric three-component velocimetry (V3V) system as used by Troolin and Longmire (2010), or even by computational means, one could measure the flow field parameters within a specific volume of fluid or calculate them within a three-dimensional computational domain. By tracking vorticity or pressure iso-surfaces a more comprehensive understanding can be attained, and thus a more realistic flow representation can be proposed as shown by Husain and Hussain,(1993).

Finally, due to limitations of the current experimental arrangement, jet-mixing, an important flow phenomenon, could not be measured. A way of quantifying jet mixing is to use the planar laser-induced fluorescence (PLIF) optical measuring technique. Although high Reynolds stress regions are linked to increased mixing, the lack of mixing quantifiability, eliminates any meaningful comparison between nozzle designs. A future study could incorporate PLIF measurements and thus address the applicability and suitability issue, of the current IO nozzle designs, in industrial applications requiring high mixing. Suppression of aeroengine overhead noise as well as internal combustion engines, especially diesel technology where more a homogeneous fuel/air mixture produces the lowest emissions, benefit from mixing.

Future work includes, planning of manuscript preparation with intent to publish parts of the current research, which have not been included in this thesis, as a lead author.

APPENDIX

c) Averaging script:

```
% PIV averaging script
clear;
clc;
A = zeros(29253,4); % creating zero matrix
B = zeros(29253,3); % creating zero matrix
C = zeros(29253,5); % creating zero matrix
D = zeros(29253,5); % creating zero matrix
E = zeros(29253,3); % creating zero matrix

for k = 0:999           % number of loops or files
    if k < 10
        M = dlmread(strcat('vel000',num2str(k),'.txt'),'\t','A1..D29253');    % reads d↙
elimited velocity txt files
        N = dlmread(strcat('vor000',num2str(k),'.txt'),'\t','A1..C29253');    % reads d↙
elimited vor txt files
    elseif (k < 100) && (k > 9)
        M = dlmread(strcat('vel00',num2str(k),'.txt'),'\t','A1..D29253');    % reads de↙
limited vel txt files
        N = dlmread(strcat('vor00',num2str(k),'.txt'),'\t','A1..C29253');    % reads de↙
limited vor txt files
    elseif (k < 1000) && (k > 99)
        M = dlmread(strcat('vel0',num2str(k),'.txt'),'\t','A1..D29253');    % reads del↙
imited vel txt files
        N = dlmread(strcat('vor0',num2str(k),'.txt'),'\t','A1..C29253');    % reads del↙
imited vor txt files
    else
        M = dlmread(strcat('vel',num2str(k),'.txt'),'\t','A1..D29253');    % reads deli↙
mited vel txt files
        N = dlmread(strcat('vor',num2str(k),'.txt'),'\t','A1..C29253');    % reads deli↙
mited vor txt files
    end
    A = A + M;          % adding to zero vel matrix
    B = B + N;          % adding to zero vor matrix
end

A = A/1000;
B = B/1000;
C = [A B(:,3)];     % combine vel and vor
dlmwrite('averaged_vel_vor.dat',C,'\t');    % write averaged result to delimited txt fi↙
le

for j = 1:29253
        D(j,1) = A(j,1);
        D(j,2) = A(j,2);
end

for k = 0:999           % number of loops or files
    if k < 10
        P = dlmread(strcat('vel000',num2str(k),'.txt'),'\t','A1..D29253');    % reads d↙
elimited vel txt files
    elseif (k < 100) && (k > 9)
        P = dlmread(strcat('vel00',num2str(k),'.txt'),'\t','A1..D29253');    % reads de↙
limited vel txt files
    elseif (k < 1000) && (k > 99)
        P = dlmread(strcat('vel0',num2str(k),'.txt'),'\t','A1..D29253');    % reads del↙
imited vel txt files
    else
        P = dlmread(strcat('vel',num2str(k),'.txt'),'\t','A1..D29253');    % reads deli↙
mited vel txt files
    end
    for j = 1:29253
```

```
D(j,3) = D(j,3) + (P(j,3)-A(j,3))*(P(j,3)-A(j,3));                % adding (u')^2 to ze↙
ro matrix first column
        D(j,4) = D(j,4) + (P(j,4)-A(j,4))*(P(j,4)-A(j,4));                % adding (v')↙
^2 to zero matrix second column
        D(j,5) = D(j,5) + (P(j,3)-A(j,3))*(P(j,4)-A(j,4));                % adding (u'v↙
') to zero matrix third column
    end
end

for j = 1:29253
       D(j,3) = D(j,3)/1000;
       D(j,4) = D(j,4)/1000;
       D(j,5) = D(j,5)/1000;
end

dlmwrite('averaged_turbulent_stresses.dat',D,'\t');    % write result to delimited txt ↙
file

for j = 1:29253
        E(j,1) = A(j,1);
        E(j,2) = A(j,2);
end

for k = 0:999           % number of loops or files
    if k < 10
        Q = dlmread(strcat('vel000',num2str(k),'.txt'),'\t','A1..D29253');    % reads d↙
elimited vel txt files
    elseif (k < 100) && (k > 9)
        Q = dlmread(strcat('vel00',num2str(k),'.txt'),'\t','A1..D29253');    % reads de↙
limited vel txt files
    elseif (k < 1000) && (k > 99)
        Q = dlmread(strcat('vel0',num2str(k),'.txt'),'\t','A1..D29253');    % reads del↙
imited vel txt files
    else
        Q = dlmread(strcat('vel',num2str(k),'.txt'),'\t','A1..D29253');    % reads deli↙
mited vel txt files
    end
    for j = 1:29253
    E(j,3) = E(j,3) + (Q(j,3)-A(j,3))*(Q(j,3)-A(j,3))+ (Q(j,4)-A(j,4))*(Q(j,4)-A(j,4));↙
  % adding (w')^2+(v')^2 to zero matrix third column
    end
end

for j = 1:29253
    E(j,3) = E(j,3)/1000;
end

dlmwrite('tke_averaged.dat',E,'\t');    % write result to delimited txt file
```

d) Half jet-width script:

```
        %% Initialisation - Half jet width
clear;
clc;
%A=load ('averaged_vel_vor_ref.dat');
x=A(:,1);
x=A(:,1);
y=A(:,2);
u=A(:,3);
v=A(:,4);
vort=A(:,5);
uslice=zeros(73,1);
i=0; % Counter for uslice variable. I will take values from 1 to 73
sp=15;
offset=sp;
mean_height_x=input('please enter nozzle mean height along x-direction (mm): ') % nozzl↙
e mean height x-direction Note: use the same as in Tecplot
k=(99-sp); %Counter for while loop below. The loop will loop 73 times,
           %going through all the data
mom_thick=zeros(k,1);
z=0;
dy=x(2)-x(1);

      %% Main program
for k=1:k %x/D position
z=z+1; %% Loop counter  (x/D position in grid units)
j=sp;
i=0;
top_momentum=0;
bottom_momentum=0;
while j<7128
i=i+1;
uslice(i)=u(j);
j=j+99;
end;
Uo=max(uslice); %find the maximum velocity in the velocity profile u(y)
norm=uslice/Uo;
[trash, centre] = min(abs(norm-1)); % position of Uo velocity (centreline for symmetric↙
 nozzles).
bottom_norm=norm(1:centre); % Lower half of the non-dimensionalised u velocity (norm)
bottom_norm=flipud(bottom_norm); %Flip the array in order to have high values on top.
top_norm=norm(centre:73); %Upper half of the non-dimensionalised u velocity (norm)
[trash, bottom_boundary] = min(abs(bottom_norm-0.5));
bottom_boundary_interpolated=bottom_boundary+((0.5 - bottom_norm(bottom_boundary))*(1/(↙
bottom_norm(bottom_boundary+1)-bottom_norm(bottom_boundary))));
[trash, top_boundary] = min(abs(top_norm-0.5));
top_boundary=top_boundary+1; % Choose the next grid point (y) as per usual.
top_boundary_interpolated=(top_boundary)-((0.5 - top_norm(top_boundary))*(1/(top_norm(t↙
op_boundary-1)-top_norm(top_boundary))));
half_jet_bottom(k)=bottom_boundary_interpolated*dy;
half_jet_top(k)=top_boundary_interpolated*dy;
sp=sp+1;
end
        %% Plotting Section
grid_size=(1:k); %Grid size, used to determine physical dimensions of measurement area ↙
(x-direction)
x_D=((grid_size*dy)- mean_height_x)/20;
x_D=x_D+offset*dy/20;
y_average=((half_jet_top+ half_jet_bottom)/40);
hold on
scatter(x_D,y_average,30,'r','o')
AXIS([0,6,0.4,1])
```

e) Momentum thickness script:

```
        %% Momentum_thickness - initialisation
clear;
clc;
A=load ('averaged_vel_vor_ref.dat');
x=A(:,1);
x=A(:,1);
y=A(:,2);
u=A(:,3);
v=A(:,4);
uslice=zeros(73,1);
i=0; % Counter for uslice variable. I will take values from 1 to 73
sp=1;
mean_height_x=input('please enter nozzle mean height along x-direction (mm): ') % nozzl↙
e mean height x-direction Note: use the same as in Tecplot
k=(99-sp); %Counter for while loop below. The loop will loop 73 times,
          %going through all the data
mom_thick=zeros(k,1);
z=0;
dy=x(2)-x(1); %Physical mesh dimentions (m)

      %% Main program
for k=1:k %x/D position
z=z+1; %% Loop counter  (x/D position in grid units)
j=sp;
i=0;
top_momentum=0;
bottom_momentum=0;
while j<7128
i=i+1;
uslice(i)=u(j);
j=j+99;
end;
Uo=max(uslice); %find the maximum velocity in the velocity profile u(y)
norm=uslice/Uo;
[trash, centre] = min(abs(norm-1)); % position of Uo velocity (centreline for symmetric↙
 nozzles).
bottom_norm=norm(1:centre); % Lower half of the non-dimensionalised u velocity (norm)
top_norm=norm(centre:73); %Upper half of the non-dimensionalised u velocity (norm)
[trash, bottom_boundary] = min(abs(bottom_norm-0.1));
[trash, top_boundary] = min(abs(top_norm-0.1));
top_boundary=top_boundary+centre;
first=norm;
second=1-norm;
int=(first.*second)*(dy/20); % Calculation of the momentum thickness integral
for i=centre:top_boundary
top_momentum=top_momentum+int(i);  %%Calculation of top shear layer mom thickness
end
for i=bottom_boundary:centre
bottom_momentum=bottom_momentum+int(i); %%Calculation of bottom shear layer mom thickne↙
ss
end
mom_thick(k)=(top_momentum+bottom_momentum)/2; %Average between top and bottom mom thic↙
kness
sp=sp+1;
end
        %% Plotting Section
grid_size=(1:k); %Grid size, used to determine physical dimensions of measurement area ↙
(x-direction)
x_D=((grid_size*dy)- mean_height_x)/20;
plot(x_D,mom_thick,'r');
AXIS([0,6,0,0.3]);
```

REFERENCES

Andreopoulos J 1985 On the structure of jets in a cross-flow *Journal of Fluid Mechanics* **157** 163-97

Angele K, Kurimoto N, Suzuki Y and Kasagi N 2006 Evolution of the streamwise vortices in a coaxial jet controlled with micro flap actuators *Journal of Turbulence* **7** 1-19

Arms R J and Hama F R 1965 Localized-induction concept on a curved vortex and motion of an elliptic vortex ring *Physics of Fluids* **8** 553-9

Boeing 2010 The Boeing Company, http://www.newairplane.com/environment/

Bradbury L J S and Khadem A H 1975 Distortion of a jet by tabs *Journal of Fluid Mechanics* **70** 801-13

Callender B, Gutmark E and Martens S 2005 Far-field acoustic investigation into chevron nozzle mechanisms and trends *AIAA Journal* **43** 87-95

Cantwell B J 1986 Viscous starting jets *Journal of Fluid Mechanics* **173** 159-89

Chassain.P, George J, Claria A and Sananes F 1974 Physical characteristics of subsonic jets in a cross-stream *Journal of Fluid Mechanics* **62** 41-64

Cimbala J M, Nagib H M and Roshko A 1988 Large structure in the far wakes of two-dimensional bluff bodies *Journal of Fluid Mechanics* **190** 265-98

Crighton D G 1973 Instability of an elliptic jet *Journal of Fluid Mechanics* **59** 665-72

Crow S C and Champagne F H 1971 Orderly structure in jet turbulence *Journal of Fluid Mechanics* **48** 547-91

Dhanak M R and Debernardinis B 1981 The evolution of an elliptic vortex ring *Journal of Fluid Mechanics* **109** 189-216

Durst F 2008 *Fluid mechanics : an introduction to the theory of fluid flows / Franz Durst* (Springer: Berlin)

Fincham A M and Spedding G R 1997 Low cost, high resolution DPIV for measurement of turbulent fluid flow *Experiments in Fluids* **23** 449-62

Ganapathisubramani B, Longmire E K, Marusic I and Pothos S 2005 Dual-plane PIV technique to determine the complete velocity gradient tensor in a turbulent boundary layer *Experiments in Fluids* **39** 222-31

Gharib M, Rambod E and Shariff K 1998 A universal time scale for vortex ring formation *Journal of Fluid Mechanics* **360** 121-40

Glezer A 1988 The formation of vortex rings *Physics of Fluids* **31** 3532-42

Grinstein F F 2001 Vortex dynamics and entrainment in rectangular free jets *Journal of Fluid Mechanics* **437** 69-101

Grinstein F F, Gutmark E and Parr T 1995 Near-field dynamics of subsonic free square jets - a computational and experimental-study *Physics of Fluids* **7** 1483-97

Gutmark E and Ho C M 1983 Preferred modes and the spreading rates of jets *Physics of Fluids* **26** 2932-8

Gutmark E J and Grinstein F F 1999 Flow control with noncircular jets *Annual Review of Fluid Mechanics* **31** 239-72

Ho C M and Gutmark E 1987 Vortex induction and mass entrainment in a small-aspect-ratio elliptic jet *Journal of Fluid Mechanics* **179** 383-405

Hu H, Kobayashi T, Saga T, Segawa S and Taniguchi N 2000a Particle image velocimetry and planar laser-induced fluorescence measurements on lobed jet mixing flows *Experiments in Fluids* **29** S141-S57

Hu H, Kobayashi T, Saga T, Taniguchi N, Liu H X and Wu S S 1999 Research on the rectangular lobed exhaust ejector/mixer systems *Transactions of the Japan Society for Aeronautical and Space Sciences* **41** 187-94

Hu H, Saga T, Kobayashi T and Taniguchi N 2000b Research on the vortical and turbulent structures in the lobed jet flow using laser induced fluorescence and particle image velocimetry techniques *Measurement Science & Technology* **11** 698-711

Hu H, Saga T, Kobayashi T and Taniguchi N 2001a A study on a lobed jet mixing flow by using stereoscopic particle image velocimetry technique *Physics of Fluids* **13** 3425-

41
Hu H, Saga T, Kobayashi T and Taniguchi N 2002a Mixing process in a lobed jet flow *AIAA Journal* **40** 1339-45
Hu H, Saga T, Kobayashi T and Taniguchi N 2002b Simultaneous measurements of all three components of velocity and vorticity vectors in a lobed jet flow by means of dual-plane stereoscopic particle image velocimetry *Physics of Fluids* **14** 2128-38
Hu H, Saga T, Kobayashi T, Taniguchi N and Yasuki M 2001b Dual-plane stereoscopic particle image velocimetry: system set-up and its application on a lobed jet mixing flow *Experiments in Fluids* **31** 277-93
Hulst H C 1981 *Light scattering by small particles / by H.C. van de Hulst* (Dover Publications: New York)
Husain H S and Hussain F 1983 Controlled excitation of elliptic jets *Physics of Fluids* **26** 2763-6
Husain H S and Hussain F 1991 Elliptic jets. Part 2. Dynamics of coherent structures. Pairing *Journal of Fluid Mechanics* **233** 439-82
Husain H S and Hussain F 1993 Elliptic jets. Part 3. Dynamics of preferred mode coherent structure *Journal of Fluid Mechanics* **248** 315-61
Husain H S and Hussain F 1999 The elliptic whistler jet *Journal of Fluid Mechanics* **397** 23-44
Hussain A 1983 Coherent structures - reality and myth *Physics of Fluids* **26** 2816-50
Hussain A 1986 Coherent structures and turbulece *Journal of Fluid Mechanics* **173** 303-56
Hussain A and Hasan M A Z 1983 The whistler-nozzle phenomenon *Journal of Fluid Mechanics* **134** 431-58
Hussain A and Zaman K 1980 Vortex pairing in a circular jet under controlled excitation .2. coherent structure dynamics *Journal of Fluid Mechanics* **101** 493-544
Hussain A and Zaman K 1981 The preferred mode of the axisymmetric jet *Journal of Fluid Mechanics* **110** 39-71
Hussain A and Zedan M F 1978 Effects of initial condition on axisymmetric free shear-layer - effects of initial momentum thickness *Physics of Fluids* **21** 1100-12
Hussain F and Husain H S 1989 Elliptic jets. Part 1. Characteristics of unexcited and excited jets *Journal of Fluid Mechanics* **208** 257-320
Kambe T, Minota T and Takaoka M 1993 Oblique collision of two vortex rings and its acoustic emission *Physical Review E* **48** 1866
Keane R D and Adrian R J 1992 Theory of cross-correlation analysis of PIV images *Applied Scientific Research* **49** 191-215
Keiderling F, Kleiser L and Bogey C 2009 Numerical study of eigenmode forcing effects on jet flow development and noise generation mechanisms *Physics of Fluids* **21** 045106-1
Kelso R M, Lim T T and Perry A E 1996 An experimental study of round jets in cross-flow *Journal of Fluid Mechanics* **306** 111-44
Kida S, Takaoka M and Hussain F 1991 Collision of two vortex rings *Journal of Fluid Mechanics* **230** 583-646
Kim M J, Kim M M J, Bird J C, Park J, Powers T R and Breuer K S 2004 Particle image velocimetry experiments on a macro-scale model for bacterial flagellar bundling *Experiments in Fluids* **37** 782-8
Lee M and Reynolds W 1982 Bifurcating and blooming jets *Bulletin of the American Physical Society* **27** 1185
Liepmann D and Gharib M 1992 The role of streamwise vorticity in the near-field entrainment of round jets *Journal of Fluid Mechanics* **245** 643-68
Lighthill M J 1952 On sound generated aerodynamically .1. general theory *Proceedings of the Royal Society of London Series a-Mathematical and Physical Sciences* **211** 564-87
Lighthill M J 1962 Sound generated aerodynamically *Proceedings of the Royal Society of London Series a-Mathematical and Physical Sciences* **267** 147-82
Lighthill M J 1963 Jet noise *AIAA Journal* **1** 1507-17

Lim T T 1998 On the breakdown of vortex rings from inclined nozzles *Physics of Fluids* **10** 1666-71
Lim T T 2000 *Flow visualization : techniques and examples / editors, A.J. Smits, T.T. Lim* (Imperial College Press: London)
Lim T T, New T H and Luo S C 2006 Scaling of trajectories of elliptic jets in crossflow *AIAA Journal* **44** 3157-60
Lim T T and Nickels T B 1992 Instability and reconnection in the head-on collision of two vortex rings *Nature* **357** 225-7
Lockheed M 2010 Lockheed Martin Coorporation, http://www.lockheedmartin.com/.
Longmire E K and Duong L H 1996 Bifurcating jets generated with stepped and sawtooth nozzles *Physics of Fluids* **8** 978-92
Longmire E K, Eaton J K and Elkins C J 1992a Control of jet structure by crown-shaped nozzles *AIAA Journal* **30** 505-12
Longmire E K, Eaton J K and Elkins C J 1992b Control of jet structure by crown-shaped nozzles *AIAA journal* **30** 505-10
Maxworth.T 1972 Structure and stability of vortex rings *Journal of Fluid Mechanics* **51** 15-32
Maxworth.T 1974 Turbulent vortex rings *Journal of Fluid Mechanics* **64** 227-40
Minota T, Kambe T and Murakami T 1988 Acoustic emission from interaction of a vortex ring with a sphere *Fluid Dynamics Research* **3** 357-62
Mollochristensen E, Kolpin M A and Martuccelli J R 1964 Experiments on jet flows and jet noise far-field spectra and directivity patterns *Journal of Fluid Mechanics* **18** 285-301
Monkewitz P and Bechert D 1988 Self-excited oscillations and mixing in a hot jet *Physics of Fluids* **31** 2386
Morris P J 1988 Instability of elliptic jets *AIAA Journal* **26** 172-8
Murakami E and Papamoschou D 2002 Mean flow development in dual-stream compressible jets *AIAA Journal* **40** 1131-8
Nathan G J, Hill S J and Luxton R E 1998 An axisymmetric 'fluidic' nozzle to generate jet precession *Journal of Fluid Mechanics* **370** 347-80
Nathan G J, Mi J, Alwahabi Z T, Newbold G J R and Nobes D S 2006 Impacts of a jet's exit flow pattern on mixing and combustion performance *Progress in Energy and Combustion Science* **32** 496-538
New T H 2008 Near-field developments of elliptic jets in crossflow *Journal of Turbulence* **9** 1-21
New T H, Lim T T and Tsai H M 2005 Vortical structures in a laminar V-notched indeterminate-origin jet *Physics of Fluids* **17** 1-14
New T H, Tan K S and Tsai H M 2007 Effects of noncircular collars on an axisymmetric jet *Physics of Fluids* **19** 084104-1
New T H and Tsai H M 2007 Experimental investigations on indeterminate-origin V- and A-notched jets *AIAA Journal* **45** 828-39
New T H and Tsovolos D 2009a Characterization of jets issuing from circular nozzles with A-shaped notch lip-modifications *Journal of Turbulence* **10** 1-20
New T H and Tsovolos D 2009b A Digital Particle Image Velocimetry Study on Jets Issuing from Hybrid Inclined Nozzles *Flow Turbulence and Combustion* **83** 485-509
New T H and Tsovolos D 2009c Influence of nozzle sharpness on the flow fields of V-notched nozzle jets *Physics of Fluids* **21** 084107-1
Oshima Y 1972 Motion of vortex rings in water *Journal of the Physical Society of Japan* **32** 1125-31
Pai S I 1954 *Fluid dynamics of jets* (New York: Van Nostrand)
Papamoschou D 1997 Mach wave elimination in supersonic jets *AIAA Journal* **35** 1604-11
Papamoschou D 2004 New method for jet noise reduction in turbofan engines *AIAA Journal* **42** 2245-53
Papamoschou D and Debiasi M 1999 Noise measurements in supersonic jets treated with the Mach wave elimination method *AIAA Journal* **37** 154-60

Papamoschou D and Debiasi M 2001 Directional suppression of noise from a high-speed jet *AIAA Journal* **39** 380-7

Parekh D, Leonard A and Reynolds W 1983 A vortex-filament simulation of a bifurcating jet *Bulletin of the American Physical Society* **28** 1353

Prasad A K and Adrian R J 1993 Stereoscopic particle image velocimetry applied to liquid flows *Experiments in Fluids* **15** 49-60

Quinn W R 2005a Measurements in the near flow field of an isosceles triangular turbulent free jet *Experiments in Fluids* **39** 111-26

Quinn W R 2005b Near-field measurements in an equilateral triangular turbulent freejet *AIAA Journal* **43** 2574-85

Raffel M, - 1998 *Particle image velocimetry : a practical guide / M. Raffel, C.E. Willert, J. Kompenhans* (Springer: Berlin)

Raman G and Cain A B 2002 Innovative actuators for active flow and noise control *Proceedings of the Institution of Mechanical Engineers Part G-Journal of Aerospace Engineering* **216** 303-24

Reeder M F and Samimy M 1996 The evolution of a jet with vortex-generating tabs: Real-time visualization and quantitative measurements *Journal of Fluid Mechanics* **311** 73-118

Rembold B, Adams N A and Kleiser L 2002 Direct numerical simulation of a transitional rectangular jet *International Journal of Heat and Fluid Flow* **23** 547-53

Reynolds W C, Parekh D E, Juvet P J D and Lee M J D 2003 Bifurcating and blooming jets *Annual Review of Fluid Mechanics* **35** 295-315

Samimy M, Kim J H, Kastner J, Adamovich I and Utkin Y 2007 Active control of high-speed and high-Reynolds-number jets using plasma actuators *Journal of Fluid Mechanics* **578** 305-30

Samimy M, Zaman K and Reeder M F 1993 Effect of tabs on the flow and noise field of an axisymmetrical jet *AIAA Journal* **31** 609-19

Schadow K C, Gutmark E, Parr D M and Wilson K J 1988 Selective control of flow coherence in triangular jet *Experiments in Fluids* **6** 129-35

Shu F 2005 Flow physics of indeterminate origin nozzle jets and passive control of sprays. (United States -- Indiana: Purdue University) p 186

Shu F, Plesniak M W and Sojka P E 2005 Indeterminate-origin nozzles to control jet structure and evolution *Journal of Turbulence* **6**

Smith T, Cain A and Chenault C 2001 Numerical simulation of enhanced mixing in jet plumes using pulsed blowing *Journal of Aircraft* **38** 458-63

Suzuki H, Kasagi N and Suzuki Y 2004 Active control of an axisymmetric jet with distributed electromagnetic flap actuators *Experiments in Fluids* **36** 498-509

Tam C K W and Zaman K 2000 Subsonic jet noise from nonaxisymmetric and tabbed nozzles *AIAA Journal* **38** 592-9

Troolin D R and Longmire E K 2010 Volumetric velocity measurements of vortex rings from inclined exits *Experiments in Fluids* **48** 409-20

Tsovolos D and New T H 2008 A flow field investigation on crown-shaped nozzles. In: *7th EUROMECH fluid Mechanics Conference,* (UK, Manchester)

Webster D R and Longmire E K 1997 Vortex dynamics in jets from inclined nozzles *Physics of Fluids* **9** 655-66

Webster D R and Longmire E K 1998 Vortex rings from cylinders with inclined exits *Physics of Fluids* **10** 400-16

Widnall S E, Bliss D B and Tsai C Y 1974 Instability of short waves on a vortex ring *Journal of Fluid Mechanics* **66** 35-47

Widnall S E and Sullivan J P 1973 Stability of vortex rings *Proceedings of the Royal Society of London Series a-Mathematical Physical and Engineering Sciences* **332** 335-53

Wiltse J and Glezer A 1993 Manipulation of free shear flow using piezoelectric actuators *Journal of Fluid Mechanics* **249** 261

Wlezien R W and Kibens V 1986 Passive control of jets with Indeterminate origins *AIAA journal* **24** 1263-70

Wong C Y, Nathan G J and Kelso R M 2008 The naturally oscillating flow emerging from a fluidic precessing jet nozzle *Journal of Fluid Mechanics* **606** 153-88

Yuan C C L, Krstic M and Bewley T R 2004 Active control of jet mixing *Iee Proceedings-Control Theory and Applications* **151** 763-72

Zaman K 1996 Axis switching and spreading of an asymmetric jet: The role of coherent structure dynamics *Journal of Fluid Mechanics* **316** 1-27

Zaman K and Hussain A 1980 Vortex pairing in a circular jet under controlled excitation .1. general jet response *Journal of Fluid Mechanics* **101** 449-91

Zaman K, Reeder M F and Samimy M 1994 Control of an axisymmetrical jet using vortex generators *Physics of Fluids* **6** 778-93

Zeng Y, New T H and Tsai H M 2009 On the use of notched collars on an axisymmetric jet *Experimental Thermal and Fluid Science* **33** 1029-34

PUBLICATIONS

Journal publications (co-authored):

- New T.H. and Tsovolos D. (2010) Cross-stream behaviour and flow characteristics of hybrid inclined nozzle jets *Journal of Turbulence* **11** N18
- New T.H. and Tsovolos D. (2009) Characterisation of jets issuing from circular nozzles with A-shaped notch lip-modifications *Journal of Turbulence* **10** 1-20
- New T.H. and Tsovolos D. (2008) Influence of nozzle sharpness on the flow fields on V-notched nozzle jets *Physics of Fluids* **20** 084107 1-18
- New T.H. and Tsovolos D. (2008) A digital particle image velocimetry study on jets issuing from hybrid inclined nozzles *Flow, Turbulence and Combustion* **83** 458-509

Conference publications:

- Tsovolos D. and New T.H. (2010) An Experimental Study on the Flow Behaviour of V-notched Elliptic Jets, *15th Int. Symp. on Applications of Laser Techniques to Fluid Mechanics*, Lisbon, Portugal
- Tsovolos D. and New T.H. (2009) Alteration of axis-switching behaviour in indeterminate-origin elliptic jets, *39th AIAA Fluid Dynamics Conference*, San Antonio, Texas, USA
- New T.H. and Tsovolos D. (2009) Flow characteristics of inclined elliptic nozzles, *Turbulence and Shear Flow Phenomena*, Seoul, Korea
- Tsovolos D. and New T.H. (2008) A flow field investigation on crown-shaped nozzles, *The 7th Euromech Fluid Mechanics Conference*, Manchester, UK